THE UNIVERSITY *of* EDINBURGH

Interaction of DC-DC Converters and Submarine Power Cables in Offshore Wind Farm DC Networks

Thomas B Wood

Doctor of Philosophy (PhD) – The University of Edinburgh – 2014

Abstract

Offshore wind power is attracting increasing levels of research and investment. The use of HVDC transmission and the development of DC grids are topics with similar high levels of interest that go hand in hand with the development of large scale, far from shore wind farms. Despite increased capital cost of some components, DC power transmission can have significant advantages over AC transmission, in particular in the offshore environment. These advantages are well established for large scale, long distance point to point transmission. This thesis assesses the suitability of a multiterminal DC power collection network, with short cables and relatively small amounts of power, addresses a number of the technical challenges in realising such a network and shows methods for overall system cost reduction.

Technical and modelling challenges result from the interaction between power electronic DC-DC converters and the cables in a DC transmission network. In particular, the propagation of the ripple current in bipole DC transmission cables constructed with a metallic sheath and armour is examined in detail. The finite element method is used to predict the response of the cable to the ripple current produced by the converters. These results are used along with wave propagation theory to demonstrate that cable design plays a crucial role in the behaviour of the DC system. The frequency dependent cable models are then integrated with time domain DC-DC converter models.

The work in the thesis is, broadly, in two parts. First, it is demonstrated that care and accuracy are required in modelling the cables in the DC transmission system and appropriate models are implemented and validated. Second, these models are combined with DC-DC converter models and used to demonstrate the practicality of the DC grid, make design recommendations and assess its suitability when compared with alternative approaches (e.g. AC collection and/or transmission).

Declaration

I declare that this thesis has been composed by myself, that the work herein is my own unless explicitly stated otherwise in the text and that the work has not been submitted for any other degree or professional qualification. Some of the work in the publications listed in Appendix F has been included in this thesis. All the work in these papers is attributable to myself.

Thomas B Wood

Acknowledgements

I would like to thank my supervisor Dr Ewen Macpherson for his support and his contribution to this work. His supervision has helped to make my time as a PhD student most enjoyable and productive.

I am also very grateful for the supervision provided by Dr Dominic Banham-Hall, Dr Stephen Finney, Dr Chris Smith and Dr Markus Mueller, who have all contributed their expertise to this work.

The friendship and support of colleagues throughout the School of Engineering and in GE have made my time enjoyable and greatly helped my studies. I would particularly like to thank Douglas Carmichael, Xiaoyun Rong, Dr Brian Flynn, Pasidu Pallawela and Dr Warren Blewitt who have contributed invaluable technical expertise and assistance.

My friends and family have reminded me that, no matter what, there is always more to life than writing a thesis.

List of Abbreviations

AC	Alternating Current
CIGRE	Conseil International des Grands Réseaux Électriques
CSC	Current Source Converter
DC	Direct Current
EMTP	ElectroMagnetic Transient Program
EPSRC	Engineering and Physical Sciences Research Council
ETP	Energy Technology Partnership
FEM	Finite Element Method
GCT	Gate Commutated Thyristor
GE	General Electric
GTO	Gate Turn-Off thyristor
HV	High Voltage
HVDC	High Voltage Direct Current
IGBT	Integrated Gate Bipolar Transistor
LV	Low Voltage
MMC	Modular Multilevel Converter
MOSFET	Metal Oxide Semiconductor Field Effect Transistor
O&M	Operation and Maintenance
PCC	Point of Common Coupling
PWM	Pulse Width Modulation
RMS	Route Mean Squared
SHE	Selective Harmonic Elimination

SLR	Series Load Resonant (converter)
UK	United Kingdom
VSC	Voltage Source Converter
XLPE	CROSS-Linked PolyEthylene

List of Symbols

α	Attenuation constant (m^{-1})
A	Area (m^2)
$\underline{A}$	Magnetic vector potential (Vsm^{-1})
β	Phase constant (radians/m)
$\underline{B}$	Magnetic flux density or magnetic B-field (T)
C	Capacitance (F)
C'	Capacitance per unit length (Fm^{-1})
C_{dc}	High voltage filter capacitance (F)
C_{res}	Resonant capacitor size (C)
C_U	Characteristic wind speed (ms^{-1})
δ	Skin depth (m)
$\underline{D}$	Displacement current (Am^{-2})
ε	Permittivity (Fm^{-1})
ε_0	Vacuum permittivity (Fm^{-1})
ε_r	Relative permittivity
$\underline{E}$	Electric field strength (Vm^{-1})
ESR	Equivalent series resistance (W)
ϕ	Scalar potential (V)
f	Frequency (Hz)
γ	Propagation constant (m^{-1})
G'	Conductance of the cable dielectric per unit length ($\Omega^{-1}m^{-1}$)
$\underline{H}$	Magnetic field strength (Am^{-1})

i	Instantaneous current (A)
I	Current (A)
I_{cable}	Current at mid-point of cable (A)
I_{HV}	Rectified, unfiltered, high voltage DC current (A)
I_{out}	Converter output current (A)
I_q	Charging Current (A)
I_R	Receiving end current (A)
I_S	Sending end current (A)
$\underline{J}$	Current density (Am^{-2})
k	Weibull shape parameter
λ	Wavelength (m)
l	Length (m)
L	Inductance (H)
L'	Inductance per unit length (Hm^{-1})
L_{res}	Resonant inductor size (H)
μ	Magnetic permeability (Hm^{-1})
μ_0	Vacuum permeability (Hm^{-1})
μ_r	Relative permeability
$P(U)$	Probability of a given wind speed
ρ	Resistivity (Ωm)
r_{core}	Core conductor radius (m)
r_{inner}	Inner conductor radius (m)
r_{outer}	Outer conductor radius (m)
R	Resistance (Ω)
R'	Resistance per unit length (Ωm^{-1})

σ	Conductivity ($\Omega^{-1}m^{-1}$)
t	Time (s)
T	Period of one switching cycle (s)
tan δ	Dielectric dissipation factor
THD	Total harmonic distortion of DC voltage (%)
U	Wind Speed (ms^{-1})
V	Voltage (V)
V_a	Phase Voltage (V)
V_b	Phase Voltage (V)
V_c	Phase Voltage (V)
V_{DC}	DC Voltage (V)
V_{out}	Output voltage of converter (V)
V_R	Receiving end Voltage (V)
V_{ripple}	Magnitudes of the frequency components of the ripple voltage (V)
V_S	Sending end voltage (V)
V_{sys}	Voltage at system node (V)
ω	Angular frequency (radians/s)
Y_C	Admittance of HV filter capacitor (Ω^{-1})
Y_{eq}	Equivalent shunt admittance (Ω^{-1})
Y_{HV}	Total admittance to I_{HV} of filter and system (Ω^{-1})
Y_{sys}	Admittance to I_{HV} of system (Ω^{-1})
Z_C	Characteristic Impedance (Ω)
Z_{eq}	Equivalent series impedance (Ω)
Z_r	Receiving end impedance (Ω)
Z_{send}	Impedance of the cable from the sending end (Ω)

Table of Contents

List of Figures

List of Tables

1 Introduction

1.1 UK and Crown Estate Strategy for Offshore Wind

Wind power is a key resource in meeting renewable energy targets at a European, UK and Scottish level. The UK Government has a target of 25GW installed capacity for the Round 3 offshore wind zones (Figure 1.2) [1, 2]. Many of these areas are far enough from shore to benefit from DC rather than AC power transmission [3, 4]. Offshore wind power is attracting increasing levels of research and investment. The use of HVDC transmission and the development of DC grids are topics with similar high levels of interest that go hand in hand with the development of large scale, far from shore wind farms. The capacity and number of developers between which each zone is divided are shown in Table 1.1 [2].

Figure 1.1. Barrow Offshore Wind Farm. By A. Dingley, edited by M. M. Karim [1].

The high level of interest across a range of sectors, including government, industrial and academic, is reflected in the funding for this PhD project. This has been provided jointly by the EPSRC, GE Power Conversion and the Energy Technology Partnership (ETP). These funding arrangements have led to very significant opportunities for collaboration and exchange of ideas both with GE Power

Conversion and with other member universities of the ETP, in particular the University of Strathclyde.

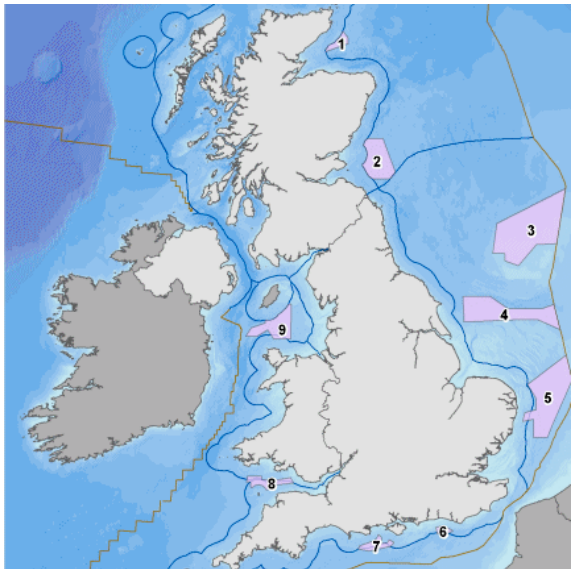

Figure 1.2. Crown Estate Round 3 Wind Farm Zones [2].

Zone	Indicative Capacity (MW)	Number of Developers
1	1300-1500	2
2	3465	1
3	9000-12800	4
4	4000	3
5	7200	2
6	665	1
7	900-1200	2
8	1500	1
9	4185	2

Table 1.1. Capacity and number of developers for each round 3 offshore wind zone [2].

The starting point for this research was a proposed solution from GE Power Conversion (previously known as Converteam) to use a DC grid to interconnect turbines, as well as for transmission to shore. To achieve this, it was proposed that each turbine have a DC-DC converter to step up the rectified generator output voltage to transmission level, as shown in Figure 1.3.

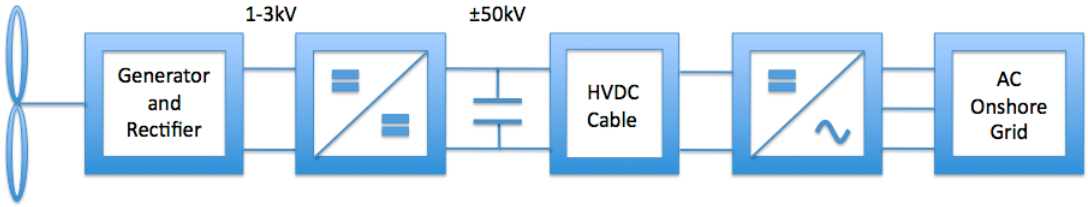

Figure 1.3. Block diagram for single wind turbine in a DC grid with approximate voltage levels.

1.2 Choice and Description of Research Topic

A wide range of topics were considered within this research area, including work on the generator, power electronic converters, the integrated system, control of the system and connection to the grid. A parallel PhD project is being undertaken by Yao Zhou (University of Edinburgh), investigating various topologies of DC-DC converter and their suitability for application in a HVDC grid.

The particular choice of research path was decided on after significant analysis of all parts of the electrical system had been undertaken. The research concentrates on the steady state modelling of a network of power electronic DC-DC converters forming a DC grid. Of particular interest are the current and voltage ripple produced by such converters, how they propagate in the cables of the DC grid and how to design the grid to mitigate any adverse effects that could be caused without significantly over engineering components in the system.

There are several reasons for this choice. Firstly, it makes this PhD project closely related to the parallel project on DC-DC converter design while still being clearly distinct. Secondly, due to the connection with GE Power Conversion, it is very important that this project make a practical contribution to the design process for the DC grid and this work dovetails well with the expertise GE Power Conversion have in the area. Finally, after reviewing a range of literature on the subject, it was found that the detailed modelling of ripple current behaviour in DC cables was an area where a significant contribution to knowledge could be made.

1.3 Project Philosophy and Contribution to Knowledge

The proposed use of a DC grid for the collection of power in a wind farm is a novel solution and the use of high power DC-DC converters is also novel. It has therefore been necessary to research very carefully the building blocks of the DC grid in order to identify the challenges this novel approach presents, to properly model the components, to assess its limitations and mitigation strategies required and to prove the practicality of such a DC grid.

Standard simulation software, in particular Simulink (by MathWorks) and PLECS (by Plexim), has been used extensively in this project. It has been an invaluable tool and produced very useful results as well as being a great aid to understanding. It is important to recognise the limitations of such software, particularly when dealing with an unusual HVDC converter topology, i.e. a DC-DC converter rather than standard Voltage Source Converter (VSC) or Current Source Converter (CSC), and when analysing behaviour of components which are operating outside conditions that may be normally anticipated, i.e. a DC cable operating with a significant amount of non-sinusoidal ripple current and voltage at a frequency (1kHz), which is also significantly different from standard AC frequency (e.g. 50Hz).

Uniquely detailed and accurate models of the DC grid have been developed. In particular, the application of the finite element method (FEM) to a range of detailed DC cable designs has led to very accurate assessment of the performance of these cables. For this, the software "Opera" (by Cobham Plc) has been used. When integrated with models for the DC-DC converters and high voltage filtering components, this has allowed a thorough understanding of the system behaviour in steady state conditions.

Major challenges exist in both the integration of different elements in the system model and in the scale of the system and resulting need for computing power and time. The system models have therefore been coded using MATLAB (MathWorks). This has enabled a rigorous approach to be adopted in connecting time domain and frequency domain models together.

The practical results of the research include:

- Assessment of cable losses throughout a DC grid, including variability along the length of a cable and mitigation.
- Predicting resonance and designing the system to avoid unwanted effects.
- Designing HV filtering.
- Assessment of the effect of DC-DC converter design on system requirements.
- Demonstrating the influence of the DC network behaviour on the operation of individual converters.
- Comparing a standard AC system solution with the proposed DC system.

The approach to cable modelling in particular has highlighted the importance of accurate assessment of cable parameters and the use of wave propagation theory in predicting cable behaviour and, in particular, resonance. These results and the methods used have applications beyond the work in this thesis including to the propagation of harmonics in AC systems and the prediction of resonance in systems with transmission cables of significant length, including many offshore systems (both AC and DC).

1.4 Validation and Verification

Due to the scale of the system being considered, experimental validation presents an obvious challenge. In particular, much of the work involves detailed modelling of power cables. There are two fundamental problems that need to be addressed:

- Power cables are expensive and bulky, so obtaining even a short section with which to validate estimates of per unit length cable parameters (inductance and resistance) is difficult and carrying out accurate measurements also problematic.
- The length of the cables involved is very important to system behaviour, but these lengths can be up to around 200km (see Figure 1.2).

Therefore, the approach has been taken is to scale the experiments in order to fit the available equipment. This has been done by altering the frequency range considered so that much smaller or shorter coaxial cables show the same behaviour as power cables. The frequencies have been adjusted as described.

- In chapter 3, the FEM is used to estimate per unit length cable parameters. In this case, the frequency of operation in the experimental work is adjusted in order to change the skin depth in cable metallic layers to compensate for their reduced thickness.
- In chapter 5, wave propagation theory is applied to the behaviour of ripple current in a transmission cable. In this case, the experimental frequency is adjusted so that the wavelength in the tested cable is reduced to compensate for its reduced length.

In addition to this, experimental validation of one DC-DC converter model is carried out in chapter 5. The converter used to carry out this validation was constructed by Xiaoyun Rong, for her BEng project [83]. Verification using Simulink is also carried out where appropriate; this is useful for ensuring that the validated models of each part of the network have been correctly coded in the MATLAB model of the entire network.

1.5 Thesis Outline

It is important to note that, throughout this thesis, when the AC components of ripple current and voltage in a DC system are calculated, the peak rather than the RMS value is always used. When AC systems are considered, for instance in section 7.2, then the AC RMS values are used.

Chapter 2 looks at other relevant research and investigates a number of background subjects, practical and theoretical, that are used in later chapters.

In chapter 3, modelling of a range HVDC cables using the finite element method (FEM) is carried out and experimentally validated.

Chapter 4 applies wave propagation theory to the behaviour of current and voltage ripple in a DC grid and uses this to explain the occurrence of resonance as well as demonstrate the importance of the results derived in chapter 3.

Chapter 5 outlines the challenges in producing an integrated model of a DC-DC converter connected to a cable with frequency dependent parameters. The approach to overcome these difficulties is described and experimentally validated. The development and verification of a multiterminal grid model is then undertaken. Resonance at a range of frequencies and locations in the system is predicted and analysed.

Chapter 6 implements the model developed in chapter 5 and analyses the effect of a range of different system components and operating conditions on system performance. The results of this chapter are used to give recommendations for a range of solutions to make the proposed DC grid topology practical.

Chapter 7 builds on the work in chapter 6 by analysing the performance of the grid in fault conditions and comparing its cable requirements to the AC alternative. A wider range of design specifications for the DC-DC converters are also considered and their effect on DC system operation analysed.

Chapter 8 analyses in more depth the approach to and results from the work and their implications for future development of the DC grid.

2 Offshore Wind Farms and Electrical Systems

2.1 Offshore Wind Power and Costs

2.1.1 Overview

Under a Crown Estate leasing scheme wind farms are in development in the seas around the UK. Rounds 1 and 2 of this leasing scheme were initiated in 2001 and 2003 and are expected to total between 5.6GW and 5.9GW of installed capacity on completion [5]. To date, there are in excess of 1,000 offshore wind turbines installed in the UK and their capacity is approaching 4GW.

Round 3, which was launched in 2010, is far more ambitious. The total capacity of the 9 sites is between 32.2GW and 36.5GW [5]. Construction is expected to begin in 2014 [6]. The largest single site is Dogger Bank; it is divided among 4 developers and has an indicative capacity of between 9GW and 12.8GW. In addition, a scheme overseen by the Scottish Government will lease 5 sites in Scottish Territorial waters with a capacity of 4.8GW. Scottish Enterprise estimate the potential investment in UK offshore wind markets over a 10 year period from 2011 is £100 billion [7].

In 2011 the cost of offshore wind energy was estimated to be in the range £149-£191/MWh. It has been claimed that cost reduction to £100/MWh is achievable by 2020, although it is acknowledged that this is a short timescale to overcome significant challenges [8]. Nevertheless, cost reduction for offshore wind energy is a major focus both for industry and the UK Government. Innovation is crucial in achieving this [8, 9].

The rapid expansion of offshore wind generation capacity and the need to innovate in order to reduce costs are the driving forces behind this research.

2.1.2 Offshore Wind Turbines and Wind Farms

Offshore wind turbines were originally the size of large onshore turbines, around 3MW. However, the size restrictions which result from transport networks do not apply in the offshore environment and larger turbines of 5MW and upwards are being produced for offshore use. The move to use a smaller number of larger turbines reduces costs for transport, foundations, cables and maintenance [10].

In [11], the cost of a 5MW offshore wind turbine is estimated at £6m. The power take-off system, which includes power converter, transformer, switchgear and cables contained in the turbine tower, is estimated to make up £400k of this total. The cost of the offshore turbines makes up a much lower proportion of the total wind farm cost than for an onshore wind farm. In addition to the increased cable costs (see below), the cost of foundation manufacture, for example, is estimated to be up to £3m for a 5MW offshore wind turbine [11].

The costs of subsea power cables are highly relevant to this project. The cost of the materials and laying is heavily dependent on distance from shore, water depth, seabed characteristics and weather conditions at the time of installation. In [12] the material cost of offshore power cables is estimated to be in the region of £330/m and the cost of installation around £300/m. These figures depend also on the size, power rating and voltage of the cables. Electrical transmission infrastructure typically makes up 10-20% of the capital outlay for an offshore wind farm [8].

2.1.3 Repair and Maintenance

Operation and maintenance (O&M) will make up between a quarter and a third of total offshore wind farm life cycle costs [9, 13]. These figures represent a significantly higher proportion than for onshore wind generation. Based on an estimate of 4,000 operating offshore wind turbines in the year 2020, this would amount to a total annual cost of £1.2bn/year [9]. Maintenance makes up the vast

majority of these costs and consists of both preventative and corrective maintenance. Average wind turbine failures during one year are estimated at 4-5% [14].

One of the major hurdles in the maintenance of offshore wind farms is access. Maintenance vessels are limited by the sea state, or significant wave height, in which they can safely transfer personnel onto a wind turbine. While preventative maintenance can usually be planned for times when the sea is sufficiently calm, corrective maintenance can be required at any time, including times when the sea state does not permit access. The result can be lost revenue from the wind farm for a period of time. Reliability is therefore critical in offshore wind turbines, more so than onshore where repairs can be more easily carried out as required [13]. It has been identified that for the electrical components (among others), innovative solutions are required to improve reliability and there is still much progress to be made [9, 13].

2.1.4 The Offshore Environment

In general, wind speeds tend to be higher, with lower turbulence levels, in the offshore environment compared to onshore. This is because the surface roughness is usually lower offshore than onshore. As a result, power outputs for offshore wind turbines can be expected to be more uniform, both in time and location, than onshore.

The wake effect is a significant source of turbulence offshore. Studies on this include both analytical work [15] and actual data from offshore wind farms [16]. The wake effect causes a reduction in power output from turbines away from the windward side of the wind farm. It is particularly pronounced when the wind direction is aligned to a row of turbines and can reduce output by as much as 40% [16].

2.2 AC Transmission and Limitations

Present day offshore wind farms in the UK are close to shore and use AC to collect and transmit power from the wind turbines. A typical block diagram for turbines

using fully fed power electronics (as opposed to a doubly-fed induction generator design in which only the slip energy is fed through the power converter) is shown in Figure 2.1. In this arrangement, the transformer is located in the turbine tower, near water level.

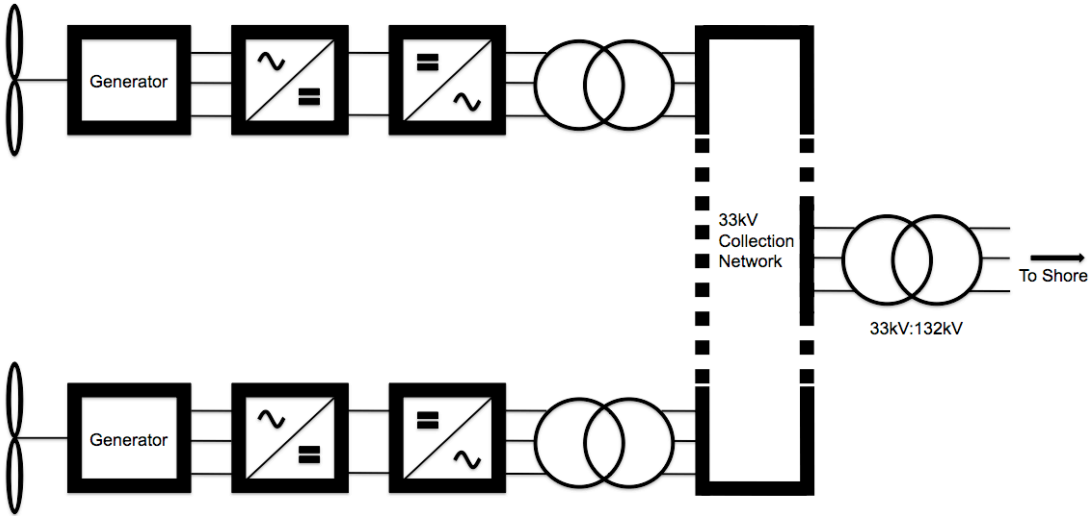

Figure 2.1. Block diagram of wind turbines with fully fed converters feeding into offshore AC system.

The output from the transformer in the turbine is typically 33kV. This power is fed into the collection network. An example of the layout for a collection network is shown in Figure 2.2.

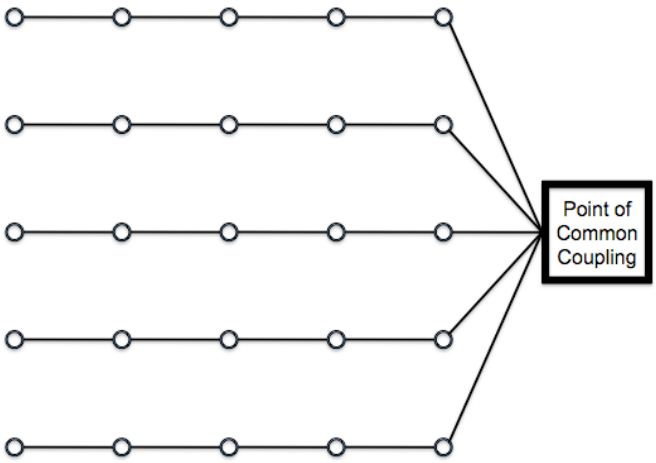

Figure 2.2. Typical 33kV AC collection network layout.

The Point of Common Coupling (PCC) is located within an offshore substation housed on an offshore platform. This platform also houses the transformer shown in Figure 2.1, which steps up the voltage to transmission level, for example 132kV.

The AC system has several limitations including:

- Within the collection network, the AC voltage of 33kV places limits on the number of turbines that can feed power into a single three core cable or set of single core cables.
- Subsea cable capacitance requires charging current that increases with transmission distance and limits the amount of useful AC power that can be transmitted.
- The size and weight of the 50Hz transformer in the wind turbine can be problematic (during installation, for instance) in the offshore environment [17].

The AC solution is examined in more detail in section 7.2.

2.3 HVDC Conversion

HVDC transmission is an alternative to HVAC, particularly in the offshore environment. Some of the most common types of HVDC converter are described here.

2.3.1 State of the Art HVDC Converters

2.3.1.1 Current Source Converters (CSC)

A three-phase, 6-pulse, current source, thyristor based converter is shown in Figure 2.3.

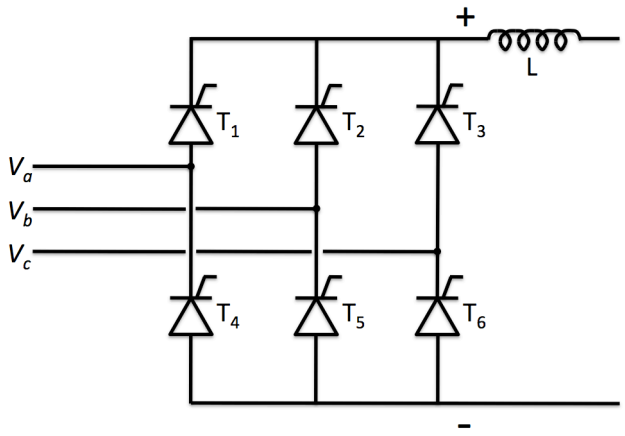

Figure 2.3. Current source HVDC converter topology.

Figure 2.4 shows the DC output voltage, i.e. the voltage of the positive pole with respect to the negative pole [18]. The sequence of conducting thyristors is also shown (beginning at the zero up-crossing point of V_a). One complete AC cycle is shown. The DC ripple voltage is at 6 times the AC frequency.

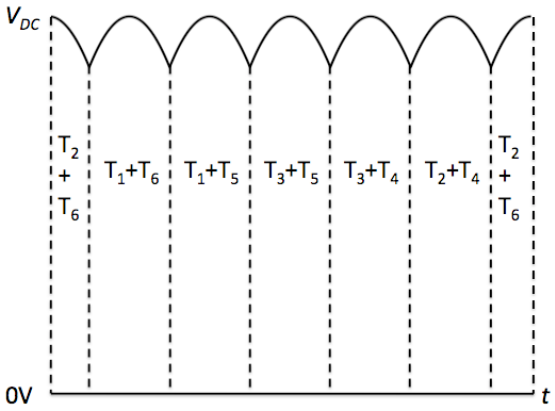

Figure 2.4. DC Voltage waveform for CSC during one complete AC cycle with delay angle zero.

In the CIGRE HVDC benchmark, 12 pulse converters are used. These consist of two thyristor bridges (as shown in Figure 2.3), which are series connected on the DC side. On the AC side the bridges are parallel connected (via the transformer), with one bridge fed from star connected and the other from delta connected AC windings. This arrangement can handle increased power levels compared to the 6-pulse converter. In addition, the output ripple voltages from each bridge are phase shifted by 30^o relative to one another. This significantly reduces the DC ripple content and increases its frequency to 12 times the AC frequency.

A key feature of both these converter designs is the line inductor (L), as shown in Figure 2.3. The value of this inductance, based on the CIGRE benchmark, is between 0.5H and 0.6H (allowing for some transmission line/cable inductance) [19]. This inductor reduces DC side harmonics, reduces current rise during DC system failures and improves system stability [20].

2.3.1.2 Voltage Source Converters (VSC)

A simple three-phase voltage source converter is shown in Figure 2.5. Each Integrated gate bipolar transistor (IGBT) has an anti-parallel diode connected (not shown here). This topology has been superseded but is still in use in many existing HVDC installations and its basic principles of operation are similar to more modern VSC designs. Note that each IGBT shown may represent several connected in series.

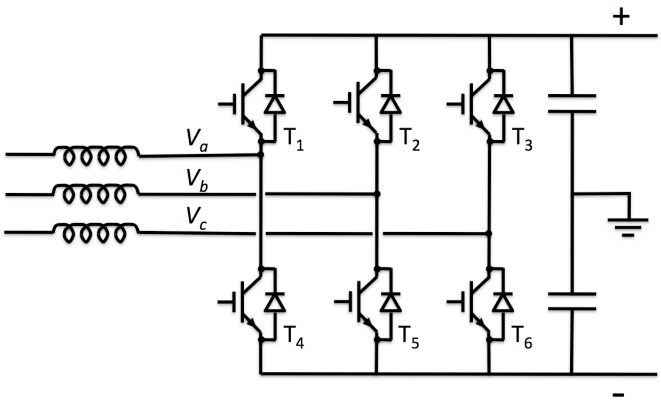

Figure 2.5. Voltage source HVDC converter topology.

There are several designs of voltage source converter. IGBTs are often used in such a circuit. These components are able to switch quickly and enable a range of switching strategies. A relatively basic strategy is the production of a sine wave using two-level pulse width modulation (PWM). Such a switching strategy for one phase is shown in Figure 2.6 along with the desired AC sine wave. The carrier wave dictates the switching of the IGBTs; when it is above the desired sine wave the positive pole IGBT is turned on, when it is below the sine wave, the negative pole IGBT is on.

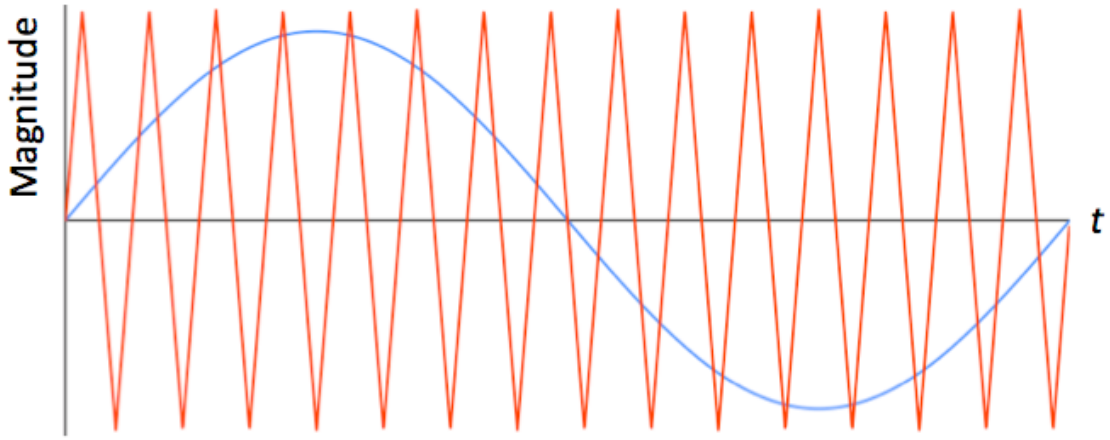

(a)

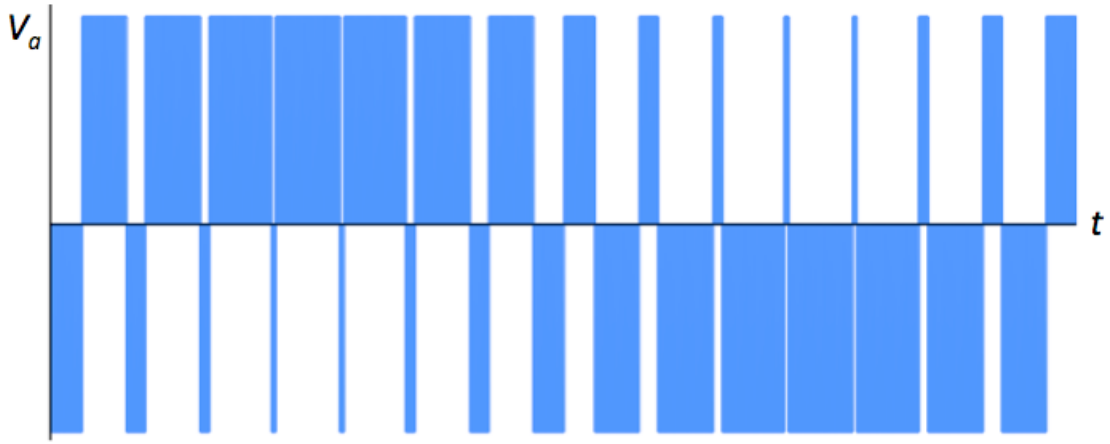

(b)

Figure 2.6. Desired AC sine wave and carrier wave used in control system (a) and resulting voltage at AC terminals (b).

The result is an AC voltage with high harmonic content. AC line reactors and filters reduce the harmonic content and produce an acceptable sine wave. On the DC side, each switching of the IGBTs causes a reversal of current flow to/from the filter capacitors with respect to a particular phase. Large capacitors reduce DC voltage ripple, as well as providing ride through capability for AC side voltage disturbances [18].

An alternative switching strategy, which can be applied to PWM converter operation, is selective harmonic elimination (SHE). SHE produces pulses which generate the

'average' fundamental sine wave as before, but their switching angles are not tied to a carrier wave. Instead, the angles are chosen in such a way that the lower order harmonics are removed from the AC voltage waveform, leaving the higher harmonics, which are generally easier to filter.

2.3.1.3 Multilevel Converters

Multilevel converters are a promising VSC topology in wind farm applications, which are attracting significant research efforts as well as becoming popular (under a variety of names) in industry [4, 21, 22, 23, 24].

The principle of multilevel conversion is to produce a close approximation to a sine wave by increasing or decreasing the voltage produced by the converter at its AC terminals in a number of steps, or levels. In some cases, PWM is used on each step to refine the waveform, in other cases each switch turns on and off only once per AC cycle. An example waveform from the latter approach is shown in Figure 2.7.

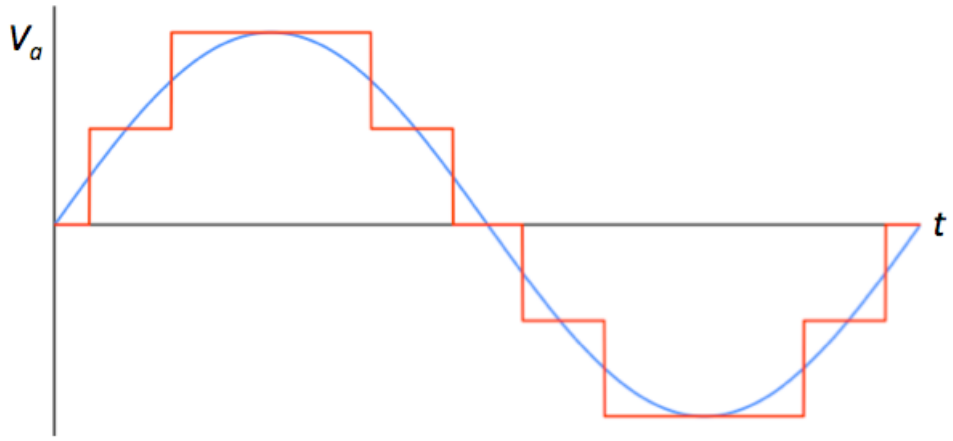

Figure 2.7. Desired AC sine wave and waveform generated by multilevel converter.

Multilevel converters have several advantages over two level converters. Switching losses are reduced, especially where each individual switch is only turned on and off once per AC cycle. This switching strategy also avoids drawing large amounts of high frequency AC current from the DC side capacitance, reducing potential problems with DC ripple currents and voltages that are the focus of this project.

In a relatively recently developed topology, the modular multilevel converter, the DC capacitance is distributed between a number of modules which also contain the switching devices. This topology is shown in Figure 2.8 [25, 26, 27]. Some research is being carried out into the possibility of including a DC link capacitance (in addition to the capacitance in each module). One significant challenge for this particular topology is balancing the voltages in each capacitor [21, 23, 24].

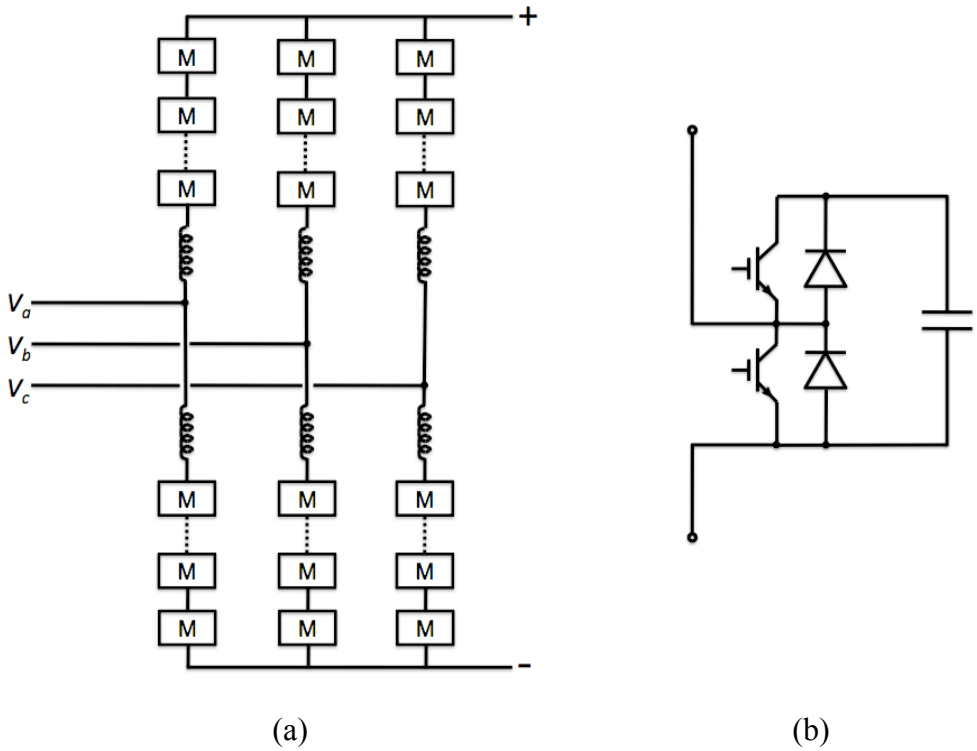

Figure 2.8. MMC topology (a) with each module labelled 'M' and equivalent circuit of each module (b).

2.3.2 Research in Multiterminal HVDC Grids

CSC technology requires the polarity of converters to be reversed in order to reverse power flow, while in VSC technology the direction of current flow is reversed. In application to a wind farm collection DC grid, uni-directional power flow is an acceptable solution, but it will necessitate an additional auxiliary power supply for

black start and to motor the blades round to a position to put the locking pin in for maintenance; this typically requires around 5% rated power [36].

Research has been carried out into VSC based multiterminal grids in a large number of papers, including the use of multilevel and modular multilevel converters, for example [28, 29, 30, 31, 32]. Much effort has been spent on control, stability and protection issues. In [32] the problem of resonance caused by a VSC with switching frequency of 3kHz connected to DC collector cables of length 30km was identified. This highlights that the construction of passive elements of a HVDC grid (such as cables and filter inductors or capacitors) provides challenges in the realisation of DC grids.

2.3.3 Comparison with AC Transmission

Due to the expenditure on power electronic converter stations, conventional DC transmission is not economic over short distances. There are a number of advantages for DC transmission that make it economic over longer distances, particularly in the offshore environment. The advantages include [18]:

- Reduced cable material costs;
- Reduced transmission losses;
- Eliminates charging current for cable capacitance;
- Eliminates reactive power flow;
- Increases lifetime of insulation materials.

In [11] it is estimated that the break point for offshore transmission, above which HVDC becomes economic, is around 80km. As a result, HVDC will be the most economic solution for power transmission for many Round 3 offshore wind zones.

2.4 DC-DC Power Electronic Converters

A DC-DC converter may form part of the power take off system for an offshore wind turbine feeding into a multiterminal DC grid, as shown in Figure 1.3. The modelling and analysis of such converters in a multiterminal grid is a major objective of this research. Their purpose is to step up the voltage to collection or transmission level.

Between the generator output and the converter input, a rectification process must take place. Design of this process is outside the scope of this project. However, there are a number of drives available for wind turbines that take variable voltage and frequency generator output, rectify it to fixed voltage DC and then invert it to fixed voltage and (AC grid) frequency. Although operated in a different fashion, the topologies of many of these drives are similar to those discussed in section 2.3.1. Initially, it is assumed that the output of the first half of the process, a fixed voltage DC (at around 2800V supplied by an active rectifier and voltage regulation stage with boost characteristic connected to the generator output) is input into the DC-DC converter. In section 7.4 the use of a DC-DC converter with variable voltage input is considered. In effect, the DC-DC converter replaces the second stage of the AC-DC-AC drive used in many wind turbines and the process becomes AC-DC-DC.

2.4.1 Proposed Topologies

In [33] a range of topologies of DC-DC converter were proposed for use in offshore wind turbines. Of the converters examined, two of the most promising designs (found to have the lowest losses at full load) were the phase shift full bridge converter and the series load resonant (SLR) converter. The topology for the SLR converter is shown in Figure 2.9. The phase shift converter has a similar topology except the resonant capacitor on the low voltage side is removed and the inductor is reduced in size.

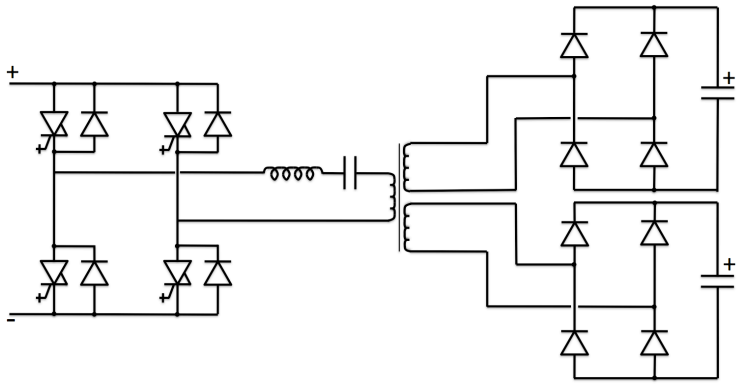

Figure 2.9. Series load resonant converter topology.

Both these topologies use a single-phase, medium frequency transformer with two secondary windings to step up the voltage to ±50kV (bipole arrangement). The switching frequency for both topologies is proposed to be 500Hz. The resonant frequency of the SLR converter is designed to be 400Hz; operating the converter above this frequency increases the power density at the expense of some hard switching of the converter.

2.4.2 Components and Reliability

2.4.2.1 Medium Frequency Transformer

A significant advantage of both the SLR and phase shift converters, when compared to a turbine connected to an AC collection topology, is the reduced size and weight of the medium frequency transformer used for stepping up voltage [34, 35].

2.4.2.2 Switching Components

Of the four devices considered in [33], thyristors cannot be hard switched off and gate turn-off thyristors (GTOs) have relatively high conduction losses and snubber requirements. The remaining two devices, gate commutated thyristors (GCTs) and IGBTs require further consideration. The GCT is mechanically much simpler than the IGBT leading to fewer problems with heat dissipation. Additionally, the GCT normally fails short circuit, while the IGBT fails open circuit. Short circuit failure is preferable as the devices are connected in series on the HV side in order to meet the

voltage rating requirements. Although IGBTs that fail short circuit exist, their structure is more complicated still [18, 33]. The GCT is limited to switching frequencies below 1kHz, which is adequate for the DC-DC converters considered. Due to the difficulties of repair in the offshore environment, GCTs are a very promising choice for switching device.

2.4.3 Power Quality

The rectified high voltage current of the DC-DC converters contains significant ripple content. In Figure 2.10 the current waveforms (after the HV diode bridge but before the filter capacitor) are shown. Table 2.1 shows the Fourier transform of these components. The filtering of this current is examined in detail in this project. Filtering components are discussed in the following section.

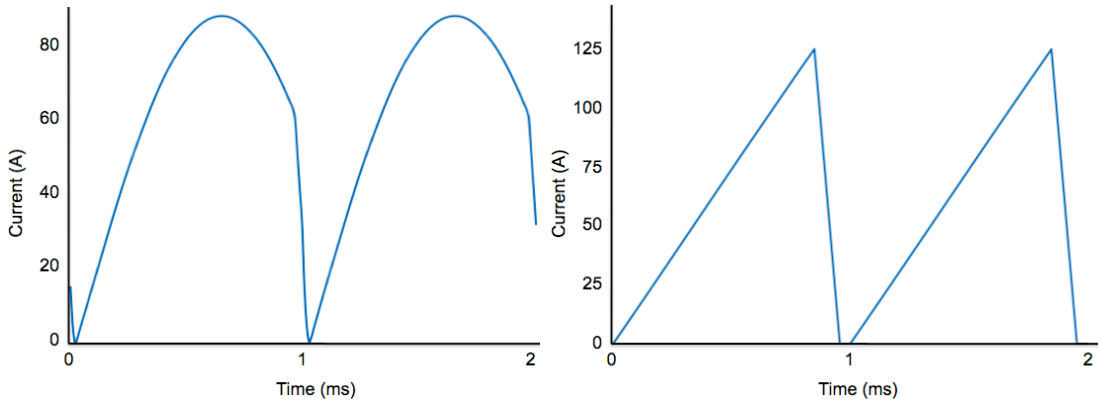

(a) (b)

Figure 2.10. High voltage diode bridge output current before filtering for (a) the SLR and (b) the phase shift converter.

Frequency (kHz)	SLR Converter Magnitude (A)	Phase Shift Converter Magnitude (A)
DC	60.00	60.00
1	32.12	46.00
2	10.53	21.46
3	6.28	12.70
4	4.43	8.01
5	3.37	5.05

Table 2.1. Frequency components of unfiltered HVDC current.

2.5 High Voltage Filter Components

Filtering of the current waveform to remove some of the ripple content is required, however, high voltage filtering components are expensive. In a point to point HVDC scheme with large amounts of power transfer, bulky and expensive filtering components can be economic; but for an offshore wind farm, with space constraints and relatively small amounts of power produced at each node, the use of large, multi-stage or tuned filtering components is undesirable.

2.5.1 Limitations on Current and Voltage Ripple

Current and voltage ripple must be limited for a number of reasons. In this project, the tolerance of the cables to current ripple is examined in detail, as well as the impact on system losses. There are other reasons to limit both voltage and current ripple.

2.5.1.1 Control

The voltage ripple in a VSC HVDC should not (typically) exceed ±2% [36]. Larger variation can cause problems for the control loop, as the voltage change will be significant between the time of measurement and the time of actuation of the resulting control action. Current ripple can cause similar problems. Time averaging methods are one solution that can be used, at the expense of the response speed of the control loop.

2.5.1.2 Interference and Inductive Coupling

Ripple currents cause magnetic fields which can interact with other metallic structures (such as pipelines) or communications cables. In the former case, this can cause dangerous voltages to build up and in the latter can cause interference [20]. Knowledge of the area local to the cable is required to determine the limitation this places on ripple content.

2.5.1.3 Component Stress

Ripple voltage and current can increase stress on all components. The HV filter capacitor is the most obvious. Current ripple will increase the operating temperature of this capacitor and limits apply (as discussed in section 2.5.2.1) [37, 38].

2.5.2 Filter Capacitors

Electrolytic capacitors are often used as filtering components in power electronic converters with a DC output. However, this type of capacitor has a relatively short lifespan and is a well known point of failure in such systems [39]. In the offshore environment, component failure must be minimised. One possible solution is to use film capacitors, although this is only possible for relatively small values of capacitance. Although this value is very much dependent on the application and environment, a reasonable cut off point for the systems considered in this project is 10μF, at or below which film capacitors are practical. In any case, a balance must be struck between the cost and reliability of the filter and the ability of the system, including cables, to tolerate current and voltage ripple.

A further consideration is resonance between the cables and the filter components in the system. The resonant frequency should not match the AC fundamental frequency or second harmonic [20]. In the case of a multiterminal grid, with many cables and capacitors, evaluation of this frequency is complex. This is covered in chapter 4.

2.5.2.1 Capacitor Characteristics

Capacitor *ESR* (equivalent series resistance (Ω)) depends on a number of factors including the resistance of the electrical connections outside and within the capacitor, and the dissipation factor (tan δ) of the dielectric. Although a formula exists which relates tan δ to the *ESR* and to capacitance, research into capacitor supply company products [38] shows that capacitor design and construction is more important than the dissipation factor in determining capacitance. Based on available capacitors, a value of *ESR* between 1.8mΩ and 17.7mΩ can be expected for a film capacitor in the

range 0.22μF to 10μF with rated voltage between 10kV and 50kV [38]. For the same range of film capacitors, the current limit is between 10A and 50A.

2.5.3 Filter Inductors

High voltage inductors, as used in CSC HVDC to reduce current ripple, are heavy, large and expensive components. This is due to a number of factors including insulation requirements. It is therefore undesirable, from an economic and practical point of view, to use these components in every wind turbine.

2.6 HVDC Subsea Cables

Modelling and understanding the behaviour of subsea cables is a subject which is considered in great depth in this thesis and this section covers a significant amount of background material. There are extensive texts available on the subject of high power and subsea cables, such as [40, 41]. This section identifies and explains aspects of cable design that are most important to the modelling that follows in subsequent chapters.

It is estimated that a total of 8000km of subsea power cables will be required for the Round 3 wind farm sites, of which around 5000km will be DC. Material costs of HVDC cables are lower than for HVAC. Estimates vary for how much lower, but in [8], it is estimated that HVDC transmission can reduce cable costs by 30%, while in [20], it is estimated that around 3 times the power can be transmitted with HVDC than HVAC with the same cable material cost.

2.6.1 Faults

Cable design is strongly influenced by behaviour during, and response after, a fault condition. Cables are typically buried at a depth of 1.5-3m to avoid disturbance. However, ocean currents, tides or sediment flows can still cause sections of a buried cable to become exposed [9, 11].

There are a range of causes for subsea cable faults including anchors, fishing activities and aging [9]. It is estimated that subsea faults occur at an approximate rate of 1 to 1.3 faults/100km of cable/year [42, 43]. Repair can potentially take several months and is very costly. The typical cost of a subsea cable repair is in the region 0.7-1.4MEuro (including the cost of a new cable section), but if the repair is urgent and must be completed in poor weather conditions this cost can be much higher; cost of cable repairs in bad weather can be over 200kEuro/day [43].

2.6.1.1 Fault Repair

Subsea cable repair is a difficult task. In water depths up to 500m the following procedure applies. The fault is located, the cable is cut and one cable end is raised to the surface and attached to a new section of cable. In doing so, the repair vessel must move away from the location of the fault, along the cable section by a distance roughly equal to the water depth. Similarly, the vessel must move in the opposite direction from the fault location in order to raise the other end of the cable to the surface. Consequently, a new section of cable equal to roughly twice the water depth is added to the existing cable. This new cable section is then lowered to the seabed forming an 'omega loop' [44].

In deeper water, special equipment, including remotely operated vehicles, is required.

2.6.2 Cable Configuration

In a bipole DC installation, two cables carry current in opposite directions, as opposed to a monopole installation in which the ground, sea and outer layers of a single cable provide the return path. Material costs of a bipole scheme are higher, however, the advantages include [18]:

- No need to replace sacrificial conductors, which would be problematic in the offshore environment;

- Redundancy: in the event of the failure of one cable, monopole operation can be used until the repair is complete;
- Cancellation of magnetic fields, especially if cables are laid close together.

The issue of how far apart to lay the bipole cables apart raises several points. Laying the cables side by side requires only one seabed trench and reduces laying costs. Additionally, there is a limit of 5^{o} on compass deviation caused by power cables. This requires cables to be laid close together in shallow water. In deep water however, this is not a factor [45].

Laying cables some distance apart prevents one mechanical incident from damaging more than one cable, in the case of single core subsea AC cables in a three-phase system this approach is often adopted [41]. Given the fault repair process outlined in section 2.6.1.1, the omega loop formed by a new section of cable following a fault repair could reduce space between cables or even cause them to overlap. To avoid this, a conservative cable spacing of 2 times water depth can be used to minimise the chance of the cables coming close together during their operational life [45].

2.6.3 Cable Components

The cable components that are modelled are shown in Figure 2.11.

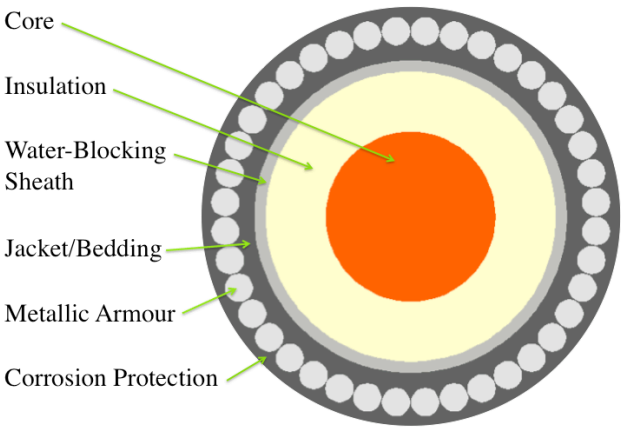

Figure 2.11. Modelled components of a HVDC cable.

2.6.3.1 Core

The main conductor is made from aluminium or copper. Solid conductors can be made up to cross sectional areas of around 400mm^2. Above this, stranded conductors are used. The conductors are compressed during manufacture, which reduces the gaps between them and a 92% filling factor (i.e. the conducting material fills 92% of the area inside the perimeter of the core) can be achieved. Profile wire conductors can also be used, for example as used in the "Estlink" HVDC cable [40]. These conductors achieve a filling factor close to 100%. Based on information from a number of suppliers, the cross sectional area of cable conductor ranges from 95mm^2 to 3000mm^2 [44, 46, 47, 48].

The resistivity of copper and aluminium depend on temperature and purity. Reference values at 20^{o}C are 1.79x10^{-8}Ωm for copper and 2.87x10^{-8}Ωm for aluminium. These values increase by around 0.392% (copper) or 0.420% (aluminium) for every degree Celsius of temperature rise [40]. The lower resistivity of copper make it attractive, however, it is relatively expensive.

2.6.3.2 Insulation

Extruded XLPE (cross-linked polyethylene) insulation has been widely used for underground HVAC cables for decades. Due to relatively low demand until recent years, the XLPE technology has not been quickly transferred to HVDC cables. Most present HVDC installations use paper insulated cables which come in three types: oil-filled, mass-impregnated or gas-pressurised [18, 20]. Extruded polymeric insulated cables, (now including a small number with XLPE) are also used in HVDC schemes [18, 44, 46]. XLPE is considered to have significant advantages over paper insulated cables [20, 49]. These advantages include:

- Relatively high conductor temperature can be used;
- No risk of oil leaks (as for oil-filled cables);
- Joining cables is relatively simple.

Based on the information in [46], the required polymeric insulation thickness increases by around 0.1mm per kV with increasing voltage. In [48], the thickness of XLPE insulation for 30kV and 45kV AC single core cables is given as 8mm.

2.6.3.3 Water Blocking Sheath

To maintain dielectric strength, the insulation must be protected from water. This is achieved with an extruded metallic sheath applied over the insulation. The construction of the water blocking sheath, including its thickness and material, depend on a number of factors including cost, ampacity requirements (during fault conditions), corrosion and expected forces during installation and operation [41, 50]. Lead is the most commonly used material for such sheaths. Extruded aluminium sheaths have been tried in submarine applications, but corrosion problems occurred [40]. Copper is more resilient to fatigue than lead and suitable where cables are suspended (e.g. from floating oil platforms) and move in ocean currents [40]. The thickness of a lead sheath in a single core subsea cable is typically around 3mm [32, 48].

A copper screen can be applied just inside the water blocking sheath to improve the fault current carrying capability of the cable. The cross sectional area of this screen can typically vary from 50mm^2 to 170mm^2 [47].

2.6.3.4 Bedding/Jacket

Outside the sheath is an extruded layer that acts as bedding for the armour. Polyethylene is often used for this layer [51, 47].

2.6.3.5 Metallic Armour

Armour wires improve cable tensile strength, which is important during installation and repair, and protect the cable from mechanical damage. The wires are wound around the cable, completing one turn for a length of every 10-30 times the cable diameter [40]. Round armour wires vary in diameter from 2-8mm. There may be one layer of wires or two layers wound in opposite directions around the cable.

Several materials can be used for these wires. Three core AC cables usually use steel wire. In [52], a range of steel armour wires from subsea cables were tested and their relative permeability below saturation was found to be in the range 100-210 [52]. In single core AC cables, non-magnetic armour is preferable, such as copper, stainless steel or aluminium [48], use of magnetic steel in a single core AC cable can lead to high losses in the armour due to induced currents (whereas in a three core cable the magnetic fields cancel out, to an extent).

Field experience of cable armour shows that corrosion of armour can, in certain circumstances, be a limiting factor in the lifetime of subsea cables. In particular, where a significant amount of cable is suspended above the seabed, the resulting tensile forces mean that corrosion of the armour can cause failure of the cable. Cables inspected after around 25 years of service were found to be at risk of failure [53]. The use of copper armour, which tends to corrode less than steel, is likely to extend the lifetime of the cables. Corrosion mechanisms and prevention are outlined in section 2.6.5.

It is only the ripple currents that interact magnetically with the steel armour in a HVDC cable (as opposed to the load current in an AC cable), and these currents are at relatively high frequency (in the kHz range compared to 50Hz or 60Hz for an AC load current). Therefore, magnetic saturation of cable armour does not need to be considered and constant permeability can be assumed. For the same reasons, hysteresis losses are very small and can be neglected [52, 54].

2.6.3.6 Optical Fibres

Optical fibres can be installed in power cables. These can be used for, among other functions, communication and distributed measurement of temperature [40, 47].

2.6.4 Connections of Outer Metallic Layers

The outer metallic layers of a subsea cable are grounded at both ends and the voltages along the length of sheath and armour can be considered to be negligible [49, 55]. In some cases, a metallic layer is covered by an insulation jacket to prevent corrosion. In AC cable lengths above approximately 3km, voltages can build up between two metallic layers or a metallic layer and the ground. As a result, electrical connections are made between the metallic sheath, armour and sea/soil [41, 43]. In the case of DC cables, although standing voltages might result from the ripple voltage produced by DC-DC converters, these voltages will be small. However, in the case of a fault, the resulting voltage/current propagates at different speeds in sheath and armour, so it is necessary to regularly connect these components together (approximately every 2-3km) to prevent damage to the extruded layer in between [45].

2.6.4.1 Induced Eddy Currents

The grounding of the outer metallic layers allows eddy currents to flow in them. Ripple currents in the cable core induce eddy currents in these layers by the transformer effect [41]. The sinusoidal (ripple) current components in the core generate a sinusoidal magnetic field in the surrounding materials. This field induces eddy currents to flow in the (metallic) water blocking sheath and protective armour in such a way that the field generated by the eddy currents is in opposition to the applied field. As a result, the magnetic field is reduced outside each of the metallic layers [41, 56, 57]. The distribution of these eddy currents is examined in detail in chapter 3.

2.6.5 Corrosion

Corrosion of the outer layers, in particular the protective armour, must be considered when designing subsea cables and the offshore DC grid [40]. There are numerous mechanisms for corrosion [41]. The two most relevant to this project are outlined here.

2.6.5.1 Salt Water Corrosion

Seawater can react with metallic layers of the cable to cause corrosion. One method to reduce corrosion rate by this mechanism is to restrict the flow of seawater to the metallic layers. By doing so, the oxygen used up in the corrosion process is not quickly replaced and the process slows.

In most cases, steel armour wires are coated with a sacrificial layer of zinc at least 50μm thick. This layer is designed to corrode before the steel does and thereby consumes the oxygen available for corrosion, protecting the steel armour. However, corrosion rates for zinc layers are estimated at 5-50μm/year [40]. After the zinc has corroded, the steel armour is estimated to corrode at a rate of 10μm/year.

Burying the cable restricts the flow of seawater. However, a buried cable can become exposed. A secondary protection of bitumen coated onto the armour during manufacture is used, restricting seawater access.

Scratches during installation or in service can reduce the effectiveness of the zinc and bitumen layers. To protect against this, an outer layer of either wound polypropylene yarn or an extruded plastic sheath can be applied. A cable with yarn layers is designed to be "semi-wet", in other words the seawater can penetrate through the yarn wires. In this case however, the flow of seawater is greatly reduced [32, 40]. An extruded plastic sheath is waterproof if undamaged. However, any damage can lead to a concentration of electric or galvanic currents which will lead to a particularly high, localised corrosion rate.

2.6.5.2 AC Corrosion

Due to the significant ripple content of the output from the DC-DC converter designs investigated in this project, AC corrosion must be considered.

Currents induced in the outer layers by transformer action flow into the sea or seabed resulting in corrosion [41]. The effect is most prominent if the three cables (in the AC case) or two cables (in the DC bipole case) are spaced apart. If the cables are laid tightly together, and the AC currents or DC ripple currents are balanced, then the effect is much reduced [41]. In the case of AC cables, increasing the size of steel armour increases its strength, but at the cost of larger induced currents and greater rate of corrosion [41]. Induced ripple currents in the armour of a DC cable are examined in chapter 3.

In [53], it was highlighted that while DC ripple currents may only play a minor role in corrosion, should the armour wires actually break (as was found to have happened on inspection of an underwater HVDC cable in the region of 25 years old) then the induced ripple currents in the armour would be forced to flow in the seawater and the corrosion process accelerated.

2.6.6 Cable Modelling Approaches

2.6.6.1 Simulation Software

Standard simulation software such as Simulink (Mathworks, Inc.) or PSCAD (EMTP (Electromagnetic transient program)) is often used for power systems research. In the case of the detailed cable modelling work required in this project, this software has some limitations. In Simulink, π-section or T-section cable models can be implemented, but these models are only valid at a single given frequency. A π-section model is shown in Figure 2.12, Y_{eq} (Ω^{-1}) and Z_{eq} (Ω) are, respectively, the distributed admittance and impedance of the cable adjusted for wave propagation effects [58]. More detail is given in chapter 4. As identified in [32], EMTP can have difficulty solving problems which fully account for the interaction between power electronic converters and frequency dependent cables.

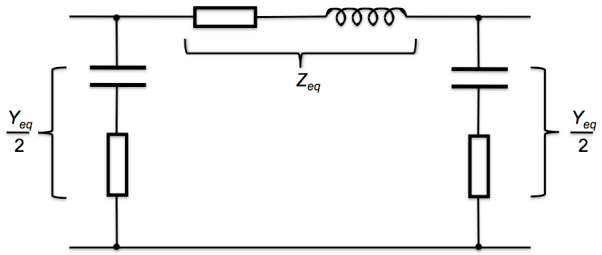

Figure 2.12. π-section equivalent model of distributed parameter transmission cable [58].

2.6.6.2 Analytical Methods

Analytical methods for solving the magnetic fields and current densities in a single multilayer coaxial cable do exist [57]. However, the additional complexity of a second cable, which introduces the proximity effect, and steel armour wires, which remove the angular symmetry, make obtaining results from such formulae problematic. Study of this theory is nonetheless invaluable in improving understanding of the results obtained from numerical methods. More details are in appendix A.

2.6.6.3 Finite Element Method

Opera (Cobham Plc) FEM electromagnetic modelling software has been used extensively to study cable behaviour and calculate parameters in this project. The FEM is an accurate and flexible way to obtain detailed information and it provides visualisations that aid understanding of and confidence in results.

2.7 Wind Farm Planning

2.7.1 Layout

To reduce power loss caused by the wake effect, wind turbines are typically separated by 5 times the diameter of their rotor blades. Turbines in offshore wind farms are often arranged in regular patterns [16, 59, 60, 61, 62], as shown in Figure 2.13.

Figure 2.13. Rødsand I and II offshore wind farms. Photograph by Koppelius [59].

2.7.2 Connections

Optimal connection of the turbines is important both to save capital costs and reduce loss of production from outages [61]. The choices include cable type and placement. In the study of Barrow offshore wind farm carried out in [61], both the actual and optimal connection strategy were found to involve connecting parallel lines of turbines and collecting the power using larger cables at one end of those lines, similar to the arrangement in Figure 2.2.

2.7.3 Control

In a point to point two terminal VSC HVDC system, one converter can be used to control DC voltage and the other power flow. Modelling in [32] demonstrated the principle of using a single (onshore) converter in a DC network to control both system voltage and power transfer into the AC grid.

2.7.4 Transmission Voltage

The estimated cost of an offshore substation, which acts as a collection point for the power from all wind turbines, is around £14m for 150MW or £50m for 500MW [10, 11]. The latter figure includes around £30m for the electrical system. The approach investigated in this project is to remove this substation and couple the power in turbine towers. Transmission is at ±50kV, the voltage produced from each wind turbine.

3 Cable Modelling

The ripple content produced by DC-DC converters requires modelling in the DC network. In order to do this accurately, its behaviour in the DC cables must be understood and cable parameters at ripple current frequencies must be derived. In order to do this, the FEM is employed to a representative range of DC subsea cable designs.

3.1 Theoretical Principles

The modelling carried out in this section makes use of the uniformity of the cable cross-section along its length which allows a 2-dimensional representation. The axis along the cable length is referred to as the z-axis and the cross-section plane as the XY plane.

The behaviour of the DC current in the cable is straightforward. The cable DC resistance is simple to calculate using equation (3.1),

$$R = \frac{\rho l}{A} \tag{3.1}$$

where R (Ω) is resistance, l (m) is length of cable, ρ (Ωm) is resistivity of the core conductor material and A (m^2) its cross-sectional area.

However, of most interest in this chapter is the behaviour of AC ripple currents in the cable. The ripple currents generated by the DC-DC converter are at a frequency of 1kHz and harmonics of that frequency. Using the principle of superposition, the ripple current is split into its (sinusoidal) frequency components and each of these modelled separately. Later in the chapter, a wider range of frequencies, including the AC grid frequency (assumed to be 50Hz) and its harmonics, are considered as AC and DC grids are not completely separated from one another.

The equations that are applied to describe the behaviour of the AC currents, the time-varying magnetic fields that they cause and the eddy currents that these magnetic fields induce are given below. The equations are derived from, among others, a subset of Maxwell's equations [57, 63].

$$\underline{\nabla} \times \underline{H} = \underline{J} + \frac{\partial \underline{D}}{\partial t} \tag{3.2}$$

$$\underline{\nabla} \times \underline{E} = \frac{-\partial \underline{B}}{\partial t} \tag{3.3}$$

$$\underline{\nabla} \bullet \underline{B} = 0 \tag{3.4}$$

$$\underline{J} = \sigma \underline{E} \tag{3.5}$$

$$\underline{B} = \mu \underline{H} \tag{3.6}$$

where

$\underline{H}$ is the magnetic field strength (Am^{-1});

$\underline{J}$ is the current density (Am^{-2});

$\underline{D}$ is the displacement current (Am^{-2}), which is negligibly small compared to the conduction current in a conductor and is ignored;

$\underline{E}$ is the electric field strength (Vm^{-1});

$\underline{B}$ is the magnetic flux density or magnetic B-field (T);

σ is the conductivity ($\Omega^{-1}m^{-1}$).

These equations are applied throughout the cable cross-sections and surrounding material. An area of surrounding material which is at least 10 times the size of the cables in each dimension is included in all models.

The FEM software solves for the magnetic vector potential $\underline{A}$ (Vsm^{-1}), defined by the equation:

$$\underline{B} = \underline{\nabla} \times \underline{A} \tag{3.7}$$

The software returns $\underline{A}$ and $\underline{J}$ at all points in the XY-plane. From this, the voltage (scalar potential, ϕ (Vm^{-1})) gradient and hence the inductance and resistance can be derived using equations (3.8) and (3.9), the latter of which applies to sinusoidal magnetic fields [63].

$$\underline{E} + \underline{\nabla}(\phi) + \frac{\partial \underline{A}}{\partial t} = 0 \tag{3.8}$$

$$\frac{\partial \underline{A}}{\partial t} = j\omega \underline{A} \tag{3.9}$$

Since the current flow is in the z-direction (ignoring any displacement currents in the insulation material, the effect of which is negligibly small by comparison), the sinusoidal components of ripple current cause a time-varying magnetic field in the XY-plane. In turn, as this magnetic field changes, it induces eddy currents to flow in the metallic layers in a direction perpendicular to the plane of the magnetic field, i.e. the z-direction.

In the cable core, the effect of the time-varying magnetic field is to concentrate the conduction current towards the edge of the core; this is the skin effect. The skin depth (δ (m)) of a conductor is given by equation (3.10).

$$\delta = \sqrt{\frac{2}{\sigma \omega \mu}} \tag{3.10}$$

The time-varying magnetic field induces eddy currents in the metallic sheath and armour. This process is known as transformer action. The eddy currents in these layers flow in such a way that they generate a magnetic field that tends to be in opposition to the applied field and therefore cancels it out. As a result, the magnetic field is reduced towards the outside of the cable.

In a bipole cable arrangement, the magnetic fields from each cable interact with the other cable; this is known as the proximity effect. The effect influences the

distribution of the eddy currents in each cable. The induced currents described are a well known source of losses in AC cable transmission, where the load current (rather than just the ripple current) causes time-varying magnetic fields.

3.2 Cable Configuration

The FEM was used to model a range of HVDC cable designs. Initially, three representative cable designs, with differing ampacities, were modelled. The specifications for these cables are shown in Table 3.1 and Table 3.2. These cables are referred to as the 'base case' cables throughout this thesis and are designated 'cable 1', 'cable 2' and 'cable 3'. In subsequent chapters, the smaller cables (1 and 2) are modelled as collection cables within an offshore wind farm, while the largest cable is modelled as the transmission cable to shore. All cables are rated for 50kV. The operating temperature is assumed to be 20°C (higher temperature is considered in section 3.5). The cables are modelled as being laid side by side, although the effect of cable separation is covered in section 3.5.2.6.

	Material	Conductivity ($\Omega \cdot m^{-1}$)	Relative Permittivity (ε_r) or Permeability (μ_r)
Core	Copper	5.599×10^7	1
Inner Insulation	Cross-Linked Polyethylene (XLPE)	0	$\varepsilon_r = 2.3$
Sheath	Lead	4.546×10^6	1
Jacket/ Bedding	Polyethylene	0	$\varepsilon_r = 2.3$
Armour	Steel	6.907×10^6	$\mu_r = 155$
Corrosion Protection	Polypropylene Yarn (wound) and Bitumen (coated onto armour)	0	$\varepsilon_r = 2.1$

Table 3.1. Material properties of cable components.

	Cable 1	Cable 2	Cable 3
Core Cross-sectional area (mm^2)	95	300	1400
Inner Insulation thickness (mm)	8	8	8
Lead Sheath thickness (mm)	1.6	2.0	2.8
Jacket/Bedding thickness (mm)	2	2.5	3
Armour wire diameter (mm)	2	3	5
Number of Armour wires	54	48	46
Cable Outer Diameter (mm)	42.2	56.5	87.8
Cable Ampacity (A)	343	662	1594
Cable Mass (kg/m)	4.8	9.6	28.7

Table 3.2. Cable construction details.

The designs are based on information derived from a number of sources including [32, 44, 46, 47, 48, 64]; in particular, core cross-sectional area, ampacity and approximate values of mass (which have been used to estimate the size of the metallic layers) and outer diameter are based on [46]. The cables have been chosen with a particular wind farm structure in mind, consisting of 25 turbines, which is described in chapter 4. Based on [46], the smallest cable available (with a $95mm^2$ core) is capable of carrying rated power from 5 turbines (300A), the next useful size of cable for the layout is rated for the power of 10 turbines (600A) and the final cable will carry the power from all turbines (up to 1500A).

To simplify the model, the steel armour was not wound around the cable (i.e. the angle of lay was zero). The external environment was modelled with a range of values of conductivity from 0 to 10 $\Omega^{-1}m^{-1}$ to account for a range of possible soil and sea water types [32]. It was found that the properties of low conductivity regions had a negligible impact on the results. The cable cores were modelled as solid (i.e. with a filling factor of 100%); this is a reasonable representation of a profile wire conductor. In order to normalise the results, the cable cores were modelled carrying a current of 1A (peak value) at frequencies from 1kHz to 10kHz, as well as DC. The results can all be scaled to larger current loads.

3.3 Cable Behaviour and Analysis

The results from cable 3 are used to illustrate the cable behaviour and comparisons are drawn with them. The components of cable structure are shown in Figure 2.11. Figure 3.1 and Figure 3.2 show the current density distribution results at 1kHz and 10kHz for cable 3.

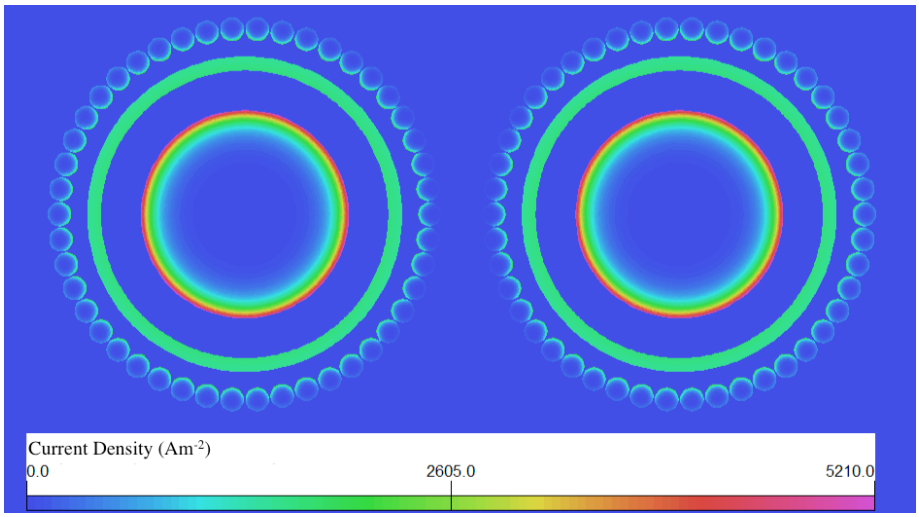

Figure 3.1. Simulated current density at 1kHz in bipole arrangement of base case cable 3.

The skin effect in the core is visible in both cases and is more pronounced at 10kHz than 1kHz. From equation (3.10), the skin depth in the core is 2.13mm at 1kHz compared to 0.67mm at 10kHz. The eddy currents induced in the metallic sheath and armour can be seen. By comparing Figure 3.2(a) and (b), the higher current density in the lead sheath at 10kHz can be seen. Again, this is caused by the reduced skin depth at higher frequency. The current density in the armour is lower at 10kHz than 1kHz. This is due to the cancellation of the magnetic fields from the core and the sheath; the larger sheath current at 10kHz results in a lower magnetic field outside the sheath and therefore lower armour currents. The percentages of current relative to the core current for the lead sheath and armour are shown in Table 3.3.

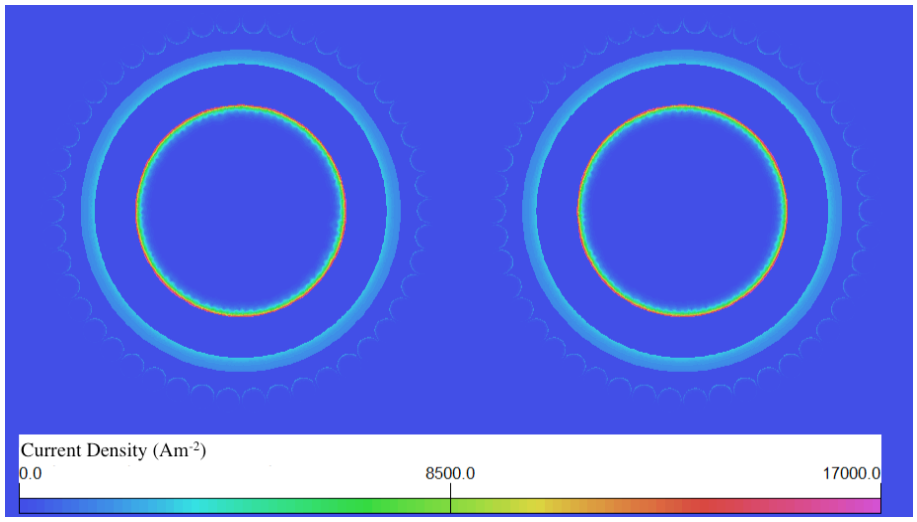

(a)

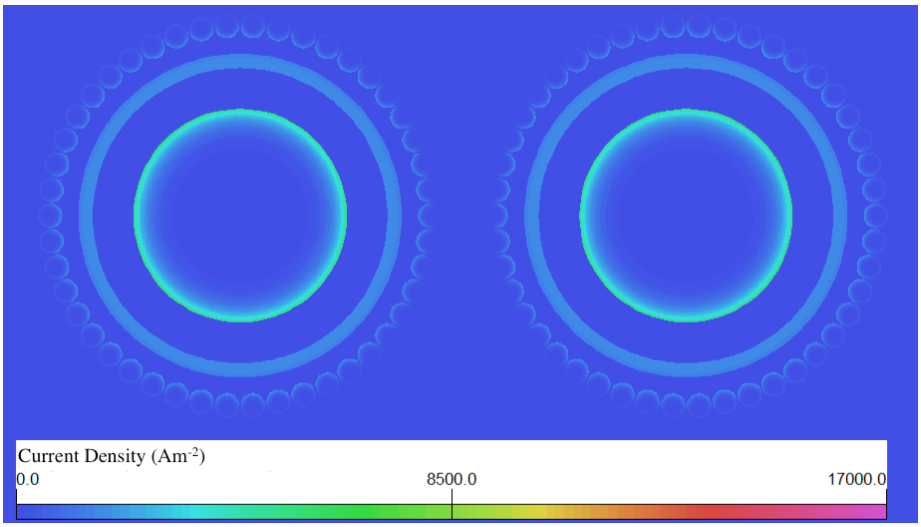

(b)

Figure 3.2. Simulated current density at (a) 10kHz in bipole arrangement of base case cable 3 and (b) 1kHz with same scale for comparison.

Figure 3.3 shows the absolute value of the currents in one cable at the point in time where the core current is at its maximum amplitude. It can be seen that the induced currents in the outer layers of each cable are the opposite sign to their respective core currents, resulting in the described cancellation of magnetic fields.

Frequency (kHz)	Lead Sheath Current as Percentage of Core Current	Armour Current as Percentage of Core Current
1	83.6%	27.1%
2	90.6%	19.1%
3	93.6%	15.2%
4	95.3%	12.8%
5	96.5%	11.1%
6	97.3%	9.9%
7	97.9%	8.9%
8	98.4%	8.2%
9	98.9%	7.5%
10	99.2%	7.0%

Table 3.3. Simulated lead sheath and steel armour current relative to the core current for base case cable 3.

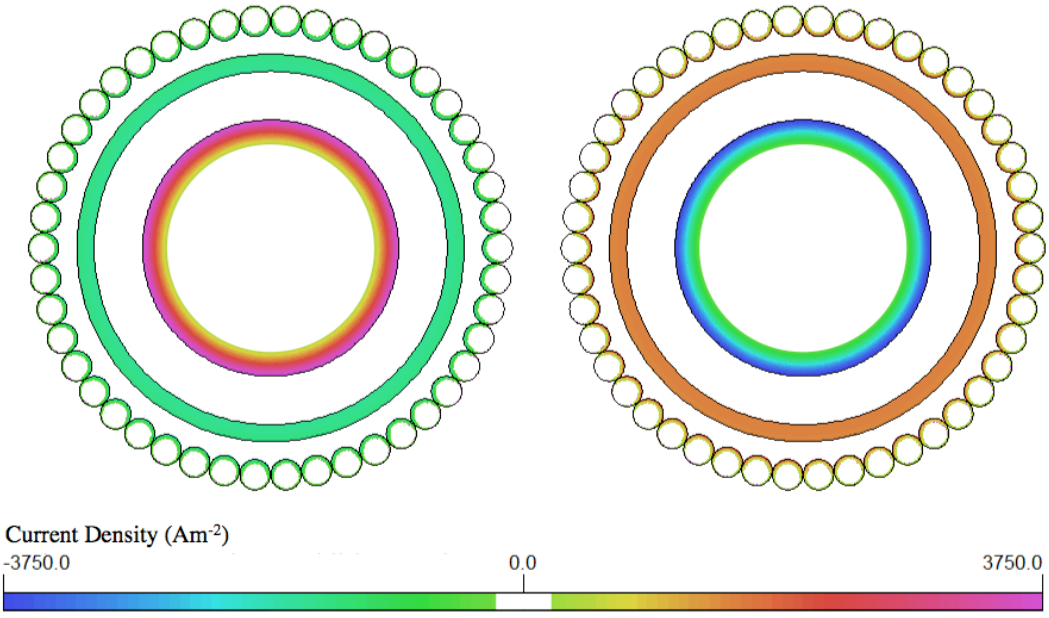

Figure 3.3. Absolute value of currents in metallic layers of the base case cable 3 simulated when the left hand core instantaneous current is 1A (at 1kHz) and the right hand core instantaneous current is -1A.

The magnitudes of the magnetic B-field for DC and 1kHz are shown in Figure 3.4. In the DC case, there are no induced currents and the only cancellation of magnetic fields results from the interaction of the two bipole cables. As a result, the magnetic fields generated by the DC current remain much larger outside the metallic sheath than in the case of the 1kHz ripple current.

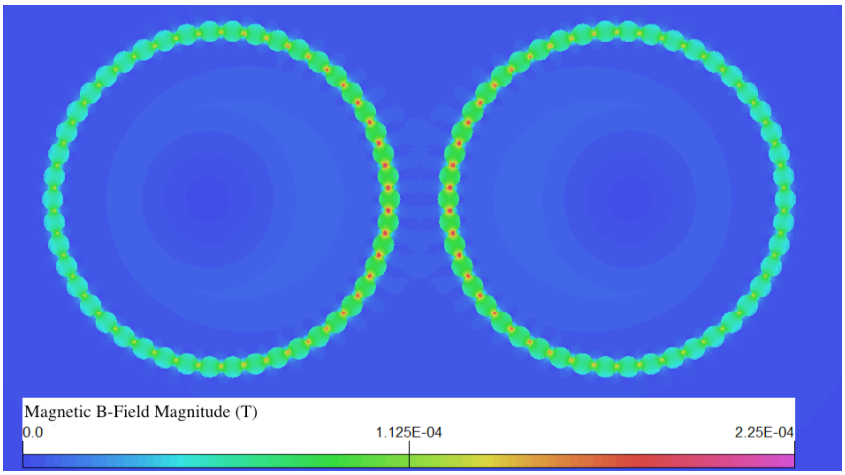

(a)

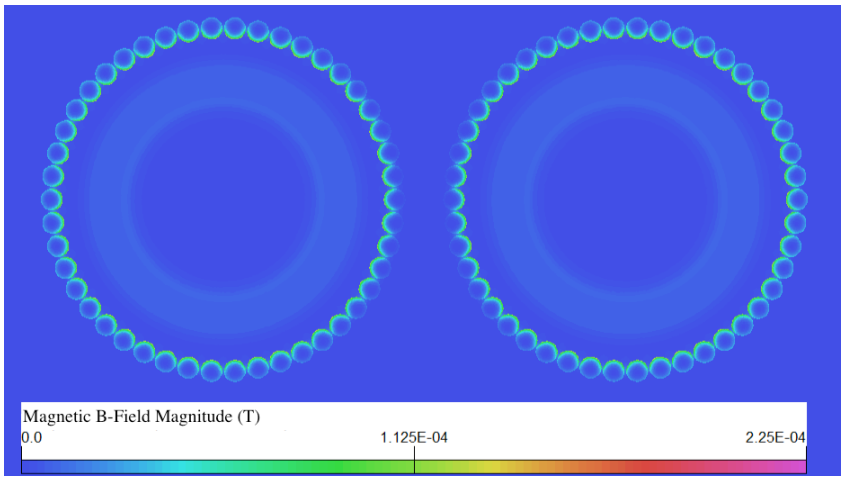

(b)

Figure 3.4. Simulated magnitude of magnetic B-field in base case cable 3 for (a) 1A DC core current and (b) 1A (peak) core current at 1kHz.

The values for the resistance and the inductance per cable are shown in Table 3.4. The increasing of resistance with frequency is explained by the skin effect which causes the current to concentrate in a smaller area with higher frequency. The reduction in inductance with frequency is accounted for by two factors:

- The reduction with higher frequency of the magnetic field outside the sheath reduces external inductance.
- The internal inductance of the core is reduced as the area in which the core current flows reduces [65].

Frequency (kHz)	Resistance (R') Ω/km	Inductance (L') mH/km
DC	0.013	0.609
1	0.401	0.097
2	0.468	0.084
3	0.508	0.080
4	0.541	0.078
5	0.570	0.077
6	0.597	0.076
7	0.624	0.075
8	0.651	0.075
9	0.677	0.074
10	0.704	0.074

Table 3.4. Simulated values per cable of resistance per unit length (R' (Ωm^{-1})) and inductance per unit length (L' (Hm^{-1})) for the base case model of cable 3.

3.4 Comparison of Cable Sizes

A comparison of the current density distribution at 1kHz for cables 1, 2 and 3 is shown in Figure 3.5. The total core current is the same in each case, so the core current density increases with reduction in core size. The lead sheath current density is also larger with decreasing radius. This can be explained by considering the integral form of Ampère's Circuital law, equation (3.11).

$$\oint_C \underline{B} \cdot d\underline{l} = \mu_0 I_{enclosed} \tag{3.11}$$

This law gives the line integral of the magnetic B-field around the closed curve C in terms of the current enclosed by that curve, $I_{enclosed}$ (A), and the permeability, in this case assumed to be μ_0 (vacuum permeability (Hm^{-1})). In each case, the current enclosed by the inner edge of the lead sheath is the same, but since the loop is smaller for smaller cables, the path length is less and so the magnetic field strength is greater. Consequently, the time-varying magnetic fields are stronger with smaller sheath inner radius and the induced currents larger.

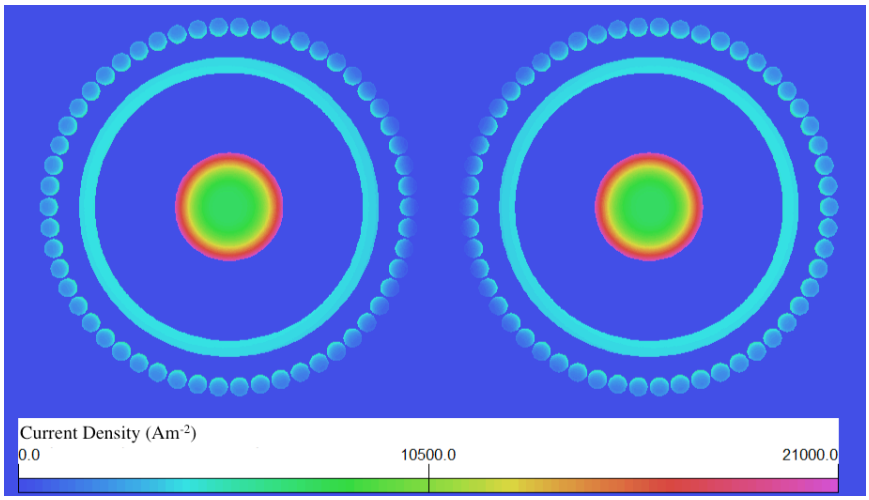

(a)

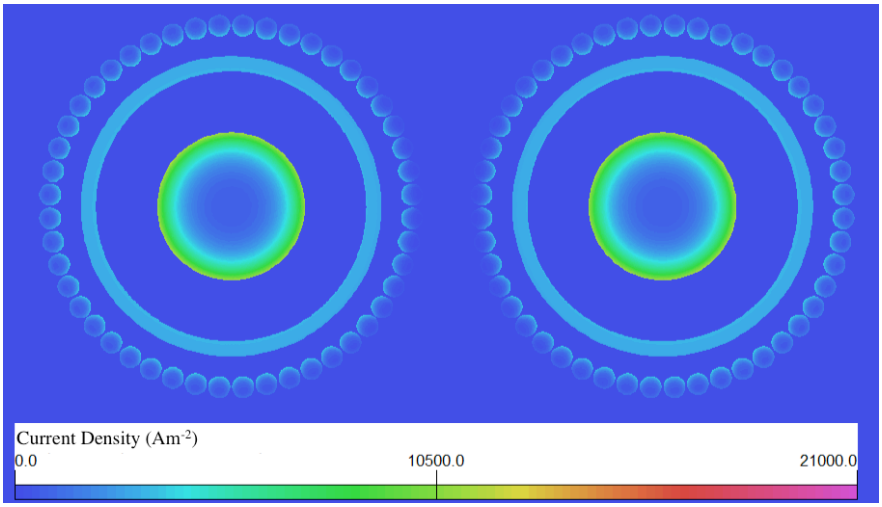

(b)

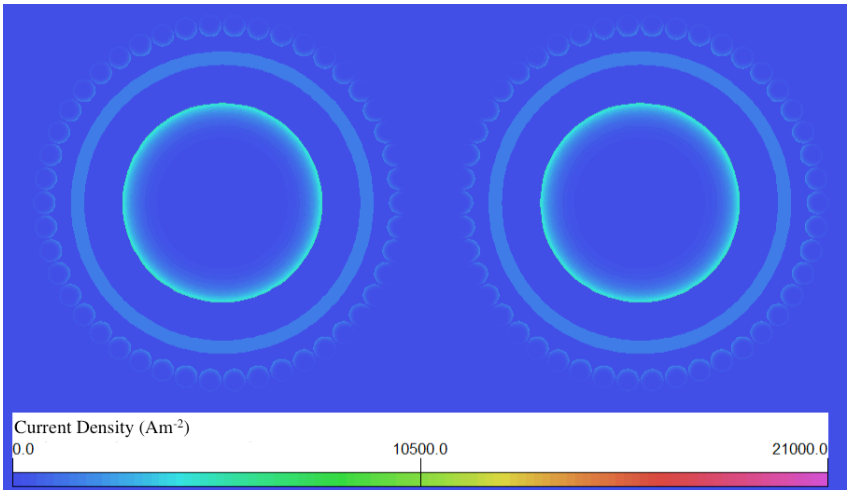

(c)

Figure 3.5. Simulated current density in base case cables: (a) cable 1, (b) cable 2 and (c) cable 3. The current density scale is the same each case for comparison. Cable diameters are different.

In spite of the high current density in the lead sheath of cable 1, it also has the highest armour currents. This is because the lead sheath is thinner for cable 1 (1.6mm) than the other cables (2.0mm and 2.8mm for cables 2 and 3 respectively).

The values for the resistance and the inductance per cable for cables 1 and 2 are shown in Table 3.5. These results are included in Figure 3.10.

	Cable 1		Cable 2	
Frequency (kHz)	Resistance (R') Ω/km	Inductance (L') mH/km	Resistance (R') Ω/km	Inductance (L') mH/km
DC	0.188	0.611	0.060	0.608
1	1.028	0.312	0.758	0.198
2	1.435	0.255	0.957	0.163
3	1.658	0.234	1.065	0.151
4	1.811	0.223	1.141	0.145
5	1.928	0.217	1.201	0.142
6	2.024	0.212	1.252	0.140
7	2.107	0.209	1.298	0.139
8	2.180	0.207	1.341	0.137
9	2.247	0.205	1.380	0.136
10	2.309	0.204	1.418	0.136

Table 3.5. Simulated values per cable of resistance per unit length and inductance per unit length for the base case models of cables 1 and 2.

Similar overall trends can be seen for cables 1 and 2 as for 3. Resistance is higher for the smaller cables, as expected. However, for the smaller cables, the resistance does not increase by such a large factor with increasing frequency. For instance, for cable 3 the 1kHz resistance is around 31 times greater than the DC resistance, but for cable 1 this multiple is only 5.5. This is primarily because the skin effect makes less difference in the smaller cables, where the areas of the conducting components are relatively small to begin with.

For the AC frequencies, the inductance is larger, the smaller the cable. This can be understood by considering the formula for the external inductance of a coaxial cable, equation (3.12) [66].

$$L' = \frac{\mu}{2\pi} \ln\left(\frac{r_{outer}}{r_{inner}}\right) \tag{3.12}$$

where r_{inner} and r_{outer} are the radii of the inner conductor and outer conductor respectively (m). Although this formula cannot be applied directly to the cables, to a great extent, the core and lead sheath act as a coaxial cable, as the current in the lead sheath is close in magnitude to that in the core (see Table 3.3) and tends to oppose it. Since the insulation is the same thickness for all cables (8mm), the ratio of the radii is given by equation (3.13):

$$\frac{r_{outer}}{r_{inner}} = \frac{r_{core} + 8mm}{r_{core}} = 1 + \frac{8mm}{r_{core}} \tag{3.13}$$

where r_{core} is the core radius (m). Hence with increasing core radius the value of L' decreases.

A breakdown of the losses in each layer of all three cables is shown in Figure 3.6. The core current is modelled at the same magnitude for all AC frequencies (1A peak) and at $1/\sqrt{2}$A for DC, in order to give the same RMS values for comparison. For an AC current of magnitude 1A at each frequency, the losses at 1kHz are approximately 4 times those for the modelled DC current in cable 1, 14 times in cable 2 and 22 times in cable 3. The majority of the losses, at all AC frequencies, are in the lead sheath. This is because it contains a large amount of current (see Table 3.3) but also has a relatively high resistance. In a DC cable, the DC current is many times the size of the ripple current; however, these results show that the ripple current can lead to significant losses.

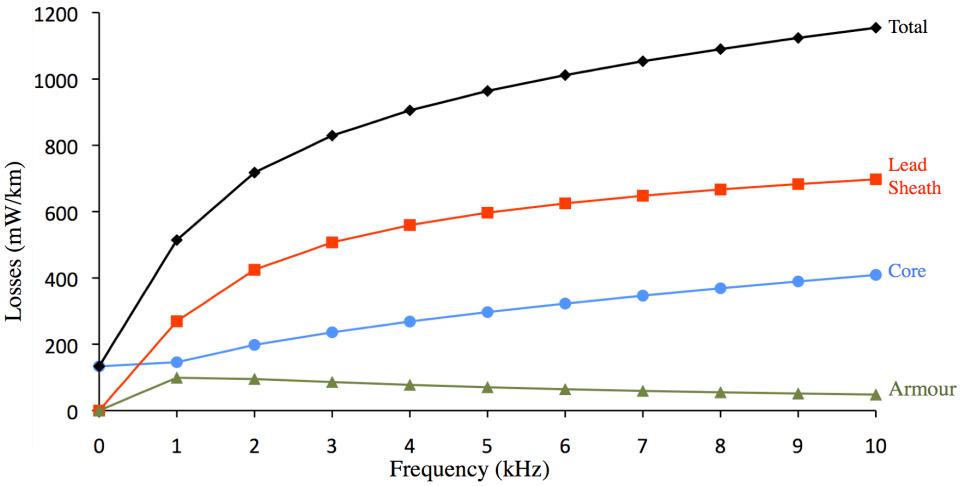

(a)

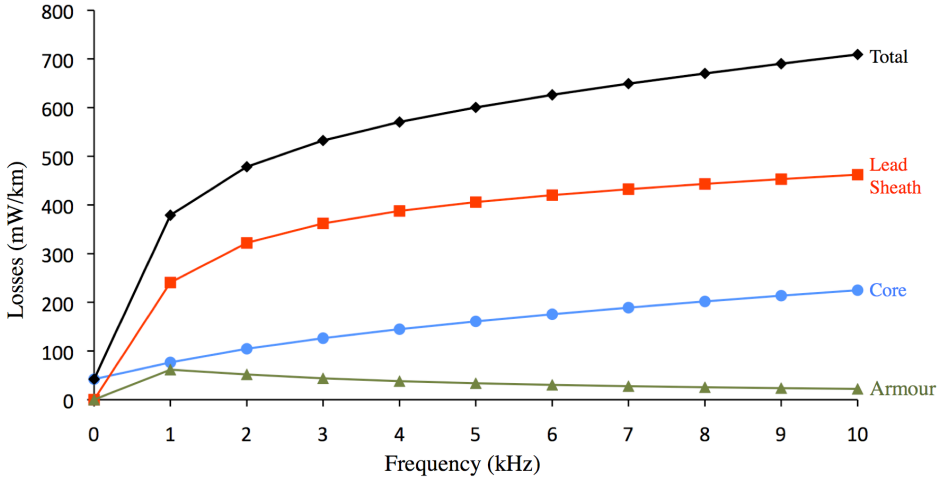

(b)

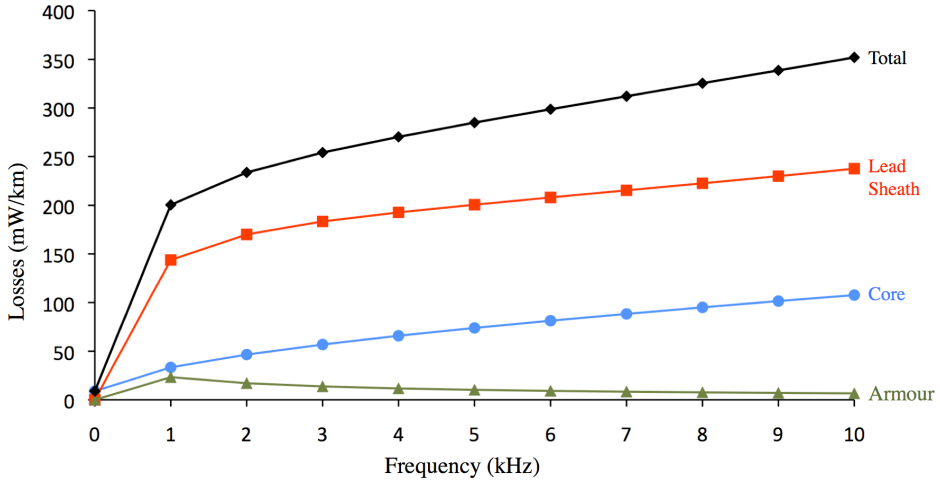

(c)

Figure 3.6. Comparison of the simulated losses in each conducting layer of the three sizes of cable at a range of frequencies: (a) cable 1, (b) cable 2, (c) cable 3.

3.5 Sensitivity Analysis

In this section a number of factors that can change cable parameters and behaviour is considered.

3.5.1 Parameters

3.5.1.1 Core Material

Aluminium has a lower conductivity ($3.480 \times 10^{7} \Omega^{-1} m^{-1}$) than copper but is cheaper and lighter and so is often used as the main conductor material. To compensate for the change in conductivity, while maintaining the required ampacity, cables with larger cores were modelled. The thickness of, and material choice for, the outer layers (including armour wire diameter) remains the same as before, but the overall cable diameter is increased due to the larger core. The required core sizes are shown in Table 3.6, along with the area of copper core that would give the same resistance.

Cable Designation	Aluminium Core Area (mm^2)	Equivalent Copper Core Area (mm^2)
1	150	93
2	500	311
3	2200	1367

Table 3.6. Aluminium core sizes modelled and size of copper core that would have the same DC resistance.

3.5.1.2 Water Blocking Sheath Construction

The sheath is designed both to block water and carry fault current. Some cable product ranges have different thickness lead sheaths for different power ratings [46, 48]. Others have the same size sheath regardless of size and rating [64]. In this modelling, the lead sheath thickness is set to 2.8mm for all cable types (therefore, cable 3 has the same parameters as before). All other parameters are the same as the base case, although the outer diameter is slightly increased for the two smaller cables.

3.5.1.3 Addition of Copper Wire Screen

A copper screen can be applied just inside the lead sheath to improve the fault current carrying capability of the cable [47]. The copper screen was modelled as a solid layer 0.5mm thick.

3.5.1.4 Cable Operating Temperature

The operating temperature limit for XLPE is 90°C [67]. Although a temperature gradient will exist within the cables, an approximation is made by modelling the entire cross-section as operating at 90°C (rather than 20°C, as in the base case). The conductivities of the materials concerned (copper, lead and steel) are shown in Table 3.7.

Material	Conductivity at 20°C ($\Omega^{-1}m^{-1}$)	Conductivity at 90°C ($\Omega^{-1}m^{-1}$)
Copper	$5.599x10^7$	$4.394x10^7$
Lead	$4.546x10^6$	$3.571x10^6$
Steel	$6.907x10^6$	$5.396x10^6$

Table 3.7. Calculated conductivity of metallic cable layers at 20°C (used in the base case) and 90°C.

3.5.1.5 Steel Armour Permeability

In [52] a range of steel armour was tested and found to have relative permeability (below saturation) in the range 100-210. Cables 1, 2 and 3 were modelled with armour relative permeability of 100 and 210 (compared to 155 in the base case).

3.5.1.6 Cable Spacing

As outlined in section 2.6.2, bipole cables are sometimes spaced apart when laid. In order to simulate the cables being spaced apart, only a single cable (rather than bipole) was modelled; this removes any interaction between cables.

3.5.2 Results and Analysis

The resistance and inductance at 1kHz for the various modelling conditions are shown in Figure 3.7 and Figure 3.8 respectively. The dashed lines represent the base case level. Analysis for each test then follows.

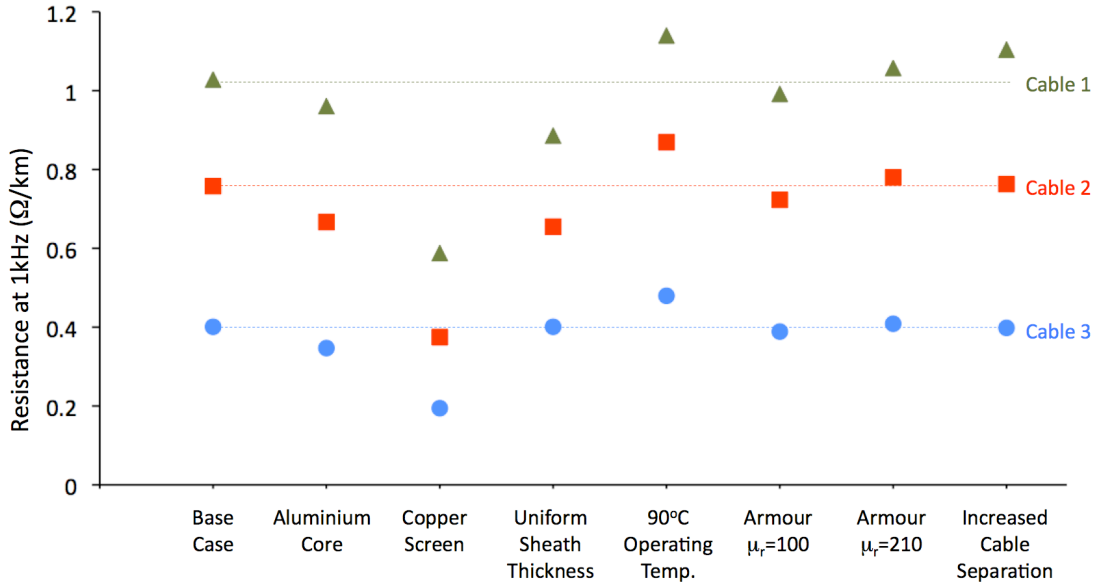

Figure 3.7. Resistance at 1kHz of the three simulated cable types and results of the sensitivity analysis.

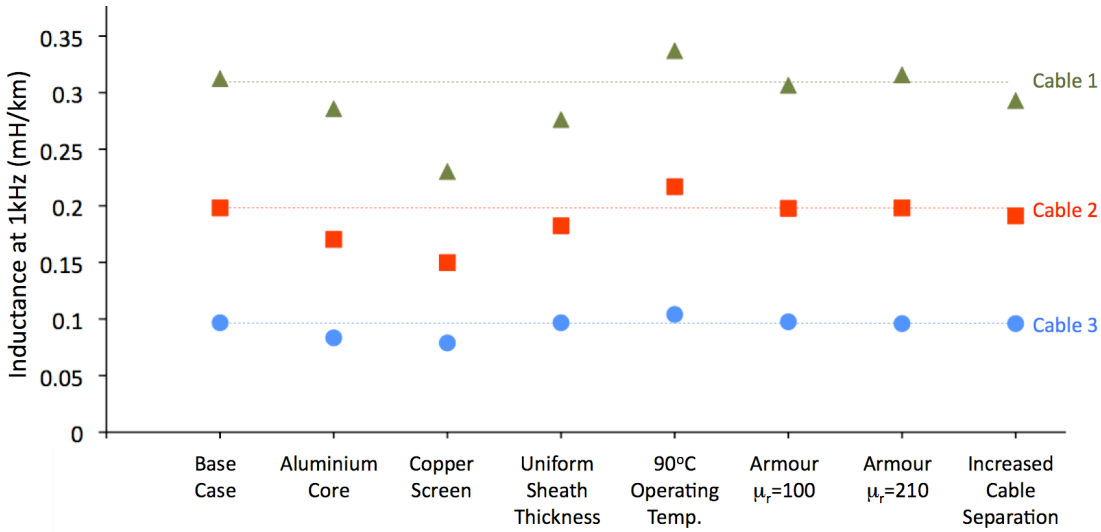

Figure 3.8. Inductance at 1kHz of the three simulated cable types and results of the sensitivity analysis.

3.5.2.1 Aluminium Core

In order to carry (approximately) the same DC current, the aluminium core must be larger than the equivalent copper core. As a result, the inductance is reduced in all cases in accordance with equations (3.12) and (3.13). The AC resistance is also reduced. Most of this reduction is attributable to the increased sheath radius. As described in section 3.4, the application of equation (3.11) shows that the time-varying magnetic field is weaker the larger the sheath radius. Therefore the induced eddy current density in the sheath is smaller and the losses lower.

3.5.2.2 Copper Screen

The inclusion of the copper screen makes the largest difference of any of the changes considered. The current density in cable 3 is shown in Figure 3.9 along with a comparison to the base case. In Figure 3.9(b), the four highest spikes are the current density in the copper screen; the next four highest are from the core and the others the outer cable layers.

Due to its high conductivity (over 10 times that of lead) and correspondingly small skin depth, the current density in the copper screen is far higher than in the lead sheath in the base case. This can be seen by comparing the particularly high spikes in Figure 3.9(b) with the currents in the outer layers seen in Figure 3.9(c). The magnetic field is therefore very much reduced outside the copper screen, leading to relatively low induced currents in the lead sheath and steel armour.

In cable 3, at 1kHz, the current in the copper screen contains 63% of all induced currents in the outer cable layers. This rises to 78% at 10kHz. The other cables follow a similar pattern. Because the copper screen has a low resistance and contains a large proportion of the induced currents, it reduces the resistance of the cable.

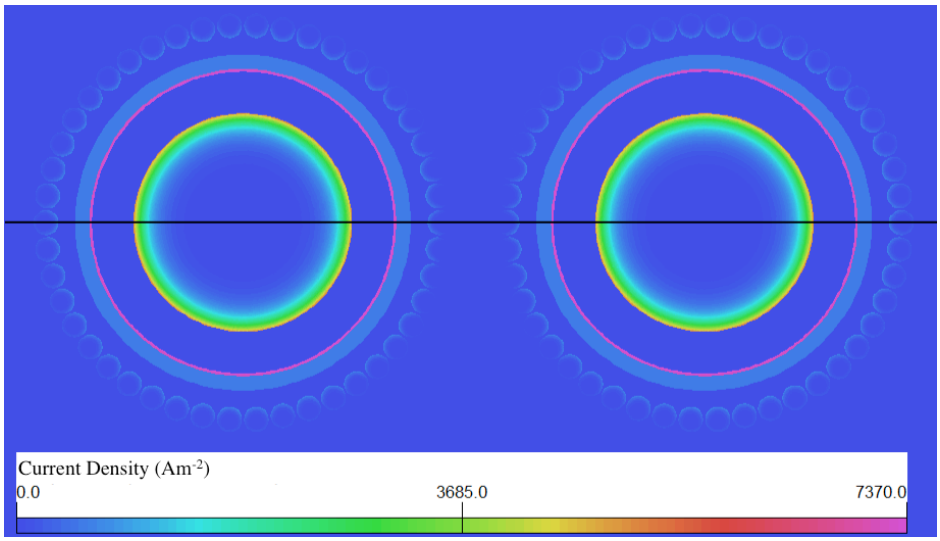

(a)

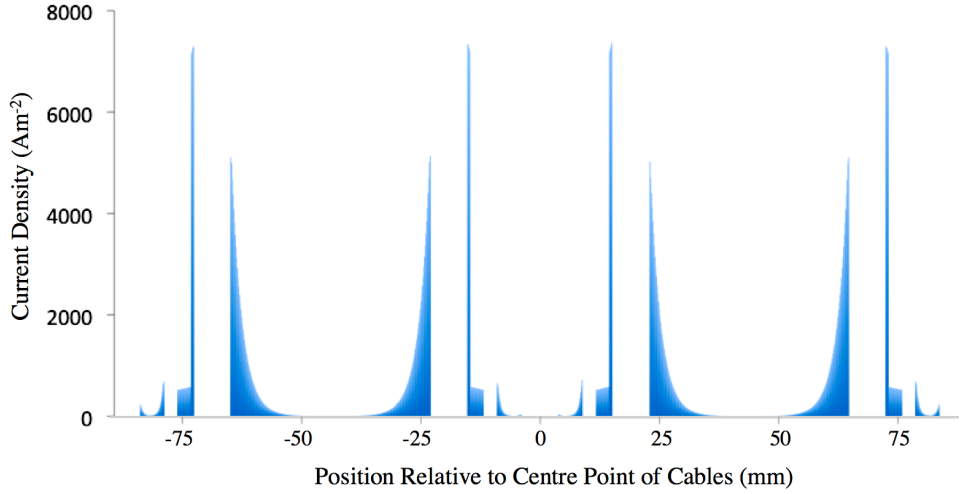

(b)

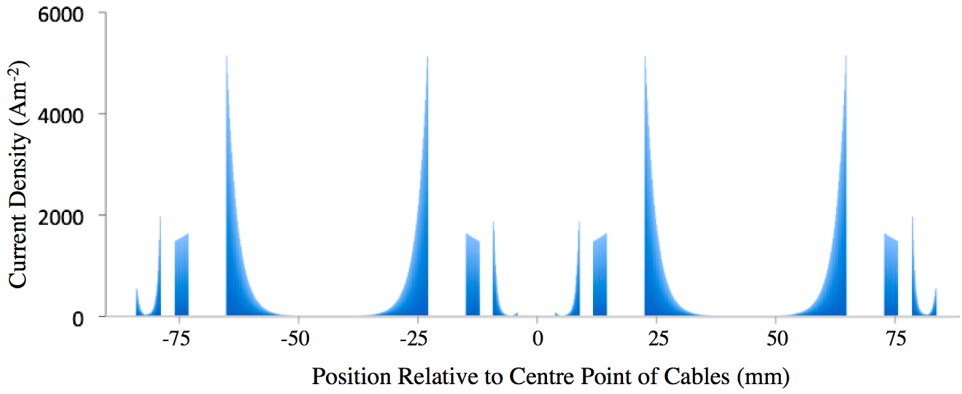

(c)

Figure 3.9. (a) Simulated current density distribution in cable 3 with copper screen included. (b) Plot of simulated current density along the black line shown in (a). (c) Equivalent plot of simulated current density along the centre line of the base case cable 3 in bipole arrangement.

The inductance is reduced compared to the base case, particularly at lower frequencies, due to the reduction of the magnetic field outside the copper screen. At higher frequencies, the induced currents in the lead sheath are larger and these reduce the magnetic field outside the lead sheath meaning that the inductance of the two cable types is very similar.

3.5.2.3 Water Blocking Sheath Construction

Increasing the sheath thickness in cables 1 and 2 results in lower resistance and inductance in both cases. Table 2.1 shows the total current and losses in each layer of cables 1 and 2, for the base case and for cables with 2.8mm lead sheath. The base case cable 1 model has a lead sheath 1.6mm thick and the cable 2 model a lead sheath 2.0mm thick.

	Cable 1		Cable 2	
	Base Case	2.8mm Lead Sheath	Base Case	2.8mm Lead Sheath
Sheath Current % of Core at 1kHz	59.2%	76.5%	71.8%	80.6%
Sheath Loss (mW/km) at 1kHz	269.2	247.1	240.7	212.9
Armour Current % of Core at 1kHz	39.6%	29.2%	36.0%	28.6%
Armour Loss (mW/km) at 1kHz	99.1	50.1	61.7	38.1

Table 3.8. Size of simulated lead sheath and armour currents in proportion to the core current along with the losses associated with these currents.

The reduced inductance results from the same mechanism as seen in the cable with a copper screen. The thicker sheath has larger current and therefore the magnetic field is lower outside it. The reduced magnetic field also results in lower currents and therefore lower losses in the armour. However, the losses in the sheath are also reduced, in spite of the increased total current. This is because of the lower resistance of the thicker sheath, which more than compensates for the increased current, therefore reducing sheath losses. The increased sheath thickness reduces the cable resistance at all the considered AC frequencies.

3.5.2.4 Operating Temperature

Higher operating temperature increases resistance for all cables at all frequencies, as expected. There is also an increase in inductance moving from 20^{o}C to 90^{o}C. At

1kHz, this increase is 7.9% for cable 1, 9.5% for cable 2 and 7.6% for cable 3. The increase in inductance is caused by two factors. First, the sheath resistivity and therefore skin depth is increased. This results in lower sheath currents and therefore higher magnetic field outside the sheath and increased inductance. Second, the increased skin depth in the core results in a larger internal inductance. These results are important as the irregular nature of wind farm power output means that the cable losses and therefore operating temperature will vary significantly over time.

3.5.2.5 Armour Permeability

Changing the armour permeability in the range considered makes only a small difference to cable resistance and inductance. Applying equation (3.10), increasing permeability reduces the skin depth in the steel wires, therefore losses increase and resistance increases. Increasing the permeability also increases the size of the B-field in the steel, which increases inductance. Neither of these effects are particularly large because the magnetic field in and around the armour is relatively small due to the eddy currents in the lead sheath.

3.5.2.6 Cable Separation

The magnitude of the lead sheath current in all cables is almost unaffected by the increased spacing, however the armour current is increased due to the lack of cancellation of the magnetic fields between the two cables. This increases losses and, as a result, resistance. It also means that the magnetic field is better contained within the cable and therefore the inductance is reduced. This is a slightly unexpected result as normally increasing the spacing between two opposing conductors increases their inductance. In this case, however, moving the return conductor away makes the steel armour, in effect, take over its role. The return current (now in the armour) is closer to the core than when the cables were close together and the inductance reduces. This result is discussed further in Appendix A.

The effect of spacing is most pronounced in cable 1 because its outer layers are relatively thin and so the magnetic field is stronger outside the cable and the

interaction (or lack of interaction) with the adjacent cable is more significant. For cable 3 there is very little effect, which shows that there is little interaction (at ripple frequencies) between these cables, even when they are laid side by side.

The most important result is for cable 3. This is because, were the bipole transmission cables to be laid side by side, they would constitute a single point of failure for the wind farm (or part thereof) and so it is more likely that the extra expense of trenching these cables separately would be met.

3.5.2.7 Frequency

In subsequent chapters, interaction with the AC grid and system resonant frequency are considered. Therefore, the base case cables were modelled at a range of frequencies. The resistance and inductance of the three cable types are shown in Figure 3.10.

The relationships between resistance and frequency, and inductance and frequency seen in these graphs have been explained in section 3.3. Note that the similarity in value of the DC inductance for the three cables at low frequency is coincidental. This value depends on a number of factors including core radius, core separation and steel armour size and position.

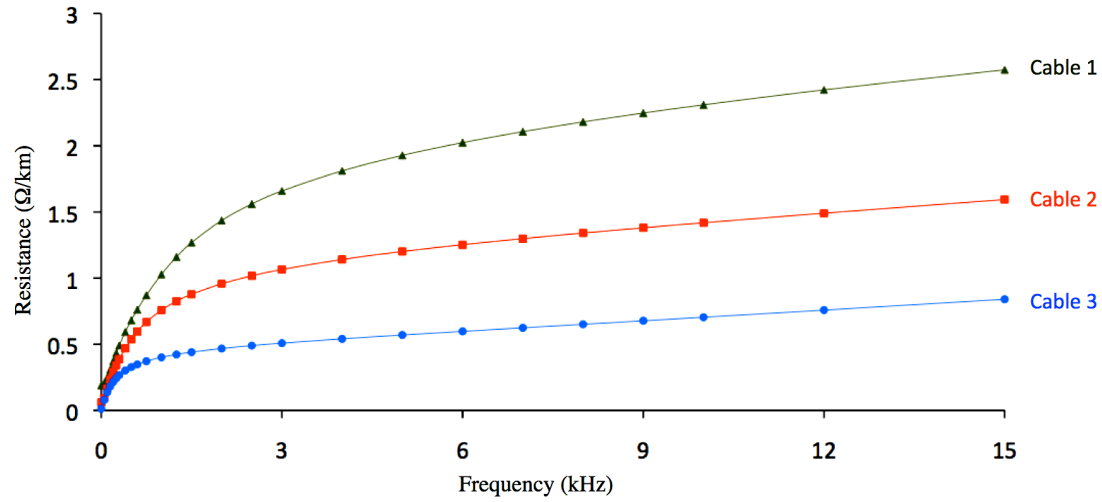

(a)

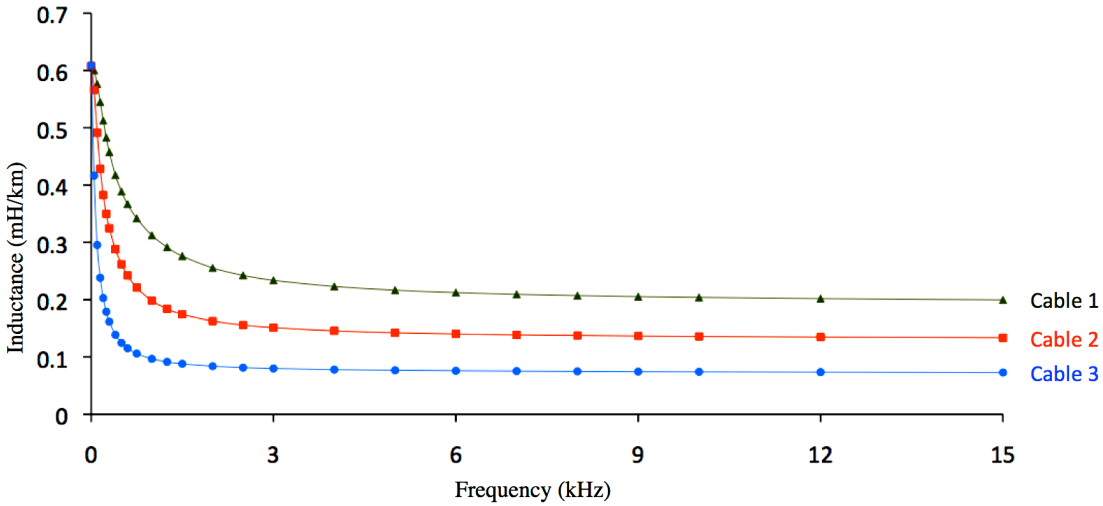

(b)

Figure 3.10. (a) Resistance and (b) inductance at a range of frequencies simulated for the base case cables.

3.6 Experimental Validation

Due to the scale and cost of the cables being modelled, it was not possible to validate the exact models used. Instead, experiments were undertaken on a smaller scale using cables with a similar construction.

3.6.1 Approach

Two coaxial cables were chosen for simulation and laboratory test. These were the Nexans 5603-AZZD [68] and the Heliax/Andrew LDF4-50A [69]. Each consists of an inner and outer conductor. The outer conductor was used to simulate the behaviour of the lead sheath in the base case cable and the inner conductor to simulate the core. The cable parameters are shown in Table 3.9 and a picture of a stripped back section of LDF4-50A cable is shown in Figure 3.11.

Cable Type	LDF4-50A	5603-AZZD
Inner Conductor Material	Copper-Clad aluminum wire	Copper
Inner Conductor Construction	1x2.4mm radius conductor	7x0.385mm radius strands
Inner Conductor DC Resistance	1.48mΩ/m	5.70mΩ/m (measured)
Outer Conductor Material	Corrugated copper	Copper
Outer Conductor Construction	Solid (with welded seam). 6.75mm inner radius, 7mm outer radius.	168x0.09mm radius wires (measured)
Outer Conductor DC Resistance	1.9mΩ/m	4.04mΩ/m (measured)
Cable Outer Radius	7.85mm	5.15mm

Table 3.9. Parameters of coaxial cables used for testing.

Figure 3.11. Stripped back section of LDF4-50A cable.

Other than the difference in size, the construction of these cables is not identical to a power cable (e.g. lack of steel armour, non-uniform construction of conductors). The possible effect of this on experimental results is discussed in the section 3.6.2.5, which covers experimental error.

The cables were set up in a bipole arrangement. The ends of the outer conductor were joined together to allow induced current to flow (this creates the same effect as grounding the lead sheath of a transmission cable regularly along its length). Two methods were used to assess the behaviour of the cables. A Wayne Kerr 'Precision Magnetics Analyzer', 3260B was used to measure the resistance and inductance of both cables. For the 5603-AZZD cable, a signal generator was used to input a current into the inner conductor and a current transformer ammeter used to measure the phase and magnitude of the current in the outer conductor.

Two frequency ranges were considered, first from 1kHz to 10kHz. Secondly, in order to make the experiments more representative of the transmission cables, the frequency was changed to make the experiment, to an extent, 'dimensionless'. In particular, the dimensionless ratio of the skin depth of the lead sheath (or outer conductor) to the thickness of the lead sheath (or outer conductor) was made the same for the experimental work as for the base case cable 3 (transmission cable). Due to the different geometry of the tested cables compared to the simulated cables (the lack of steel armour and relative size of core/inner conductor, for instance), it was only possible to non-dimensionalise this one parameter. However, the most important factor for changing inductance with frequency is the reduction of the magnetic field outside the lead sheath and the largest losses are from the induced currents in the lead sheath. Therefore, this is the most sensible parameter to keep constant.

For the transmission cable, the ratio in question is 2.66:1 at 1kHz, i.e. 7.46mm (skin depth of lead) : 2.8mm (lead sheath thickness). The outer conductor for the 5603-

AZZD cable is equivalent to a solid layer 0.174mm thick. Using equation (3.10) it has been calculated that, at a frequency of 21.85kHz, the skin depth of the outer conductor material is 2.66 times this value. For the LDF4-50A cable, the outer conductor thickness is 0.25mm and the required frequency is 11.72kHz.

The same bipole arrangement was modelled using the FEM.

3.6.2 Results and Analysis

Results and discussion of the FEM analysis and experimental work follow. Sources of error are considered in section 3.6.2.5.

3.6.2.1 Current and Magnetic Field Distribution from FEM Analysis

Figure 3.12 shows the current distribution in LDF4-50A cable at 11.72kHz from the FEM modelling and Figure 3.13 shows the magnetic B-field.

Figure 3.12 can be compared to the current density distribution results for the base case transmission cable shown in Figure 3.1. In both cases a relatively high induced current density is seen in the metallic outer layer(s) of the cable.

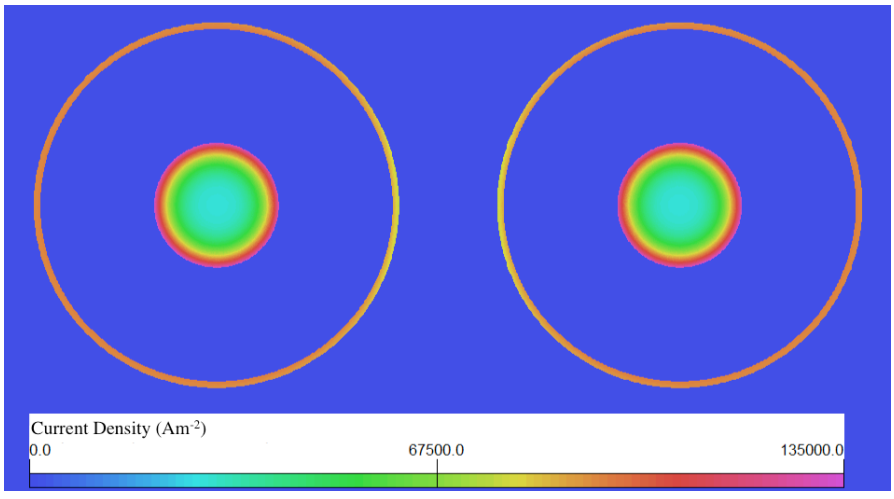

Figure 3.12. FEM simulation of current density at 11.72kHz with 1A (peak) of core current for the LDF4-50A cable in bipole arrangement.

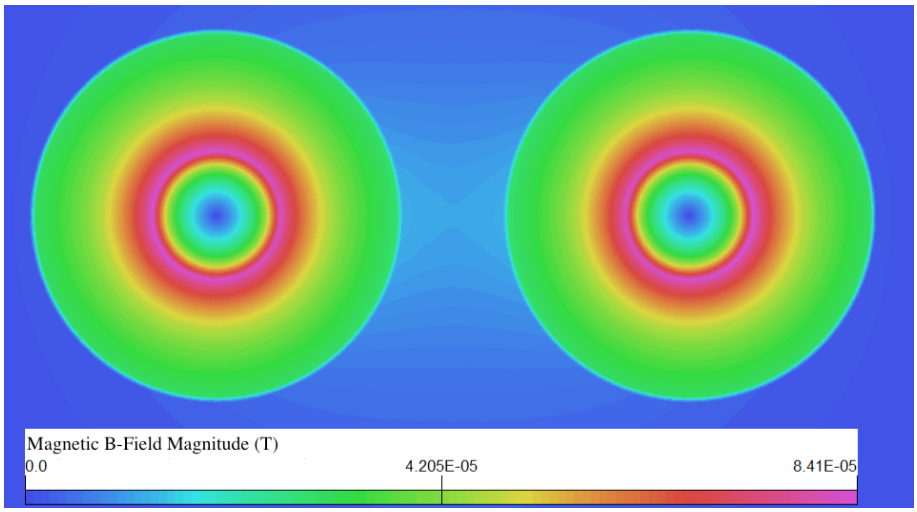

Figure 3.13. FEM simulation of magnetic B-field at 11.72kHz with 1A (peak) of core current for the LDF4-50A cable in bipole arrangement.

The comparison is a little more difficult for the magnetic field distribution in Figure 3.13 (compared to Figure 3.4), due to the lack of magnetic armour in the experimental cables, however, the magnetic field is largely contained within the metallic layers of each cable in both cases. This verifies the principle of using an increased frequency to compensate for the reduced thickness of the outer conductor, in the experimental work.

3.6.2.2 Inductance and Resistance Measurements

Figure 3.14, Figure 3.15, Figure 3.16 and Figure 3.17 show the values of resistance and inductance derived from the FEM and the experimental work, for both frequency ranges, for the 5603-AZZD and LDF4-50A cables respectively. For the experimental results, the DC inductance was approximated to be the same as low frequency AC inductance to allow measurement with the magnetic analyser. In each case, ±10% error bands are shown around the FEM results.

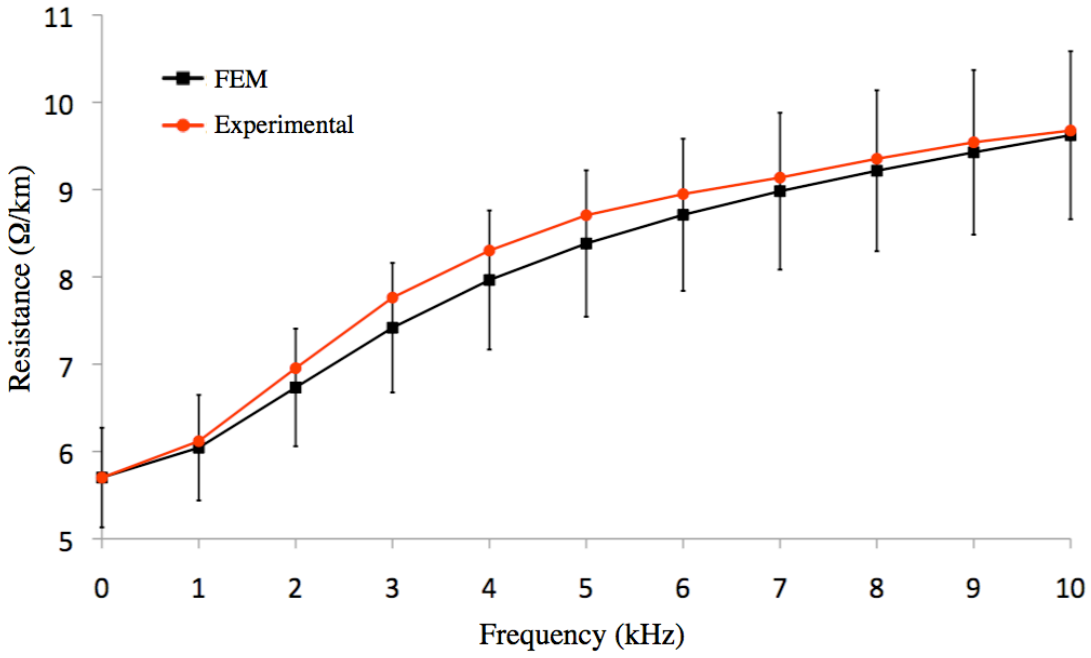

(a)

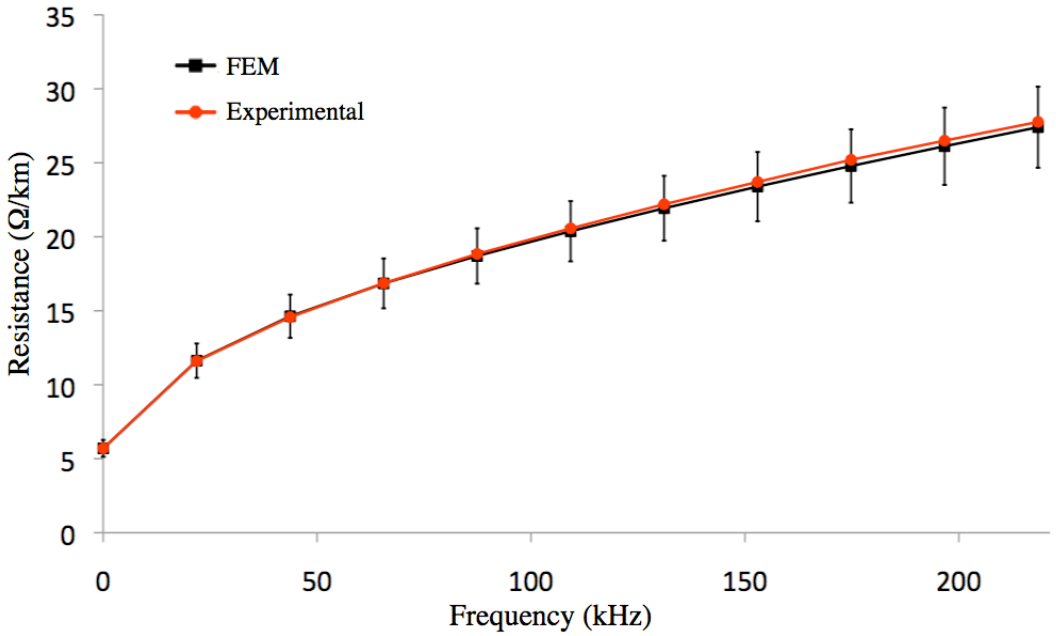

(b)

Figure 3.14. FEM simulation and experimental measurements for the resistance for the 5603-AZZD cable at both tested frequency ranges.

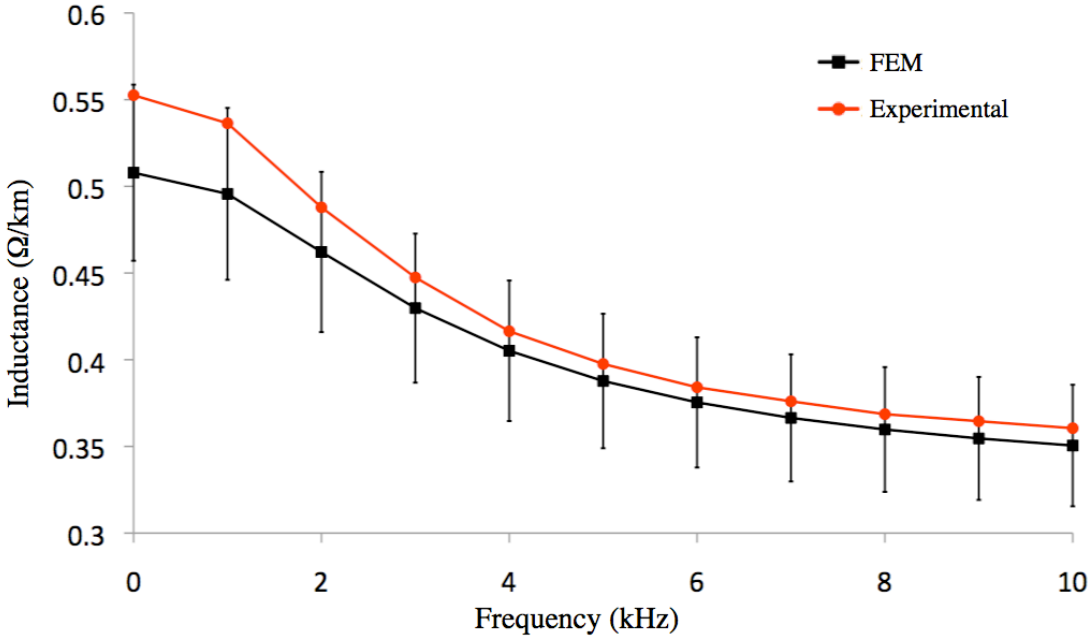

(a)

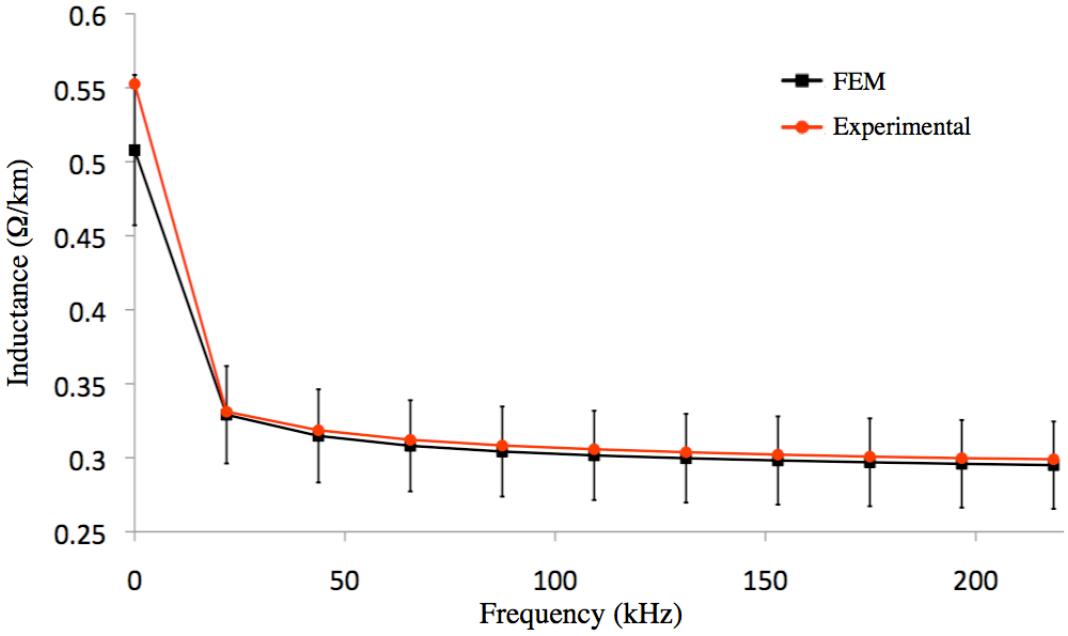

(b)

Figure 3.15 FEM simulation and experimental measurements for the inductance for the 5603-AZZD cable at both tested frequency ranges.

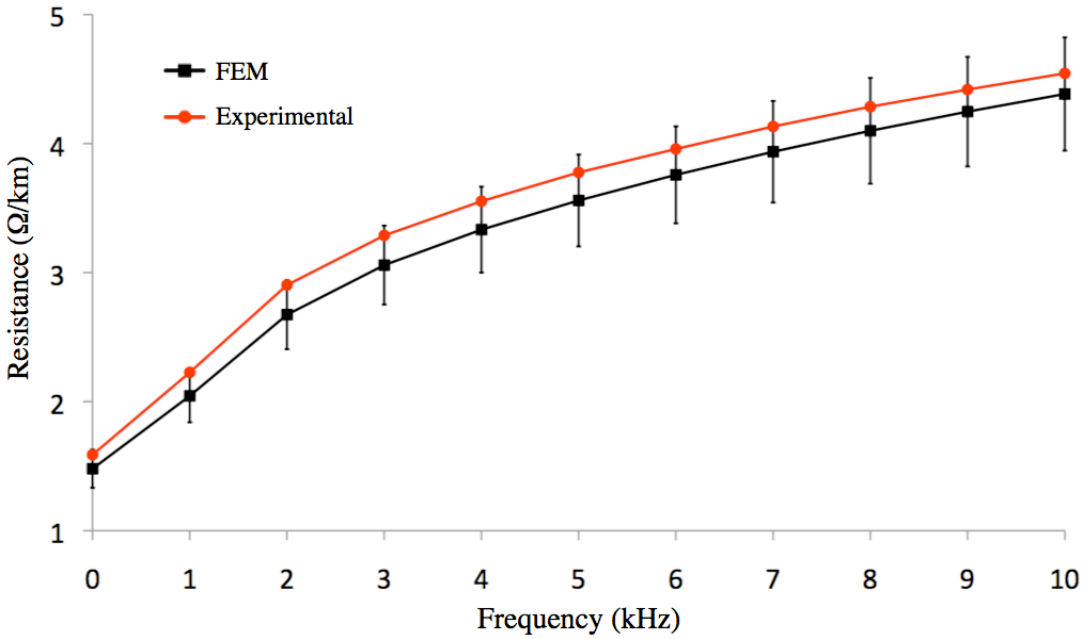

(a)

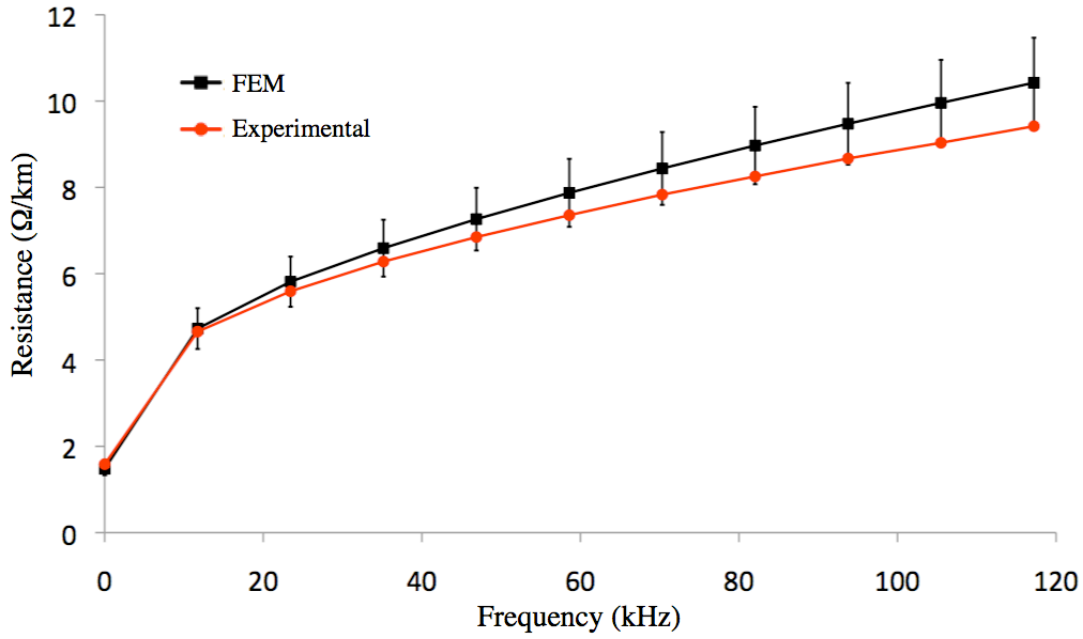

(b)

Figure 3.16. FEM simulation and experimental measurements for the resistance for the LDF4-50A cable at both tested frequency ranges.

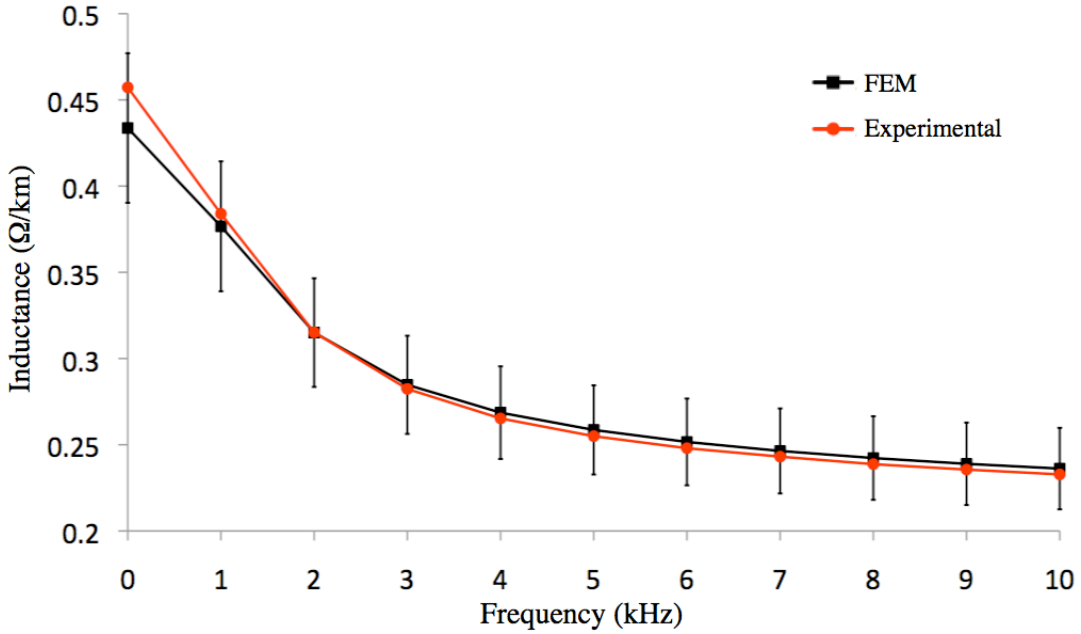

(a)

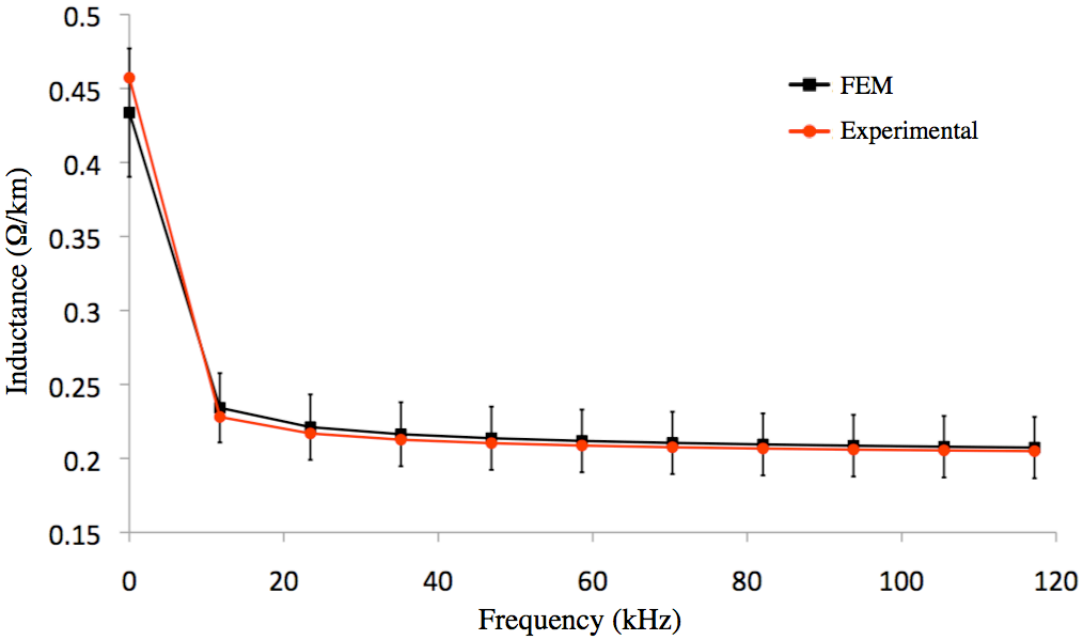

(b)

Figure 3.17. FEM simulation and experimental measurements for the inductance for the LDF4-50A cable at both tested frequency ranges.

3.6.2.3 Analysis of Inductance and Resistance Measurements

The vast majority of the experimental and FEM results fall well within the 10% error margins shown on each graph. To be more precise, all results fall within 9% of each other and most results are within a 2% error margin.

Figure 3.14(b) and Figure 3.16(b) show resistance and Figure 3.15(b) and Figure 3.17(b) show inductance for the frequency range chosen to make cable behaviour representative of transmission cable behaviour. Comparing the graphs for resistance, they both have a similar shape, showing a steady rise of resistance with frequency that becomes shallower as frequency increases. The graphs for inductance also have a similar shape to one another, with a sharp fall in inductance when comparing the DC result to the first AC frequency result, then a very slow fall as AC frequency increases. For both resistance and inductance, these graphs show similar behaviour to that seen in the transmission cable in Figure 3.10.

The use of non-dimensionalised cable metallic sheath thickness has successfully recreated the predicted behaviour of a transmission cable in the much smaller cables on test. As discussed in section 3.6.1, there are other cable parameters that could not be non-dimensionalised and therefore the results are not directly scalable. However, the importance of induced eddy currents in the cable metallic sheath in determining distributed cable parameters has been emphasised.

3.6.2.4 Direct Measurements of Induced Currents

The magnitude and phase of the outer conductor current for the 5603-AZZD cable from the FEM and from experimental results for the frequency range 1kHz to 10kHz are shown in Table 3.10.

The results from FEM analysis and experimental work closely match again. In this case, the frequency range is clearly at a transition from relatively low induced currents to high induced currents in the outer metallic layers of the cable.

	FEM Results		Experimental Results	
Frequency (kHz)	Outer conductor current magnitude as % of inner conductor current	Phase of outer conductor current relative to inner conductor current (degrees)	Outer conductor current magnitude as % of inner conductor current	Phase of outer conductor current relative to inner conductor current (degrees)
1	26.4%	-106.9	29.6%	-109.7
2	46.9%	-121.0	52.1%	-129.8
3	60.7%	-131.6	65.9%	-137.1
4	69.6%	-139.2	77.5%	-142.6
5	75.6%	-144.8	80.4%	-148.4
6	79.7%	-148.9	84.1%	-152.4
7	82.8%	-152.1	86.4%	-155.1
8	85.1%	-154.7	88.2%	-157.8
9	87.0%	-156.8	89.6%	-159.8
10	88.5%	-158.5	90.6%	-161.6

Table 3.10. Magnitude and phase of the 5603-AZZD cable outer conductor current from FEM simulation and experimental measurements.

The results show that the magnitude of the induced currents are very sensitive to frequency. For example, increasing the frequency from 1kHz to 4kHz causes the skin depth of the outer conductor material to halve, but in both experimental and FEM results the magnitude of outer conductor current more than doubles. This result is not particularly intuitive and it emphasises the value of using the FEM and checking it with experimental work in order to give confidence in the results. These results and the use of FEM are discussed further in Appendix A.

Interestingly, if these results are non-dimensionalised for comparison to a subsea transmission cable with lead sheath 2.8mm thick, the frequency of 1kHz in the experimental work is equivalent to 46Hz for the transmission cable. There are a number of implications from this, including:

- For a 50Hz AC underground cable with lead sheath approximately 2.8mm thick (but without armour), cable parameters for harmonic currents (i.e.

150Hz, 250Hz etc) could be significantly different to the 50Hz parameters and accurate modelling of AC harmonics may need to account for this.

- The ratio of the thickness of the lead sheath to the skin depth also changes as the lead sheath thickness changes. For example, increasing the lead sheath thickness by √2 (to 4.0mm) could, based on the results here, almost double the induced currents. Induced currents in metallic armour may also be similarly affected, but further work is required to determine this.

3.6.2.5 Experimental and FEM Sources of Error

At the higher frequency ranges the FEM and experimental results are particularly close, with one exception. Figure 3.16(b) shows a discrepancy between the value of resistance from experimental and FEM work that increases with frequency. The most likely reason is the construction of the corrugated outer conductor in the LDF4-50A cable, which can be seen in Figure 3.11, compared to the FEM model of a uniform layer. The non-uniform geometry in the LDF4-50A reduces the skin effect in the outer conductor and therefore reduces the resistance in the experimental results, particularly at high frequencies.

The errors at lower frequencies are greater. The principal reason is the measuring equipment used. At low frequency, the absolute impedances of the sections of cable measured are low and this leads to less accurate results from the magnetics analyser. Other possible sources of error for the experimental approach include:

- The construction of components, such as a stranded inner or outer conductor or copper cladding on an aluminium conductor, is different from the FEM simulation of solid, uniform layers;
- Inexact cable arrangement and connections in the experimental set up;
- Inaccuracy of information (either from datasheets or from measurements) on material parameters and dimensions;
- Non-uniformity of material parameters or dimensions;
- For the FEM modelling, there is an error of up to 2% given by the software.

Taken together, these errors account for the discrepancy between the experimental and FEM results, with the larger error likely to be in the experimental results.

A very similar pattern of induced currents has been observed in the tested coaxial cables and in the transmission cables modelled. The results for the distributed parameters also follow the same pattern with changing frequency as in the transmission cables. This, together with the closeness of the experimental and FEM results, means that the FEM results for the transmission cables can be used with confidence.

3.7 Cable Capacitance

As discussed in section 2.6.2, the voltage of the (metallic) water blocking sheath can be assumed to be, effectively, zero along its length. Therefore the capacitance of the cable per unit length (C' (Fm^{-1})) can be calculated using equation (3.14) [70],

$$C' = \frac{2\pi\varepsilon}{\ln\left(\frac{r_{outer}}{r_{inner}}\right)} \tag{3.14}$$

where $\varepsilon = \varepsilon_r\varepsilon_0$ (Fm^{-1}) and ε_r is relative permittivity of the insulating (dielectric) material.

The value of relative permittivity for XLPE is temperature dependent. In [71] the value was found to decrease by 5.7% with an increase in temperature from 20^{o}C to 70^{o}C, representing a decrease of 0.114% per ^{o}C. In [72], ε_r was found to decrease by 11.9% with a temperature increase from 20^{o}C to 90^{o}C, a decrease of 0.170% per ^{o}C. Using a value of 0.14% decrease in ε per ^{o}C and starting with a value of $\varepsilon_r = 2.3$ at 20^{o}C, gives $\varepsilon_r = 2.075$ at 90^{o}C.

The only other factor in the sensitivity analysis that affects capacitance is the core material. In the case of the aluminium conductor, the increased size changes the ratio of r_{outer} to r_{inner} in equation (3.14) and therefore changes the capacitance. The value of ε does change a very small amount with frequency, by around 0.1% in XLPE from 1kHz to 10kHz, based on experimental results in [73]. This change is small enough to be neglected.

The capacitances of the three cable types, at 20°C and 90°C, with either core material, are shown in Table 3.11.

	Copper Conductor			Aluminium Conductor		
Core Area (mm^2)	95	300	1400	150	500	2200
Cable Capacitance at 20°C (μF/km)	0.142	0.214	0.398	0.166	0.261	0.484
Cable Capacitance at 90°C (μF/km)	0.129	0.193	0.359	0.150	0.235	0.437

Table 3.11. Calculated capacitance for cables with copper and aluminium core at 20°C and 90°C.

3.8 AC Corrosion

As discussed in section 2.6.5.2, electrical corrosion is a potentially significant problem in a three-phase AC cable system consisting of single core cables spaced some distance apart. In order to assess the magnitude of induced armour currents caused by a DC ripple compared to a 50Hz AC current, the base case FEM models for cables 1, 2 and 3 were used. Although there are differences between the construction of AC and DC cables, the designs are generally similar enough [48] to give a qualitative assessment of whether a 1kHz ripple may pose a corrosion risk.

Table 3.12 shows the magnitude of total armour current as a percentage of core current in each cable type at 50Hz and 1kHz. At 1kHz, both closely laid and widely separated cables are shown.

	Cable 1	Cable 2	Cable 3
Armour Current as Percentage of Core Current at 50Hz, wide spacing	28.3%	44.1%	59.1%
Armour Current as Percentage of Core Current at 1kHz, wide spacing	48.9%	41.6%	29.4%
Armour Current as Percentage of Core Current at 1kHz, closely laid	39.6%	36.0%	27.1%

Table 3.12. FEM simulation results for magnitude of total armour current as a percentage of core current in each cable type at 50Hz and 1kHz.

The armour currents are larger at 1kHz for widely spaced cables and, again, the effect of spacing is largest in cable 1. The effect of spacing at 1kHz is less pronounced than would be expected at 50Hz because of the reduced interaction between cables at 1kHz (see section 3.5.2.6).

Given that the magnitude of the 50Hz AC current would be many times the magnitude of a DC ripple current, these figures show that, in absolute terms, the induced armour currents in a DC cable will be only a small fraction of those in an equivalent AC cable.

Some caution is advisable, however. A study on subsea passive metallic materials (such as pipelines) in [74] states that the threshold above which AC corrosion becomes significant is 20A/m^2, while another study ([75]) gives this number as 30A/m^2. The studies state that, above 100A/m^2, AC corrosion is likely and could accelerate the overall corrosion rate by a factor between 2 times and 5 times. From Figure 3.5, it can be seen that for a 1kHz core current of magnitude 1A, armour currents exceed 100A/m^2 for all cables. The implication is that AC corrosion may become a problem after a number of years cable service, if protective measures, such as burying or coating, are compromised and a section of steel wire breaks, forcing induced currents into the seawater. In this case, it is possible that the currents will not exclusively flow to the other broken end of armour wire, but may also flow to unbroken but exposed sections, contributing to corrosion of those wires.

3.9 Chapter Summary

The finite element method has been used to obtain values of resistance and inductance for three cable types that are used in the system modelling in this thesis. Capacitance has also been calculated. A sensitivity analysis showed that cable operating temperature and the construction of the water blocking metallic sheath along with the possible addition of a copper screen can significantly affect cable parameters. The modelling approach was experimentally validated, showing that the finite element method results can be used with confidence.

4 Ripple Propagation in the Offshore DC Grid

The cable parameters calculated in chapter 3 are combined with wave propagation theory to describe the propagation of ripple current and voltage in a DC grid. The work is verified using standard simulation software (Simulink). The same models are then used to investigate resonant circuits that may be formed in the system.

4.1 Transmission Line Modelling and Wave Propagation Theory

Figure 2.12 shows a π-section representation of a transmission line. This model consists of a series branch with resistance and inductance and two shunt branches, each with a capacitance and resistance. In the shunt branches, the resistance accounts for the dielectric loss factor of the cable insulation. This loss factor is negligibly small for XLPE and so this resistance is ignored.

4.1.1 Short Cables

For a short section of cable, the shunt capacitance is negligible and can be excluded; the nominal values of cable inductance and (series) resistance can be used. For longer distances however, this is inaccurate.

4.1.2 Medium Length Cables

The voltage and current ripples produced by the DC-DC converters propagate through the cables as waves. In a sufficiently short cable section, the phase of the wave is almost identical at both sending end and receiving end, so consequently the series impedance alone (as described in section 4.1.1) is an adequate cable model. With increasing transmission distance, the shunt capacitance must also be included. For a medium length cable (the definition of medium depends on the level of accuracy required, the frequency and the cable parameters), using the nominal values of inductance, resistance and capacitance (the latter is split equally between the two shunt branches, as shown in Figure 2.12) gives adequate results.

4.1.3 Long Cables

For longer cables, an exact calculation, which fully accounts for the behaviour of the ripple as a wave in the cable, must be carried out to obtain the equivalent impedance and admittance of the cable.

4.1.3.1 π-Section Transmission Line Equivalent Parameters

To calculate the equivalent cable parameters, two important quantities first need to be computed: the characteristic impedance, Z_C (Ω), and the propagation constant, γ (m^{-1}). These are defined in equations (4.1) and (4.2) [58, 66].

$$Z_C = \sqrt{\frac{R' + j\omega L'}{G' + j\omega C'}} \tag{4.1}$$

$$\gamma = \sqrt{(R' + j\omega L')(G' + j\omega C')} \tag{4.2}$$

where R', L', C' are the per unit distance values for cable resistance, inductance and capacitance respectively. G' (the conductance of the dielectric per km ($\Omega^{-1}m^{-1}$)) can be neglected due to the small dielectric loss factor for XLPE [32].

The propagation constant can be written as (equation (4.3)):

$$\gamma = \alpha + j\beta \tag{4.3}$$

where α is the attenuation constant (m^{-1}) (which determines the level of attenuation as the wave travels along the able) and β the phase constant (radians/m) (which determines the change of phase as the wave travels along the cable). The wavelength, λ (m), is then given by equation (4.4).

$$\lambda = \frac{2\pi}{\beta} \tag{4.4}$$

Full details of the derivation of the voltage and current along the transmission line are covered in a number of texts, including [58]. This derivation is not repeated here. The analysis in this section begins with the hyperbolic forms of the current and voltage in a transmission line, as given in equations (4.5) and (4.6) [58].

$$I(x) = I_R \cosh(x\gamma) + \frac{V_R}{Z_c} \sinh(x\gamma) \tag{4.5}$$

$$V(x) = V_R \cosh(x\gamma) + I_R Z_C \sinh(x\gamma) \tag{4.6}$$

where *I(x)* and *V(x)* are the magnitudes of the AC current and voltage respectively, at a distance *x* from the receiving end of the cable. I_R and V_R are the current and voltage respectively at the receiving end of the cable.

From these equations, it is possible to derive equations (4.7) and (4.8), which give the values of Z_{eq} and Y_{eq} in Figure 2.12 needed to obtain accurate values for current and voltage at the two ends of the transmission line [58].

$$Z_{eq} = Z_c \sinh l\gamma = Z \frac{\sinh l\gamma}{l\gamma} \tag{4.7}$$

$$\frac{Y_{eq}}{2} = \frac{1}{Z_c} \tanh \frac{l\gamma}{2} = \frac{Y}{2} \frac{\tanh \frac{l\gamma}{2}}{\frac{l\gamma}{2}} \tag{4.8}$$

where Z_{eq} and Y_{eq} (split in half at either end of the line) are the π-equivalent impedance and admittance respectively, as shown in Figure 2.12. *Z* and *Y* are the nominal impedance and admittance and *l* is the length of the line.

This model does still have some drawbacks. Firstly, while it provides current and voltage at each end of the line, it does not provide information on their values anywhere else along the line. Secondly, when modelling a section of line with significant length in comparison to the wavelength (over one quarter of the wavelength) it is not possible to use the formulae above with a single π-section: multiple π-sections must be used to represent the cable, which impacts negatively on simulation speed and increases model complexity [76].

Therefore, the approach taken here has been to directly apply equations (4.5) and (4.6) to model the propagation of the ripple in the cables. The model has been coded in MATLAB.

4.1.4 Transmission Cable

4.1.4.1 Direct Application of Wave Propagation Equations to Transmission Cables

By setting $x = l$, where l is the length of the cable, equations (4.5) and (4.6) become equations (4.9) and (4.10) [58].

$$I_S = I_R \cosh(l\gamma) + \frac{V_R}{Z_c} \sinh(l\gamma) \tag{4.9}$$

$$V_S = V_R \cosh(l\gamma) + I_R Z_C \sinh(l\gamma) \tag{4.10}$$

where I_S and V_S are the current and voltage respectively at the sending end of the cable. Then, defining Z_R (Ω) as the receiving end impedance in equation (4.11),

$$V_R = I_R Z_R \tag{4.11}$$

and dividing equation (4.10) by (4.9), the impedance of the cable from the sending end, Z_{send} (Ω), can be calculated from equation (4.12).

$$Z_{send} = Z_C \frac{Z_R \cosh(l\gamma) + Z_C \sinh(l\gamma)}{Z_C \cosh(l\gamma) + Z_R \sinh(l\gamma)} \tag{4.12}$$

where $V_s = I_s Z_{send}$.

It is assumed that at the receiving end of the cable, i.e. onshore, there is a voltage source converter with a large DC link capacitance. Choosing a capacitance of 1mF (approximately based on the DC link time constant being of the order of 10ms) and neglecting capacitor *ESR* and series inductance gives a value of Z_R of -j0.159Ω at 1kHz. The value of Z_C at 1kHz for the base case transmission cable (cable 3), calculated using equation (4.1) is 16.34-j4.91Ω. Therefore, the exact size of the onshore capacitor is not a major factor in determining the sending end impedance of

the cable. A 1mF capacitor is used to represent the onshore converter's impedance to ripple current in the modelling throughout this thesis, unless otherwise stated.

The real part, imaginary part and magnitude of Z_{send} for the base case transmission cable at 1kHz for a range of transmission distances are plotted in Figure 4.1.

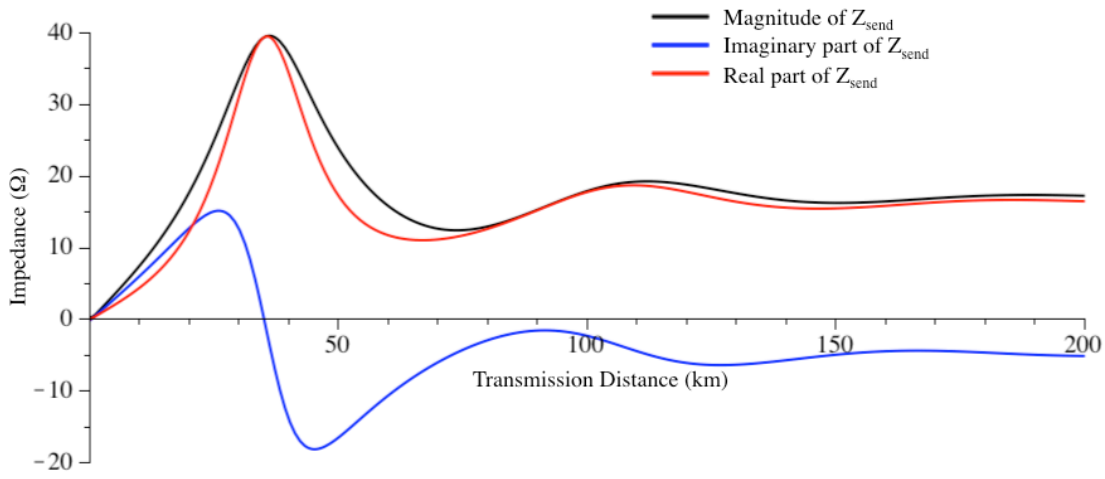

Figure 4.1. Calculated Z_{send} components and magnitude for a 1kHz ripple at a range of transmission distances for the base case transmission cable (cable 3).

It can be seen that the cable impedance does not vary uniformly with distance. This graph also provides an indication of the distance for which nominal π-section cable models are appropriate. These models approximate cable impedance (real, imaginary and total) to a straight line function of distance. From the graph it is apparent that such an approximation is valid up to around 10km, but quickly becomes inaccurate at distances above this.

The wavelength of the 1kHz ripple in this cable is 153.7km. The transmission distances considered correspond to those that will be encountered in round 3 offshore wind farm zones. The ripple current and voltage propagate up and down the length of the cable, being reflected at each end. For some lengths of cable, for example half the wavelength, the current waveform and its reflections add together at the sending end of the cable leading to a high current and low value of Z_{send}. This is a form of resonance. For other transmission distances, such as one quarter of the wavelength,

current waveforms cancel at the sending end of the cable and a high impedance results. As distance increases significantly beyond the wavelength, the cable impedance gradually approaches the value of the characteristic impedance.

In Figure 4.2 the magnitude of Z_{send} at 1kHz and 2kHz, for the same cable, is plotted. Maintaining the same speed of propagation of a wave, while doubling the frequency, halves the wavelength. Half of the wavelength at 1kHz is 76.9km. The wavelength at 2kHz is 84.6km, which is around 10% more than half the 1kHz wavelength. This discrepancy is accounted for by the reduction in cable inductance at 2kHz, which increases the propagation speed. The peaks and troughs in cable impedance are more exaggerated at 2kHz; this is because they occur at shorter transmission distances and therefore are less damped by the attenuation that occurs as the waves travel along the cable.

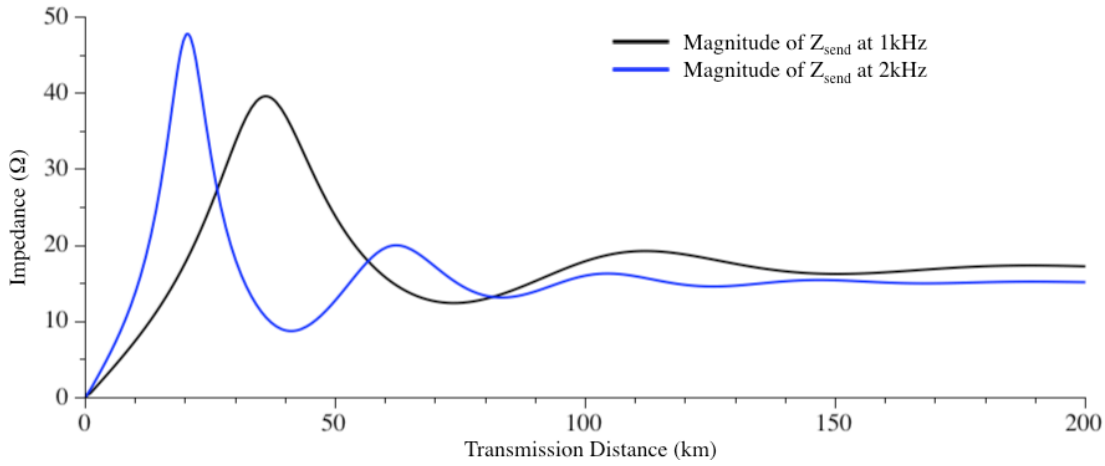

Figure 4.2. Calculated magnitude of Z_{send} for 1kHz and 2kHz ripple at a range of transmission distances for base case transmission cable (cable 3).

Figure 4.3 shows a comparison of the magnitude of Z_{send} at 1kHz against transmission distance for three of the configurations studied in the sensitivity analysis in chapter 3.

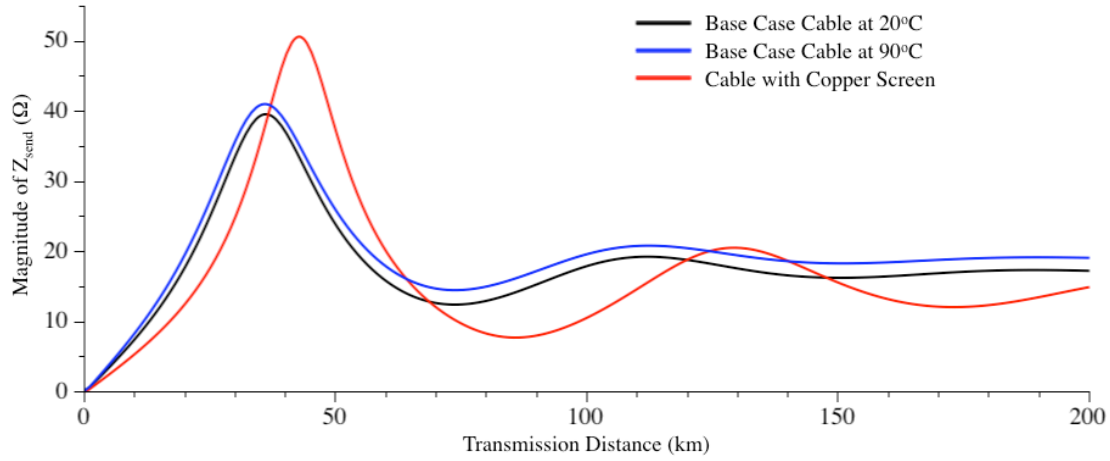

Figure 4.3. Calculated magnitude of Z_{send} for a 1kHz ripple at a range of transmission distances for different configurations/conditions of transmission cable (cable 3).

The wavelength of a 1kHz ripple in the cable with copper screen is 175.2km, which is larger than for the base case due to the reduced inductance of the former. The wavelength for a 1kHz ripple in the base case cable at 90°C is 154.6km, which is very similar to that for the base case (at 20°C), even though the inductance at 90°C is significantly increased. The reason is that while the inductance is increased, the capacitance decreases with temperature and the two effects (almost) cancel out. For the cable with the copper screen, the peak value of impedance is significantly higher and the trough lower due to the lower attenuation constant (α). In the case of this cable, the low value of α results from the low value of R', which effectively means that less energy is dissipated as the ripple moves up and down the cable leading to less damping of any resonances.

This is an important result. In an AC system, it is desirable to reduce resistance at the fundamental frequency. In the case of a DC system, losses caused per unit of ripple current are lower when the cable resistance is lower; however, resistance at ripple frequency also plays an important role in damping any oscillations and reducing the impact of resonance.

A selection of transmission cable characteristics based on the results from the sensitivity analysis in chapter 3 are shown in Table 4.1. Values of Z_{send} are likely to be the maximum (at $\lambda/4$) and minimum (at $\lambda/2$) encountered for the chosen onshore DC link capacitance (1mF) and any significant DC transmission distance.

	Base Case	Aluminium Core	Copper Screen	Base Case at 90°C	Armour μ_r=100	Armour μ_r=210	Increased Cable Separation
Wavelength, λ (km)	153.7	150.1	175.2	154.6	153.6	154.0	154.3
Magnitude of Z_{send} for cable length λ/4 (Ω)	38.63	32.44	50.21	39.89	39.71	37.91	38.47
Magnitude of Z_{send} for cable length λ/2 (Ω)	12.59	10.63	7.80	14.68	12.32	12.76	12.55
Resistance (Ω/km)	0.401	0.347	0.194	0.480	0.389	0.409	0.398

Table 4.1. Transmission cable information calculated for a range of configurations/conditions at 1kHz.

The most significant result is that the impedance of the cable to ripple current is very sensitive to transmission distance and to cable parameters. This shows the necessity of the work in chapter 3 in accurately determining these parameters. For example, for a transmission distance of 100km, the base case transmission cable (at 20ºC) has an impedance to a 1kHz ripple of magnitude 17.95Ω, while for the cable with copper screen it is 10.57Ω. This is a significant consideration when designing the wind farm to manage the current and voltage ripple produced by a DC-DC converter.

4.1.4.2 Current and Voltage Waveforms along the Cable

As stated, one limitation of the π-section transmission line equivalent model is that it only gives an accurate current and voltage at the receiving and sending ends of the line. Direct application of equations (4.5) and (4.6), together with some combination of (4.9), (4.10) and (4.12), depending on what voltage or current information is known, can be used to evaluate the current and voltage at each frequency at any point in the line.

4.1.4.3 Case Study of 100km Transmission Cable

Based on a 1kHz voltage ripple of 1pu at the sending end of the cable and a base resistance of 1pu = 10Ω (chosen arbitrarily), the per unit values of voltage and

current along two transmission cable designs, each 100km in length, are shown in Figure 4.4.

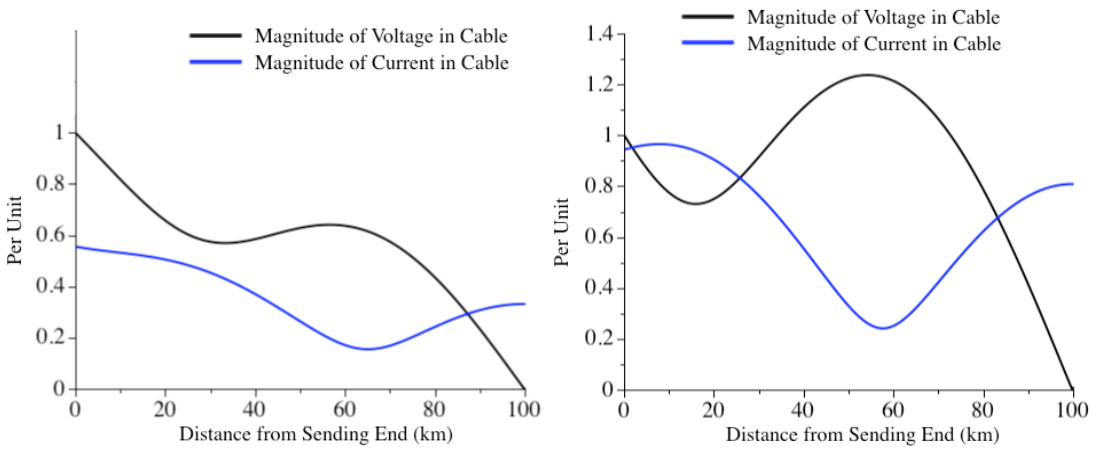

Figure 4.4. Calculated per unit values of current and voltage along (a) base case transmission cable (cable 3) and (b) transmission cable with copper screen.

Significant differences result from the choice of cable. The reduced damping in the cable with the copper screen, combined with the fact that the chosen transmission distance is closer to one of the resonant points for this cable (at $\lambda/2$), result in significantly higher ripple currents. The losses along the length of each cable are shown in Figure 4.5.

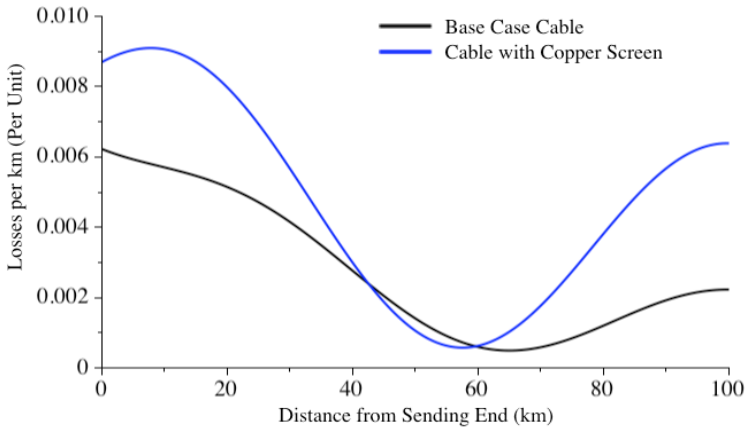

Figure 4.5. Calculated per Unit losses along two cable types, each 100km long, with a voltage of 1pu at the sending end and the base resistance set at 10Ω.

Although the cable with copper screen has a resistance per unit length of less than half that of the base case cable (0.194Ω/km compared to 0.401Ω/km), the losses are greater along most of its length. Additionally, in this cable, the peak current and therefore peak losses occur away from the ends of the cable. This shows that in order to ensure that the losses caused by ripple current do not overheat the cable, it may be necessary to monitor cable temperature along its entire length, as mentioned in section 2.6.3.6.

It is important to note that the cable with copper screen may have lower losses than the base case cable for certain transmission distances, e.g. for a transmission distance of 130km, the losses along the cables are shown in Figure 4.6.

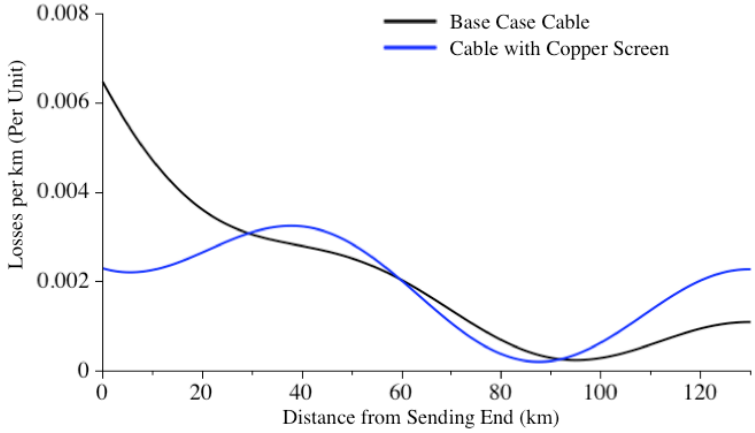

Figure 4.6. Calculated per Unit losses along two cable types, each 130km long, with a voltage of 1pu at the sending end and the base resistance set at 10Ω.

4.2 Application of Wave Propagation Equations to a Network

4.2.1 Network Design

The aim of this section is to take the principles developed in section 4.1 and use them to model the flow of ripple current around a 25 node DC grid. The topology of the grid is shown in Figure 4.7. This is a relatively straightforward layout and is used throughout the modelling process. It is based on based on layouts in [16, 59, 60, 61, 62].

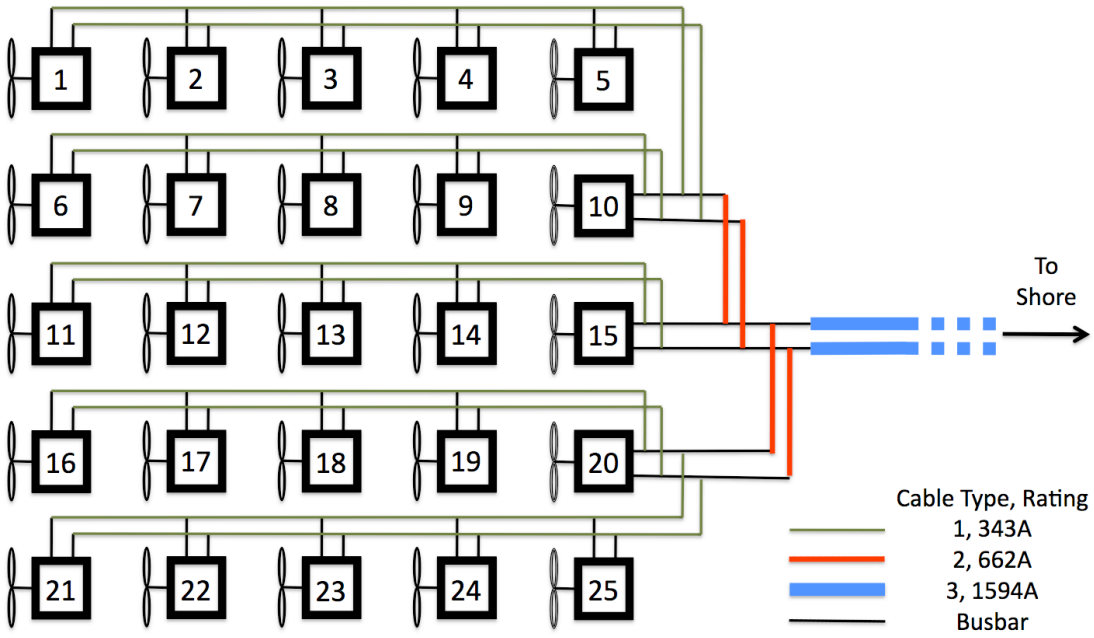

Figure 4.7. Layout of grid with cable types for 25 offshore wind turbines, each with 6MW power output and 600m spacing between turbines.

The three types of cable modelled in chapter 3 are used in the grid, the choice of which cable depends on the amount of DC current it is designed to carry. The required cable types are indicated in Figure 4.7.

It can be seen in Table 3.2 that the cables chosen are slightly overrated. The reason is simply that cables are offered by manufacturers in discrete steps of power rating so a small cable overrating is to be expected. The smallest cable available from the range of suppliers considered [46, 47, 48, 64] has a 95mm^2 core. This cable is therefore used in sections of the wind farm which are only anticipated to carry a relatively small DC current.

Each turbine is assumed to have a rated power of 6MW (giving 3MW per pole from the converter). The blade diameter is assumed to be 120m [77] and the wind turbines separated by 5 times this diameter ("5D" separation), leading to 0.6km sections of cable between each turbine.

4.2.2 Network Modelling

A brief overview of the modelling approach follows. More details are in Appendix C.

The reciprocal of equation (4.12) was applied multiple times to calculate the admittance of each path in the network and then the admittance of the network at each node, which is simply the sum of the admittances accounting for all the current paths available. An example calculation is given in Appendix C. In subsequent chapters, the Fourier transform of the unfiltered current output from the high voltage diode bridge is used as the input current for the frequency dependent cable (and HV filter) network in Figure 4.7. To calculate the volt rise, the admittance of both the filter capacitance and the network must be accounted for, which is simply the sum of the two. The volt rise caused by a component of ripple current at a given node can be used with the calculated value of admittance for each path to determine the current that flows from the node along each of those paths. Equations (4.9) and (4.10) can then be used (having been rearranged in terms of V_R and I_R - see Appendix C) to find the phase and magnitude of the current component when it reaches the next node. For each frequency component of ripple current and voltage from 1kHz to 10kHz (and DC), from each converter, the model calculates its value at every node in the network and then aggregates the results to give the network currents and voltages. Again, an example calculation is given in Appendix C.

Due to the number of calculations involved, the use of a model coded in MATLAB is beneficial in keeping run times manageable.

4.2.3 Model Testing and Verification

The coded model was verified against a model produced using standard simulation software (Simulink).

A range of HV filter capacitors was modelled on the converters, namely 1μF, 10μF, 100μF and 1mF. The capacitor *ESR* was modelled as 5mΩ in all cases. The capacitor series inductance was neglected.

The testing and verification was performed for a 1kHz ripple. The magnitude of that ripple before the filter capacitor was set at 32.12A, based on the Fourier transform of the unfiltered DC current when the SLR converter is operating at full power, as shown in Table 2.1. Two scenarios for the relative phase angle of the ripple current were modelled. First, with all the converters switching in phase. Second, with the phases offset, as shown in Table 4.2. These are the phases on the 500Hz, low voltage side of the transformer. On the high voltage side, after the diode bridge, the ripple frequency is double and the phase angles are also double.

Phase Angle	Turbines
0°	1, 6, 11, 16, 21
36°	2, 7, 12, 17, 22
72°	3, 8, 13, 18, 23
108°	4, 9, 14, 19, 24
144°	5, 10, 15, 20, 25

Table 4.2. Offset switching phases for the converters (in their respective turbines) on the 500Hz low voltage side of the transformer.

A transmission distance of 100km was chosen. The Simulink model is shown in Figure 4.9. The representation of a single converter and cable section from the model is shown in Figure 4.8. For the 0.6km collection cables, nominal π-section values are sufficiently accurate, so these were used. For the transmission cable, 3 π-sections connected in series were required. A 1kHz current source connected in parallel to the filter capacitor was used at each node to simulate the unfiltered ripple current component.

4.2.3.1 Results

The results for the MATLAB and Simulink models matched closely for all tests. A sample is shown in Table 4.3. The converter numbers in the left hand column refer to Figure 4.7.

Measured at Sending end of cable:	Magnitude of Current (A)		Phase of Current (degrees)	
	MATLAB Model	Simulink Model	MATLAB Model	Simulink Model
1 -> 2	32.94	32.94	0.0	0.2
2 -> 3	53.25	53.25	37.2	37.4
3 -> 4	52.74	52.75	74.3	74.5
4 -> 5	31.76	31.77	111.4	111.6
5 -> 10	1.23	1.22	357.3	358.0
10 -> 15	2.40	2.39	356.9	357.6
15 -> Shore	5.89	5.87	356.3	357.1

Table 4.3. Selected results from MATLAB and Simulink model for propagation of 1kHz current ripple in DC grid with 1μF filter capacitors at each node and switching phase angles offset.

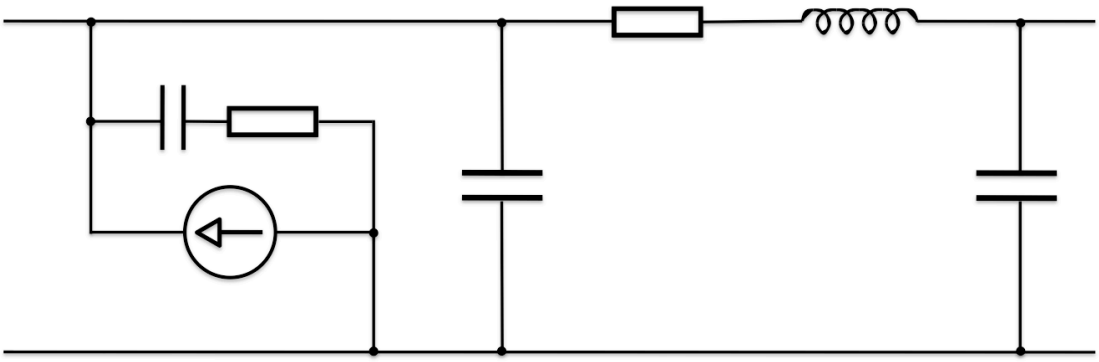

Figure 4.8. Representation of 1kHz ripple current using Simulink with a current source feeding into a capacitive filter with *ESR* and a π-section model of a wind farm power collection cable.

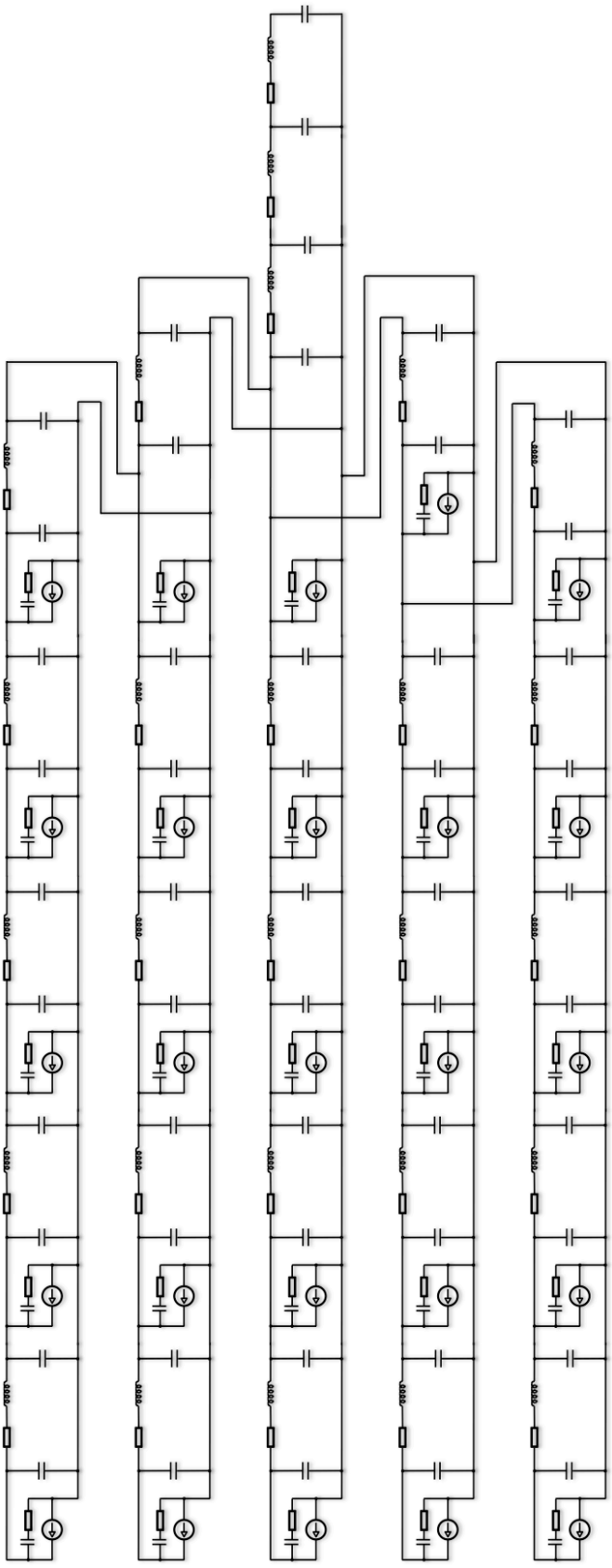

Figure 4.9. Simulink model for propagation of 1kHz ripple in the DC grid.

4.3 Resonance with AC System

The complex network of transmission cable and DC grid can lead to resonance at certain frequencies. The system should be designed so that these frequencies do not match the AC frequency or its second or third harmonic (depending on the onshore converter design) [20, 78].

Two types of resonant circuit are considered. First, the resonant circuit formed by the transmission cable and grid which may be excited by a voltage ripple on the DC output of the onshore converter. Second, a resonant circuit formed by the DC link capacitance together with the offshore system; this circuit may be excited by AC current input into the onshore DC link capacitance. The design of the onshore converter determines which of these types of resonance is most significant.

4.3.1 Resonance of Offshore System

It is assumed that the DC grid and selection of base case cables are as shown in Figure 4.7. The size of the HV filter capacitance in the turbines is therefore the variable that determines the admittance of the system. Figure 4.10 shows the admittance of the system at 50Hz, 100Hz and 150Hz for a range of filter capacitances and transmission distances.

A higher admittance into the offshore system from the onshore converter would cause higher currents to flow as a result of, for example, any steady state voltage ripple or unbalanced voltage conditions on the AC side [78]. In general, the system admittance reduces with transmission distance, which is due to the increased damping of the longer transmission cable.

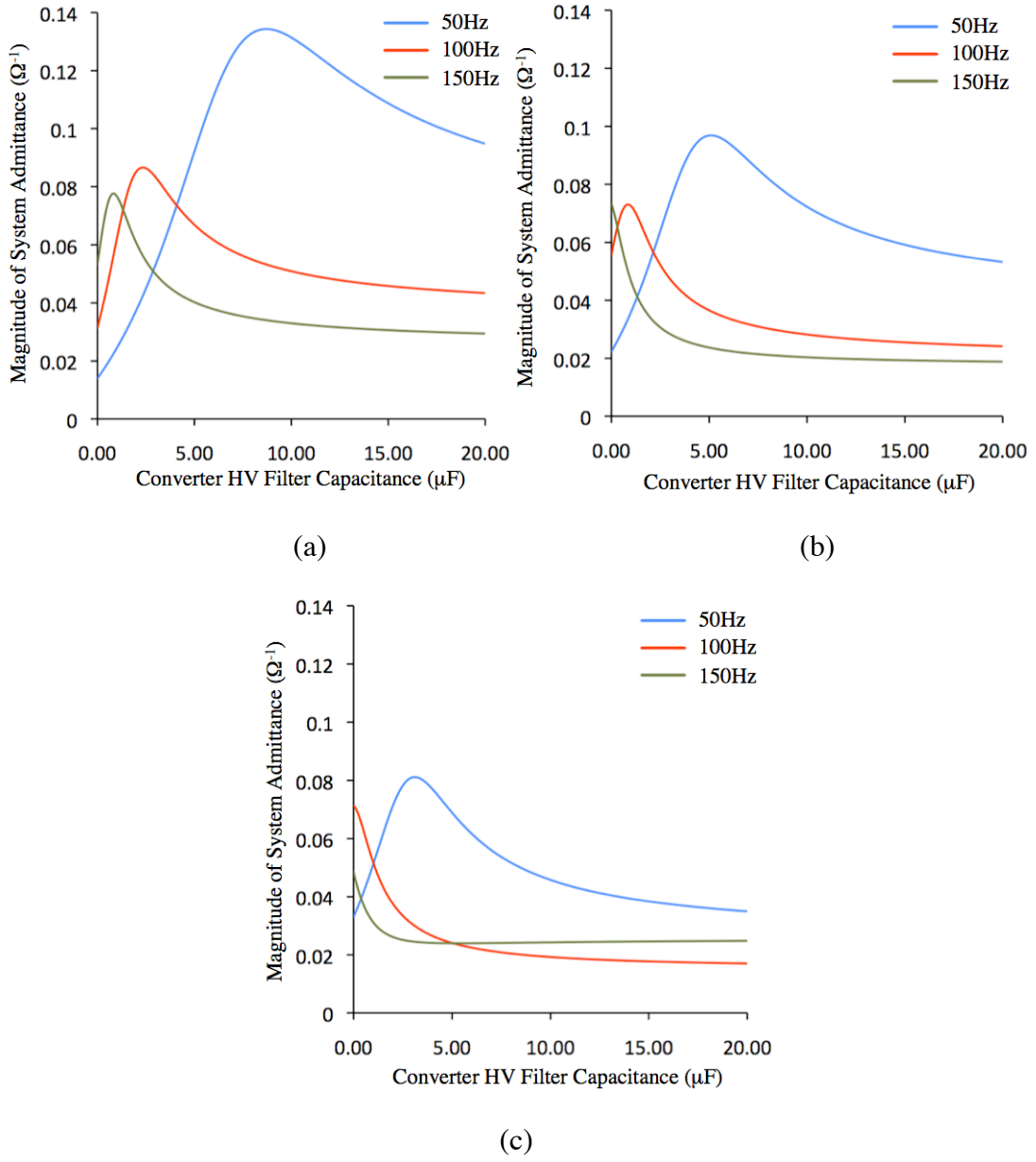

Figure 4.10. Calculated offshore system admittance from onshore converter, for a range of offshore HV filter capacitances, with a transmission cable length of (a) 100km, (b) 150km and (c) 200km.

The design and operation of the onshore converter will determine whether the currents relating to these admittances are problematic. For example, a ±1% voltage ripple at 50Hz in a 50kV system (which is relatively large) equates to 500V (peak) AC. For a transmission distance of 100km, choosing a filter capacitance of 8μF would result in a ripple with magnitude 66.5A. Reducing the capacitance to 4μF would reduce the ripple to 35.9A. In any case, the rated DC current for the line

would be (for the network under consideration) 1500A, so the 50Hz ripple content is unlikely to be problematic.

In addition to the ripple current, the choice of filter capacitance affects the propagation of any voltage ripple from the onshore converter. Figure 4.11 shows the voltage at the wind farm end of the transmission cable which results from a 100V (peak) AC ripple at the DC output of the onshore converter.

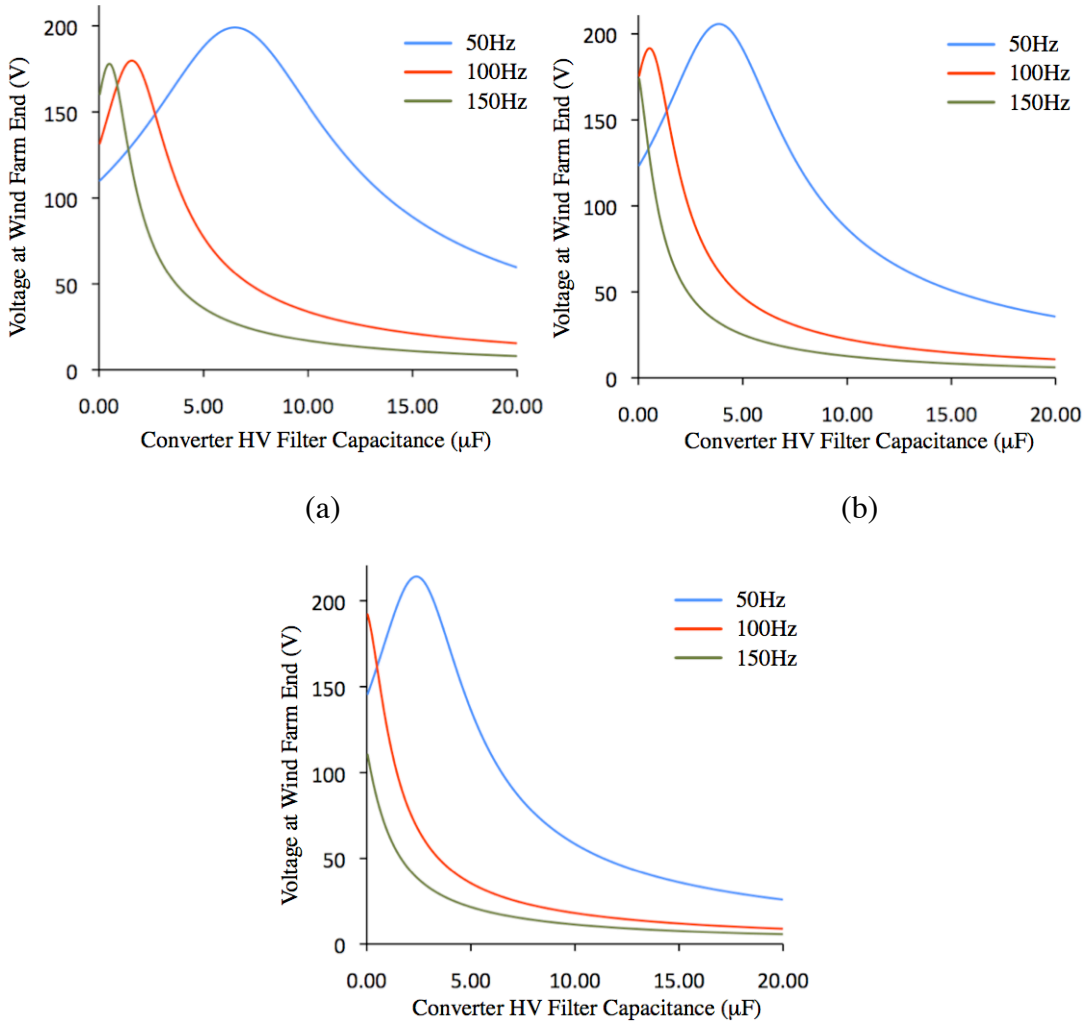

Figure 4.11. Calculated voltage at wind farm end of transmission cable which results from a 100V ripple at the onshore converter DC link. Calculated for a range of offshore HV filter capacitances, frequencies and with a transmission cable length of (a) 100km, (b) 150km and (c) 200km.

The position of the peak values (i.e. the size of filter capacitance that causes them) is related to the position of the peaks in Figure 4.10. A high offshore system admittance at the onshore converter leads to a (relatively) high current in the system. When this current reaches the point of common coupling in the wind farm (i.e. turbine 15), it leads to a voltage rise which is determined by the impedance of the wind farm. In Figure 4.11(a), at 50Hz, the peak voltage at the wind farm end of the cable occurs at around 7μF. In this instance, the impedance of the offshore system at the onshore converter is 7.15 - j3.57Ω. When the current reaches turbine 15, the impedance of the wind farm is 0.0577 - j18.0Ω. Although the current is attenuated along the length of the transmission cable from a magnitude of 12.6A to 11.0A, the volt rise that results from the higher impedance when it reaches the wind farm is around double the voltage at the onshore converter.

Significant voltage ripple can be problematic for a number of reasons, including in the stabilisation and operation of the control system (although this can be addressed by sampling appropriately) and in current waveform distortion in the converters (as discussed in section 6.1.1.2).

4.3.2 Resonance Between Onshore Converter and Offshore System

A further consideration is the resonant circuit formed by the DC link capacitance in the onshore inverter and the offshore transmission cable and DC grid. The DC link capacitor has a large, positive, imaginary admittance. In order for it to resonate with the offshore system, the offshore system must have a similar sized, negative (i.e. inductive), imaginary component of admittance. The admittance 1mF capacitor at 50Hz is j0.314Ω, and larger at 100Hz and 150Hz. The imaginary component of the admittance of the offshore network from the onshore converter, with a transmission distance of 100km, is shown in Figure 4.12.

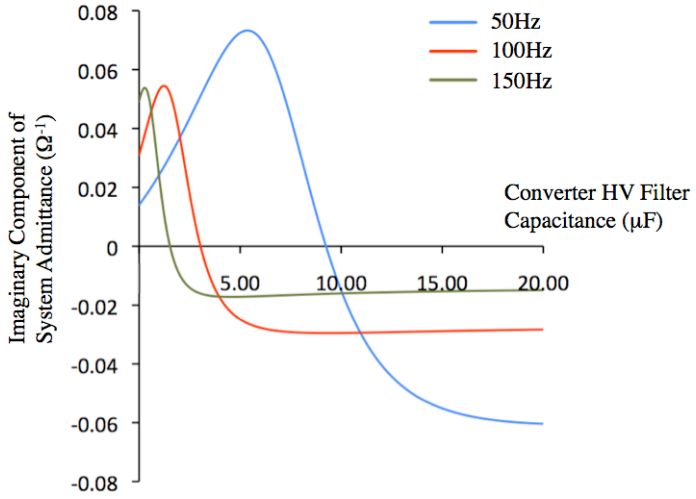

Figure 4.12. Imaginary component of admittance of the offshore system calculated for a 100km transmission cable and range of frequencies and offshore filter capacitances.

It can be seen that the imaginary component of admittance is not large enough to resonate with the DC link capacitance. This is because the cable is sufficiently long that the damping effect of its resistance keeps its admittance small. The results for 150km and 200km cables show even lower values of admittance. Were a shorter cable to be used, i.e. the wind farm significantly closer to shore, then resonance could be a problem. Also, if the DC link capacitance were around 5 times smaller, then the offshore filter capacitances in the wind turbines would need to be carefully selected.

4.3.3 Application to AC Systems

Although it is beyond the scope of this thesis, it is very clear from the results in section 4.3.1 that amplification of AC voltage and its harmonics can result from the interaction between cable capacitance, which causes relatively high admittance at whichever is the sending end of the cable with respect to a given voltage, and the impedance of the offshore wind farm or onshore system connection, whichever is at the receiving end. In the DC system examined here, the problem is likely to be manageable. However, in an AC system a much larger voltage (i.e. the full load voltage or low order harmonic) may be affected. These issues have been highlighted

in [79, 80], as has the fact that they are more problematic in AC transmission systems than DC.

The approach taken in this thesis so far can be applied to predict or understand resonance in an AC offshore wind farm.

4.4 Resonance of Low Frequency Oscillations

Power oscillations at a range of frequencies are produced by wind turbines. The sources of these can be electrical or mechanical systems. The causes are not examined in detail here, but it is important to calculate the resonant frequency of the circuit consisting of the offshore network and the onshore DC link capacitance.

In the system under consideration, with a 100km transmission cable, the resonant frequency is 19Hz. A ripple voltage at or very close to this frequency at the wind farm end would give rise to a voltage approximately 2.5 times greater at the onshore converter. The explanation is similar to that in section 4.3.1, i.e. at 19Hz, the admittance of the transmission cable at the wind farm end is much higher than the admittance of the onshore DC link capacitance.

The resonant frequency is dependent on the size of DC link capacitance. Reducing the capacitance to 0.5mF increases the resonant frequency to 27Hz. The voltage rises from the wind farm to the shore by a factor of approximately 2.4 in this case. The lower voltage rise results from the higher cable resistance at this frequency, compared to 19Hz, which leads to greater damping.

4.5 Chapter Summary

The significance of the transmission distance in system modelling has been identified; because this distance is likely to be of the same magnitude as the wavelength of the fundamental ripple current in the DC cable, the behaviour of the ripple must be modelled using wave propagation theory.

The requisite wave propagation theory has been applied to model and explain the behaviour of ripple currents and voltages in the offshore DC grid and the results have been verified using standard cable models in Simulink. It has been shown that cable impedance to ripple frequency varies significantly with cable design, operating conditions (i.e. temperature) and transmission distance. The same theory has been applied to AC frequency (i.e. 50Hz) ripple content and to identify low frequency resonance.

5 DC-DC Converter and Integration with Network

In this chapter, a range of options for conversion from low to high voltage DC are considered. These options are:

- Single-Phase SLR Converter - see Figure 2.9, Figure 2.10 and Table 2.1
- Phase Shift Converter - see Figure 2.10 and Table 2.1
- Three-phase SLR Converter
- Three-phase voltage source inverter feeding medium frequency transformer and diode bridge.

The options and their modelling are described in more detail in section 5.1. The integration of these models into a network model with frequency dependent parameters is covered in section 5.2 and the validation of this model in section 5.3.

5.1 Converter Modelling

In order to model 25 converters (as shown in Figure 4.7) and integrate them into a network model, without excessive run times, a simplified model of each converter was programmed in MATLAB. The model uses a time stepping iterative process based on the fundamental equations that describe passive component behaviour, i.e.

$$V = iR; \qquad V = L\frac{di}{dt}; \qquad i = C\frac{dV}{dt}.$$

A number of simplifications were made to the power electronic model, including:

- Modelling of components (e.g. switching devices, the transformer) as ideal;
- The input was modelled as a large (10mF) capacitor fed from a constant power source.

The ultimate objective is to design the DC grid in order to manage the ripple content generated by the converters. To show that the simplifications are appropriate, it is necessary to show that the converter models are a close enough representation of the converter performance to meet the objective. This is shown in section 5.3. The actual design of the DC grid is undertaken in chapter 6.

In each converter, the transformer has two secondary windings, giving a bipole output. Only the positive pole was modelled. The circuit topologies (e.g. in Figure 2.9), in theory, produce equal and opposite currents and voltages in positive and negative poles (including any ripple components). Making the assumption that the respective cable connections are symmetrical, the currents and voltages will cancel at the receiving end of the cables and there will be no returning earth currents. This allows modelling as a single pole with zero impedance return, much as balanced three-phase AC systems are often modelled as a single-phase with the neutral return path excluded.

Component parameters for the single-phase SLR and phase shift converters are based on the work conducted in the parallel PhD project [33]. For the modelling here (and subsequent validation), the low voltage side is modelled as if it were only connected to a single pole high voltage output. In practice, the low voltage current (and resonant capacitor voltage in the SLR converter topologies) would be double that modelled here and the resulting losses and voltage stresses increased accordingly. However, since detailed converter analysis is not undertaken, this is an acceptable simplification.

5.1.1 Single-Phase Series Load Resonant Converter

The single-phase SLR converter was modelled as shown in Figure 2.9.

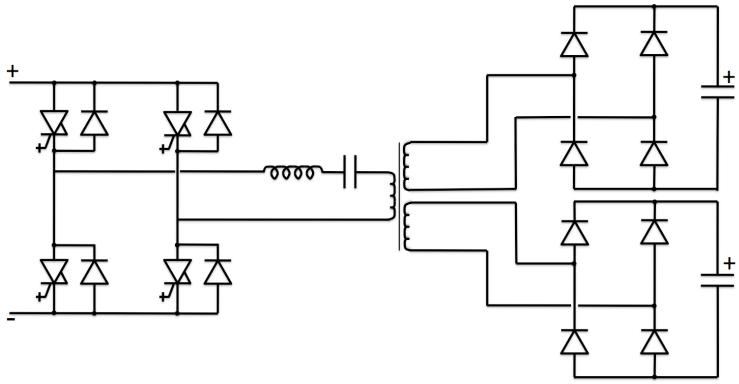

Figure 5.1. Series load resonant converter topology.

Component parameters for the converter are given in Table 5.1.

Component	Value
Input Voltage (approx.)	2800V
Output Voltage (approx.)	±50kV
Rated Power	3MW x 2 poles
Resonant Capacitance	1mF
Resonant Inductance	158μH
Resonant Frequency	400Hz
Switching Frequency	500Hz
Transformer Turns Ratio	1:19
Output Filter Capacitor	As required

Table 5.1. Component parameters for single-phase SLR converter.

A Simulink model was also built to help develop and verify the MATLAB model. A selection of the most important waveforms from the two models are shown in Figure 5.2.

The waveforms from the two models match closely. The MATLAB model gives slightly higher values, for both current and voltage, as this is a more idealised model which neglects some losses.

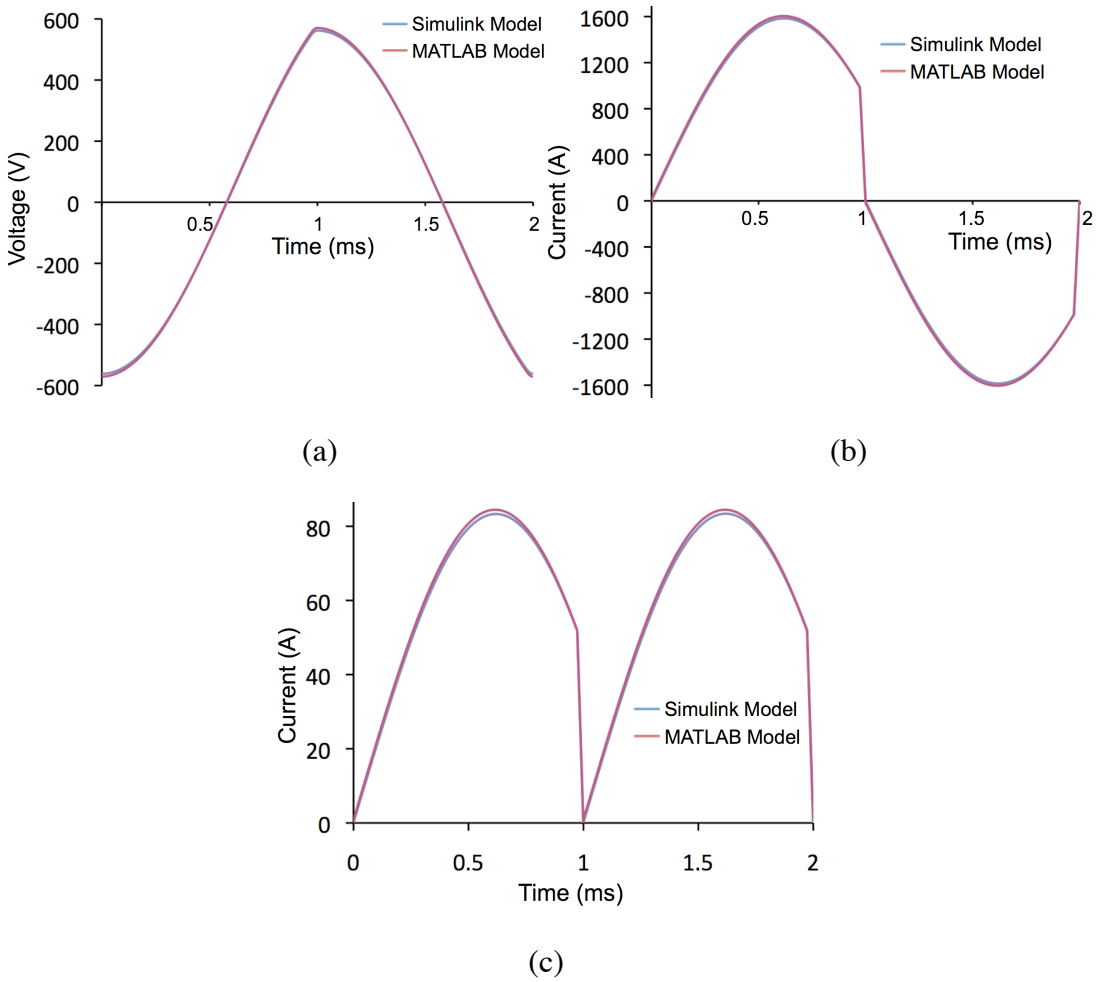

Figure 5.2. Waveforms from the models of the single-phase SLR DC-DC converter for one cycle at 500Hz, operating at full power. (a) Voltage in resonant capacitor. (b) Current in low voltage side resonant tank and transformer primary. (c) Unfiltered, rectified high voltage DC current output from the diode bridge.

5.1.2 Phase Shift Converter

The phase shift converter was modelled as shown in Figure 5.3. The converter parameters are shown in Table 5.2. Again, a Simulink model was produced in addition to the MATLAB model and the results are shown in Figure 5.4.

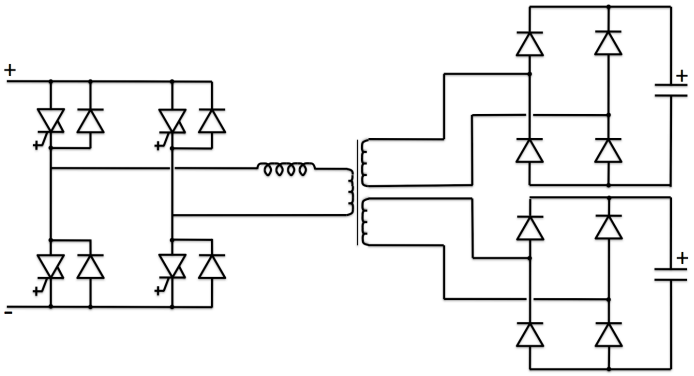

Figure 5.3. Phase shift converter topology.

Component	Value
Input Voltage (approx.)	2800V
Output Voltage (approx.)	±50kV
Rated Power	3MW x 2 poles
Low Voltage Side Inductance	50μH
Switching Frequency	500Hz
Transformer Turns Ratio	1:19
Output Filter Capacitor	As required

Table 5.2. Component parameters for phase shift converter.

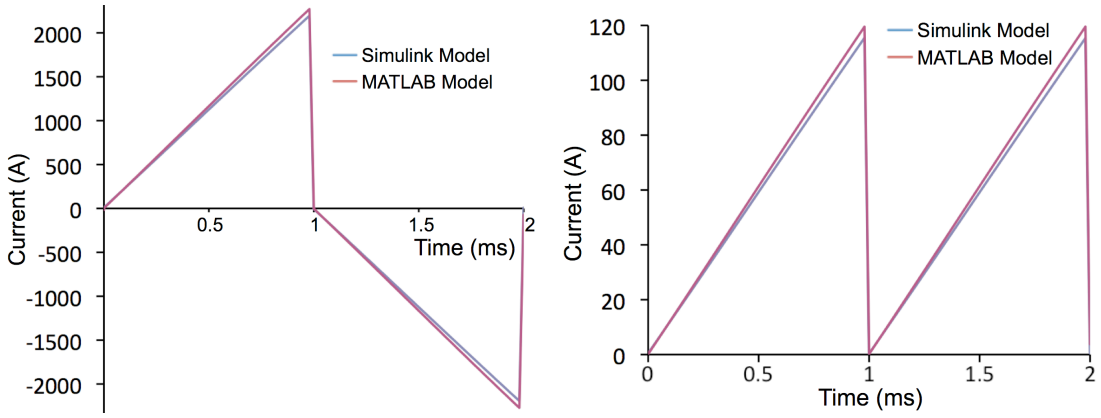

(a) (b)

Figure 5.4. Waveforms from the models of the phase shift DC-DC converter for one cycle at 500Hz, operating at full power. (a) Current in low voltage side resonant tank and transformer primary. (b) Unfiltered, rectified high voltage DC current output from the diode bridge.

Once again, the waveforms from the two models are close, with the idealised MATLAB model giving a larger current reading.

5.1.3 Three-Phase SLR Converter

The topology for the three-phase SLR converter is shown in Figure 5.5.

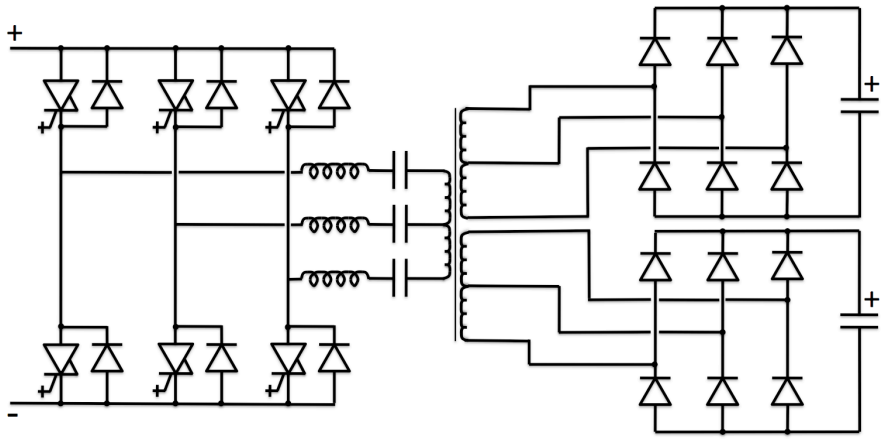

Figure 5.5. Topology for the three-phase SLR DC-DC converter.

The component parameters for the converter are given in Table 5.3.

Component	Value
Input Voltage (approx.)	2800V
Output Voltage (approx.)	±50kV
Rated Power	3MW x 2 poles
Resonant Capacitance	130μF per phase
Resonant Inductance	1mH per phase
Resonant Frequency	441Hz
Switching Frequency	500Hz
Transformer Turns Ratio	1:19
Output Filter Capacitor	As required

Table 5.3. Component parameters for the three-phase SLR converter.

The required product $L_{res}C_{res}$ (resonant inductance multiplied by resonant capacitance) is largely determined by the desired resonant frequency. In selecting the resonant components, it is important to strike a balance between the values of the two. A larger inductor reduces harmonic distortion in the primary side current and therefore reduces losses in the inductor and transformer. A larger capacitor reduces the peak voltage in that capacitor, reducing the voltage rating required for the capacitor and for other system components, such as the GCTs.

For the selected component parameters, the voltage waveform in one of the resonant capacitors and the corresponding low voltage side current for the same phase are shown in Figure 5.4. The unfiltered DC current output from one pole of the HV diode bridge is also shown. Again, a Simulink model was used to check the results.

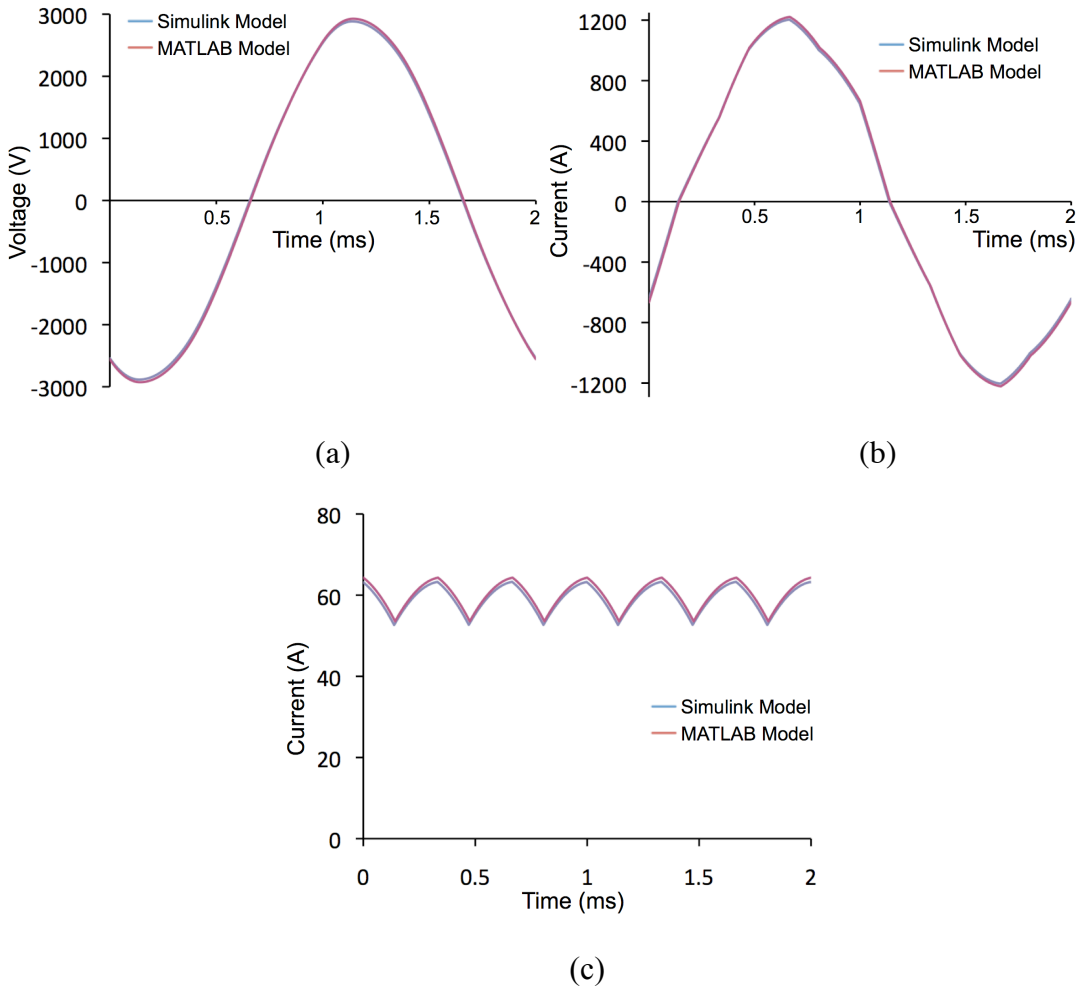

Figure 5.6. Waveforms from the models of the three-phase SLR DC-DC converter for one cycle at 500Hz, operating at full power. (a) Voltage in a resonant capacitor with (b) showing the current in the same phase on the low voltage side. (c) Unfiltered, rectified high voltage DC current.

It is immediately apparent from the waveform in Figure 5.6, that HV filtering requirements for the three-phase converter are significantly less than for the single-phase version. This is studied in detail in chapter 6.

5.1.4 Voltage Source Inverter and Diode Bridge

There are a number of commercially available drives for wind turbines with AC-DC-AC configuration which take variable voltage and frequency input and convert it to fixed voltage and (AC grid) frequency output. One possible configuration for the converters that feed the DC grid is to use such a (three-phase) system, but adapted to produce a 500Hz AC output which is then fed into a transformer and diode rectifier.

The 500Hz voltage waveform generated by such a converter is likely to be relatively high in harmonics. If the chosen converter topology uses PWM, then due to the frequency of the generated sine wave (500Hz rather than 50Hz), the number of times each device can switch per cycle is relatively small, giving a coarse sine wave. If a multilevel converter is used (such as described in [81] or [82]), due to the relatively low voltage level, only a small number of levels would be required and, again, the resulting waveform would be high in harmonics. As a result, significant filtering components (to remove low order harmonics) along with a line inductor for each phase (to further smooth the current waveforms) are required in order to reduce losses in the transformer and other components.

The design of the drive and filters is complex. The magnitude and frequency of any distorting harmonics in the AC waveforms would depend on the type of the AC-DC-AC drive, as well as the filtering. For the purpose of this research, the AC current waveforms entering the transformer on the low voltage side is modelled as pure sine waves and their source (including the filter components and line inductors) treated as a pure current source. The resulting unfiltered DC current waveform is a shown in Figure 5.7.

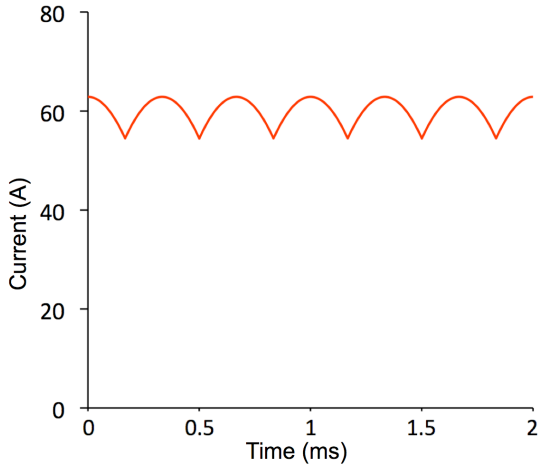

Figure 5.7. Unfiltered, rectified, high voltage DC current output from diode bridge of converter based on idealised voltage source inverter.

Note that the frequency of the low voltage waveform for this converter (sometimes called the intermediate frequency) is referred to as the switching frequency. This is valid for topologies in which devices only switch once per AC cycle (e.g. the MMC), but will not be the case where PWM is used and devices switch more frequently, in which case any reference to the switching frequency made here should be regarded as referring to the intermediate frequency.

5.2 Integration of Converter and DC Grid Models

5.2.1 Solving the DC Power Flow

Although, in comparison to calculating the AC power flow, the DC power flow is a less complex task, it still requires careful consideration. The DC current produced by each converter is a function of the DC power output and the voltage at the converter output. The DC voltage depends, in part, on the current produced by each converter, as this causes a voltage rise along the resistive cables in the network. In a small system, with just a few nodes, it may be practical to solve the power flow equations directly. However, in a 25 node system, an iterative approach is more straightforward and computationally efficient. This approach is applied here.

As discussed in section 2.7.3, the system DC voltage will be controlled at the onshore converter and here it is assumed to be constant at ±50kV. Based on this and the resistance of the cables in the system, an initial estimate for the DC current from each node can be made and then used to calculate the voltage at each node, which in turn can be used to find a more accurate value of DC current. The process continues until a sufficiently accurate result is obtained.

Based on the network shown in Figure 4.7, with all turbines operating at full power and a transmission distance of 100km, the derived DC output currents and voltages from each converter are shown in Figure 5.8.

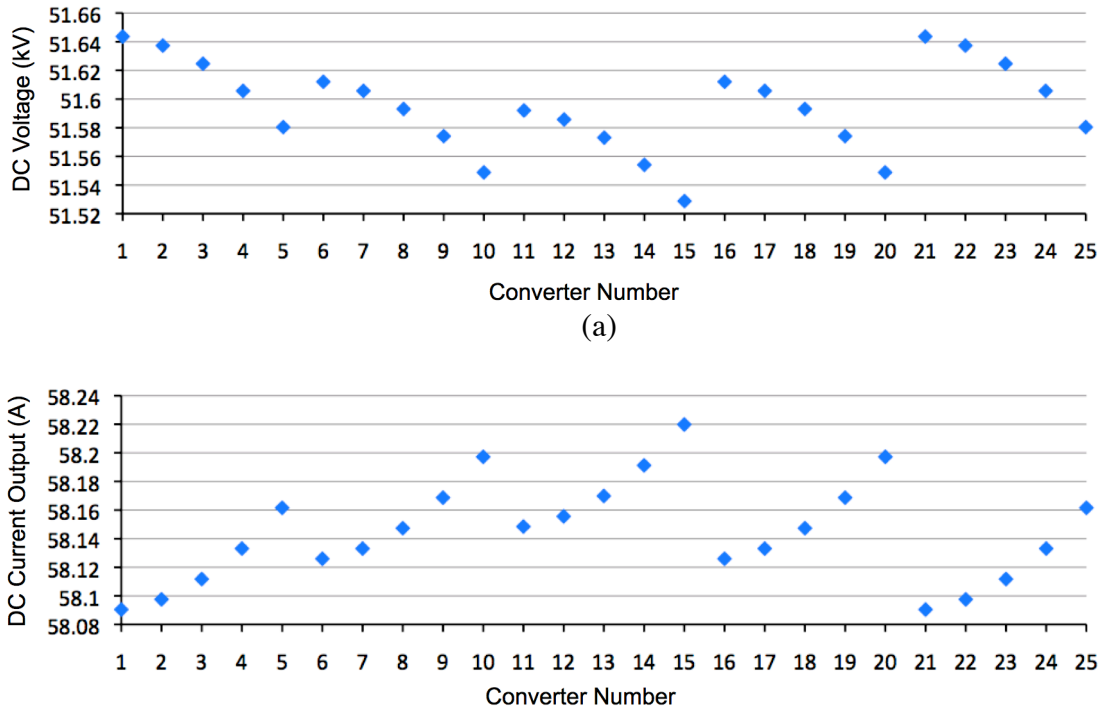

Figure 5.8. (a) DC voltage and (b) DC current calculated in a 25 turbine network (see Figure 4.7), operating at full power, with +50kV onshore voltage.

In Figure 5.8, within each row of five turbines, the turbine furthest from the shore has the highest voltage and (since all power outputs are the same) the lowest current. This is because the rise in DC voltage caused by the current accumulates as the point of calculation moves along each cable, away from the receiving node for the power.

For the same reason, the rows which are furthest from the point of common coupling (turbine 15) have a higher average voltage and lower current than those closer to turbine 15.

These results are used to give the DC component of output voltage which is used both for the frequency domain DC grid model and for the time domain models of each DC-DC converter.

These results were checked against results from a Simulink model of the grid and found to be within 0.1% of those results.

5.2.2 Modelling Complete System Power Flow

The process of solving the system power flows including DC and AC ripple currents and voltages is also an iterative one. The method is described below. More detail is given in Appendix D.

The DC voltages derived in section 5.2.1 are used as a fixed output voltage in the first iteration for the time domain models of each converter. This is computationally efficient, as it avoids modelling HV filter components (which can be more quickly dealt with in the frequency domain). The required output from each model is the unfiltered HV current from the diode bridge (I_{HV}).

The Fourier transform is then used to convert the unfiltered HV current from each converter in the DC grid to its frequency domain components. An approximation is made by ignoring frequencies above 10kHz as their magnitude is small and passive filtering components are generally more effective at higher frequency. The network model developed in chapter 4 is then used to model the propagation of the ripple current in the cables and filtering components of a DC grid.

The resulting system voltages at each node are then converted back to the time domain and the converter models run again with the output voltage waveforms set accordingly. The process is repeated until the results in the time and frequency domain converge.

Two alternatives to this approach were considered. One option was to model only in the time domain, the other to model only in the frequency domain. Both models use the approximation that only a finite number of frequencies need to be modelled. In the time domain, the cable network can be modelled using a large number of π-sections and tuned filters, which are carefully chosen so that the impedance (at multiple frequencies) in the desired frequency range is correct. In the frequency domain model, a similar approach can applied to the converter. The voltage output from the H-bridge (approximately a square wave) can be converted to the frequency domain using the Fourier transform. The components in the system can then be represented by their impedance at each frequency and the output waveform derived.

Both methods were less effective than the adopted modelling approach. In the case of the time domain model, complexity and run times were a problem, due to the increased number of energy storage components required to build the cable models. In the frequency domain model, the difficulty results from the discontinuous nature of the operation of the converter. For example, accurately calculating the time at which the current on the low voltage side falls to zero, which causes a change in the input voltage to the *LC* resonant tank, is difficult when working in the frequency domain and results in an excessively complex model.

5.2.3 Resonance between the Filter Capacitor and DC Grid

Where the DC grid impedance at the output of a converter is inductive, there is a possibility of resonance between the grid and filter capacitor.

For example, with a 10μF capacitor at each converter, the output system admittance (Y_{sys}) at 1kHz (taking account of all cables, capacitors and the link to shore) from converter 1 is 0.0961-j0.0397ohms, i.e. inductive. The admittance of the filter capacitor at converter 1 is 0.0004+j0.0628ohms (Y_C). One way of assessing the effectiveness of the capacitor as a current filter is to calculate the ratio of the 1kHz component of ripple current after the filter (I_{out}) to before the filter (I_{HV}); i.e. the smaller the ratio, the more effective the filter. The derivation of this ratio follows.

First, calculate the total admittance into which I_{HV} flows (Y_{HV}) using equation (5.1).

$$Y_{HV} = Y_{sys} + Y_C \tag{5.1}$$

Then the resulting component of voltage at the output of the converter (V_{out}) is given by equation (5.2).

$$V_{out} = \frac{I_{HV}}{Y_{HV}} \tag{5.2}$$

The output current is then calculated using equation (5.3).

$$I_{out} = V_{out} Y_{sys} \tag{5.3}$$

Substituting (5.1) into (5.2) and then (5.2) into (5.3) yields equation (5.4).

$$I_{out} = I_{HV} \frac{Y_{sys}}{Y_{sys} + Y_C} \tag{5.4}$$

In the example of converter 1,

$$\left|Y_{sys}\right| = 0.104\Omega \qquad \text{and} \qquad \left|Y_{sys} + Y_C\right| = 0.099\Omega$$

So, due to some cancellation of the imaginary parts of the inductive Y_{sys} and capacitive Y_C, the sum of the two has a smaller magnitude than Y_{sys} alone.

Substituting these values into (5.4) yields a ratio I_{out}:I_{HV} of 1.05, i.e. a magnitude of I_{out} greater than that of I_{HV}. Thus the filter actually amplifies the 1kHz current ripple slightly.

This is not an isolated case. Figure 5.9 shows the ratio I_{out}:I_{HV} at all 25 converters for a range of filter capacitances. Converter numbers refer to Figure 4.7. It can be seen that even a large filter capacitor (1mF) is not necessarily completely effective at eliminating 1kHz current ripple (note the results at converters 10, 15 and 20), while a small capacitor (1μF) does not, in general, amplify current ripple as much as a 10μF capacitor does. This is because the smaller capacitor has a lower admittance which does not cancel out a significant portion of the imaginary component of an inductive system admittance.

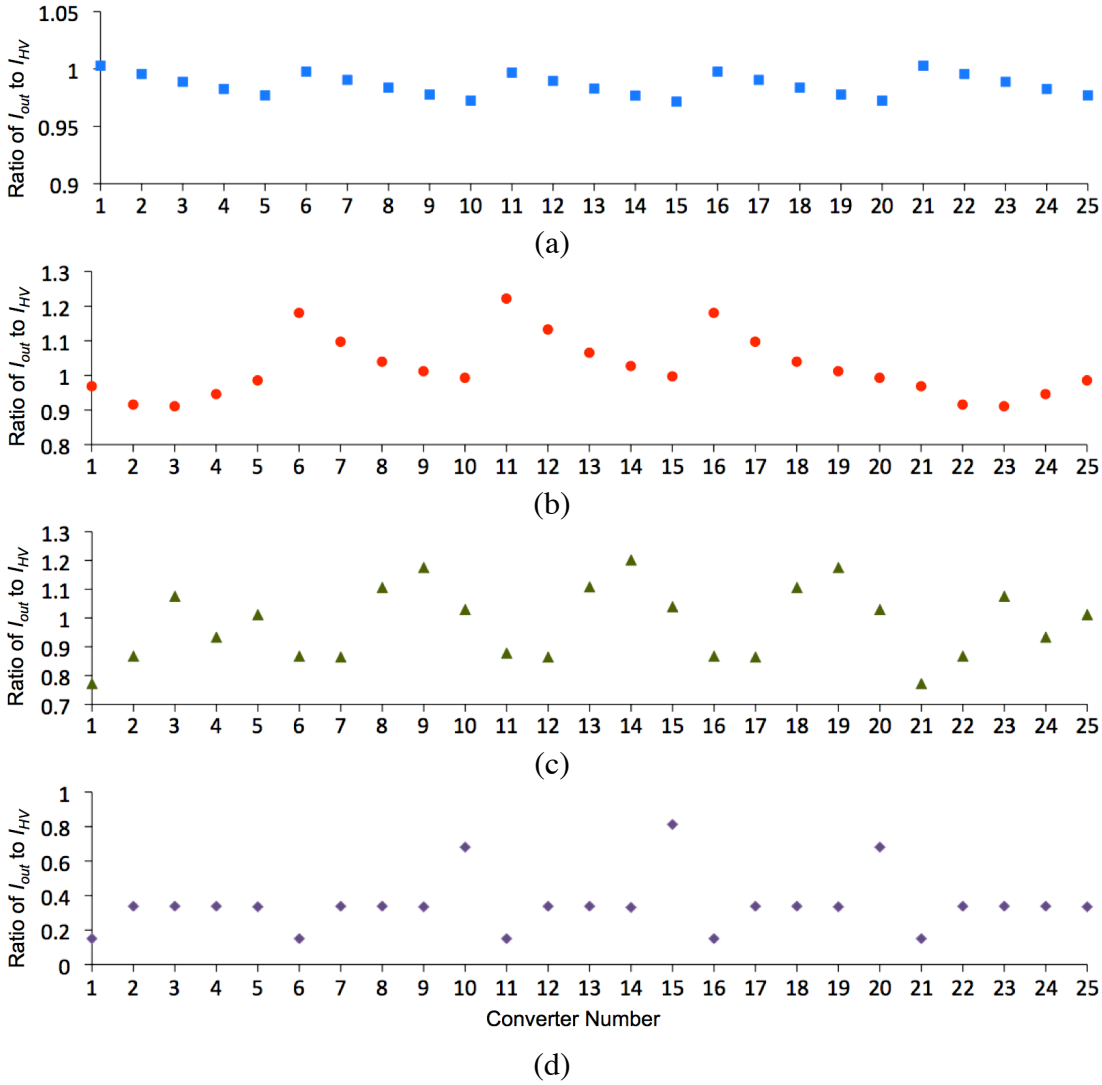

Figure 5.9. Ratio of output 1kHz ripple current to unfiltered 1kHz ripple current calculated at all converters in the wind farm with a range of filter capacitors: (a) 1μf, (b) 10μF, (c) 100μF and (d) 1mF. Note the different scales used on each graph.

The maximum values of the ratio of I_{out} to I_{HV} for a range of capacitances, as well as the mean of the ratios for all the converters, are plotted in Figure 5.10.

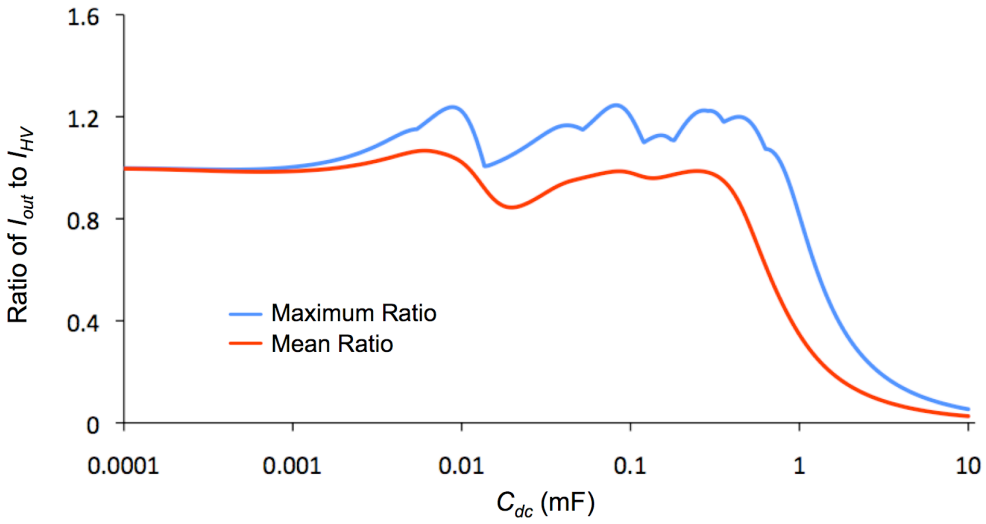

Figure 5.10. Maximum and mean values of the ratio of I_{out} to I_{HV} calculated for a range of sizes of filter capacitors (C_{dc}).

It can be seen that until the size of the filter capacitors approaches 1mF, using them as the only means of reducing current ripple is unlikely to be effective. This result and its implications for designing the DC grid is examined in detail in chapters 6 and 7.

5.3 Experimental Validation

In addition to the verification using Simulink models, laboratory experiments were carried out to validate a number of aspects of the work from this chapter and from chapter 4, including:

- The time domain model of the single-phase SLR converter in MATLAB and its connection to a cable with frequency dependent parameters;
- The effect of cable length and ripple wavelength on cable impedance at various frequencies;
- The variability of ripple current along the length of a transmission cable;

- The interaction between the converter and cable, including resonance between the two.

To achieve this, a single converter was constructed and the system was scaled so that it became manageable in the laboratory.

5.3.1 Experimental Setup

When considering ripple propagation in this project, transmission distances of the order of magnitude of the wavelength of the fundamental ripple component are of most interest, because these are likely to be encountered in the Round 3 offshore wind farm zones. The wavelength of a 1kHz ripple in the base case transmission cable (cable 3) is approximately 154km. As seen in Figure 4.3, the impedance is particularly high (around 38.6 ohms) for a transmission distance of $\lambda/4$ and particularly low (around 12.6 ohms) for a transmission distance of $\lambda/2$. In order to create these conditions in the laboratory it was necessary to build a converter operating at a much higher frequency so that its ripple current would have a much smaller wavelength. A SLR converter capable of switching in the 100's of kHz range was constructed.

Specifying the converter, including the choice of switching frequency and resonant frequency, operating current, voltage and power, transformer turns ratio and output filtering was carried out as part of this project in order to meet the requirements above. The converter was then designed and constructed as part of a BEng project carried out by Xiaoyun Rong [83]. After construction, the converter was modified as part of this project in order to optimise the choice/construction of resonant components and high voltage filtering.

URM 70 Coaxial cable [84] was used to simulate the transmission cable. The outer conductor was used to simulate the water blocking metallic sheath (as described in

the experimental work in chapter 3) and was connected to earth regularly along its length. The first two tests were carried out at a switching frequency of 235.5kHz, so the fundamental ripple frequency was 471kHz. The cable is available in lengths of 100m; therefore it is necessary to join sections of cable together for greater lengths than this (the experiments were designed to use a maximum of 200m of cable).

The converter parameters are shown in Table 5.4 and the cable parameters at 471kHz and its harmonics in Table 5.5. Cable parameters were measured using the Wayne Kerr 'Precision Magnetics Analyzer', 3260B. Despite the increased frequency, the dielectric loss factor is still very low and can be ignored. More component parameters are given in Appendix B. A photograph of the converter is shown in Figure 5.11.

Parameter	Value
Input Voltage Range	0V to 10V
Resonant Capacitance	2x124nF in parallel
Resonant Inductance	3.752μH
Resonant Frequency	165.0kHz
Operating Frequency Range	160kHz to 315kHz
H-Bridge Duty Cycle	0.8
Transformer Turns Ratio	1:10
Output Filter Capacitance	As Required

Table 5.4. Parameters for single-phase SLR converter used in the experimental work.

Frequency (kHz)	Resistance Ω/km	Inductance mH/km	Capacitance nF/km
DC	95	-	-
471	170	0.4176	67.5
942	240	0.4064	67.5
1413	270	0.3940	67.5
1884	290	0.3770	67.5
2355	300	0.3680	67.5

Table 5.5. Measured parameters for URM 70 coaxial cable.

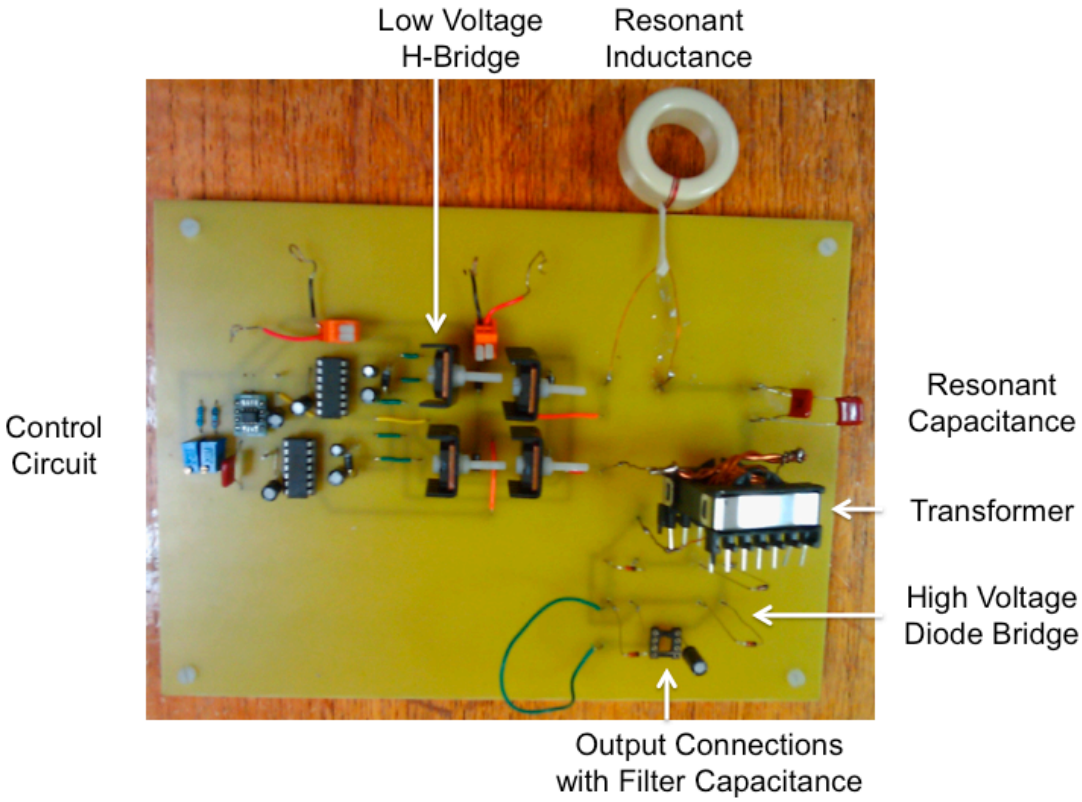

Figure 5.11. Photograph of the single-phase SLR converter used in experimental work.

The laboratory SLR converter is not an exact scale representation of a high power converter. The increased resistive losses due to the high frequency of operation make it necessary to add a 3.6Ω resistor to the low voltage side of the converter in the MATLAB model. Additionally, the voltage drop of 0.45V across each diode is significant in comparison to the output voltage and so this has also been included in the MATLAB model.

The losses can also cause overheating and so it was necessary to run with a relatively low output current. This low output current presented some difficulties with taking accurate current measurements. However, it was possible to take sufficiently accurate measurements of the fundamental and 2nd harmonic ripple frequencies. The error due to background noise was significant at higher frequencies (where the magnitude of ripple is much lower) and these results are not included in detail. Importantly, however, the results were sufficient to validate the models for ripple

propagation and the application of the principle of superposition to calculate total ripple current. Three tests were carried out, as described in section 5.3.2.

5.3.2 Transmission through a Cable with Length λ/2

For the chosen frequency, the wavelength in the cable is 399m[1]. A 200m section of cable was used to represent one pole of a bipole arrangement. The connections of cable (inner and outer conductors), converter and receiving end components are shown in Figure 5.12. The outer conductor was grounded approximately every 8m along its length to simulate regular grounding of the outer layers of a subsea cable, as described in [41, 55]. Due to the high frequency and correspondingly small skin depth of the outer conductor, the AC magnetic field associated with the ripple current is sufficiently well contained within the cable to ignore interaction with the surroundings.

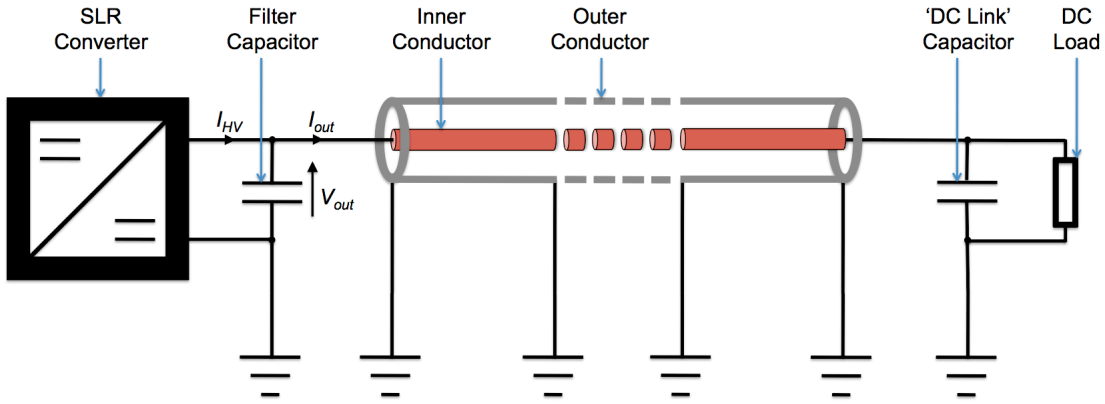

Figure 5.12. Experimental setup showing connections of cable, converter and 'onshore' (receiving end) components.

The other system component parameters were:

- 22nF filter capacitor on the converter output
- 1mF DC link capacitor
- 100Ω DC load resistor.

Measurements of current and voltage were taken at multiple points in the converter including the voltage in the resonant capacitor, the output voltage and the rectified HV current before and after the capacitive filter. In addition, current was measured at approximately 8m intervals along the length of the cable.

5.3.2.1 Results

Figure 5.13 shows the waveforms for the resonant capacitor voltage, the unfiltered current output from the high voltage diode bridge (I_{HV}) and the output voltage measured across the filter capacitor (V_{out}). T is the period of the low voltage side switching cycle and is equal to 1/235.5kHz.

The experimental and MATLAB results match well. There is some asymmetry between the two half-cycles in the experimental work. This is caused by a number of small differences between the two half-cycles including in the components and connections between components.

The experimental results also show some higher frequency ripple components. Some of this is noise from the surroundings and some from parasitic inductance or capacitance in the converter components. Fourier analysis of the waveform from the experimental results shown in Figure 5.13(b) showed peaks at (approximately) 7 times, 12 times, 17 times, 20 times and 22 times the fundamental ripple frequency of 471kHz. In Figure 5.13(c) peaks were found at 10 times, 14 times and 20 times the fundamental frequency. It is therefore difficult to ascertain the exact source of the additional high frequency ripple.

---

[1] The cable length is slightly longer than $\lambda/2$ because the switching frequency of the converter is difficult to set precisely and changes with operating temperature. The frequency used is measured more accurately when the results are analysed on a PC.

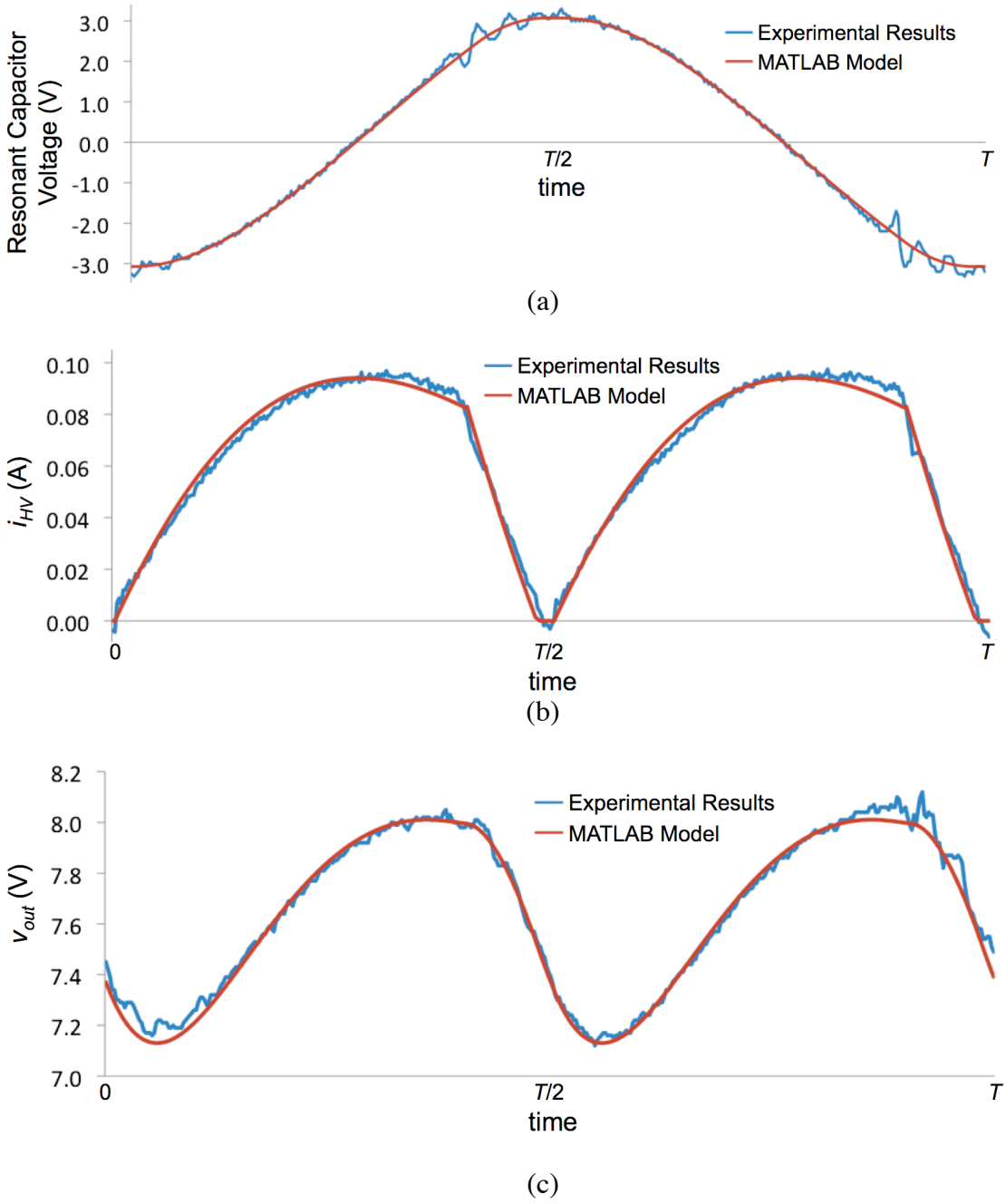

Figure 5.13. Waveforms for (a) the resonant capacitor voltage, (b) the unfiltered current output from the high voltage diode bridge (I_{HV}) and (c) the output voltage across the filter capacitor (V_{out}).

The additional ripple is greatest around the time the H-bridge MOSFETs are turned off, as can be seen in Figure 5.13(a). In Figure 5.13(b), a small amount of negative current can be seen in the rectified high voltage current. This is caused by the reverse recovery of the diodes in the rectifier. It is relatively pronounced in this experiment

(compared to what would be expected in the full scale SLR converter) due to the relatively small current in the diodes, which makes the discharge current from the parallel capacitance significant by comparison.

Figure 5.14 shows the output current waveform (I_{out}) and the current waveform measured at approximately the mid-point of the transmission cable. T=1/235.5kHz.

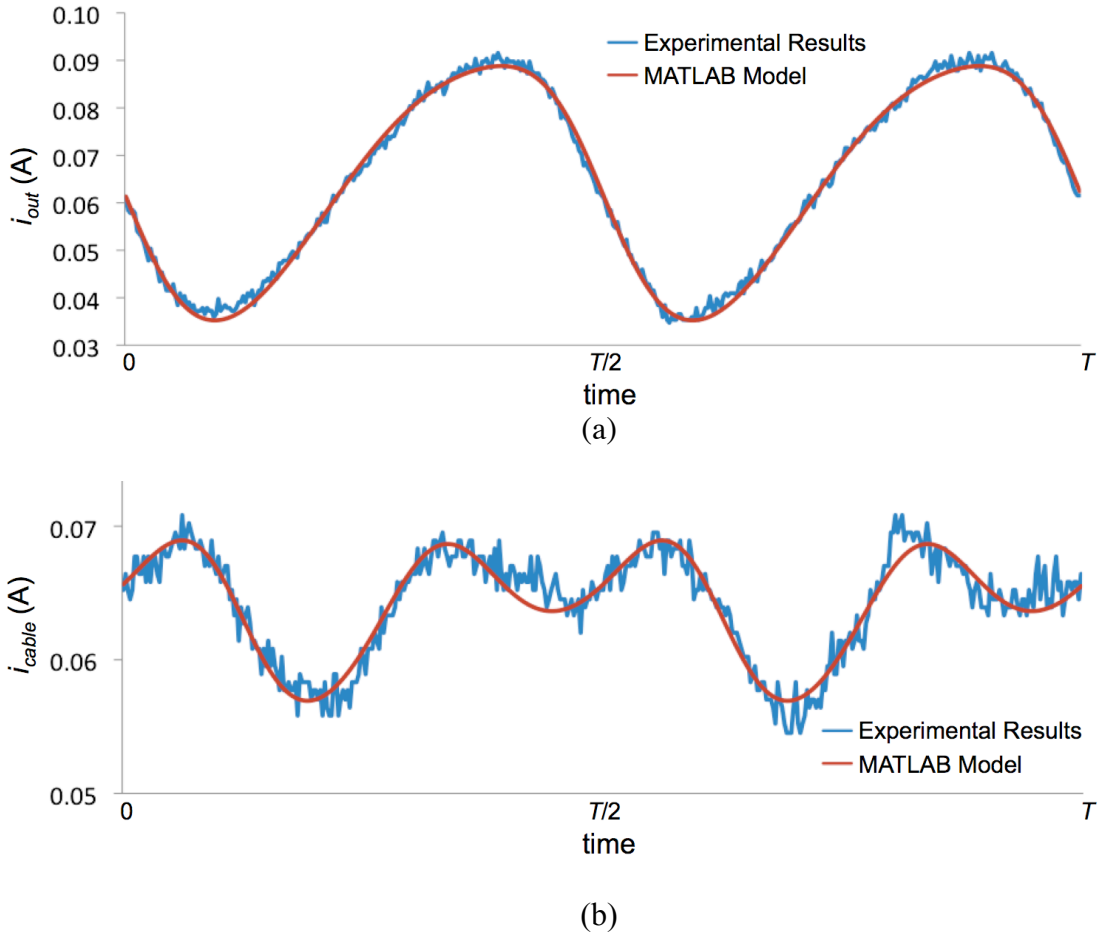

Figure 5.14. (a) output current waveform (I_{out}) and (b) current waveform at approximately the mid-point of the transmission cable (I_{cable}).

It was previously seen, in Figure 4.3, that the impedance of a cable with length $\lambda/2$ is particularly low. The equivalent plot for the URM 70 cable, at the fundamental and 2nd harmonic ripple frequencies, is shown in Figure 5.15.

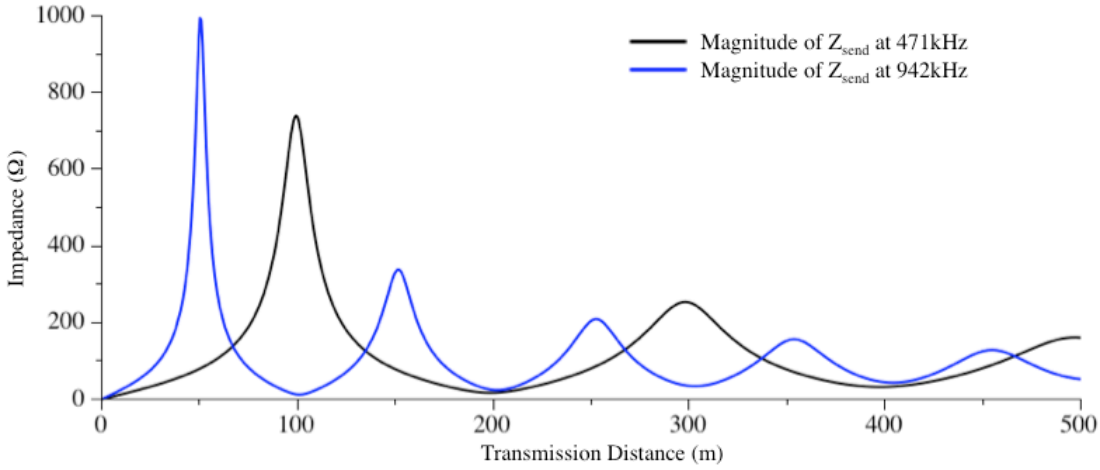

Figure 5.15. Magnitude of Z_{send} calculated for a range of transmission distances at 471kHz and 942kHz for the URM 70 cable.

The large current magnitude of the fundamental ripple frequency seen in Figure 5.14(a) is a result of the low impedance of a 200m cable (c. $\lambda/2$). As discussed in section 4.1.4, the ripple current varies along the length of the cable. Measured at (roughly) the mid-point of the cable, the current ripple magnitude is much lower, as seen in Figure 5.14 (b). The phase of the fundamental ripple current is also different in Figure 5.14 (b) compared to Figure 5.14 (a) and the 2nd harmonic ripple current is now noticeable due to the reduced size of the fundamental. It is also clear that the losses caused by the ripple current are different at these two points in the cable.

Figure 5.16 shows the magnitudes of the fundamental frequency ripple current and its 2nd harmonic along the length of the transmission cable. In Figure 5.16(a), the reduction in the magnitude of the fundamental ripple current at the mid-point of the cable can be seen clearly. The variation of the 2nd harmonic ripple can be seen in Figure 5.16(b). At the mid-point of the cable, this ripple component is larger than the fundamental, which explains why it is prominent in Figure 5.14(b).

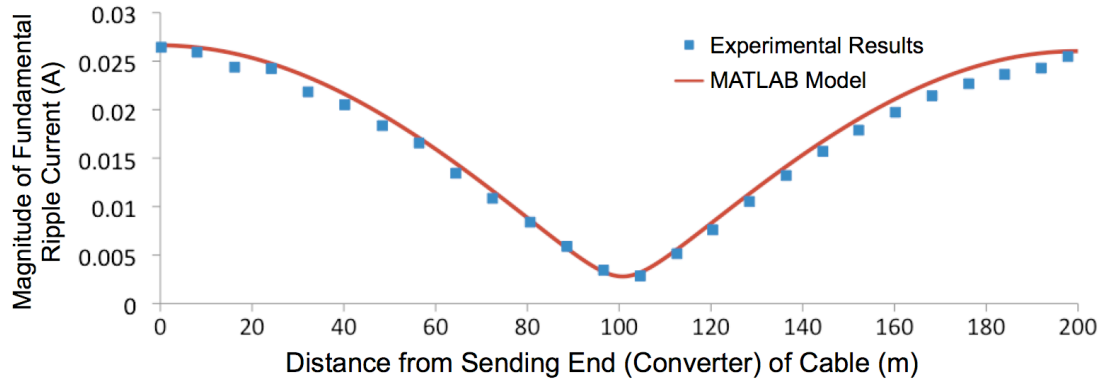

(a)

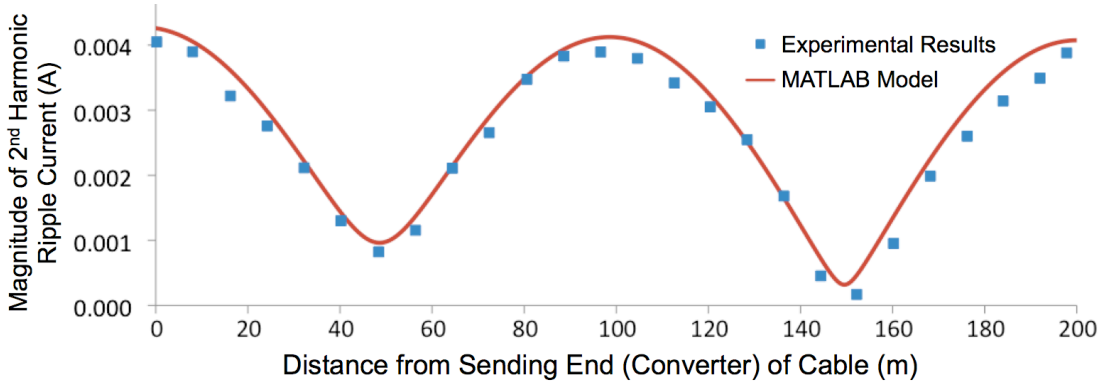

(b)

Figure 5.16. Magnitude of (a) the fundamental frequency ripple current and (b) its 2nd harmonic along the length of the 200m URM 70 cable.

All the results from the MATLAB modelling and practical work for this experiment match well.

5.3.3 Transmission through a Cable with Length λ/4

In this case, a 100m section of cable was used. The connections were the same, including grounding of the outer conductor every 8m, as were the measurements taken.

Figure 5.17 shows the waveforms for the unfiltered current output from the high voltage diode bridge (I_{HV}) and the output voltage measured across the filter capacitor (V_{out}). T=1/235.5kHz.

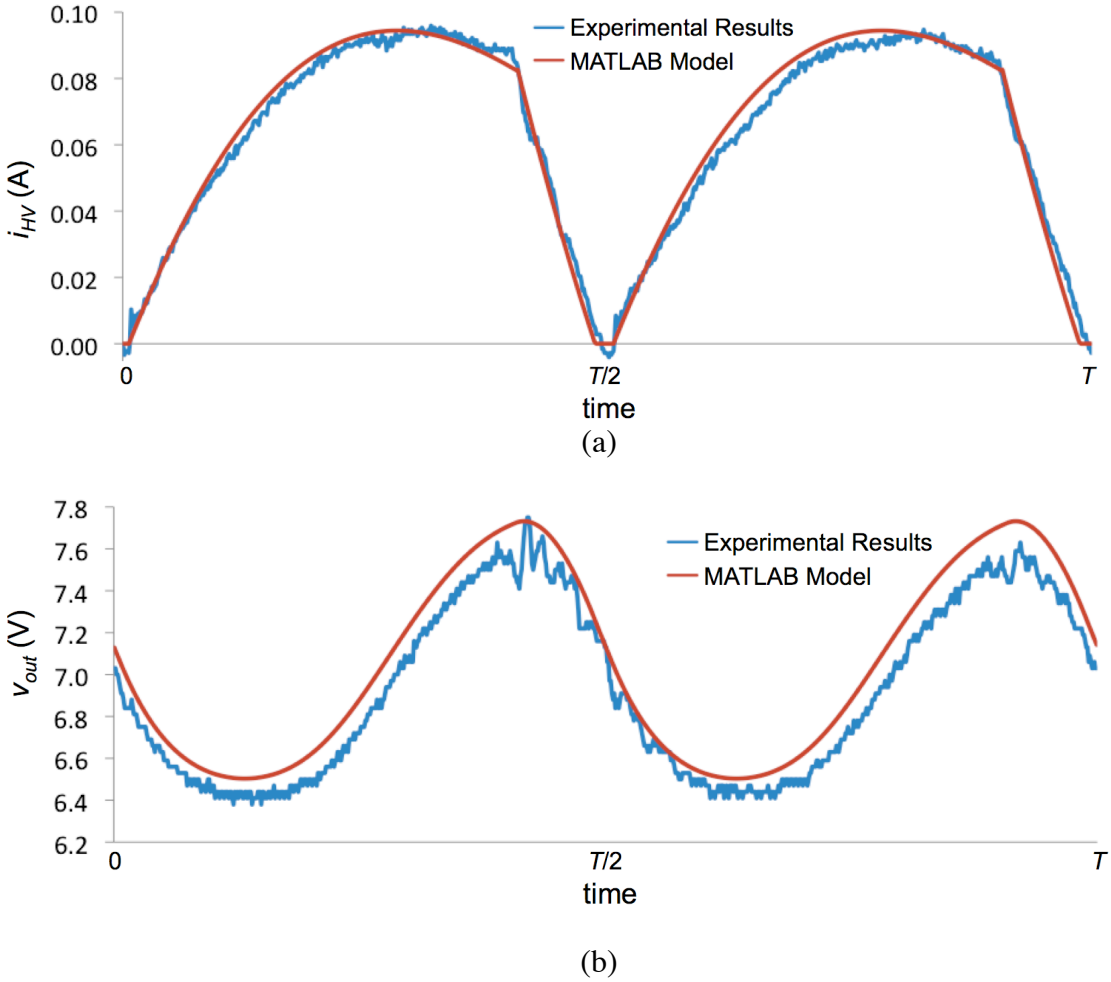

Figure 5.17. Waveforms for (a) the unfiltered current output from the high voltage diode bridge (I_{HV}) and (b) the output voltage across the filter capacitor (V_{out}).

Again, the waveforms match well. There is an error in the DC voltage in Figure 5.17(b) of around 1-2%. The most likely cause is measuring equipment error. In most measurements, there is a DC offset in the readings from the oscilloscope. Repeated measurements reduce this offset in most cases, but it is difficult to entirely eliminate. The error may also be caused by the modelling of the converter losses as a single resistance. This is because, from one point a view, the converter, cable and load resistor act as a DC voltage divider - so some of the input DC voltage is dropped across each one. To model exactly the voltage that is dropped in the converter, and therefore the remaining output DC voltage, a more accurate model of the losses would be necessary. However, the results with the adopted approach match the experimental results well and, given that the model must be directly transferable to

the high power application, the added complexity of a more accurate model that is only required for the experimental work is unnecessary.

Figure 5.18 shows the output current waveform (I_{out}) and the current waveform measured at approximately the mid-point of the transmission cable. T=1/235.5kHz.

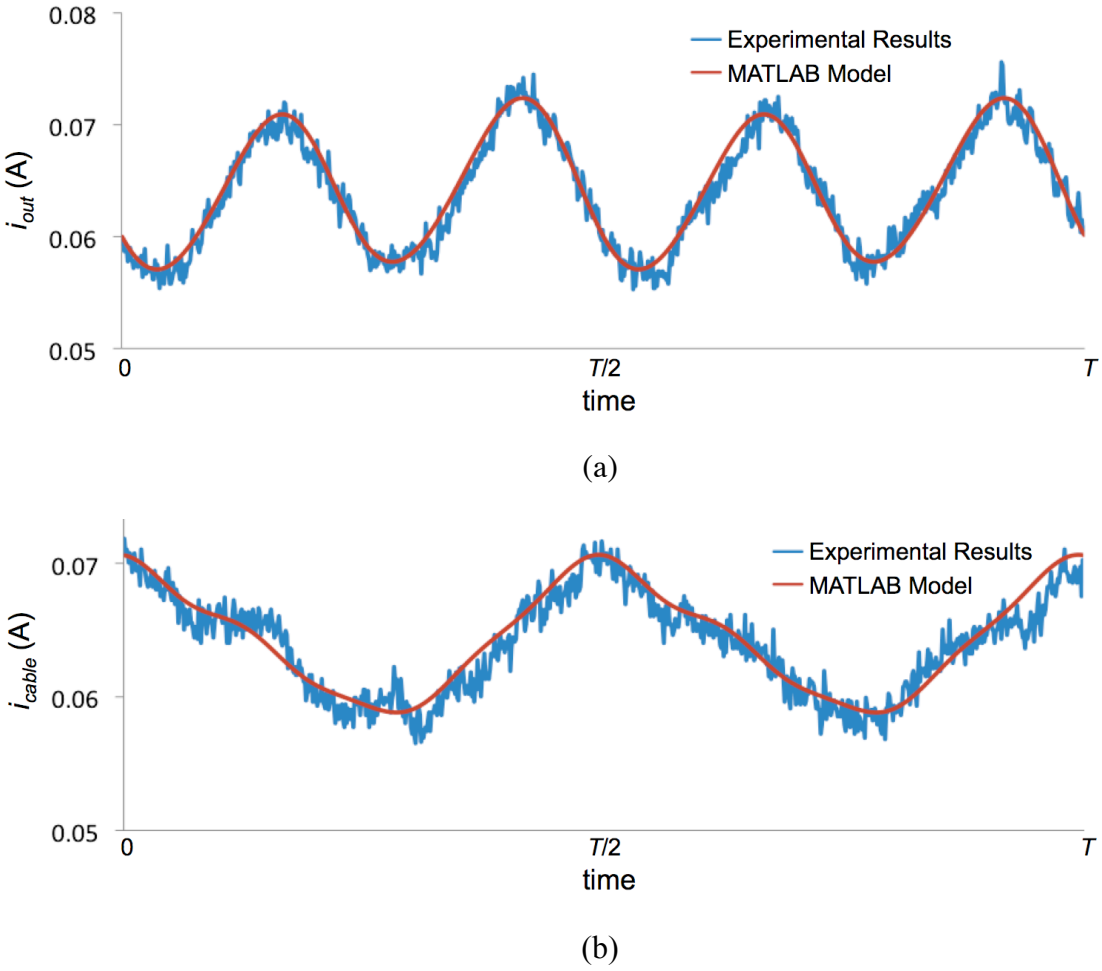

Figure 5.18. (a) Output current waveform (I_{out}) and (b) the current waveform at approximately the mid-point of the transmission cable.

The frequency of the ripple current at the converter output, as shown in Figure 5.18(a), appears to be at double the frequency of the output voltage ripple in Figure 5.18(b). This can be understood by considering Figure 5.15. For a transmission distance of 100m, the impedance of the cable is very high to the fundamental ripple component and therefore this component of ripple voltage results in very little

current. Meanwhile, the impedance to the 2nd harmonic is very low and this component of ripple voltage, although too small to be particularly noticeable in Figure 5.17(b), causes the majority of current ripple at the converter output.

Measured half way along the cable, as shown in Figure 5.18(b), the fundamental ripple component is again apparent. This demonstrates the point that measurements of the ripple and losses at the sending end of the cable may not represent the maximum losses for all points in the cable. This point is emphasised by Figure 5.19(a), below. Figure 5.19 shows the magnitudes of the fundamental frequency ripple current and its 2nd harmonic measured along the length of the transmission cable.

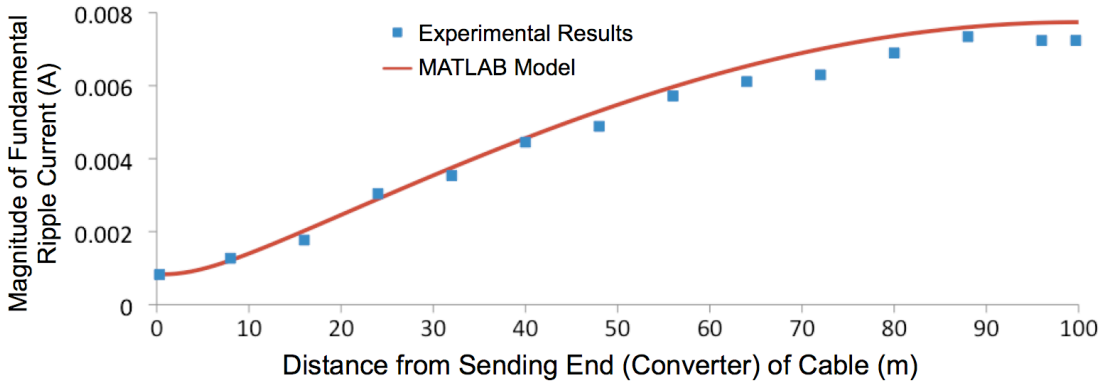

(a)

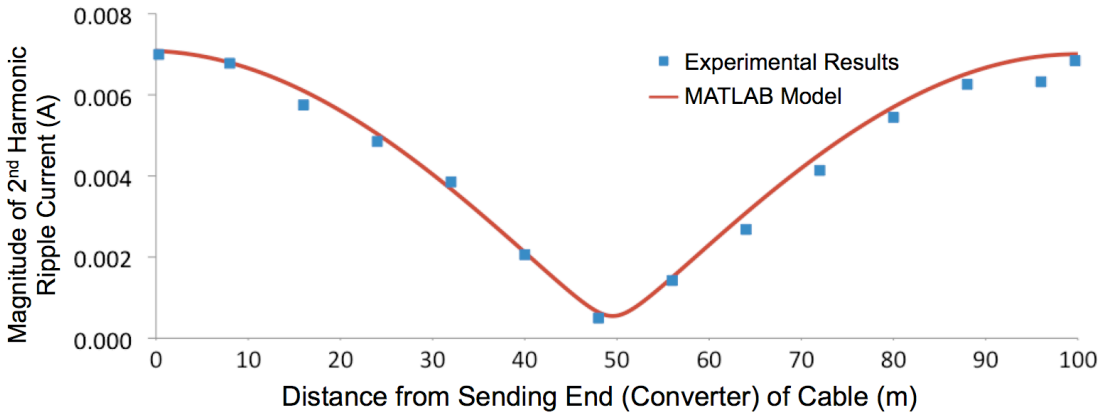

(b)

Figure 5.19. Magnitude of (a) the fundamental frequency ripple current and (b) its 2nd harmonic along the length of the 100m URM 70 cable.

Figure 5.19(b) is similar in shape to Figure 5.16(a). This is because both graphs show the magnitude of a component of ripple frequency in a cable (approximately) half its wavelength. The low value of the 2nd harmonic at the mid-point of the 100m cable explains why it is not apparent in Figure 5.18(b). The distortion from the fundamental in this case is caused by higher harmonics.

5.3.4 Resonance between Converter and Cable

In section 5.2.3, resonance between each DC-DC converter, in particular its filter capacitor, and the rest of the DC grid is examined. One important result is that the filter capacitor can amplify the ripple current, rather than reduce it, due to interaction with the DC grid. This result is demonstrated in practice in this section.

5.3.4.1 Approach

Amplification of the ripple current occurs when the imaginary parts of system admittance and filter capacitor admittance cancel out. The real and imaginary components of Y_{send} (the cable admittance from the sending end, equal to $1/Z_{send}$) and its magnitude for a range of transmission distances are shown in Figure 5.20.

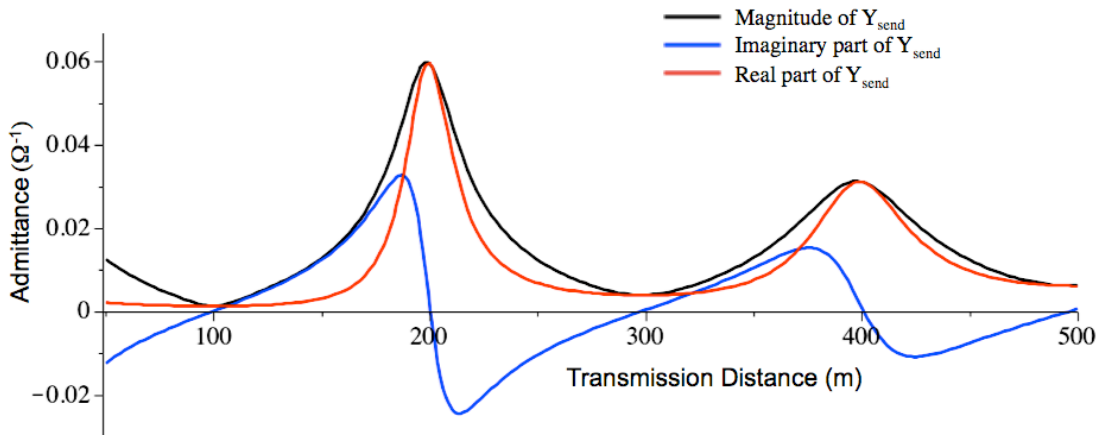

Figure 5.20. Y_{send} components and magnitude for a 471kHz ripple calculated at a range of transmission distances for the URM 70 cable.

A filter capacitor of 10nF was used for the experiment, which has an admittance of $j0.0296\Omega^{-1}$. It can be seen from Figure 5.20 that the cancellation with the cable admittance is likely to be greatest for transmission distances a little over 200m. This

presents a practical problem, as joining short lengths of cable is difficult to achieve without introducing additional error, due to the change in impedance at the join, or damaging the cables being joined (the construction of the inner conductor of the cable is relatively fragile).

However, the important parameter is not necessarily the cable length, but the ratio of transmission distance to wavelength. While maintaining a cable length of 200m, this ratio was altered by changing the switching frequency. In doing so, it was necessary to allow for the change in cable parameters, although this is relatively small over the frequency range that needs to be considered. In Figure 5.21, the admittance of the 200m cable at a range of frequencies from 423kHz to 609kHz is plotted against the ratio of the cable length (fixed) to the wavelength (variable) at the given frequency. The graph is very similar to Figure 5.20 for the corresponding values of ratio of cable length (variable) to wavelength (fixed), i.e. from roughly 180m to 230m.

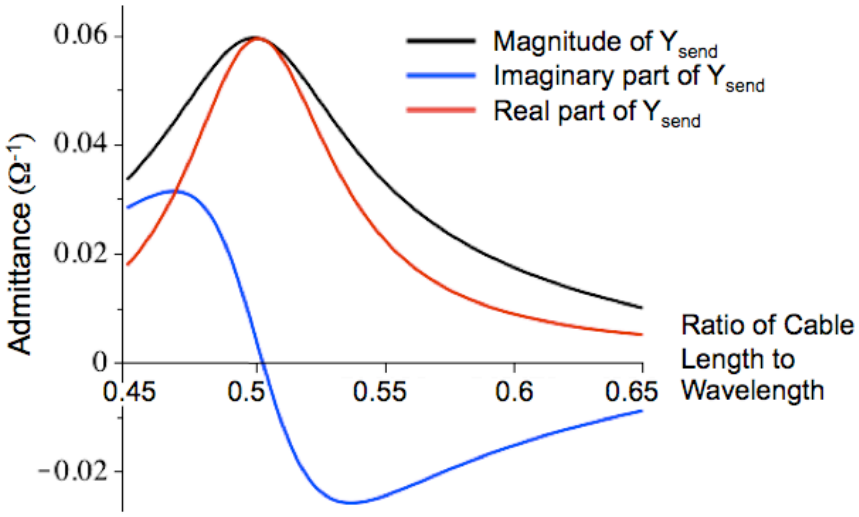

Figure 5.21. Y_{send} components and magnitude of the 200m cable calculated at a range of frequencies from 423kHz to 609kHz plotted against the ratio of the cable length (fixed) to the wavelength (variable) at each frequency.

5.3.4.2 Results

In Figure 5.22, experimental results and those from the MATLAB model, for the ratio of the magnitude of fundamental ripple frequency in the output current (I_{out}) to

that in the unfiltered, rectified HV current (I_{HV}), are plotted against the ratio of cable length to wavelength. The phase shift from I_{HV} to I_{out} is also plotted.

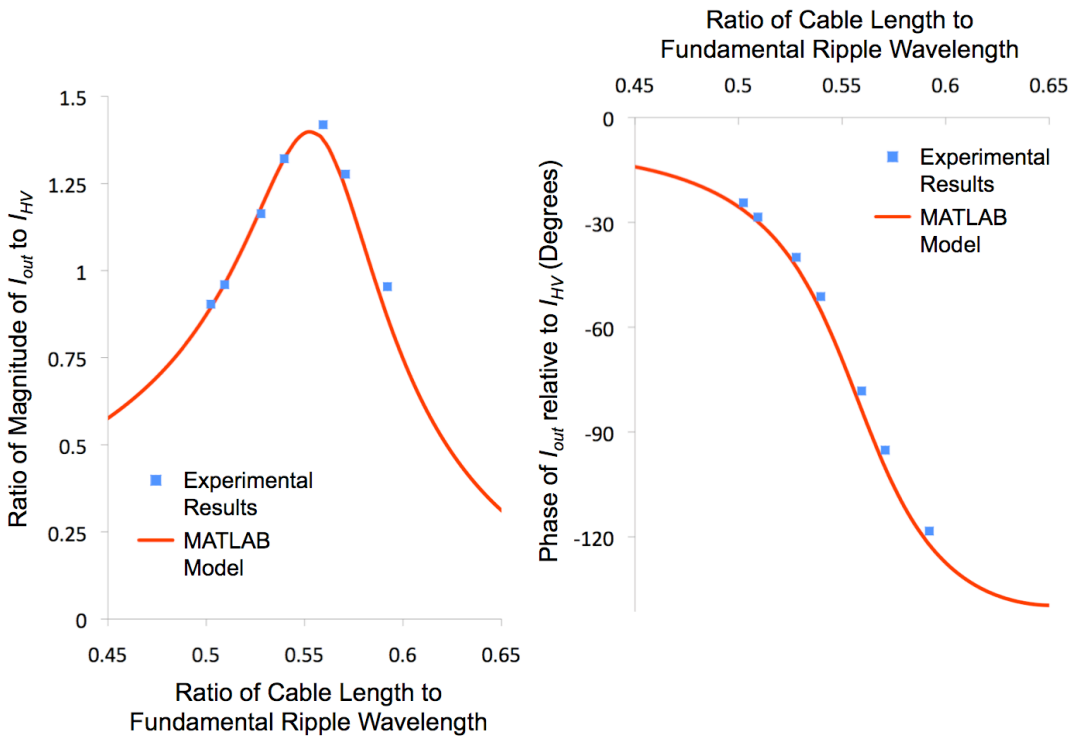

(a) (b)

Figure 5.22. (a) Ratio of the magnitude of fundamental ripple frequency in the output current (I_{out}) to that in the unfiltered, rectified HV current (I_{HV}) and (b) phase shift from I_{HV} to I_{out}, against the ratio of cable length to wavelength

The experimental results show the amplification of the ripple current after the filter capacitor and agree with the results from the MATLAB model. The peak amplification is by a factor of 1.4 times and this occurs at a transmission distance 0.55 times the wavelength. Recall equation (5.4).

$$I_{out} = I_{HV} \frac{Y_{sys}}{Y_{sys} + Y_C} \tag{5.4}$$

From Figure 5.21, it can be seen that the peak amplification corresponds to a high (but not peak) negative value of the imaginary part of system (or cable) admittance, which cancels with the positive admittance of the filter capacitor. The reason it does not occur at the peak negative value is that the real part of admittance is larger at this

point and this dominates the numerator and denominator in equation (5.4), reducing the amplification.

The chosen capacitor size may seem small, at 10nF. However, in order to compare this to a filter capacitor in a 6MW converter, two factors must be considered. First, the magnitude of the DC current is approximately 1000 times larger in the 6MW version (compare Figure 5.13(b) to Figure 5.2(c)). Secondly, the frequency is 471 times lower in the 6MW version. Therefore, an approximately equivalent filter capacitor would be 471,000 times larger, i.e. 4.71mF. A smaller capacitor could reasonably have been used in this experiment, which would have resulted in a larger amplification at certain frequencies.

5.3.5 Analysis and Assessment of Error

The results here validate the following:

- Time domain model of the single-phase SLR converter;
- Application of wave propagation equations to model the behaviour of ripple in a cable;
- Integration of these two models;
- Prediction of resonance between the converter and cable that can lead to amplification of the ripple current.

There are a number of factors that account for the discrepancy between the results from the model and those from the experiment. These can be broken down into model errors and experimental errors. Error in the results from the MATLAB model may be caused by the following simplifications.

- Transformer modelled as ideal;
- No parasitic inductances and capacitances modelled;
- No diode reverse recovery modelled;

- Converter losses simplified into a single resistor.

Error in the results from the experiment may be caused by:

- Measuring equipment error;
- Component parameter inconsistencies with each other and with datasheet values;
- Impedance of connections and tracks on circuit board;
- Change in impedance at the join of two (100m) cables.

Given the additional difficulties caused by working with and accurately measuring relatively high frequency and low magnitude currents/voltages, any difference between the results is accounted for by these sources of error.

The results presented not only validate the model but also highlight some important system behaviour. It has been shown that certain lengths of cable can result in particularly low or high ripple currents at the converter. Just as importantly, it has also been shown that the size of this ripple is not fixed along the length of the cable. This is a crucial result when considering a cable's rating; it may appear when measured at one end of the cable that the current ripple is small, but at another point, perhaps where it cannot be measured, it may be much more significant. This must be considered when designing the system to meet cable ampacity limits.

5.4 Chapter Summary

Simple but effective MATLAB models of three power electronic DC-DC converters have been developed in this chapter, along with the outline for a representation of a standard inverter as a basis for a DC-DC converter. The difficulties in integrating these models into a multiterminal DC grid model, with frequency dependent cable parameters and a significant number of nodes, while maintaining manageable run

times have been addressed. Throughout the work, the coded MATLAB models have been compared to Simulink models to verify their accuracy, and a number of validation experiments have been carried out to demonstrate that the models correctly represent the converters, the frequency dependent cables and the integration of the two.

6 DC Network Analysis and Design

The aim of this chapter is to bring together all the modelling work in the thesis so far and use it to begin to design the components of the DC grid. The models developed in the previous chapters for the offshore wind farm DC grid are used to assess the performance of the grid in a range of steady state conditions and make design recommendations for the system.

A range of system requirements and operating conditions are assessed including:

- Turbine power output;
- Disconnection of turbine(s) from the DC grid;
- Transmission distance from the wind farm to shore;
- Operating temperature of the cables.

A range of system design choices are considered, including:

- Choice of DC-DC converter design;
- Size of capacitive filter;
- Switching phase of the converters;
- Use of filter inductors in the wind farm.

Further system variables are considered in chapter 7.

There are a large number of variables and the approach to analysing them all was carefully considered. The approach taken was to model the single-phase SLR converter in a DC grid with a range of operating conditions and constraints and design its filtering components and switching strategy, with the aim of managing the current and voltage ripple in the system. The knowledge gained from this design

process was then applied to the configuration of DC grid designs for each of the other three converter topologies. Finally, a number of other design criteria are addressed and the suitability of each converter evaluated.

In this chapter, the most important results are presented and discussed. A selection of more detailed results is found in Appendix E.

6.1 Modelling and Design of the DC Grid Using the Single-Phase Series Load Resonant Converter

6.1.1 Filter Capacitance

Sizing the filter capacitor was carried out with two requirements in mind: to limit voltage ripple and manage ripple current losses in the cables.

In chapter 2, a level of ±2% was given as a reasonable limit for the voltage ripple. In this chapter, because the voltage ripple is computed in the frequency domain, a limit of 2% for the Total Harmonic Distortion (*THD*) of the first 10 ripple frequencies was applied. For the purpose of this work, *THD* is defined by equation 6.1.

$$THD = \frac{\sqrt{\sum_{1kHz}^{10kHz} V_{ripple}^2}}{V_{DC}} \tag{6.1}$$

where V_{ripple} are the magnitudes of the frequency domain components of the ripple voltage.

The second criteria is to ensure that all the cables (collection and transmission) operate within their current limits.

6.1.1.1 Model Setup

The model of the network in Figure 4.7. was initially set up with the following conditions:

- All turbines operating at full power;
- All converters switching in phase;
- 100km transmission distance;
- Cables operating at 20ºC;
- Base Case cable configuration as described in chapter 3;
- Capacitor *ESR* 5mΩ;
- Fixed 50kV DC component of voltage at the onshore converter.

The model was run for a range of filter capacitances. With respect to the modelling of converters switching in phase, it is assumed that control of the switching phase is achievable by the central wind farm controller. This does not mean that the central controller directly controls each converter; rather that it periodically corrects any change in the timing of each converter's switching before the change in its phase angle becomes significant. This control will require communication within the wind farm, most likely provided by fibre optics installed within the collection network cables (as shown in [47, 85], for example). Whether this level of control is necessary in all system designs is discussed in chapter 8.

6.1.1.2 Results and Analysis

Figure 6.1 shows the peak voltage distortion anywhere in the system and the magnitude of the fundamental frequency of ripple current at the sending end of the transmission cable for a range of filter capacitance values.

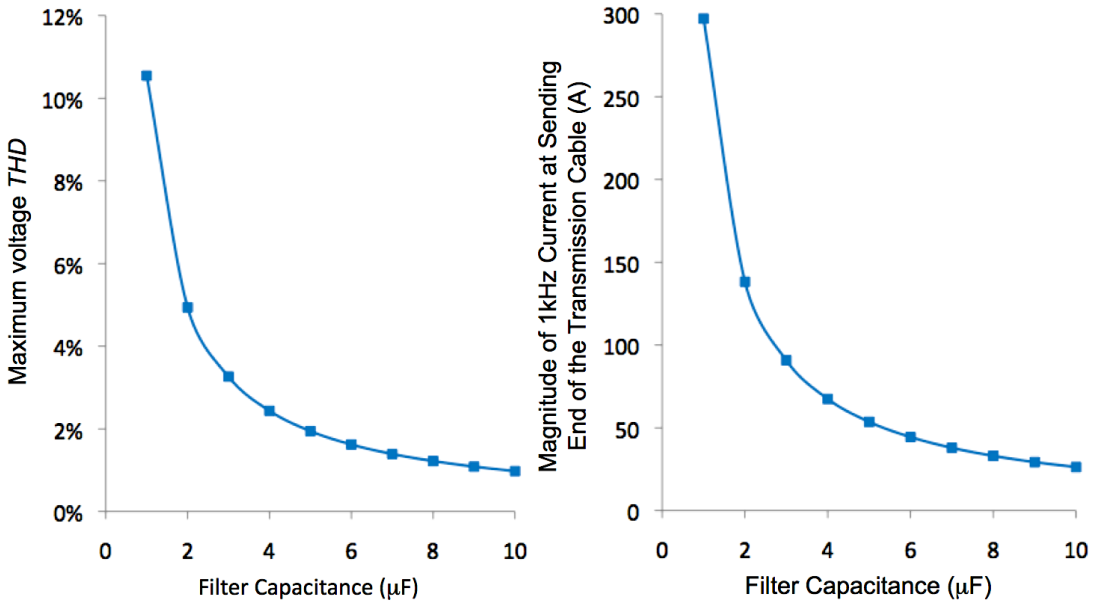

(a) (b)

Figure 6.1. (a) Peak voltage *THD* in the collection network and (b) magnitude of fundamental ripple frequency current at the sending end of the transmission cable calculated for a range of filter capacitances.

As expected, the filter capacitor is effective in limiting the ripple voltage. The target of 2% *THD* can be achieved with a 4.9μF capacitor. The reduction in the ripple voltage with increasing capacitance also reduces the ripple current in the transmission cable, as can be seen in Figure 6.1(b).

By keeping the voltage ripple within limits, the filter capacitance ensures correct operation of the converter. The unfiltered DC current (I_{HV}) for one AC cycle is shown in Figure 6.2 for a range of filter capacitances, including 4.9μF.

It can be seen that, if the filter capacitance is too small, voltage ripple in the system can lead to distortion of the waveform in the converter. This can increase converter losses. The peak current with a 4.9μF capacitor is 83.7A, compared to 93.4A for a 1μF capacitor; the latter will cause higher conduction losses in the converter.

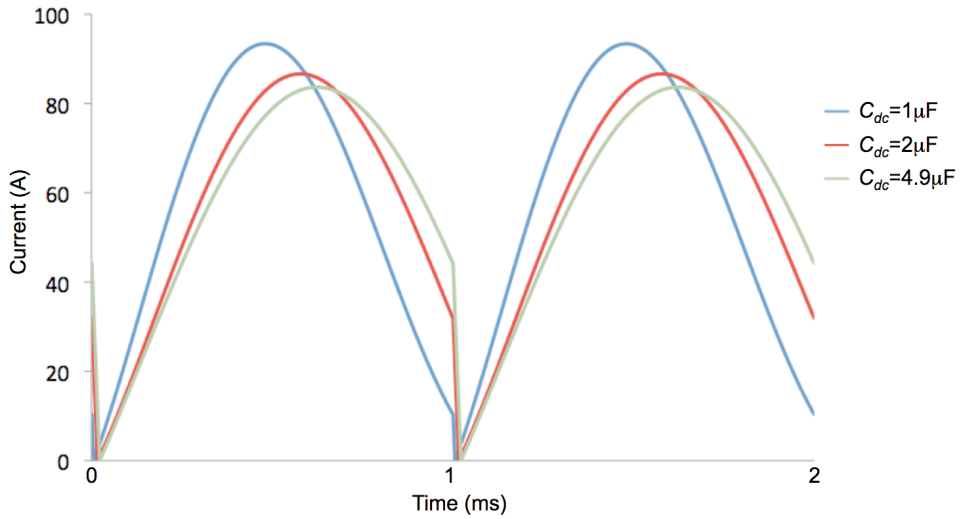

Figure 6.2. Rectified, unfiltered current waveform for the single-phase SLR converters switching in phase simulated with a range of filter capacitances.

The second aim was to make sure all cables operate within their current limits. The allowable losses for each type of cable were calculated using ampacity data given in [46]. Making the assumption that the maximum operating temperature for the cables is 90ºC, the allowable losses are calculated with core resistivity at 90ºC. The DC ampacity and corresponding allowable losses for the base case cables are shown in Table 6.1.

Cable Type	DC Current Limit (A)	Maximum Losses (W/m)
1	343	28.2
2	662	33.2
3	1594	41.3

Table 6.1. Permissible losses per cable based on [46] for temperate climate with cables laid close together in bipole arrangement.

In order to make sure that each cable was within the limits in Table 6.1, it was necessary to model them operating at their temperature limit. An approximation was made by modelling all cables operating at 90ºC, even though it is unlikely that this will be the case in reality, especially for lightly loaded cables.

It was found that changing the operating temperature made little difference to the voltage *THD*. For filter capacitors of 4.9μF, the maximum *THD* at any converter was reduced slightly, from 1.99% to 1.95%.

The cable closest to its current limit was the transmission cable. The peak losses in this cable for a range of values of filter capacitance (C_{dc}) are shown in Figure 6.3.

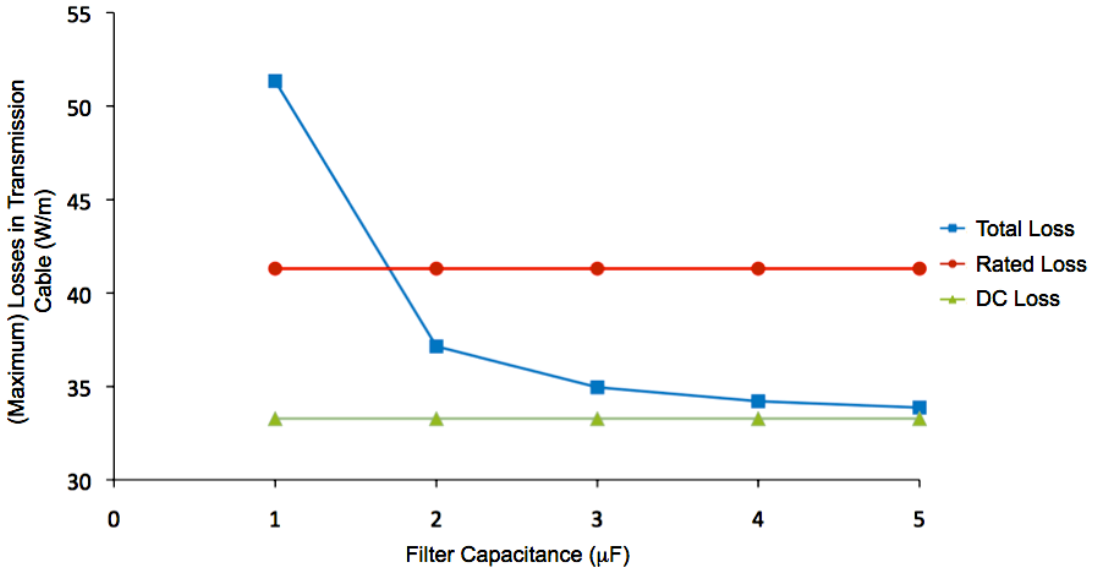

Figure 6.3. Rated and simulated losses per transmission cable at 90°C for a range of filter capacitance values with the SLR converters switching in phase and operating at full power.

It can be seen that the DC losses are significantly below the cable limit, even though the wind farm is operating at full power. There are two reasons for this. First, the transmission cable has a current limit of 1594A DC, while the modelled rated current output of the 25 turbines at 50kV is a total of 1500A. Secondly, because the onshore converter was modelled as controlling the voltage to be 50kV, the actual DC voltage at the wind farm was higher due to the volt rise caused by the DC current in the cable. The DC voltage at converter 15 (the point of common connection, PCC) is 51.9kV. Consequently, the total current produced at rated power is lower than 1500A.

In this case, the limiting factor for the size of the capacitance is the voltage *THD* requirement. Cables are available in discrete steps of current rating [32, 44, 46, 47, 48, 64], so for a different size wind farm or for a different cable supplier, the gap between the maximum DC losses and rated DC losses (as seen in Figure 6.3) may not be so large and, in that case, the current ripple could be a more important factor.

The temperature of the cables is not necessarily solely dependent on the current that they carry; other factors include the heat capacity of the cable and surrounding seabed. Accurate dynamic modelling of cable temperature is a complex task and beyond the scope of this thesis. However, to give an idea of the magnitude of the time constants involved, a calculation for the heat capacity of the base case transmission cable has been carried out, which gave its heat capacity as approximately $15kJK^{-1}m^{-1}$. Without modelling any heat dissipation to the surroundings (which would slow cable temperature rise), the cable operating with rated losses of $41.3Wm^{-1}$ would need roughly 6 minutes to increase in temperature by 1K. Given the variability of wind turbine power output, a wide range of cable temperatures are therefore possible for any level of output power. It is important to account for this fact when modelling the DC grid.

6.1.2 Switching Phase

6.1.2.1 Model Setup

The switching phases of the converters were offset from each other in three different patterns, as shown in Table 6.2. The angles shown are for the switching phase on the low voltage side of the transformer; the ripple of the rectified DC current is at twice the low voltage AC frequency and the phase angle for the fundamental ripple is also doubled. In all cases, the principle is that, across the wind farm, much of the ripple voltage and current cancels out. In case 1, turbines on a single string are in phase with one another, but each string has a different phase. In case 2, the turbines on a single string are out of phase so that the ripple within each string cancels out. Case 3 is similar to case 2, but the phase offsets are arranged in a different pattern.

Phase Angle	Case Number and Turbines for which Phase Angle Applies		
	Case 1	Case 2	Case 3
0°	1, 2, 3, 4, 5	1, 6, 11, 16, 21	1, 10, 14, 18, 22
36°	6, 7, 8, 9, 10	2, 7, 12, 17, 22	2, 6, 15, 19, 23
72°	11, 12, 13, 14, 15	3, 8, 13, 18, 23	3, 7, 11, 20, 24
108°	16, 17, 18, 19, 20	4, 9, 14, 19, 24	4, 8, 12, 16, 25
144°	21, 22, 23, 24, 25	5, 10, 15, 20, 25	5, 9, 13, 17, 21

Table 6.2. Converter switching phases used in modelling.

6.1.2.2 Results and Analysis

6.1.2.2.1 Case 1

The results show an increase in the voltage *THD* for the wind farm operating at full power, with a filter capacitance of 4.9μF, from 1.99% for switching in phase to 3.25% in case 1. More significant, however, is that large circulating currents flow in the cables connecting strings of turbines (i.e. cables connecting converters 5 & 10, 10 & 15, 15 & 20 and 20 & 25). The largest ripple current component is the 1kHz component in the cable connecting converters 10 and 15, which is 440A in magnitude. This cable is rated to carry a DC current of 662A, but the AC losses alone are 73.6Wm^{-1}, over twice the losses for which the cable is rated.

To an extent, due to the low impedance sections of cable connecting them, the capacitors in the DC grid act as a single large capacitor . For example, a 600m length of the base case cable 1 has a 1kHz impedance of magnitude 0.0022Ω. A 4.9μF capacitor has a 1kHz impedance of magnitude 32.5Ω. As a result, ripple current can flow almost as easily into an adjacent capacitor as into the capacitor in the converter from which it is generated. This leads to the circulating currents between adjacent turbine strings as their aggregated current ripples are out of phase.

This result is, perhaps, not surprising. The intention of this case is to demonstrate the effect of poorly chosen switching phases for converters. Although this should not happen by design, if the converters were allowed to switch independently, then it is

likely that for some periods of time similar conditions might result (since subtle differences in switching frequency would cause the phases to change relative to each other over time). The conclusion is, therefore, that converter switching phase must be actively monitored and controlled.

6.1.2.2.2 Cases 2 and 3

The results from cases 2 and 3 show that these strategies are much more effective. In both cases, with all converters operating at full power, the voltage *THD* everywhere in the system is below 2% without the use of any filter capacitance. Without any filter capacitors, in case 2 the maximum *THD* is 1.93%, while in case 3 it is 1.94%.

Both cases 2 and 3 result in effective cancellation of the fundamental ripple and its 2nd, 3rd and 4th harmonics. However, the converters are actually all in phase with respect to the 5th and 10th harmonics. The resulting voltage distortion at one converter output can be seen in Figure 6.4. The *THD* in this case is 1.94% (case 3). Figure 6.5 shows the resulting unfiltered DC current waveforms for this converter and for the same converter from the model with switching in phase and 4.9μF filter capacitors used. In the latter case the voltage output *THD* is slightly higher at 1.99%.

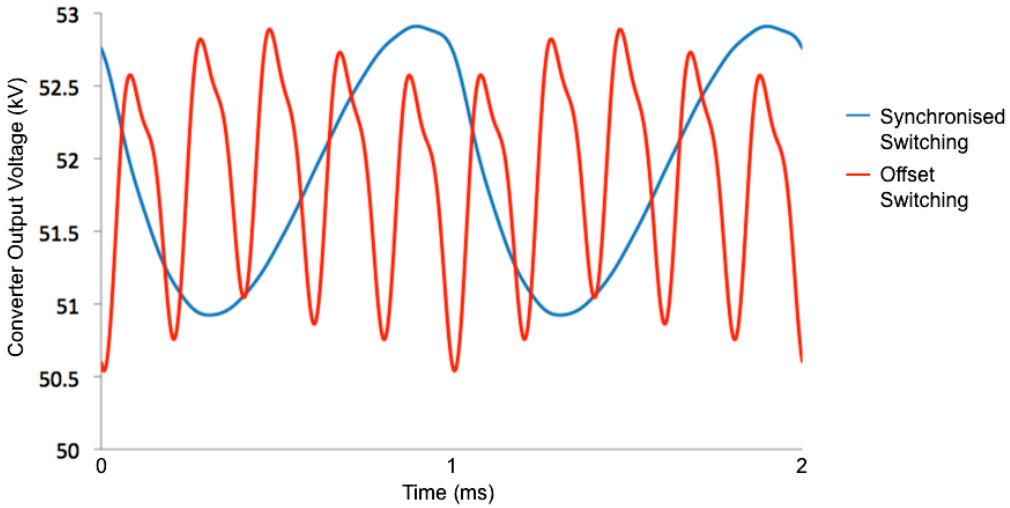

Figure 6.4. Converter output voltage waveforms simulated for switching offset and switching in phase with similar levels of *THD*.

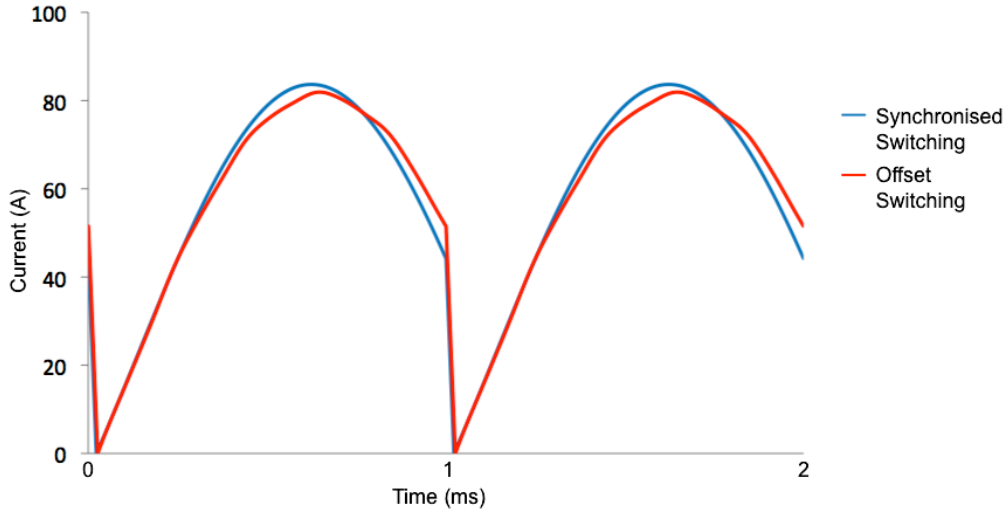

Figure 6.5. Simulated, rectified, unfiltered current waveforms corresponding to the voltage waveforms in Figure 6.4.

The voltage ripple and resulting current waveform distortion can be seen clearly. One strategy to reduce the effect of this harmonic would be to offset switching phases between different strings by a small amount. However, doing so would increase the flow of 5th harmonic circulating currents in the heavily loaded cables linking adjoining strings. In addition, it is important not to be overly reliant on a sophisticated switching strategy that will not necessarily be any more effective once the effects of disconnections or variable power output from turbines are considered. For these reasons, the modelling was restricted to the switching strategies already considered.

In cases 2 and 3, there are also circulating currents at the fundamental and lower harmonics in the network. However, these currents are largely confined within each string of turbines. As a result, the currents are small in comparison to case 1 and flow in lightly loaded cables. Again, no filter capacitance is required to achieve the current limit requirement.

Although it may be possible to operate without a filter capacitor and still meet the requirements for system voltage and current ripple, there are other reasons that a

capacitor is necessary: in operating the control system and for protection during an open circuit fault on the converter output [36].

With respect to the control system, in the absence of a filter capacitor, the voltage at the output of each converter would be susceptible to rapid changes or spikes caused by, for example, switching transients. The source of such transients could be any other converter in the network and, therefore, programming the controller to compensate would be difficult.

In the event of an open circuit fault on the converter output, a device is required to protect the diode bridge from the over voltage resulting from the interruption of the current in the transformer windings and low voltage inductance. Devices such as varistors or crowbar circuits are possible solutions, however a capacitor of approximately 2μF (dependent on transformer design and circuit topology) is the most cost effective solution [36]. Further modelling in this chapter is therefore carried out with a minimum filter capacitance of 2μF.

Figure 6.6 shows the make up of the losses along one current path in the wind farm. This is typical of other current paths starting from the turbines on the left hand side of the wind farm as it is shown in Figure 4.7. All turbines are operating at full power and a filter capacitance of 2μF is used in each converter. The total area of the pie chart is proportional to the total allowable losses in each cable (so the white area in each pie chart represents spare capacity). The model uses cables at 90°C. The converter numbers refer to Figure 4.7.

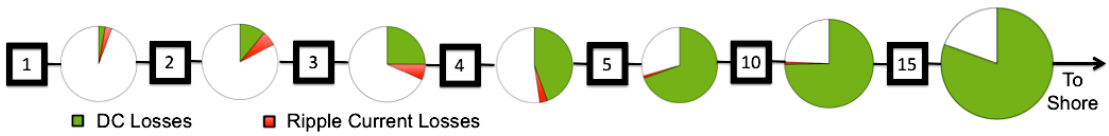

Figure 6.6. Make up and magnitude of losses (relative to total allowable losses) in a selection of cables simulated for switching case 3.

Again, it is noticeable that all the cables are well within their limits. The cables where the AC losses are greatest are lightly loaded with DC current, whereas in cables that are more heavily loaded with DC current, the AC losses are small.

Although it is clear that, in the case of the system being modelled, switching converters out of phase can be advantageous, it must be noted that this may not always be the case. The offset switching strategy, in effect, makes best use of the lightly loaded cables in the strings of turbines. The cables which join adjacent strings together are more heavily loaded with DC current and therefore it is important that large circulating currents do not flow here. In a larger wind farm, with more turbines connected to each string, only the cables at the periphery would be lightly loaded. For cables closer to the point of common connection, it would be necessary either to overrate the cables or to ensure significant circulating currents did not flow by switching the converters in phase. In practice, the cost of cables is much higher than filter capacitors so the solution would be to have the converters switch in phase and increase the size of filter capacitance. It would still be possible to offset switching in converters connected to lightly loaded cables, which would reduce the overall filtering requirements in the wind farm. Due to this consideration, the operation of converters in the DC grid switching in phase, as well as with phases offset, is considered as an option throughout.

6.1.3 Transmission Distance

In the cases where switching phases are offset, the ripple currents are largely contained within the collection network and the ripple in the transmission cable is small. In addition, with a filter capacitance of 2μF in each converter, the voltage *THD* at the sending end of the transmission cable is 0.28% in case 2 and 0.12% in case 3. However, with switching in phase, the ripple voltage and current in the transmission cable are significantly larger and dependent on the length of the cable.

The model was run with all converters operating at full power, switching in phase and each with a filter capacitance of 4.9μF. The results at 20ºC and 90ºC for a range of transmission distances are shown in Figure 6.7.

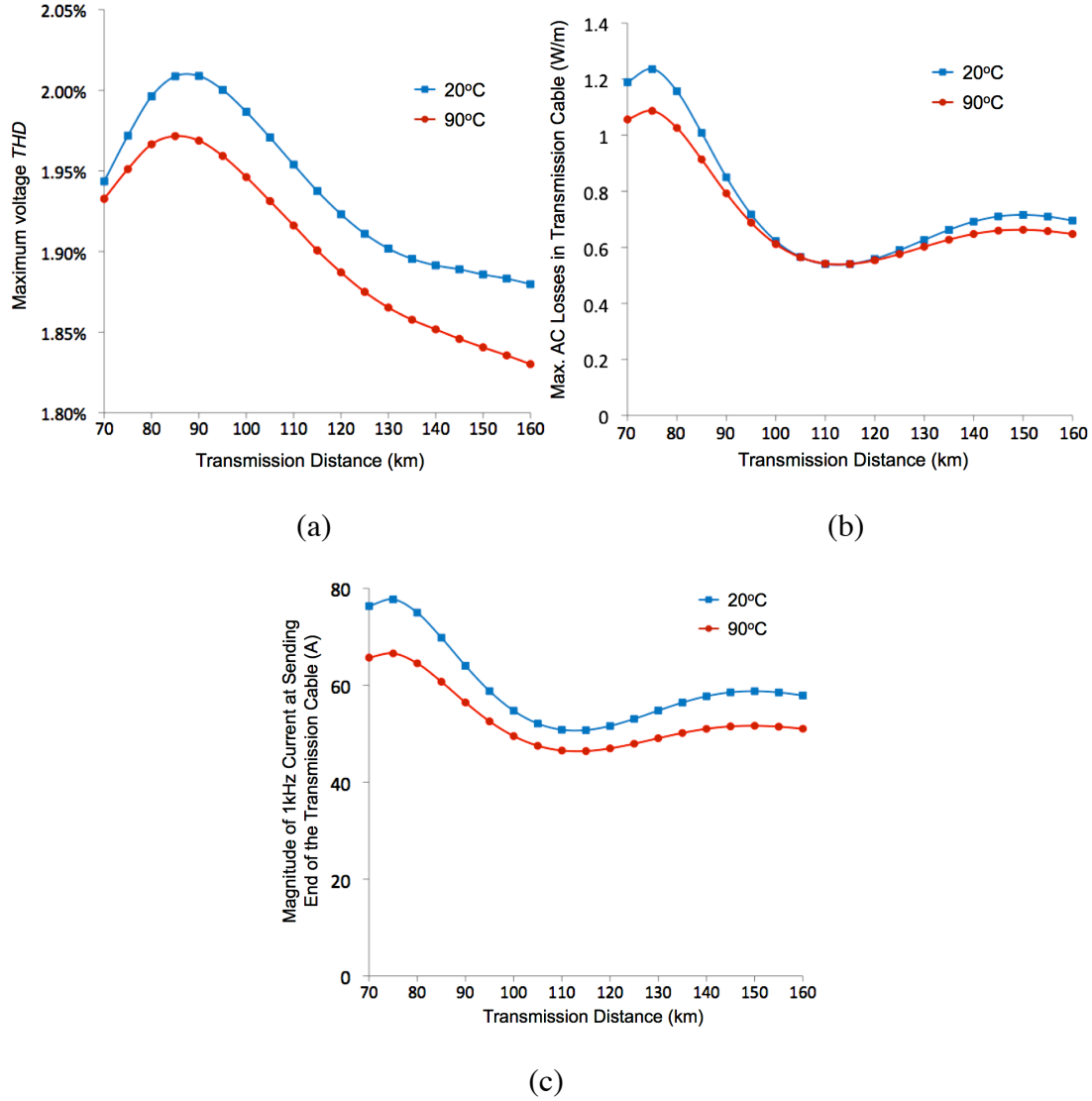

Figure 6.7. Simulated results for a range of transmission distances showing (a) the peak collection network voltage *THD*, (b) the peak loss in the transmission cable and (c) 1kHz current at the sending end of transmission cable.

The system voltage *THD* is not heavily dependent on the transmission distance. However, the size of the fundamental ripple current and, correspondingly, the AC losses in the transmission cable were both significantly affected by transmission distance. In order to explain these results, Figure 6.8 shows the components of cable admittance at 1kHz for the same range of transmission distances shown in Figure 6.7.

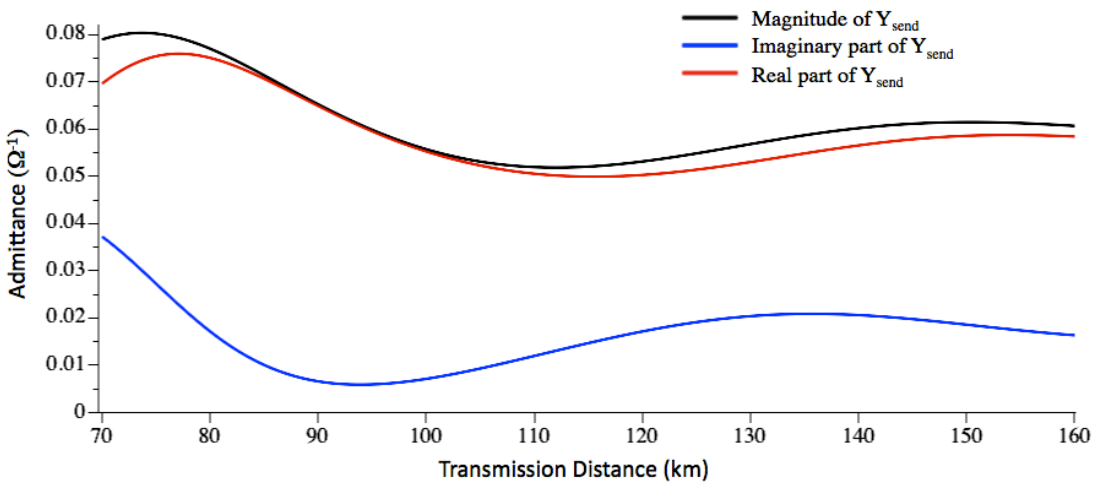

Figure 6.8. Components of transmission cable admittance simulated at 20°C for a range of transmission distances.

The *THD* is affected little by cable admittance because the filter capacitors in the converters throughout the collection network play the most important role in limiting voltage ripple. It is still possible to see a correlation between the peak in voltage *THD* and the minimum in the reactive (capacitive) component of cable admittance at around 90km.

The peaks and troughs in both AC losses and 1kHz current component correlate with the total transmission cable admittance. This is simply because, with the voltage ripple being similar in each case, the cable admittance is the defining factor for the magnitude of ripple current in the cable.

The limit on the losses in the transmission cable is 41.3Wm^{-1}. The 1kHz losses as a proportion of this range from 2.99% (75km) to 1.31% (110km) at 20ºC and from 2.63% (75km) to 1.31% (115km) at 90ºC.

6.1.4 Choice of Cable

In chapter 3, it was found that the parameters of the cable with copper screen vary significantly from the base case cable. In Figure 4.3, the impedance of the cable with

copper screen can be seen to be particularly low for a transmission distance of around 85km. Based on the analysis in section 6.1.3, this could lead to particularly high losses for this transmission distance.

Figure 6.9 shows the maximum AC losses in the transmission cable for the cable with copper screen compared to the base case cable.

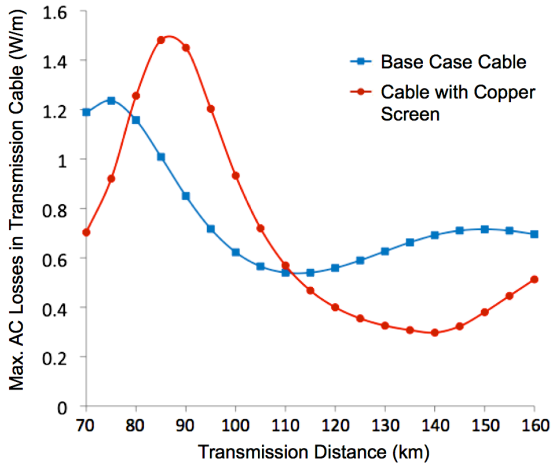

Figure 6.9. Maximum AC losses for two transmission cable types simulated at 20°C and a range of transmission distances.

In this case, the losses range from 3.59% (at 85km) to 0.72% (at 140km) of the allowable losses in the transmission cable. It can be seen that the choice of cable significantly affects the losses caused by the ripple current. To put these losses into context, it is assumed that losses caused by the AC ripple reduce the allowable DC losses by the same amount. Then, a reduction of 3.59% in the allowable losses for the transmission cable changes reduces the DC current limit in that cable by around 29A (from 1594A to 1565A). The current rating of the next size up of cable available in [46] is 1720A (core area 1600mm^2), an increase of 126A. Therefore, the ripple current losses have the potential to significantly affect cable rating calculations and must be considered when selecting the transmission cable.

6.1.5 Line Inductance

Two uses of inductors to manage current and voltage ripple were examined. First, the use of filter inductors on each of the converters and second, the use of a line inductor at the wind farm end of the transmission cable. A range of filter inductor sizes, used as a second stage filter on each converter, were considered. The addition of this inductance was found to:

- Be ineffective in limiting current ripple;
- Cause increased voltage ripple;
- In some cases result in extremely high currents due to resonance with capacitance in the system.

The description of the use of a line inductor at the wind farm end of the transmission cable follows.

6.1.5.1 Model Setup

In the case where switching of converters is in phase, the addition of a single line inductor at the start of the transmission cable was considered as a method of reducing the current ripple and voltage ripple in this cable.

The impedance from the wind farm end of a 100km base case transmission cable at 1kHz is 17.8-j2.30Ω, i.e. it is capacitive. Placing too small an inductor at the start of the cable will only cancel out some of its impedance and increase the ripple current it carries. At 1kHz, a 0.37mH inductor has an impedance of j2.30Ω, which would cancel exactly with the cable capacitance. Therefore, for the inductor to reduce current it needs to be over twice this value.

6.1.5.2 Results

A range of inductors starting at 1mH were modelled at the sending end of the transmission cable. The resulting current and losses in the transmission cable are shown in Figure 6.10.

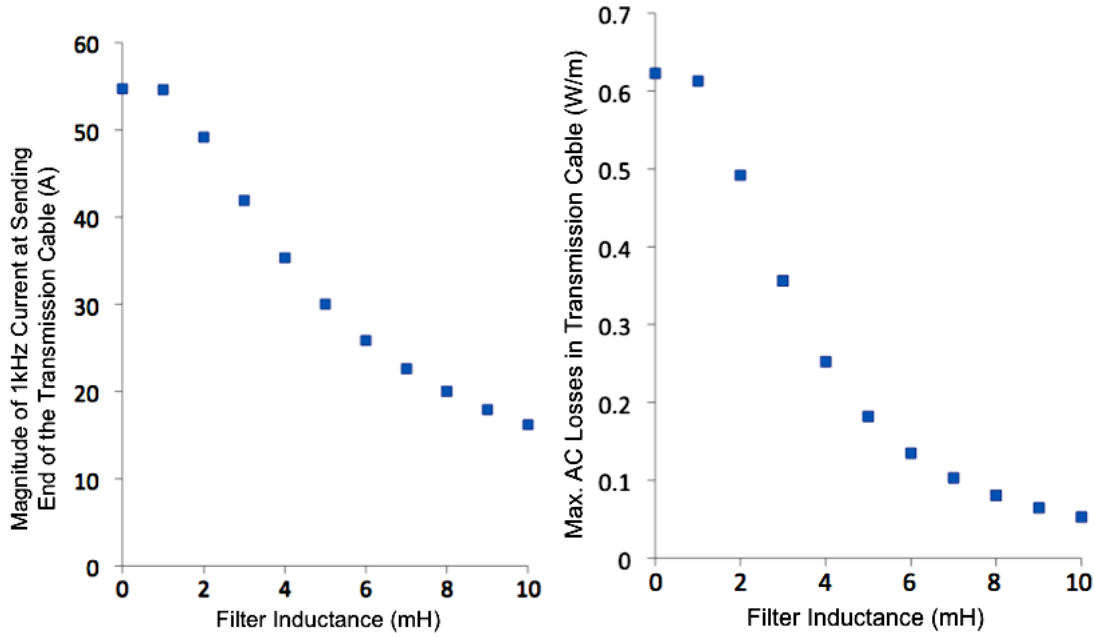

(a) (b)

Figure 6.10. Simulated effect on (a) ripple current content and (b) AC losses in transmission cable 100km in length of a range of smoothing inductors installed at the sending end.

The line inductor is an effective method of reducing ripple current and losses in the transmission cable. In the case shown here, a 10mH inductor reduces the peak losses in the transmission cable from 0.62Wm^{-1} to 0.053Wm^{-1}, a reduction of over 90%.

The effectiveness of the line inductor depends on the cable impedance, which in turn depends on transmission distance. As stated, the 100km cable considered above has an impedance of 17.8-j2.30Ω. The equivalent 70km cable (for example) has an impedance of 11.2-j5.97Ω. In this case, a larger inductance is required to cancel out the capacitive reactance of the cable. On the other hand, because the magnitude of the cable impedance is lower, the proportion by which a 10mH inductor (with impedance 62.8Ω at 1kHz) reduces the AC losses is greater than in the case of the

100km cable. A reduction from 1.19Wm^{-1} to 0.064Wm^{-1} is achieved for a 10mH inductor.

The line inductor also reduces the voltage ripple in the cable. With no inductor, the maximum voltage *THD* in the cable is 1.92%; with the 10mH inductor, this is reduced to 0.56% (for 100km transmission distance).

Reducing the ripple current in the cable not only reduces losses, but also reduces the possibility of AC corrosion occurring. Based on the results of the study in [53], as discussed in section 2.6.3.5, this is particularly important where it is necessary to suspend the cable above the seabed due to the water depth or the seabed geography. In this situation, the cable will be subject to tensile forces that the armour will be required to withstand throughout the cable's lifespan and so protecting against corrosion is a high priority.

The possibility of resonance caused by the line inductor must be considered. The results show no resonance at the ripple frequencies. At AC grid frequency (50Hz), the value of line inductance is relatively small compared to the cable inductance. For example, the base case transmission cable has inductance of 4.16x10^{-7}Hm^{-1} at 50Hz, so for 100km the inductance (which is not significantly altered by the effect of wave propagation) is 41.6mH. The line inductor does not, therefore, make a large difference to the low frequency resonance, although it would need to be accounted for when calculating the resonant frequency.

Finally, it must be noted that such a line inductor, rated for the full load current and operating at 50kV, would be a large and heavy component (also, one would be required for each pole). Designing it to fit in a wind turbine (since there is no offshore substation), could be a difficult task.

6.1.6 Wind Turbine Power Output and Disconnection

The power output from the turbines will not be uniform. While offshore wind is generally less turbulent than onshore, variations caused by, for example, the wake effect are important. [16] includes modelling and actual measurements from the Horns Rev wind farm showing the magnitude of the wake effect, which is especially strong when the wind direction is in line with a row of turbines. Reducing the power output from a converter also reduces the absolute value of its ripple content. This results in significant AC currents flowing between adjacent turbines even if they switch in phase. Additionally, in strong wind conditions, turbines will shut down above a certain wind speed. Due to the wake effect and other factors affecting localised wind speed, not all turbines will shut down at the same time. In the cases where converter switching phases are offset, this will affect the cancellation of ripple currents and voltages, given that the switching phases of the turbines that shut down are unlikely to be balanced. Turbines will also need to be shut down on occasion for maintenance or repair. In the case of a fault in a wind farm cable, some turbines will be disconnected completely until the fault is repaired.

There are a vast range of permutations of the above scenarios. Many of these were modelled and results for the 'worst case scenarios' based on reasonable assumptions for what may happen in an actual wind farm are presented here.

6.1.6.1 Model Setup

A transmission distance of 100km was again modelled. For switching phase offset cases 2 and 3, a 2μF capacitor was modelled at each converter.

6.1.6.1.1 Wake Effect Modelling

The wake effect was modelled with prevailing wind direction either along a straight or diagonal line of turbines. The turbine closest to the wind direction in each case was modelled at full power and the turbines behind it with decreasing output as shown in Table 6.3.

Turbine Position Relative to Wind Direction	Power Output
First	100%
2nd	70%
3rd	67%
4th	63%
5th	60%

Table 6.3. Reduction in output power caused by wake effect with wind direction aligned to a line of turbines [16].

6.1.6.1.2 Turbines Switched off for Strong Winds

In this case, it was modelled that either a number of horizontal or vertical rows of turbines were switched off. Alternatively (when testing the effect on case 3) a triangular section of turbines (either 1, 3, 6, 10 or 15 turbines) starting at one corner were switched off.

Since switching off a turbine in strong winds is no indication of any malfunction, it was assumed that the filter capacitor can safely remain connected to the network. It was found that by keeping the capacitor connected, particularly in the cases where the turbines have their switching phases offset, that the voltage ripple in the system remains lower in worst case conditions. In order to enable the capacitor to remain connected, a second isolator/switch is required (i.e. one each side of the capacitor); this has a cost penalty. Whether it is necessary in all situations to keep the capacitor connected is discussed in chapter 8.

6.1.6.1.3 Turbines Disconnected from the Grid

In this case, converters and their filter capacitors were modelled as being completely disconnected from the DC grid. The most extreme case was in simulating the loss of a section of the wind farm due to a fault in one of the collector cables.

6.1.6.2 Results and Analysis

A selection of the most significant and important results are presented here. Further results are given in Appendix E.

It was found that, of the scenarios modelled, the wake effect made least difference to the system operation. This is because, in terms of the losses, where there was some increase in circulating currents, it was more than balanced by the reduction in DC losses. In terms of the voltage ripple, the wake effect has less impact than fully turning off a number of turbines.

Modelling turbines switching off for strong winds increased the voltage *THD* in the cases where switching phase is offset. For case 2, the highest *THD* was 1.71%, which resulted from the shut down of three vertical rows of turbines on the right of the wind farm as shown in Figure 4.7 (i.e. turbine numbers 3, 4, 5, 8, 9, 10, 13, 14, 15, 18, 19, 20, 23, 24, 25). For Case 3, the highest *THD* was 1.25%, which resulted from the shut down of a 6 turbine triangle at the bottom right of Figure 4.7 (i.e. turbine numbers 15, 19, 20, 23, 24, 25).

In the case where switching is in phase, reducing the power output or switching off turbines was found to reduce cable losses and voltage *THD*. Disconnecting turbines did increase the voltage *THD* slightly, due to the loss of distributed capacitance. The worst case was to simulate a fault in the cable connecting turbines 15 and 20, resulting in the disconnection of 10 turbines. In this case, the required filter capacitance to achieve the target of 2% voltage *THD* increased from 4.9μF to 5.1μF.

In general, the case where the converters switch in phase was found to be the least affected by the range of operating conditions. This is mainly because this case requires larger values of filter capacitance to begin with, so the hardware in the system is more robust. The cases where the switching phases are offset also performed well, in particular case 3, and this case requires only the minimum filter capacitance of 2μF.

6.2 Application to other Converter Designs

The design principles developed were applied to the other three converter configurations. It is useful to begin by showing the frequency domain components of the unfiltered DC current of each converter. Table 6.4 shows the first five frequency components for the single-phase converters and Table 6.5 shows the three-phase converters.

Frequency (kHz)	SLR Converter Magnitude (A)	Phase Shift Converter Magnitude (A)
DC	60.00	60.00
1	32.12	46.00
2	10.53	21.46
3	6.28	12.70
4	4.43	8.01
5	3.37	5.05

Table 6.4. Frequency components of unfiltered HVDC current for simulated single-phase converters.

Frequency (kHz)	3-Phase SLR Converter Magnitude (A)	3-Phase Voltage Source Inverter Magnitude (A)
DC	60.00	60.00
3	4.46	3.43
6	0.77	0.84
9	0.43	0.37
12	0.24	0.21
15	0.12	0.13

Table 6.5. Frequency components of unfiltered HVDC current for simulated three-phase converters.

It is clear that the current and voltage ripple output from the three-phase converters require much less filtering than for the single-phase converters.

6.2.1 Results and Analysis

Table 6.6 shows the voltage *THD* for each converter with two switching strategies, operating at full power and operating in the worst case scenario for that strategy. The

capacitance is either the minimum of 2μF, or the value required to limit the *THD* to 2%.

		Single Phase SLR		Phase Shift		3-Phase SLR		3-Phase Voltage Source Inverter	
		C_{dc} (μF)	Max. Voltage THD	C_{dc} (μF)	Max. Voltage THD	C_{dc} (μF)	Max. Voltage THD	C_{dc} (μF)	Max. Voltage THD
Switching in Phase	Full Power	4.9	1.99%	7.6	1.98%	2.0	0.23%	2.0	0.18%
	Cable 15=>20 Disconnected	5.1	1.99%	7.9	1.99%	2.0	0.24%	2.0	0.19%
Switching Offset Case 3	Full Power	2.0	0.52%	2.0	0.89%	2.0	0.23%	2.0	0.17%
	Turbines 15, 19, 20, 23, 24, 25 Off	2.0	1.25%	2.0	1.74%	2.0	0.26%	2.0	0.20%

Table 6.6. Maximum collection network voltage *THD* for simulated DC grids constructed with each type of converter for a range of operating conditions.

The increased harmonic content of the phase shift converter leads to higher filter requirements when switching is in phase than for the single-phase SLR converter. However, with the switching phase offset as in case 3, the minimum capacitance of 2μF is adequate. The three-phase converters produce very little ripple in comparison to the single-phase converters and this is reflected in the low *THD* with the minimum 2μF capacitor installed.

With the system operating at full power, Figure 6.11 shows the maximum losses at any point in the transmission cable and in any cable in the collection network. Note that some results for transmission cable losses are practically zero (although not actually zero) and so do not show up on the graphs.

The high harmonic content of the unfiltered DC waveform in the phase shift converter is again reflected in the results. In particular, when switching phases are offset, the circulating currents in the collector cables are higher than for the single-phase SLR converter. The three-phase converters produce much lower AC cable losses than the single-phase converters. The only losses of comparable magnitude are caused by the circulating currents when switching phases are offset.

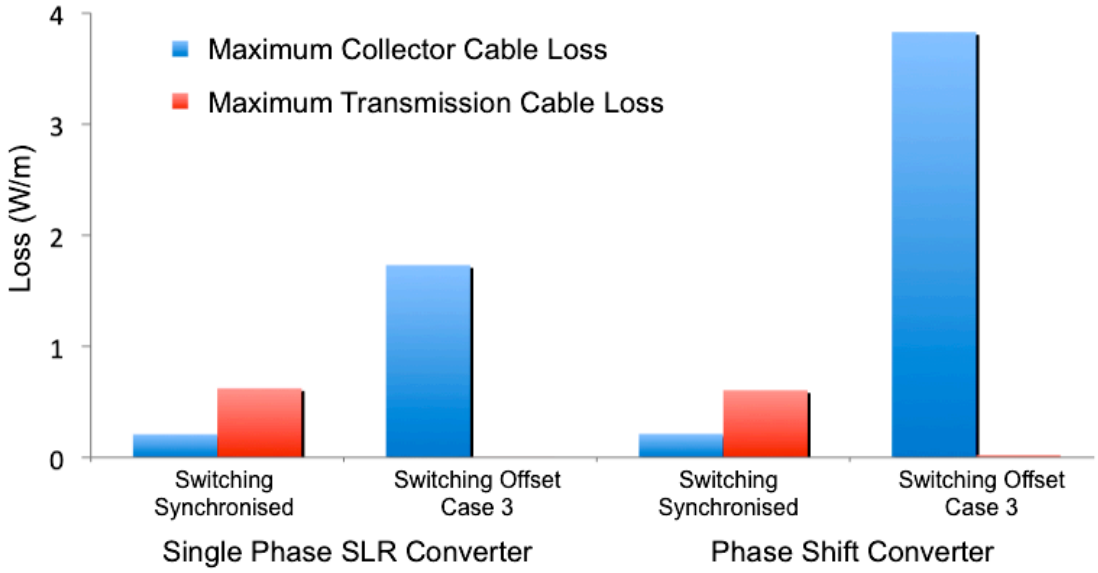

(a)

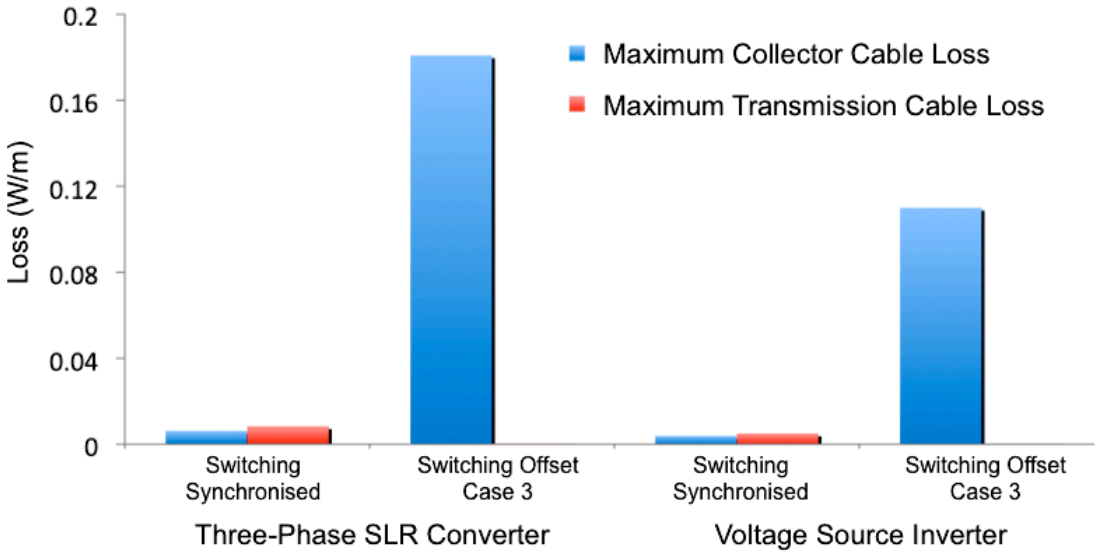

(b)

Figure 6.11. Ripple current losses and where they occur for the simulated DC grid constructed with each converter type, operating at full power. (a) Single-phase converters, (b) three-phase converters.

Overall, of the single-phase converters, the ripple currents and voltages generated by the phase shift converter cause larger losses and require greater filtering than the SLR converter. The three-phase converters produce a much smaller ripple and

offsetting their switching phases does not give a significant advantage over switching the converters in phase.

6.3 Overall Power Flow Losses

Up until now, system losses have been considered only with respect to their influence on cable choice. In this section, the losses caused by both load current and ripple current in the collection and transmission system are analysed.

6.3.1 Results

The models developed in previous sections were used to calculate the system losses under various load conditions. The results are shown in Table 6.7.

Converter	Single Phase SLR		Phase Shift		Three-Phase SLR		Three-Phase VSC	
Switching Phases	In Phase	Offset Case 3	In Phase	Offset Case 3	In Phase	Offset Case 3	In Phase	Offset Case 3
C_{dc} (μF)	5.1	2	7.9	2	2	2	2	2
Total Collection and Transmission Losses (MW)	5.58	5.56	5.57	5.60	5.52	5.53	5.52	5.53
Losses as % of Wind Farm Power	3.72%	3.70%	3.72%	3.73%	3.68%	3.68%	3.68%	3.68%
Ripple Current Losses as % of Total Losses	0.93%	0.56%	0.90%	1.32%	0.01%	0.03%	0.01%	0.02%
Collection Network Losses as % of Total Losses	3.58%	4.13%	3.58%	4.83%	3.59%	3.62%	3.59%	3.61%

Table 6.7. Breakdown of total system losses when operating with cables at 20°C for the simulated DC grid constructed with each converter type, at full power.

The losses in the system are predominantly caused by the DC current. In addition the losses in the transmission cable far outweigh those in the collection network. This is explained by the fact that the transmission cables are 100km long compared to total of 14.4km for the collection cables. In addition, the losses per km are lower in the collection network, due to the many lightly loaded cables as seen in Figure 6.6.

The modelling with the single-phase SLR converter was repeated with the cable temperature at 90ºC. This increased the total losses at full power to 6.94MW, i.e. 4.63% of the total wind farm output power.

Operating the same model setup with the wind farm at 50% power (i.e. all turbines at 50% power), this time with the cable temperature at 20ºC, reduced the losses to 1.44MW, i.e. 0.96% of total output power. The losses are approximately a quarter of those at full power. This is because the useful power generated is proportional to the current, while the cable losses are proportional to the current squared.

Further assessment of system losses, including financial impact and comparison with an equivalent AC system, is undertaken in chapter 7.

6.4 Chapter Summary

This chapter has demonstrated the practicality of the offshore wind farm DC grid operating in steady state conditions. The four different converter designs have been compared. It has been demonstrated that a combination of filter capacitance and control of converter switching phase is sufficient to maintain the system within the chosen current and voltage ripple limits. Furthermore, it has been shown that for all converters in the considered grid layout, a 2μF filter capacitor is adequate to meet the ripple limits, which allows the use of film rather than electrolytic capacitors.

7 Practical Aspects and Further Development of the DC Network

In the previous chapter, the viability of the DC grid based on DC-DC converters was demonstrated. This chapter moves on to examine further topics including:

- The performance of the DC grid in comparison with the AC alternative;
- The limitations of the DC grid;
- Grid behaviour under fault conditions and recommended protection measures;
- Alternative converter configurations.

In addition, more emphasis is placed on the cost implications of the design decisions, as well as the technical challenges and constraints. In all cases, while it is useful to estimate costs in order to put each part of the system into context, the costs given here are only intended to be indicative and are subject to change over time.

7.1 Fault Current and Protection Measures

Due to the lack of the natural current zero crossing that is present in AC systems, fault current in DC systems is difficult to break. In addition, in a system with significant DC link capacitance or filter capacitance connected to the DC Cable, a pole to ground or pole to pole fault in that cable results in the energy from the capacitor rapidly converting into fault current in the cable. After the discharge of the capacitance, that fault current will then freewheel through the high voltage diodes, sustained by the cable inductance, which can damage the diodes. The discharge of the capacitor itself results in a one off surge current and this must be limited in accordance with the rating of the capacitor. [38, 86]

In general, it is advantageous to use as small a capacitor as possible, as this reduces the amount of energy available to flow into any fault. In the case of the single-phase converters, it is therefore preferable to use a switching strategy that offsets converter phases and reduces the required value of C_{dc}.

7.1.1 Limiting the Capacitor Current in the Event of a Fault

The construction of the HV filter capacitance may require a number of capacitors in parallel and/or series in order to achieve the desired size and voltage rating. Based on film capacitors available from [38], two indicative surge ratings were derived for two different capacitance values. First, a 0.5μF, E51 capacitor rated at 50kV with a surge current rating of 8.7kA is available. Connecting four of these in parallel would provide the required minimum of 2μF. The total surge current that this arrangement could tolerate is 34.8kA. The second case is the 10μF, 25kV, E51 capacitor with a surge current rating of 12.9kA. Connecting two of these in series would give 5μF at a rating of 50kV. The surge current rating would be 12.9kA.

The simplest solution to limit the current is to place a resistor in series with the filter capacitors, sized to limit the surge current at 50kV. In the first case, a 1.5Ω resistor would suffice (this would be a single resistor connected after the point of common coupling of the capacitor currents). In the second case, a 3.9Ω resistor would be adequate.

The effect of this resistor on system operation was tested for two cases where the system is close to the limit on voltage *THD*.

- The single-phase SLR converter with switching in phase, operating at full power. This arrangement requires a 4.9μF capacitor and therefore a 3.9Ω resistor was modelled.
- The phase shift converter with switching phases offset as in case 3, operating with a corner of turbines (turbine numbers 15, 19, 20, 23, 24 and 25 as shown

in Figure 4.7) producing no power. This arrangement requires a 2μF capacitor and therefore a 1.5Ω resistor was modelled in series with this capacitance.

It was found that the inclusion of the resistor resulted in very little change in system behaviour. In the first case voltage *THD* was reduced from 1.99% to 1.97% and in the second from 1.74% to 1.71%. The small change is explained by the magnitude of the resistance in comparison to the reactance of the filter capacitor which, for a 2μF capacitor at 1kHz, is -j79.6Ω.

7.1.2 Modelling the Collection Network in Fault Conditions

This section examines the behaviour of the collection network in the event of a short circuit. The operation of the low voltage side of the converters is not considered. The SLR converters (single- and three-phase) and the phase shift converter require protection measures to limit damaging currents and/or voltages on the low voltage side. These measures will limit the amount of energy that is fed into the fault from the low voltage side to a level that can be reasonably neglected in this section. The effect the fault has on the onshore converter is not considered, as this will require specific protection measures.

Although DC circuit breakers have recently become commercially available, these devices are large and potentially expensive [36, 87]. The modelling examines whether fault levels can be managed without such devices.

As discussed in [86], there are several stages following a fault in the type of DC system modelled in this thesis. The modelling concentrates on finding the size of the initial surge current and deciding what measures are necessary to keep this within limits. Based on [64, 88], estimated surge current ratings of the cables and diodes are as listed below:

Cable 1:	Core: 13.8kA	Lead Sheath: 4.03kA
Cable 2:	Core: 43.5kA	Lead Sheath: 6.64kA
Cable 3:	Core: 202kA	Lead Sheath: 15.1kA
HV Diodes:	10kA	

For the cables, the surge current limits are for a one second duration. For the diodes, the fault current is divided between the two or three branches of the rectifier. Some care must be taken as diodes do not necessarily share current equally.

7.1.2.1 Cable FEM Modelling

As is the case for ripple currents, the time-varying fault current in the core induces currents to flow in the outer metallic layers of the cables. Due to the relatively low fault current rating for the lead sheath in each cable (when compared to that of the core), it is necessary to evaluate the amount of sheath current that results from a fault. The sheath current depends on both the magnitude and rate of change of current in the core. Additionally, the values of cable resistance and inductance, which are required to model fault propagation, depend on the magnitude and rate of change of core current. The FEM models developed in chapter 3 were used to calculate the cable parameters and induced currents in the cable outer layers.

The modelling of a fault in the 25 node DC grid is extremely complex. In order to calculate exact values for the cable parameters, it is necessary to know the current and voltage transient in each cable (and actually at each point in each cable at each point in time) in the system. In turn, to find the value of fault current and voltage, it is necessary to know the cable parameters everywhere in the system. Consequently, it has been necessary to make some approximations, as are described.

The base case cables in the collection network (cable 1 and cable 2 as described in chapter 3) were modelled with the fault current rise approximated to a ramp function,

i.e. a constant rate of current rise for a fixed period of time. The results are shown in Figure 7.1.

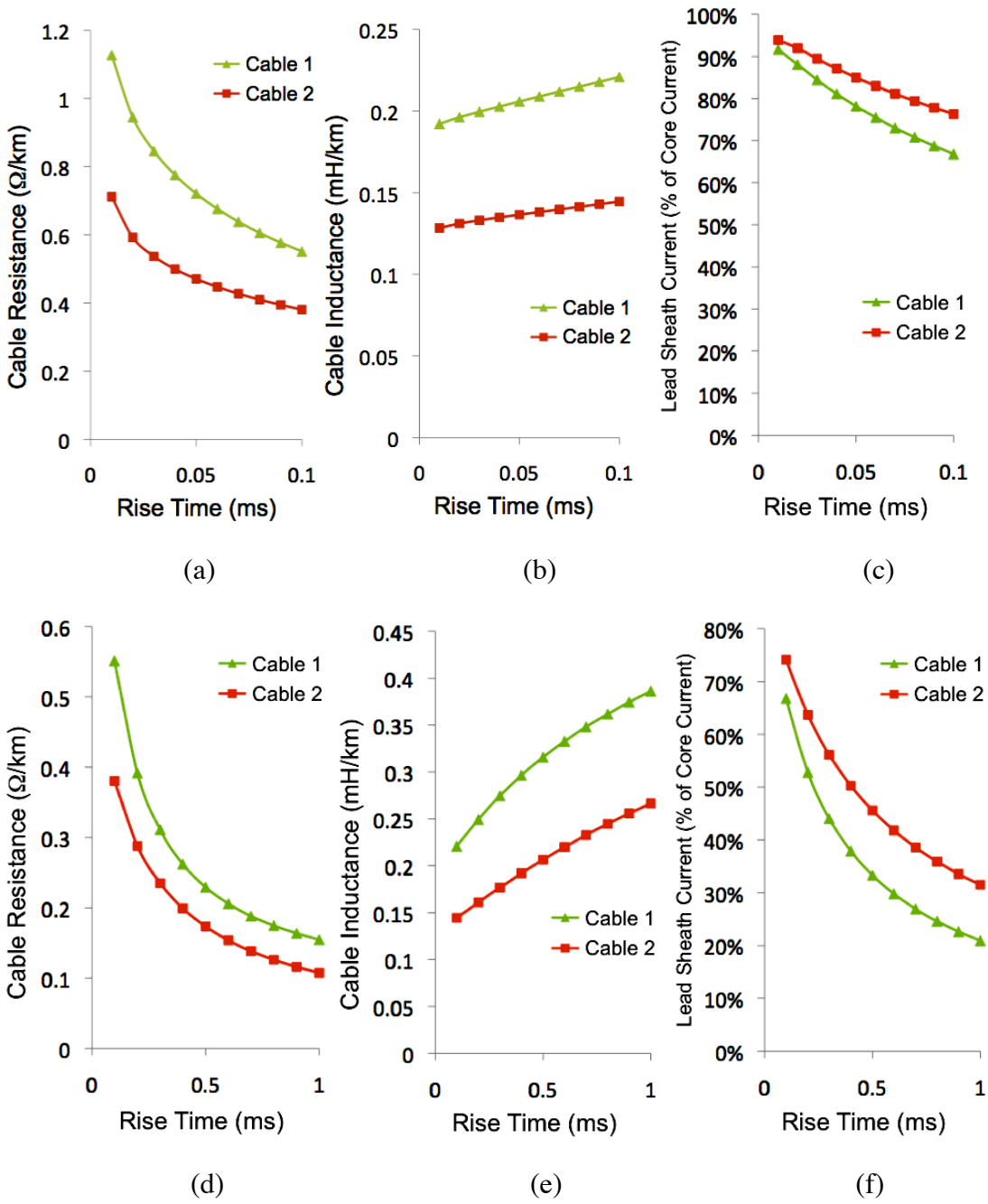

Figure 7.1. Collection network cable parameters (a, b, d, e) and lead sheath current (c, f) simulated under fault conditions for a range of d*i*/d*t*.

The shapes of each curve are as expected. Resistance and lead sheath currents are larger for short rise times due to increased skin effect and induced currents caused by

the high d*i*/d*t*. Inductance reduces with shorter rise times for the same reasons. The results are used in the following sections.

7.1.2.2 Single Converter Modelling

It is useful to begin the analysis with a single converter. The resistance of the fault is modelled as zero. The current flowing in the cable just before the fault is neglected.

The discharge of the HV filter capacitor and resulting current rise can be analysed by reducing it to the circuit as shown in Figure 7.2 [86]. *C* is the size of the filter capacitor. *L* is the inductance in the circuit including the subsea cable and the inductance in any cabling in the turbine tower connecting the converter to the subsea collector cable. *R* is the resistance of the aforementioned cables added to the capacitor *ESR* and any protective resistance placed in series with the capacitance.

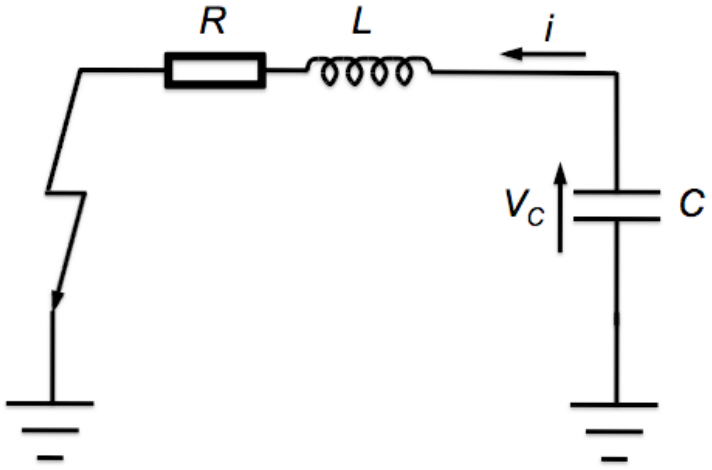

Figure 7.2. Equivalent circuit for discharge of filter capacitor into short circuit fault.

Approximating *L* and *R* to being constant values, equation (7.1) describes the initial discharge current of the filter capacitor. This equation is only valid while the capacitor discharges. Subsequent stages of the fault are not considered here (as the peak current from the initial discharge is not exceeded), but once the capacitor has discharged, the current sustained by the cable inductance can cause it to recharge to a lower voltage level than 50kV and an oscillation can follow. More details are given in [86] (for example).

$$\frac{d^2i}{dt^2} + \frac{R}{L}\frac{di}{dt} + \frac{i}{CL} = 0 \tag{7.1}$$

Equation (7.1) was used to model the discharge current for a converter feeding into a 600m length of cable type 1 with a short circuit at the end. There is an iterative process to this solution, as first the cable parameters must be estimated in order to obtain the rise time for the ramp function, which in turn gives more accurate cable parameters and so on. The final parameters for the model were:

- $C_{dc} = 2\mu F$
- Protective Resistor = 0
- Cable Inductance = 0.20mH/km
- Cable Resistance = 0.91Ω/km

The solution to equation (7.1) is:

$$i(t) = 6459e^{-2275t}\sin(4.16\times10^9 t)$$

The resulting fault current and capacitor voltage waveforms are shown in Figure 7.3. The results were verified using a Simulink model. The peak current was found to be the same value within <0.1% and the time of the peak current within <0.5%.

The peak current is 6.1kA, which is within the one second limit for the cable core. Given the rise time for the fault current, the peak sheath current is expected to be 86% of the core current, i.e. 5.2kA. This is over the rated value for the cable sheath. However, the current is very short lived, due to the small amount of inductance in the cable. The cable ratings are based on the amount of energy dissipated in the cable and therefore, if the current is short lived, a higher value can be tolerated. Although it is necessary to consult cable manufacturers for a rating that accounts for the shorter period of time, an estimate is that the rating can be divided by the square root of the time (in seconds) for which the fault current flows. This is equivalent to maintaining

the value of i^2t constant for faults of varying lengths of time. The approximation is valid for times of roughly 0.1s and larger. For a fault current that lasts 0.1s, the sheath rating is estimated to be 12.7kA. In the example here, the duration of the fault current is of the order of milliseconds.

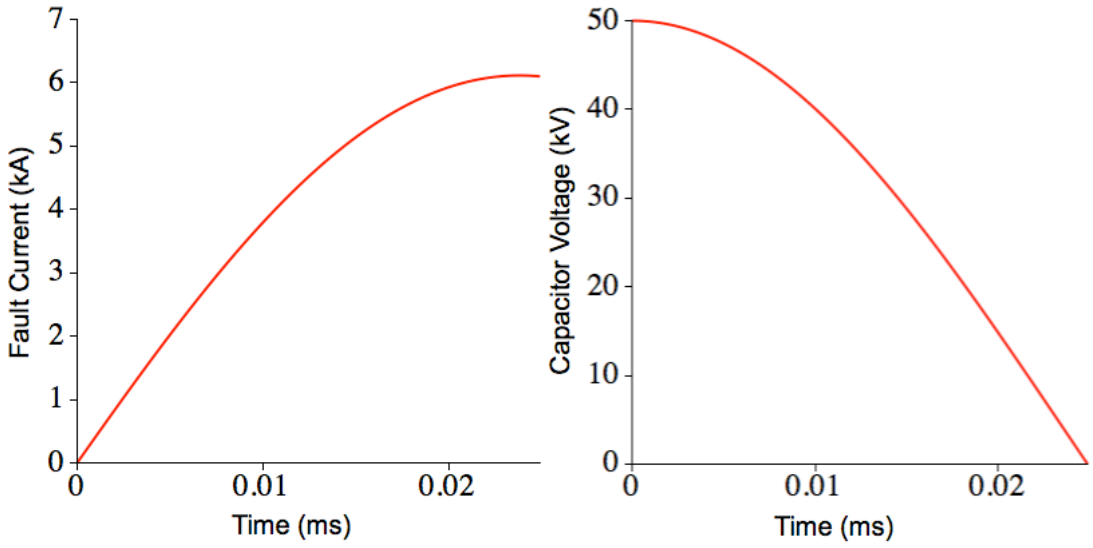

(a) (b)

Figure 7.3. (a) Fault current and (b) capacitor voltage waveform calculated during discharge of high voltage filter capacitor into 600m of collection network cable terminated in a pole to earth fault.

7.1.2.2.1 Mitigation

In the case considered above, the inductance in the 600m of cable limits the rate of rise of the fault current. Were the fault to occur close to a wind turbine, then this rate of rise would be increased, as would the value of the fault current. Although the current would flow for only a very short amount of time, it would be necessary to consult cable manufacturers on the limit for such a current.

In cases where mitigation is necessary, the current could be limited by a resistor placed in series with the HV filter capacitor, just as is required to protect the capacitor itself. Due to the very short rise time, the lead sheath current is close to

100% of the core current, as can be seen from Figure 7.1(c). A 14Ω resistor would be sufficient to limit the current spike in the lead sheath to below 4kA (its 1s rating).

The effect of this additional resistance on the voltage ripple in the DC grid was modelled. The same scenarios as in 7.1.1 (SLR converter and phase shift converter) were modelled. In the first, the 14Ω resistor increased the *THD* from 1.99% (with zero resistance) to 2.06%. In the second case the *THD* was reduced from 1.74% to 1.59%. The losses in the resistors were also calculated and found to be highest in the first case (SLR converters switching in phase) at 72.4kW when operating at full power. To put this in context, it represents 1.3% of the total cable losses. For converters switching with offset phases or for three-phase converters, the losses are much less due to (respectively) cancellation of ripple currents and lower *THD*.

When deemed necessary, the protective resistor is a simple way of limiting the fault current in the cable, as well as the surge current in the capacitor.

7.1.2.3 Network of Converters

The Simulink model used for verification in the previous section was developed to model the fault current in the entire DC collection network. It was found that the fault location that resulted in the largest current relative to the cable rating was in the cable connecting turbine numbers 14 and 15 (as shown in Figure 4.7), close to turbine 15. The reason is that this cable has a relatively low current rating and a fault in this location can be fed (from the direction of turbine number 15) by 21 converters in the grid.

A 14Ω resistor is included in series with the filter capacitor in the following modelling. Initially, the model was run with the parameters shown in Table 7.1. The fault current flowing in the faulted section of cable is shown in Figure 7.4.

High Voltage Filter Capacitance	2μF	5μF	10μF
Cable Type 1 Resistance (Ω/km)	0.65	0.55	0.49
Cable Type 1 Inductance (mH/km)	0.21	0.22	0.23
Cable Type 2 Resistance (Ω/km)	0.44	0.38	0.34
Cable Type 2 Inductance (mH/km)	0.14	0.14	0.15
Peak Current (kA)	19.3	26.8	32.8
Peak Lead Sheath Current (kA)	13.9	17.4	19.4

Table 7.1. Cable parameters and peak fault currents in the cable core and lead sheath simulated during a short circuit fault at the 'worst case' location for a range of values of high voltage filter capacitance.

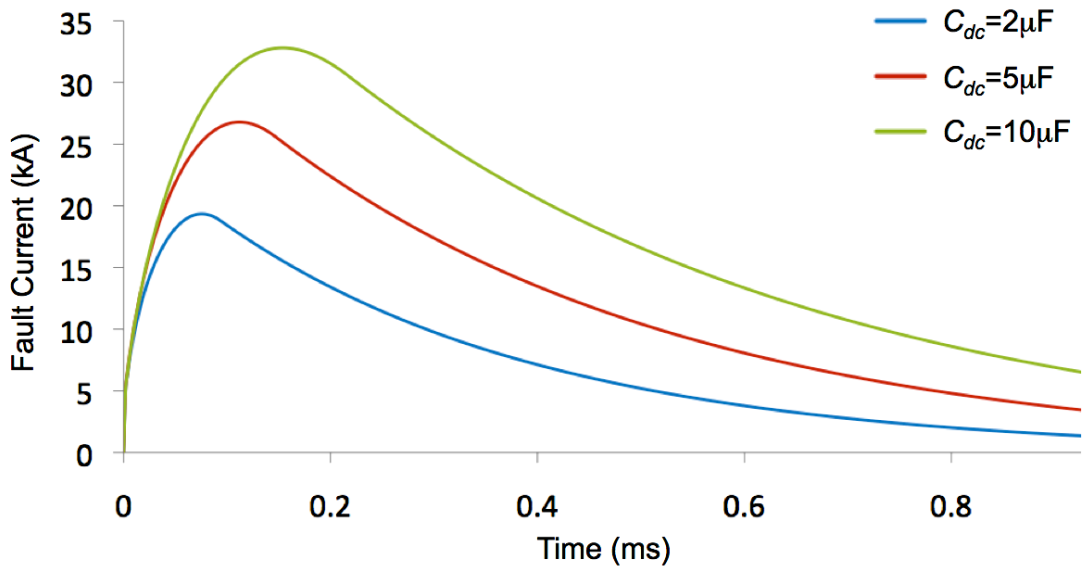

Figure 7.4. Fault current waveforms simulated in the faulted cable section corresponding to the results in Table 7.1.

The peak fault current is dependent on the size of the HV filter capacitance. This is understandable, as the energy in this capacitance depends on its size, which correlates to the energy in the cable inductance and hence the size of the current resulting from a fault.

There is a very steep initial rise up to around 5kA. This is caused by the filter capacitor in converter 15 discharging into the short section of cable between it and the fault; it is limited by the resistor in series with C_{dc}. The peak currents in the core are within the limit for its surge current, once this limit has been adjusted to a period

of 0.1s. For the sheath, the currents for all three capacitor sizes are above its corresponding rating. However, these currents are once again very short lived and consultation with cable manufacturers should be carried out to establish whether they can be tolerated by the cable.

7.1.3 Section Summary

Although there are some areas in which consultation with cable suppliers will be necessary, the energy dissipated by the fault currents resulting from the discharge of the HV filter capacitors in the DC grid is well below the energy which the cables can tolerate for a longer duration fault. If necessary, the addition of a protective resistor in series with the HV filter capacitor can limit the magnitude of the current. It was found that this resistor (up to the tested size of 14Ω) has very little negative impact on system operation and losses.

It should also be noted that the resistance of the fault path to earth has been neglected in these calculations. This resistance will further limit fault current magnitude and dissipate energy from the fault, reducing energy dissipation in the cable and causing the current to fall more quickly.

7.2 Cable Costs, Losses and Comparison with AC System

Note that in this section, when referring to AC systems, RMS values of current and voltage are used.

Advantages of DC transmission over AC for long distances, especially offshore, are well understood. However, the novel DC solution proposed here is considered a viable alternative for close to shore wind farms. The use of DC is not generally considered cost effective for short distances due to the power electronic converter capital costs. However, in the case of the proposed system, the capital costs of the power electronics need not be greater than for the AC alternative. In particular, in

comparison to a wind turbine with fully fed converter producing 50Hz AC output, the change to the DC converter topology described in section 5.1.4, based on the VSC feeding a 500Hz transformer and rectifier, does not necessarily increase costs. The main differences between the AC and DC topologies in this case are:

- DC topology uses a 500Hz transformer, which reduces size compared to 50Hz;
- Low voltage side 500Hz current and voltage are higher in harmonics due to reduction in the number of switching events in each cycle, this increases filter requirements;
- The addition of HV diodes, filter capacitor and protective resistor in the DC case.

Since the transformer is a very large component (especially at 50Hz), it is not clear which solution is most cost effective. Assessment of this is an item for further work. Similarly, assessing the cost implications of replacing part or all of the fully fed converter topology with a DC-DC converter requires further research.

Therefore, this section considers a range of sizes of wind farms both near to and far from shore. Cable losses in an AC system are calculated for comparison with the DC system and the cable material and laying requirements are also assessed. The AC system is modelled with the collection network operating at 33kV and the transmission cable at 132kV. The step up in voltage necessitates the use of an offshore substation (as discussed in section **Error! Reference source not found.**), with an estimated cost of £14M for a 150MW substation.

7.2.1 AC Cable Modelling

Each section of cable was chosen according to its required ampacity. For a single converter operating at full power (6MW), the current per phase at 33kV is 105A. It was necessary to change the layout of the cables in the wind farm. In the previous

design, cables feeding from nodes 10 and 20 into node 15 (the point of common coupling, as shown in Figure 4.7) carried the power from 10 turbines. In the AC system, this would require a cable ampacity of 1050A. A three core cable with copper conductor size of 300mm^2 has an ampacity of 530A, while the same design with cores of 1000mm^2 has ampacity of 825A [48]. It therefore makes more sense to connect each string of 5 turbines directly to the PCC, even though this requires longer cables from the two more distant turbine strings. Therefore, the cables in the collection network range from a required ampacity of approximately 105A/phase to 525A/phase (neglecting reactive power flow).

In the transmission cable, charging current must be taken into account. Initially, to account for the fact that the DC grid is a possible solution for wind farms close to as well as far from shore, this is neglected.

Cable designs were based on three core cables available in [48, 85]. The details of the five cable types used are shown in Table 7.2. The smallest available cable at 33kV appears to be with cross-sectional area of 50mm^2 (per core) and ampacity of 211A (per phase). Based on the data in [48, 85], the core filling factor was found to be in the range of 90-95%. Rather than modelling each strand in the core, this figure was approximated to 100%.

Operating Voltage (kV)	33	33	33	33	132
Core Cross-sectional area (mm^2)	50	120	185	300	630
Inner Insulation thickness (mm)	8	8	8	8	18
Metallic Sheath Size and Construction	Copper, 16mm^2	Copper, 16mm^2	Copper, 25mm^2	Copper, 25mm^2	Lead, 2.4mm thick
Jacket/Bedding thickness (mm)	2	2	2	2	2
Armour wire diameter (mm)	2	2	2	2	3
Number of Armour wires	48	48	60	60	84
Cable Ampacity (A)	211	346	430	543	715

Table 7.2. Parameters for cables used in AC system modelling.

The FEM was used to calculate the cable resistance, including the effect of any losses caused by induced currents in the metallic sheath or armour. Table 7.3 shows

the resistance of each cable type along with a breakdown of the losses in each cable component.

Core Cross-sectional area (mm^2)	50	120	185	300	630
Cable Resistance (Ω/km)	0.365	0.156	0.108	0.071	0.047
Core Losses as Proportion of Total	98.06%	95.96%	91.24%	88.40%	69.54%
Metallic Sheath Losses as Proportion of Total	1.09%	2.10%	5.30%	6.56%	15.93%
Metallic Armour Losses as Proportion of Total	0.84%	1.94%	3.46%	5.05%	14.53%

Table 7.3. Resistance and losses in each metallic layer for the simulated cables used in modelling the AC system.

For the larger cables, the losses in the outer metallic layers contribute significantly to the overall losses. In the smaller cables, the core is relatively small and so the losses in it dominate. The current density distribution in the cables with cross-sectional area of $300mm^2$ and $630mm^2$ per core, when carrying their respective maximum load currents for this wind farm layout (525A and 656A), are shown in Figure 7.5.

The proximity effect is visible. The skin effect is not particularly noticeable (except in the armour wires). At this frequency, the skin depth for copper is around 9.3mm and the core radius of the largest cable ($630mm^2$) is approximately 14.2mm. For larger conductors (typically $1000mm^2$ and larger [47]), segmental conductors are used to reduce the skin effect, which also reduces proximity effect.

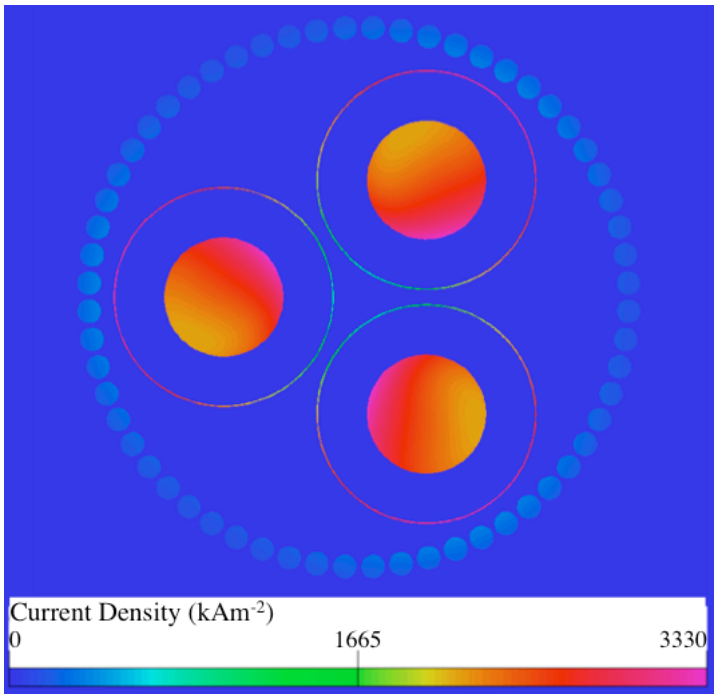

(a)

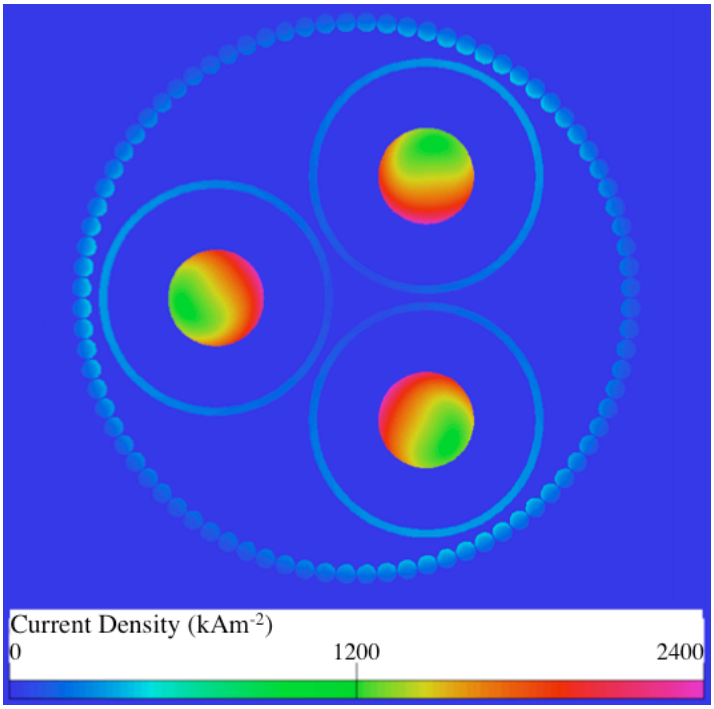

(b)

Figure 7.5. Magnitude of current density in simulated three core AC cables. (a) The largest collection network cable with core cross-sectional area of 300mm^2 and current of 525A (RMS). (b) Transmission cable with core area 630mm^2 and current of 656A (RMS).

7.2.2 Losses in AC System

The difficulties of transmitting AC power over long distances using a subsea cable is discussed in subsequent sections, however, to give an initial comparison of the AC and DC losses, it is assumed that the AC current is equivalent to the real part of the load current. The losses in the system for AC and DC (using the three-phase SLR converter with converters switching in phase as a comparison) is shown in Table 7.4.

	DC System	AC System
Collection Network Losses (MW)	0.20	0.70
Transmission Cable Losses (MW)	5.33	6.06
Total Losses (MW)	5.52	6.77

Table 7.4. Cable losses in the simulated AC and DC systems when operating at full power.

In both cases the transmission losses dominate. The transmission losses are also comparable in each case. The underlying reason for this is that the losses that a subsea cable can tolerate depend on the amount of heat that can be dissipated from the cable while it is operating at its temperature limit. In the collection network, the same theory applies, however, due to the availability of smaller cables for AC (with cores of 50mm^2) compared to DC (95mm^2), the losses in the AC case are higher. It is not clear why the allowable losses are somewhat higher for the AC transmission cable. The results are based on figures from the same manufacturer [46, 48] and the total surface area of the cables is similar for AC and DC. It is possible that there is some discrepancy between the models developed here and those used for rating the cables. Consultation with cable suppliers is therefore necessary to clarify this.

While the required cable choice in each case makes these losses comparable for AC and DC, there are two other factors to consider. First, for larger wind farms, the maximum power that can be transmitted in each case without need for additional cables and second, the cost.

7.2.3 AC Charging Current

The effect of charging current must be considered. This is the main limiting factor for the use of HVAC for long distance subsea power transmission [89]. The required charging current (I_q) is given by equation (7.2) [90]

$$I_q = V\omega C' l \tag{7.2}$$

where

V is the transmission voltage;

$\omega = 2\pi f;$

f = AC frequency;

C'= Cable capacitance per unit length;

l = Cable length.

The charging current can be supplied equally from both ends of the cable [89, 90, 91], so the maximum charging current required at any point in the cable is only half the value of I_q.

7.2.4 Power Transfer Limitations

This section examines the theoretical power carrying limits of AC and DC cables. In the case of AC transmission, charging current is initially neglected in order to compare AC and DC solutions for near to shore applications.

7.2.4.1 Collection Network

The first consideration is the design of the collection grid. Based on the data in [46, 48], both cable datasheets from the same supplier, the number of turbines that can be supported on a string in the wind farm for a range of AC and DC cable sizes are shown in Figure 7.6.

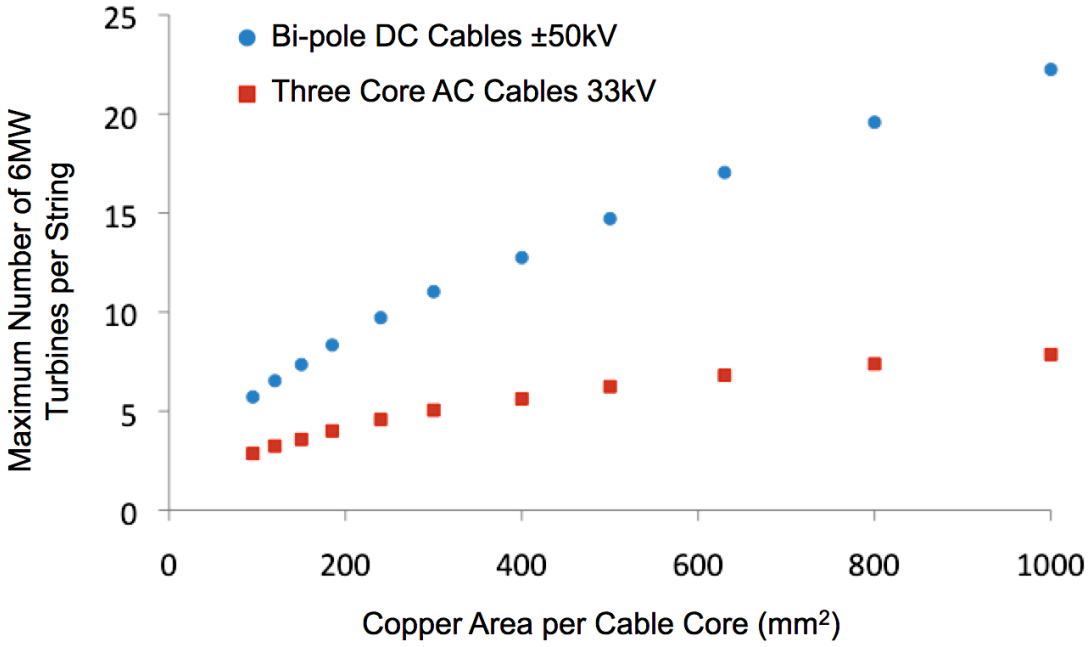

Figure 7.6. Calculated limit on number of 6MW turbines connected to a single three core AC cable at 33kV compared to DC bipole cables at ±50kV.

Although there is less copper used in the DC cables (due to there being 2 cores rather than 3), these cables can carry power from significantly more turbines than the AC cable. In addition, there is a decreasing return in the AC cables as core size increases, so it is likely to be more economic to use a larger number of smaller cables, as has been proposed in section 7.2.1. The DC solution provides much more flexibility in the layout of the wind farm cables and avoids the additional cost of laying extra cables in a large wind farm.

7.2.4.2 Power Transmission to Shore

For power transmission to shore, increasing AC voltage to 132kV is essential. Table 7.5 shows the maximum power transfer capacity of a selection of AC and DC cables. The selection is based on [46, 47, 48, 64, 85] and shows the largest three core AC cable, a DC cable with approximately equivalent amount of total copper core area (two cores for DC, three for AC) and the largest single core AC and DC cables available. For the single core cables, it is assumed that they are laid close together.

Voltage	±50kV DC	132kV AC	±50kV DC	132kV AC
Cable Arrangement	Bi-Pole Cables	Three Core Cable	Bi-Pole Cables	Three Single Core Cables
Area per core (mm^2)	1400	1000	3000	2500
Maximum Power Transfer (MW)	159	189	247	320
Equivalent Number of 6MW Turbines	26	31	41	53

Table 7.5. Comparison between calculated power transfer limits at transmission voltage.

As charging current has not been accounted for, Table 7.5 is, in effect, valid for wind farms close to shore. For the largest available AC and DC cables, the maximum useful power that can be transmitted is plotted against transmission distance in Figure 7.7. For the AC cables, it is assumed that a segmental conductor with a filling factor of 86% is used [47], which gives a value of distributed capacitance of 0.275μF/km. It is also assumed that charging current is supplied from both ends of the cable.

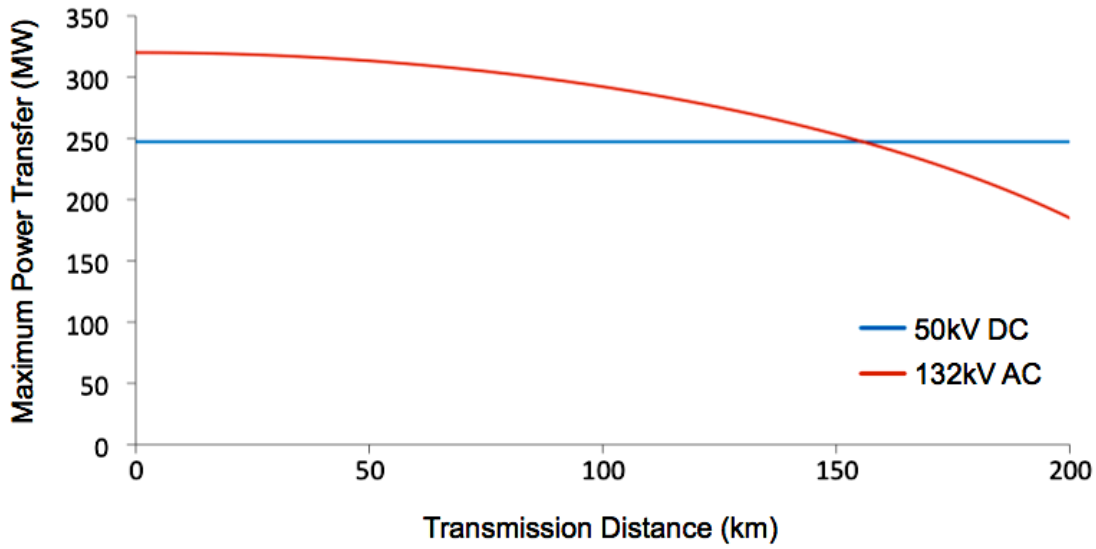

Figure 7.7. Calculated power transfer limit for selected AC and DC cables showing the effect of charging current on AC power flow.

Figure 7.7 in effect shows the size limit for a wind farm or section thereof that is connected with one set of closely laid cables. For significantly more power to be transmitted, either more cables or a higher voltage is required.

7.2.5 Cost of Losses

In order to put the losses into context, it is necessary to estimate the value of the lost energy. There are two key parameters that are required in order to do this; the predicted power output of the wind farm over its lifetime and the price at which the energy generated can be sold. A Weibull distribution was used to model the wind speed, as shown in equation (7.3).

$$P(U) = \frac{k}{C_U}\left(\frac{U}{C_U}\right)^{k-1} e^{-\left(\left(\frac{U}{C_U}\right)^{k}\right)} \tag{7.3}$$

where $P(U)$ is the probability of a given wind speed U;

k=2.1 and C_U=11.1m/s are the Weibull shape parameter and characteristic wind speed respectively, taken from wind measurements in [92] (taken at 53°13'04"N 3°13'13"E). These same measurements give an average wind speed of 9.8m/s.

An estimate from [93] of wind turbine availability of 0.95 was assumed. The 6MW wind turbine was modelled based on data in [94], with cut-in wind speed of 4m/s, rated wind speed of 13m/s and cut-out wind speed of 25m/s. It was assumed that, between cut-in and rated speed, the power output is proportional to wind speed cubed. The price of energy was assumed to be £135/MWh, based on the provisional strike price for 2018/19 in [95].

For the 150MW wind farm, shown in Figure 4.7, a distance of 100km from shore, the estimated monetary value of the losses over a 25 year period are shown in Table 7.6. The charging current in the AC case was accounted for in the losses and this increased the required cable core size to 800mm^2 (from 630mm^2). The other cables were modelled as described in section 7.2.1.

	Collection Cables	Transmission Cable	Total
Cost of AC System Losses (£/25yrs)	292,000	2,247,000	2,540,000
Cost of DC System Losses (£/25yrs)	89,000	2,389,000	2,478,000

Table 7.6. Indicative cost of losses for proposed AC and DC cable networks.

The total cost of the losses is roughly the same in the AC and DC cases, this is for the same reason that AC and DC losses in Table 7.4 were similar, i.e. the allowable losses are defined by the amount of heat that can be dissipated from the cable.

These figures are only indicative. For example, wind conditions vary from site to site, availability is an unknown variable and the strike price may not be sustained at the 2018/19 level, assuming costs in the sector fall over time. The losses are calculated based on a cable temperature of 20ºC. In addition, these figures cannot be compared directly with capital costs, due to factors including inflation and interest rates/investment returns.

7.2.6 Cost of Cable Network

Estimating the costs of cables and cable laying is a difficult task. Due to the small number of providers for subsea cables, there is no defined market cost [36]. Although sources in academic literature are available, such as [12, 54], the ultimate sources for these numbers may be out of date. For example, the price of a metric tonne of copper in January 2009 was around 3,200US$, in February 2011 around 9,800US$ and in October 2013 around 7,200US$ [96]. A further example is the adaptation of XLPE for use in DC cables in recent years (as discussed in section 2.6.3.2), which has been partly driven by increased demand for DC cables. As a result, estimates of the costs and choices of materials and processes for cable manufacture can quickly become out of date.

Cable laying costs are perhaps even more difficult to estimate as they vary according to the seabed conditions (which may not be foreseeable) as well as water depth and cable size. Experience of cable installation [36] has shown that costs can vary enormously with seabed conditions. For instance, delays of months have been encountered due to the seabed being rockier than expected. Given that the cost of a transmission cable laying vessel is estimated at £75-125k per day [11], it is easy to see that costs can escalate quickly. In addition, the type of vessel used is dependent on the cable size. As well as increased costs, larger cable laying vessels are becoming scarce [36]. Approximately, this applies to cables with greater than 1500mm^2 total copper cross-section.

Based on figures in [12], which include an estimated cost of 396Euro/m for the cable and 365Euro/m for installation, the total cost for a 100km transmission cable would be 76MEuros or £63M (assuming an exchange rate of 1.2 Euros to the pound). These figures do not account for cable parameters and are only included to give an indication of the scale of costs. For the size of wind farm considered and distance from shore, the transmission cable costs will dominate the collection cable costs.

7.2.6.1 Comparison of AC and DC Cables

In order to make a comparison between AC and DC cases, as direct cost comparisons are unreliable, a different approach is taken. For the cable designs considered, the following parameters that strongly influence cable material cost and laying cost are estimated:

- Mass of copper;
- Mass of lead;
- Cable dimensions;
- Cable weight.

For single core AC cables, magnetic (e.g. steel) armour can be a source of large losses due to induced eddy currents. This is because the skin depth of the magnetic

armour is reduced by its magnetic permeability, which leads to large induced currents. Non-magnetic material may be used instead [48], such as copper (hard drawn to increase tensile strength), aluminium or stainless steel [40]. However, these materials are more expensive than steel and in some cases (such as aluminium) are unsuitable for use due to corrosion.

An alternative solution is to use a copper (rather than lead) metallic water blocking sheath. As seen in the modelling of the copper screen in chapter 3, such a layer reduces induced losses in metallic cable layers outside it. However, in this case, a significantly thicker layer of copper would be required in order to compensate for the lower frequency (50Hz compared to 1kHz modelled in chapter 3).

7.2.6.2 Modelling

Datasheets from the same supplier for AC and DC cables [46, 48] were used to estimate the dimensions of the metallic sheath, insulation and core. Further parameters came from these and [47, 85]. In accordance with [41], the required armour strength is proportional to the weight of the cable. The required cross-sectional area of the wires is proportional to the required strength and inversely proportional to the tensile strength of the material used. For single core AC cables, hard drawn copper wire was modelled. Derived from figures in [97, 98, 99, 100], the tensile strength of hard drawn copper wire is estimated to be 1.7 times lower than that of utility grade galvanized steel.

Three case studies were examined, as shown in Table 7.7.

Case Study	1	2	3
Rated Power (MW)	150	150	240
Distance to Shore (km)	20	100	100

Table 7.7. Parameters for case studies comparing AC and DC power grid solutions.

In each case and for both AC and DC, the size of armour was chosen so that the ratio of cable weight to armour strength was the same. This ratio is dependent on a number of factors including water depth and seabed conditions.

7.2.6.3 Results and Analysis

The results for the transmission cables are shown in Table 7.8. The mass and cross-sectional area figures account for the number of cables.

Case Study	1		2		3	
System Type	AC	DC	AC	DC	AC	DC
Cable Arrangement	Three Core (1 Cable)	Bi-pole (2 Cables)	Three Core (1 Cable)	Bi-pole (2 Cables)	Single Core (3 Cables)	Bi-pole (2 Cables)
Mass of Copper (including copper armour) (kgm^{-1})	16.9	25.1	21.5	25.1	126.8	53.8
Mass of Lead (kgm^{-1})	15.4	12.2	17.2	12.2	26.4	18.5
Diameter of Each Cable (mm)	185	89	194	89	127	114
Total Cross Sectional Area (m^2)	0.108	0.050	0.118	0.050	0.153	0.082
Mass of Cable(s) (kgm^{-1})	46.9	58.8	52.8	58.8	174.9	108.6

Table 7.8. Range of estimated cable parameters for AC and DC power grids in three case studies.

For case studies 1 and 2 (the 150MW wind farm 20km and 100km from shore respectively) the results show some advantages for the AC solution (less copper and lower cable weight) and some for the DC solution (less lead and smaller overall dimensions).

For case study 3, there is a very clear advantage in using the DC solution. The use of single core AC cables and the required change in armour material is the main source of the increased copper usage and mass. The cable dimensions are also significantly increased as the advantage of sharing some cable components (as happens in the three core arrangement) is lost. Figure 7.7 showed the power transfer limit for AC and DC systems based on the use of single core cables in the AC case. However, this result shows that the use of single core AC cables have significant disadvantages and, if suitable three core cables are not available for a given power rating, then the DC solution (if it is practical) is likely to have lower cable material and laying costs.

Based on figures for a three core cable with core cross-sectional area of 1000mm^2 in [48], the limit on power transfer at 132kV from 100km is reduced to 157MW (from 292MW for single core cables with core area of 2500mm^2). For wind farms close enough to shore to neglect charging current, the power transfer limit is reduced to 189MW from 320MW. Larger three core cables are available on request, however the power transfer limit with a three core cable is still significantly less than with single core cables.

In the case of the collection cables for the 150MW wind farm, the average mass of copper used in total for the bipole cables is 2.01kgm^{-1} compared to 3.95kgm^{-1} for the AC case. This is mainly due to the higher operating voltage and advantages with DC power transfer. In addition, as explained in section 7.2.1, around 8% less cable length is required in the DC case.

7.2.7 Section Summary

For the modelled AC and DC systems, losses are comparable and it is likely that cable costs will be broadly similar in cases where three core AC cables can be used. There is a large step up in cable material use, size and weight when single core AC cables are required. This could be the limiting factor for power transfer using AC, above which DC is clearly more economic. However, a range of options for single core AC cable design remain to be examined, including the use of stainless steel armour or a large copper water blocking sheath, that may be more cost effective than the solution examined here (use of hard drawn copper armour). Assessing these options is a topic for further work that would benefit from the application of FEM analysis.

Once the cost saving from eliminating the AC substation is accounted for, the DC solution presented here is more than competitive with the equivalent AC solution in all the case studies analysed, including for a wind farm close to shore. However,

costs of the electrical system within the turbine have not been included and this is another topic for further research.

The limit for power transfer at ±50kV DC is equivalent to a wind farm with forty-one 6MW turbines. Above this, transmission cables can be laid apart from one another, (which may be necessary in any case, as discussed in section 2.6.2) increasing the size to fifty-one wind turbines. Above that figure, it is possible that a higher DC voltage will be required, which will necessitate an offshore substation to house the converter. Design of this converter and analysis of its economic viability are very promising topics for further research.

7.3 Switching Frequency

So far, a switching frequency of 500Hz has been assumed. In this section, the effect of switching the converters at a range of lower frequencies, i.e. 350Hz, 250Hz and 150Hz, is considered. The advantages of this include:

- Reduced skin effect in the wiring within the turbine, which reduces the need for expensive Litz wire.
- Reduced switching losses.
- For the converter based on a voltage source inverter, the frequency is closer to that which these inverters typically operate at (i.e. 50Hz or 60Hz), making its design and operation more straightforward (e.g. in terms of reduced switching harmonics and simpler filter design).

These advantages come at the expense of larger components. Determining the optimal frequency is a subject for further research. The aim of this section is to consider the implications for the HV filtering requirements and collection and transmission network operation.

7.3.1 Changes to system components

The required size of the HV filter capacitor is affected by the change in frequency. The lower frequency necessitates a larger transformer and larger low voltage side inductor, and this increases the minimum size of capacitor needed to protect the HV diode bridge from over voltage caused by an open circuit fault on the converter output. The minimum capacitor size is therefore increased from 2μF in inverse proportion to the change in frequency. This gives a capacitance of 2.9μF at 350Hz, 4μF at 250Hz and 6.7μF at 150Hz, which is used throughout the modelling in this section. The resistance and inductance of the cables in the system were recalculated at the new range of ripple frequencies using the FEM models. The values of low voltage inductance and capacitance in the SLR converters were also increased in inverse proportion to the change in frequency in order to maintain the ratio of resonant to switching frequency. The low voltage inductance in the phase shift converter was adjusted in the same way in order to maintain the value of its impedance at the switching frequency.

7.3.2 Assessment of DC Grid Performance

7.3.2.1 Voltage *THD*

The same set of tests as carried out as in chapter 6 and the equivalent results as shown in Table 6.6 are shown in Table 7.9, Table 7.10 and Table 7.11 for the lower range of frequencies.

		Single Phase SLR		Phase Shift		3-Phase SLR		3-Phase Voltage Source Inverter	
		C_{dc} (μF)	Max. Voltage THD	C_{dc} (μF)	Max. Voltage THD	C_{dc} (μF)	Max. Voltage THD	C_{dc} (μF)	Max. Voltage THD
Switching in Phase	Full Power	6.8	1.99%	10.2	2.00%	2.9	0.30%	2.9	0.23%
	Cable 15=>20 Disconnected	6.9	2.00%	10.5	1.99%	2.9	0.25%	2.9	0.19%
Switching Offset Case 3	Full Power	2.9	0.39%	2.9	0.69%	2.9	0.09%	2.9	0.07%
	Turbines 15, 19, 20, 23, 24, 25 Off	2.9	1.07%	2.9	1.45%	2.9	0.14%	2.9	0.11%

Table 7.9. Maximum collection network voltage *THD* for simulated DC grids constructed with each type of converter for a range of operating conditions, operating at 350Hz switching frequency.

		Single Phase SLR		Phase Shift		3-Phase SLR		3-Phase Voltage Source Inverter	
		C_{dc} (μF)	Max. Voltage THD	C_{dc} (μF)	Max. Voltage THD	C_{dc} (μF)	Max. Voltage THD	C_{dc} (μF)	Max. Voltage THD
Switching in Phase	Full Power	9.4	2.00%	14.2	2.00%	4.0	0.30%	4.0	0.23%
	Cable 15=>20 Disconnected	9.4	1.99%	14.3	2.00%	4.0	0.24%	4.0	0.18%
Switching Offset Case 3	Full Power	4.0	0.32%	4.0	0.58%	4.0	0.07%	4.0	0.06%
	Turbines 15, 19, 20, 23, 24, 25 Off	4.0	0.97%	4.0	1.32%	4.0	0.12%	4.0	0.09%

Table 7.10. Maximum collection network voltage *THD* for simulated DC grids constructed with each type of converter for a range of operating conditions, operating at 250Hz switching frequency.

		Single Phase SLR		Phase Shift		3-Phase SLR		3-Phase Voltage Source Inverter	
		C_{dc} (μF)	Max. Voltage THD	C_{dc} (μF)	Max. Voltage THD	C_{dc} (μF)	Max. Voltage THD	C_{dc} (μF)	Max. Voltage THD
Switching in Phase	Full Power	16.1	2.00%	24.1	2.00%	6.7	0.30%	6.7	0.23%
	Cable 15=>20 Disconnected	16.5	1.99%	24.6	2.00%	6.7	0.23%	6.7	0.18%
Switching Offset Case 3	Full Power	6.7	0.25%	6.7	0.47%	6.7	0.05%	6.7	0.04%
	Turbines 15, 19, 20, 23, 24, 25 Off	6.7	0.92%	6.7	1.23%	6.7	0.10%	6.7	0.08%

Table 7.11. Maximum collection network voltage *THD* for simulated DC grids constructed with each type of converter for a range of operating conditions, operating at 150Hz switching frequency.

In comparison to the results at 500Hz switching frequency, the required capacitance to achieve the same level of *THD* is significantly increased in the cases where the single-phase converters switch in phase. This increases the required capacitance to a level close to or above the practical limit for a film capacitor. However, in all other cases the minimum required capacitance is sufficient to keep the voltage *THD* within limits.

In comparison to the results at 500Hz switching frequency, the *THD* is significantly reduced for the cases where switching phase is offset and the minimum capacitance used. Obviously the minimum capacitance is now larger, and it's reactance

approximately the same as the 2μF capacitor at 500Hz switching frequency. However, the cable parameters have not changed as much as the capacitor size has (in cable 1 at a switching frequency of 250Hz, for example, the inductance at the fundamental ripple frequency is 24% higher and the resistance 34% lower at the fundamental ripple frequency). The result is that at 250Hz switching frequency, both cable resistance and inductive reactance are reduced compared to 500Hz switching frequency and the cancellation of the ripple currents and voltages is more effective as a result of the converters being connected by cable sections with a lower impedance.

7.3.2.2 Losses

The DC losses and therefore the total losses are not affected significantly by the change in switching frequency. At 250Hz switching frequency, for example, the proportion of total cable losses that result from ripple current were calculated for the single-phase SLR converter and found to be reduced from 0.93% to 0.75% where converters switch in phase and from 0.56% to 0.34% where they are offset in case 3 (operating at full power with C_{dc} as shown in Table 6.7 and Table 7.10). In the former case this is because the cable resistance is lower and in the latter case because the *THD* and cable resistance are both lower at 250Hz switching frequency.

The transmission cable impedance was calculated at the fundamental ripple frequency for switching at 250Hz and compared to that at 500Hz switching (Z_{send} is therefore computed at 500Hz in the former case and 1kHz in the latter). The result for a range of transmission distances is shown in Figure 7.8.

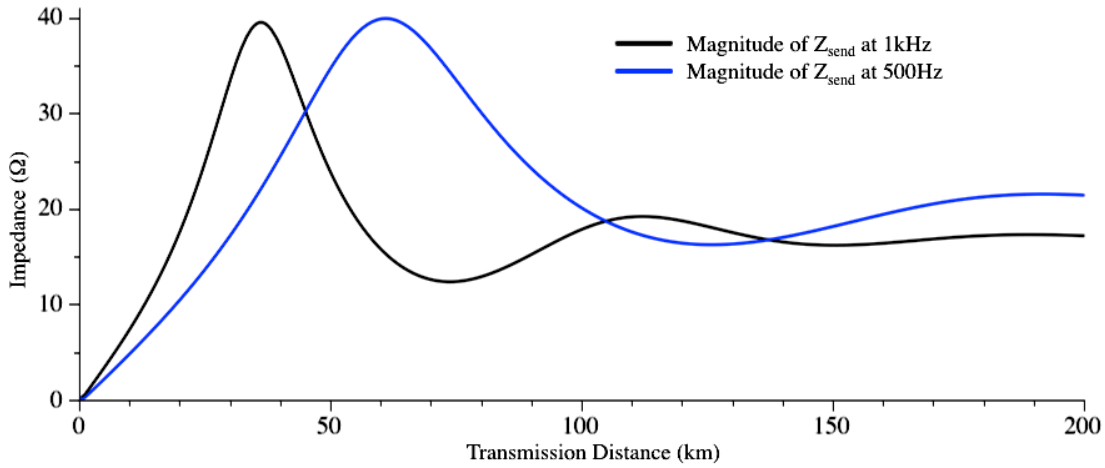

Figure 7.8. Transmission cable impedance calculated for a range of transmission distances for fundamental ripple frequencies of 500Hz (corresponds to 250Hz switching frequency) and 1kHz (corresponds to 500Hz switching frequency).

It can be seen that for the chosen transmission distance of 100km and ripple frequency of 500Hz, the value of Z_{send} is close to its minimum at $\lambda/2$ (c. 125km). Therefore, the relatively low ripple current losses described above are representative of the upper range of the ripple losses in the transmission cable that can be expected (as shown in section 6.1.3, a low value of cable impedance causes high ripple current to flow and correspondingly high losses).

7.3.2.3 Fault Current Considerations

The larger HV filter capacitances required at lower switching frequencies provide more energy to feed into a fault in the system. This can be seen in Figure 7.4. However, the energy dissipated in the cables during a fault is still well below the total energy the cable can tolerate in a 1 second period. Again, due to the large d*i*/d*t* in the early stage of the fault, consultation with cable suppliers is necessary.

7.3.3 Section Summary

In general, changing the converters to a switching frequency of 150Hz, 250Hz or 350Hz does not present any significant additional challenges to the design of the DC grid. However, in the case of the single-phase converters, particularly the phase shift converter, switching the converters in phase may necessitate the use of an electrolytic

rather than a film capacitor. For the wind farm considered here, this can be avoided by offsetting the switching phases. However, as discussed in section 6.1.2.2.2, for larger wind farms this may not be possible and the use of these converters would have the disadvantages associated with significantly larger filter capacitance.

7.4 Connecting the DC-DC Converter Directly to Rectified Generator Output

So far, it has been assumed that the DC-DC converter topologies are fed with a fixed voltage DC input provided by an active rectifier and voltage regulation stage with boost characteristic connected to the generator output. The exception is the converter built on the AC-DC-AC drive topology connected to a medium frequency transformer and HV rectifier stage; the input AC is variable voltage and frequency, i.e. it is connected to the unrectified generator output.

Both the SLR converter designs and the phase shift converter are suitable to use with a variable voltage input. This means that the rectified generator output need not be voltage regulated.

The phase shift converter controls the ratio of input to output voltage by adjusting the phase of the switching devices relative to one another. The SLR topologies are controlled by changing the frequency of the switching. The resulting ripple content of the output waveforms from the converters operated in this way is discussed in this section, along with their effects on the operation of the DC grid.

7.4.1 Single-Phase SLR

With a variable input voltage, the frequency of the SLR converter is not fixed and therefore the switching frequencies and phases of the converters must be independent from each other.

With respect to the switching phases, a situation similar to that observed in section 6.1.2.2.1 when the phases were offset in case 1 would result at some time. This caused the ripple current losses in certain sections of cable to become larger than those for which the cable is rated.

With respect to converter switching frequency, since it is likely that all converters will operate at different frequencies to each other, the ripple currents and the resulting losses from each converter must be calculated separately to find the time averaged system losses. This makes it impossible to reduce losses by cancellation of ripple current flows.

The single-phase SLR, operating with variable input voltage, is therefore not suitable for use in the DC grid.

7.4.2 Three-phase SLR Converter

Although the voltage regulation of the three-phase SLR is performed using frequency control, its much lower ripple output means that the problems this causes are much less severe than for the single-phase version. For example, operating the single-phase converter with phases offset as in section 6.1.2.2, case 1, resulted in AC losses of 73.6Wm^{-1} in the cable linking converters 10 and 15 (Figure 4.7) (which is rated for losses of around 33.2Wm^{-1}). The same conditions using the three-phase SLR converters result in AC losses of only 1.04Wm^{-1} in the same cable.

As in the case of the single-phase SLR converter, losses must be calculated separately for the ripple currents from each converter and added together. Again, however, this does not present a problem. The magnitude of the fundamental ripple current for the three-phase SLR is 4.46A (from Table 6.5) while for the single-phase converter it is 32.14A (from Table 2.1). Since the losses are proportional to the

current squared, the total losses from a large number of three-phase converters are not problematic, even accounting for the higher cable resistance at the fundamental frequency of 3kHz for the three-phase converter (for cable type 1 the resistance is $1.03\Omega km^{-1}$ at 1kHz and $1.66\Omega km^{-1}$ at 3kHz).

7.4.2.1 Design of Three-Phase SLR

The design of this converter poses some challenges. The voltage step up ratio of the converter is at its highest when the input power is small and at its lowest when the input power is large.

Based on a wind turbine cut-in speed of $4ms^{-1}$ and rated speed of $13ms^{-1}$ [94] and assuming that the tip speed ratio is constant and generator voltage is proportional to speed of blade rotation, the maximum input converter voltage is estimated to be 3.25 times the minimum. To accommodate the variable input voltage, the transformer turns ratio must be increased by a factor of 3.25.

One challenge for designing the converter is the increased magnitude of the low voltage current. The peak current in the transformer secondary is close to the value of the DC current (see Figure 5.6). At full power, this is approximately 60A. Therefore, if the transformer turns ratio is 3.25 times the case where the converter has a fixed voltage input, then the transformer primary current is also 3.25 times larger. This means that all the low voltage components, including switching devices, must be rated for this current. In addition, the larger low voltage current increases the voltage magnitude in the resonant capacitor, unless this capacitor is made larger in comparison to the inductor, in which case harmonic current in the transformer primary is increased.

One way to reduce this low voltage current is to choose a different cut in speed for the turbine; the turbine described in [94] has a range of cut in speeds from $3ms^{-1}$ to $5ms^{-1}$. Choosing $5ms^{-1}$ reduces the ratio of voltage inputs to 2.6:1. In addition, based

on a typical power curve for a wind turbine [101], it is possible to run the turbine with a small over speed (10% for example) without making a significant reduction to the power generated. Doing so at low speed further reduces the ratio of input voltages to 2.36:1 (for a 10% over speed). The disadvantage of this approach is the loss of energy. This disadvantage may become more important as increasing amounts of wind power are connected to the UK grid. On days when the wind is light across the UK and its offshore wind farm areas, the market price is likely to reflect this much more than it does now. Therefore, the value of energy generated in light wind conditions could be disproportionally high.

Finding the optimal cut in speed and degree of over speed is an interesting topic for further research which can be combined with the optimisation of converter design. The challenges of managing the current at high power are likely to be similar in a range of converter designs in which a variable input voltage is assumed. This research is covered in the parallel PhD project described in chapter 1.

7.4.3 Phase shift converter

The phase shift converter has the advantage over the single-phase SLR converter that its switching frequency is set and therefore its switching phase can be controlled. It has the same disadvantages as identified in section 7.4.2.1 for DC-DC converters with variable voltage input. In this case, not only does this result in large currents on the low voltage side when operating at full power, but the current is in discontinuous mode operation. Possible mitigation strategies are the same as described previously (i.e. changing the cut-in speed or operating the turbine with over speed at low power).

7.4.3.1 Converter Modelling

In order to assess its interaction with the DC grid, the converter was modelled with two different ranges of input voltage, which necessitate two different values for transformer turns ratio. The ranges were 3.25:1 and 2.36:1, derived as described in

section 7.4.2.1. The rectified, unfiltered high voltage current waveforms with each converter operating at full power are shown in Figure 7.9.

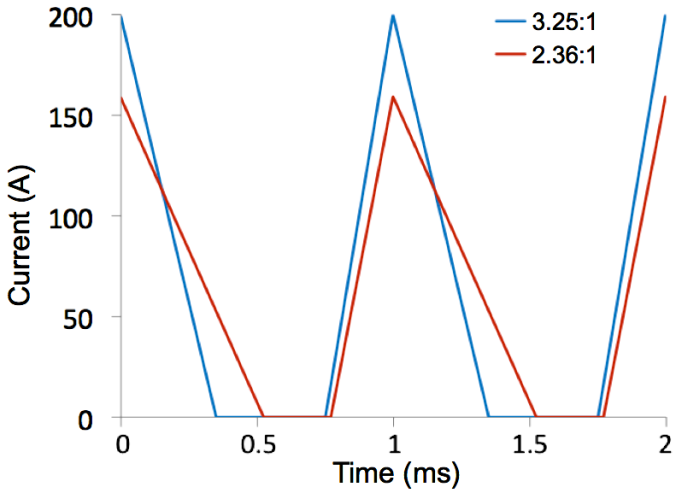

Figure 7.9. Unfiltered DC current output from phase shift converters simulated operating at full power with two ranges of input voltage.

In both cases the converter operates in discontinuous mode. The peak current is higher and the conduction time lower in the case where the range of input voltages is 3.25:1. The frequency components of these waveforms along with the components for the phase shift converter with fixed voltage input operating at full power are shown in Table 7.12. It can be seen that the ripple current content is very significantly increased in comparison to the converter operating with fixed voltage input. As a result, larger filters are required.

	Magnitude of Unfiltered DC Current Component (A) for Range of Ratios of Maximum to Minimum Input Voltage		
Frequency (kHz)	3.25:1	2.36:1	1:1
DC	60.00	60.00	60.00
1	88.20	71.59	46.00
2	30.62	17.65	21.46
3	7.48	9.17	12.70
4	3.49	1.83	8.01
5	3.83	2.18	5.05

Table 7.12. Frequency components of unfiltered DC current output from phase shift converters simulated operating at full power with three ranges of input voltage.

Although the phase shift converter maintains its switching frequency with varying power and input voltage, the phase of the current ripple on the output voltage does change and is dependent to a large extent on the delay angle. However, in the case where the range of input voltages is 3.25:1, it was found that at full power the delay angle is 139º while at 60% power (chosen to reflect variation in operating power caused by the wake effect, as shown in Table 6.3) the delay angle is 140º. In general, it would be expected that the lower voltage input (at 60% power) would result in a smaller delay angle. In this case, the reduction in current on the low voltage side reduces the voltage dropped across the low voltage inductor, which almost exactly compensates for the reduction in input voltage. This makes control of the switching phase angles in the system significantly simpler as they change little with output power, until the power is reduced to a level well below maximum output, at which point the absolute size of the ripple current is correspondingly small.

7.4.3.2 System Modelling

A range of operating conditions and switching strategies were considered. In the case where switching phases are offset, it was found that large circulating ripple currents can occur when the wind farm is not operating at full power. Even with a filter capacitance of 100μF in each turbine, it was found that cables could easily become overloaded, and that this happened in quite unpredictable patterns. For example, turning off a corner of six turbines caused a cable in the diagonally opposite corner of the wind farm, in which the DC losses were only $0.6Wm^{-1}$, to have AC losses of $27.9Wm^{-1}$, which took the total to in excess of the cable's rating.

The problems were similar but more manageable with the converters switching in phase. In this case a filter capacitance of 20μF was found to be adequate to keep system currents and voltages within limits in the range of conditions studied. One disadvantage of the larger capacitance is the increased fault current. Testing the system with a 5Ω protective resistor in series with the filter capacitor, it was found that the ripple content was still within limits, however a 10Ω resistor caused the limits to be exceeded. It should be noted that the magnitude of the impedance of the

20μF filter capacitor at 1kHz is 8.0Ω, so it is easy to see that its effectiveness is compromised by a significant size of protective resistor.

Although in the range of tests conducted, it was found that a filter capacitance of 20μF was sufficient to meet the ripple current and voltage requirements, this set of tests does not cover all possible operating conditions. As seen in Figure 5.9, for relatively large values of capacitance, resonance can occur at certain points in the system under certain conditions, causing amplification of ripple current. With larger filter capacitance it is far more difficult to predict these resonant points than with the smaller capacitors (as can be seen in Figure 5.9(d)). Consequently, the choice of capacitor here is to be treated with caution, it is not a recommendation. In reality, it may not be possible to predict the occurrence of resonance in a wind farm, as any modelling always includes approximations and, with this size of capacitance, small errors can make a very large difference.

7.4.4 Control

In all previous sections, the DC-DC converter has been modelled as, in effect, a DC transformer with a constant ratio of voltage input to output. In changing to a variable voltage input, the part the DC-DC converter plays in the control of the system becomes more important. Effectively, the input voltage of the converter is determined by the wind speed. The output voltage is determined by the nominal DC grid voltage and the total power flow in the system. Changes in either the desired input (to achieve MPPT) or the output voltage are therefore independent of the converter, but the converter must respond appropriately, while taking account of the action of other control systems in the wind turbine and the DC grid in general.

The design of the converter control is a very significant task that is best carried out with due consideration for the control of the entire system. This is a topic for further research.

7.4.5 Section Summary

Although only a small range of converters have been considered here, it seems that the use of a three-phase converter will make the design process much more manageable. The choice of topology for this converter and its design is a very important piece of work for further research, much of which is already being undertaken in the PhD project running parallel to this one. Preliminary modelling of the three-phase SLR converter show that it is promising in theory, however practical challenges in the choice of resonant components, increased low voltage side current and consideration of the optimal range of input voltages must be addressed.

8 Evaluation and Discussion

This chapter evaluates the research that has been carried out, the resulting predictions for the proposed DC grid's performance and outlines the challenges and opportunities for future work.

8.1 Cable Modelling

8.1.1 Methodology and Applicability outside this Research

A great deal of knowledge and experience exists regarding cable systems and has done so for decades. When the research began, it was not anticipated that this subject would require a great deal of attention. It seemed that a DC cable would be much simpler to model than an AC cable, as its inductance and capacitance can be ignored for a pure, constant, DC power flow.

The modelling work that followed has shown that this is an area that required, and still does require, a great deal of research. The importance of cable design, as well as temperature and layout, on its distributed parameters has been demonstrated. The variability of losses along the length of a transmission cable has been shown, along with other important results including that cable resistance at ripple frequencies can damp resonance and therefore reduce ripple current losses.

Modelling power flows at the ripple frequency of 1kHz and its harmonics is only one example. In AC systems, the proliferation of grid connected power electronic equipment has caused an increase in system harmonics in recent years. This increase seems set to continue. A second example is research into AC systems at frequencies other than 50Hz, in particular their application to offshore power transmission where reducing frequency reduces the AC cable charging current (see equation (7.2)) and therefore increases the range from shore at which AC transmission can be used.

All these examples have something in common. They all result in AC power flows at frequencies for which power cables have not necessarily been designed or tested. In addition, formulae used to calculate cable resistance or inductance at 50Hz are not valid at other frequencies. Appendix A goes into detail on why the FEM approach is well suited to computing cable parameters at a range of frequencies.

The application of the FEM to assessing AC cable performance at a range of frequencies is an area for further research. This includes research into ways to address the problem of large induced currents in magnetic armour as described in section 7.2.6.1. Possible solutions include:

- Use of a range of armour materials;
- Use of a copper water blocking sheath;
- Reducing the frequency of AC transmission.

The relative impact on cable design of each of these solutions can be quantified using the FEM.

8.1.2 Cable Longevity

In chapter 3, it was shown using the FEM that the induced ripple current density in the cable's steel armour is theoretically sufficient to contribute to cable corrosion. This raises the issue of subsea cable longevity. Although it might be anticipated that the life of a wind turbine is around 25 years (for example), it is reasonable to expect that the offshore wind zones will be in use for much longer (possibly indefinitely). It therefore seems that there is good reason to construct the cables that connect these areas to shore so that they last in excess of 25 years. Although it is arguable that these cables may become outdated, for example by increased voltage levels, the cost of cable material and laying is so significant that it may make re-using cables economic.

It was noted in [53] that the points where the cable was most likely to fail as a result of damage to its armour were places where the cable was suspended above the seabed and therefore subject to tensile forces caused by its own weight. In addition to this, cables that are suspended move with sea currents and are more likely to be subject to fatigue, which can be a problem for a water blocking sheath constructed from lead.

One solution that can help to address both these problems is the use of a copper water blocking sheath. This is less susceptible to fatigue than lead and also reduces induced ripple currents in cable armour (as demonstrated by the modelling of a copper screen in chapter 3). Determining exactly how much this change in design can increase cable lifespan and whether this outweighs the additional cost is an interesting topic for further research.

8.2 DC Grid

8.2.1 Modelling Approach

The approach taken has been thorough and the results have in many cases shown exactly why this approach was required. For example:

- The unfiltered HVDC current waveforms shown in Figure 6.2 and Figure 6.5, which show distortion of the converter current waveform caused by voltage ripple in the DC grid, demonstrate the importance of accurately modelling the DC network, accounting for the frequency dependence of cable parameters.
- The results in Table E.3, showing the large AC losses in sections of cable caused when the chosen switching phases of a single-phase SLR converter cause large circulating currents in the DC grid, demonstrate the importance of accurate calculation of the losses caused by induced ripple currents.
- The variability of current ripple along a transmission cable (Figure 4.4) and the predicted resonance between individual HV filter capacitors and the rest of the DC network, show the importance of application of wave propagation

theory to the ripple current power flow. This issue of resonance is particularly well illustrated by the variability of filter capacitor effectiveness shown in Figure 5.9.

The approach has allowed predictions to be made with confidence on the components required for the DC grid. For example, the small requirement for filter capacitance, which enables the use of film capacitors, is a significant boost to the viability of the DC grid both in terms of cost and reliability. Without the exactness of the modelling, such a prediction might have seemed overly optimistic. The modelling has also quantified the benefits of three-phase converters compared to single-phase converters. This hinges on the fact that cable losses caused by ripple currents are difficult to manage for single-phase converters but not problematic for three-phase converters. Again, without the application of FEM analysis accompanied with experimental validation, the relatively high level of losses caused by ripple currents could not have been predicted quantifiably and with confidence.

The coding of the models in MATLAB has not only achieved the required level of accuracy, but also allowed the modelling of a 25 node DC grid with a single desktop or laptop computer. Even without taking account of the iterative process between time and frequency domains, undertaking this task with simpler cable models in standard simulation software may not have been achievable and run times would certainly have been prohibitive.

Finally, the experimental work in chapters 3 and 5 has demonstrated that the modelling approaches taken are reliable and some of the less intuitive results, such as amplification of ripple current by filter capacitance or large ripple current losses in a metallic sheath that is much less thick than the skin depth of the material, have been validated.

8.2.2 DC Grid Assessment

The work has shown that the main high voltage components required in the DC-DC converters feeding into the DC grid are:

- Diodes;
- Film Capacitor(s);
- Protective Resistor.

In section 2.3.1, the state of the art in HVDC was considered and the MMC was identified as one of the most promising topologies; it is a topology that is presently attracting a great deal of research interest. By comparison with the components listed above, the components required for an equivalent MMC used to rectify the HV current are greater in number and complexity, including:

- Multiple switching devices that must be actively controlled;
- A large number of small capacitors;
- HV inductors with associated insulation requirements.

In return for this, the MMC has many advantages including:

- Bi-directional power flow that enables black start capability;
- Low DC ripple content.

The simplicity of the HV side of the DC-DC converter is clearly a great advantage, especially offshore, where minimising failure rates is key. The issue of current ripple propagation has been analysed in great depth and found to be easily manageable for three-phase DC-DC converters. The requirement for black start capability is an interesting topic for further research.

The MMC, along with other HVDC conversion topologies, is suitable for use in the low voltage side of the power converter [81, 82], in conjunction with the high voltage DC side arrangement described here. The implication of this is that the relatively simplistic HV arrangement can be used in a large number of DC grid applications in which the main power flow is uni-directional.

The last is a particularly important point. As stated in the beginning, the DC grid is a novel approach. With novelty there is always an amount of risk (and perceived risk that may be greater than the actual risk). This is important in offshore wind, where failures can take a long time to repair and where there is a significant amount of public and media attention. In order for the research in this thesis to be used in practice, it is a great advantage that it can be applied to a wide range of DC conversion techniques. The modelling of the DC-DC converter that is based on a VSC was done for exactly this reason. This topology is relatively close to technology that is already tried and tested in AC wind farms. The differences are:

- The low voltage inverter switches at 500Hz, 350Hz, 250Hz or 150Hz rather than 50Hz;
- The transformer design is changed according to the frequency change;
- The output from the transformer is rectified before being fed into the collection network.

These changes are still very significant and require a large amount of product development and proofing in order to make them marketable on a wide scale. However, in comparison to changing the entire power electronic system from a AC-DC-AC drive topology to a DC-DC converter, the changes are far more manageable without unacceptable risk (or perceived risk). The successful introduction of this topology to the market would undoubtedly make the idea of a single stage DC-DC converter more appealing. In any of these topologies, the research here is applicable.

8.3 Comparison of AC and DC Systems

8.3.1 Comparison of AC and DC Cable Costs

Based on the results in section 7.2, the DC grid solution compared favourably with the AC alternative. The size of the wind farm significantly affects the comparison and there are certain power levels at which the assessment of the two solutions changes significantly, as outlined here.

- For wind farms small enough to use three core AC cables for power transmission at 132kV (approximately <190MW for wind farms close to shore), the cable costs are likely to be similar, while the absence of the offshore substation is an advantage of the DC solution. This is the case for wind farms close to and far from shore.
- For wind farms that require single core AC cables at 132kV and are small enough to be supplied by one pair of closely laid DC cables at ±50kV (roughly 190MW to 250MW for wind farms close to shore), the cable costs for the DC solution are likely to be significantly lower than the AC solution. Again, along with the absence of an offshore substation, this makes the DC solution advantageous, even close to shore.
- For wind farms that are too large to be supplied by one pair of cables at ±50kV cables, but that can be supplied by closely laid AC single core cables (roughly 250MW to 320MW for wind farms close to shore), the DC solution as presented is not an option, whereas the AC solution will work.

For the third of these cases and for higher powers, for the DC solution to be viable, there are three alternatives to increase power transfer capability:

- Laying one pair of DC cables apart from each other increases their ampacity and the maximum power transfer at ±50kV increases to roughly 310MW. In the case of AC cables, the same action does not provide such a clear cut

benefit, as increasing separation also increases induced currents in the outer metallic layers of each cable.

- Additional pairs of DC cables can be installed.
- An offshore substation with additional converter(s) can be used in order to increase the DC voltage to a higher level.

The first solution has the added benefit of reducing the risk of both DC transmission cables being damaged simultaneously by some external incident. For power transfer above the limit for the first solution, the choice between the second and third solutions depends on transmission distance. The offshore substation is a fixed cost, while the cost of additional cables depends on their required length. The use of additional cables increases the chance of a fault, but reduces the impact of any fault on power transfer capability. In any case, the costs of the DC system are increased. Further research is required; in particular to design, estimate the cost of and losses caused by an additional DC-DC conversion stage.

For power levels below the limit for ±50kV DC transfer, wind farms far from shore could also benefit from higher DC voltage. Both the material cost and cable laying cost of large cables could be reduced by increasing voltage. Again, there is likely to be a breakpoint for the transmission distance, above which higher voltage DC becomes the most economic solution. However, realistic estimation of cable costs is required to judge this point.

For the collection network, the DC system has very clear advantages over the AC system in terms of cabling, losses and flexibility of layout. Since many of the DC cables chosen are overrated (due to unavailability of smaller cables), further savings may be possible once a market for such smaller cables is shown to exist. For wind farms that are close to shore, the relative importance of the collection network in total cable costs and system performance is greater and, therefore, the benefits of the

DC collection network strengthen the case for using the proposed DC grid solution for close to shore wind farms.

8.3.2 Complete Comparison of AC and DC systems

The work in this thesis concentrates on the cable costs. Although this makes up a significant proportion of the electrical system, there are other factors that need to be included before a conclusion on the overall merits of the two solutions (or a hybrid solution involving an AC collection network and DC transmission). Additional factors that would require consideration include:

- Converter and transformer losses and costs;
- Estimation of failure rates of power electronic components and mean time to repair;
- Cost and implementation of reactive power (charging current) compensation;
- AC system resonance including the effect of reactive power compensation;
- Cost and utility (in terms of onshore AC grid support) of onshore DC-AC converter;
- For systems with too much power for one pair of ±50kV DC cables, the costs of the adjusted DC solution compared to the AC alternative;
- Use of higher voltage AC.

A thorough economic comparison of the DC and AC solutions is a very promising topic for further research.

8.3.3 Modelling Assumptions Affecting DC Power Transfer

The limit on the number of turbines that can be connected to a single pair of cables for the ±50kV DC solution is clearly a critical parameter. In calculating the power transfer, several assumptions have been made that may not hold in reality and must be accounted for. These are:

- The transmission voltage at the wind farm is ±50kV. This will be higher, if ±50kV is maintained onshore, as shown in Figure 5.8.
- The output from the wind turbine electrical system into the collection network is 6MW. This may be different after accounting for losses in the turbine.
- The cable ampacity is based on seabed temperature of 15ºC, burial depth of 1m and soil thermal conductivity of 1kWm^{-1} [46]. This figure is therefore dependent on, for example, location and seabed conditions.

The power transfer limits must, therefore, be assessed on a case by case basis. The choice of where to fix the voltage at ±50kV needs to account for the benefits (including greater power transfer) and the disadvantages (such as increased insulation requirements) of operating the offshore converters at slightly higher than 50kV.

8.4 Control

Control of the DC grid is a major topic that requires further research. The approach in this work has been to address the question of what components are required in the DC grid. Once the choices of and requirements for grid components are understood, then the control system can be designed.

There are a number of factors that have been identified during the course of this work, which will play a part in control system design. These are:

- The use of a small HV filter capacitor;
- Voltage and current ripple magnitude at the converter output;
- Interaction between different control loops, such as turbine maximum power point tracking and DC system voltage control.

The last of these is the reason that it is important to have a very clear idea of the system components, a task to which this thesis contributes, before the control of the DC-DC converters and DC system as a whole can be addressed.

In designing the control system, some of the constraints that were applied in specifying components (such as the limit on voltage *THD* of 2% and the minimum HV filter capacitance of, for example, 2μF at 500Hz switching) may need to be adjusted.

8.5 Protection

The work analysed the discharge of the DC filter capacitors under fault conditions, and it was found that there is a significant advantage in using small filter capacitors, due to the correspondingly small energy available to feed into a fault. It was also found that, where required, peak fault current can be reduced significantly by using a protective resistor in series with the cable capacitance.

In general, metallic water proofing sheaths are designed to carry fault current. In the proposed DC grid, the fault is short lived enough that the use of a polymeric water blocking sheath may be possible, with the cable armour able to carry the fault return current. This has significant advantages in terms of cable weight and, to an extent, cost. However, a polymeric sheath does allow some water vapour to diffuse and is only suitable where the electric field strength is relatively low, namely in medium voltage applications [40]. Consultation with cable suppliers would be needed to assess whether this could be an appropriate solution at ±50kV.

Further consideration must also be given to fault current supplied from the low voltage side of the DC-DC converter and from the onshore inverter. In both cases, the choice of converter topology is critical.

8.6 Single-phase and Three-phase Comparison

In the parallel PhD project, the performance of a large range of converter topologies are analysed. The work here has analysed the performance of a small number of topologies in a network. An important result is the distinction between the performance of the single-phase converters compared to the three-phase converters.

While the single-phase converters performed well in some situations, in others they are less promising. System design is more difficult for the single-phase converters considered and in some cases may not even be possible for certain topologies, such as connecting the single-phase SLR converter to a variable voltage input (see section 7.4.1). By comparison, the three-phase converters have the following advantages:

- Reduced voltage and current ripple content.
- Minimal HV filter capacitance required. This ensures that film capacitors, rather than electrolytic capacitors, can be used.
- As discussed in section 7.4.2, the ripple current losses in the cables are manageable and the voltage *THD* is well within limits for the three-phase SLR converter even when the switching phases of the converters are chosen to cause large ripple currents. This implies that three-phase converters do not necessarily require control of switching phases. (It is required for the single-phase converters considered.)
- The three-phase converters considered, with the minimum filter capacitance installed, produce voltage *THD* that is well below the chosen limit. This is almost unaffected by the complete disconnection of turbines from the grid (as opposed to turning off turbines but leaving their filter capacitance connected). Therefore, it is not necessary for the converter filter capacitance to remain connected to the grid when the turbine is off due to high wind conditions. This eliminates the need for an additional isolator/switch between the diode bridge and filter capacitor.

While the use of single-phase converters is still possible, as other topologies not considered here may perform better, all other things being equal, it is clearly advantageous to use three-phase converters. In general, it was found that the lower the ripple content (in particular the size of the largest frequency component of the ripple) in the unfiltered, HVDC current, the easier the DC grid is to design.

8.7 Application to Round 3 Offshore Wind Zones

The power transfer limit for the DC solution at ±50kV with a single set of bipole cables is relatively small compared to many of the round 3 offshore wind zones, as shown in Figure 1.2 and Table 1.1. Nevertheless, the solution is still very much applicable.

Some of the zones are relatively small and close to shore, such as zones 6 and 7. For these zones, the proposed DC solution has the advantage of eliminating the offshore substation, which is a higher proportion of the total cost, the smaller the wind farm.

For large zones, especially which are far from shore, a higher transmission voltage may be required. In these cases, the use of a ±50kV DC collection grid has advantages over an AC grid in terms of collection cable costs, power losses and flexibility of collection network layout. The advantages of the ±50kV DC solution are likely to be even greater when a large wind farm collection network is designed, since the limit of a small number of turbines that can be connected to each 33kV AC cable is potentially prohibitive.

9 Conclusions

9.1 Modelling Approach

The research has tackled some difficult challenges in terms of accurately modelling ripple current propagation in the DC grid. These are:

- Accurate calculation of cable parameters for a range of cable designs at a range of frequencies.
- Managing computational power and time required to model a wide range of operating conditions in a DC grid consisting of 25 interconnected DC-DC converters.
- Integration of time domain and frequency domain models to ensure that each part of the system is modelled appropriately.

The rigorous development, verification and validation of these models have given confidence in the resulting detailed predictions for DC grid performance.

9.2 Cable Behaviour

DC cable modelling using the FEM, along with the application of wave propagation theory to ripple currents in a DC system, have shown that even relatively subtle changes in cable design (which would not change the rating of a cable) can very significantly affect cable performance. Modelling with this level of accuracy is necessary for:

- Assessment of cable losses throughout a DC grid, including their variability along the length of a cable;
- Choosing the optimal cable design;
- Predicting resonance or system instability;

- Understanding the effect of the cable on power electronic converter performance and designing HV filtering.

It has been shown that the current ripple can cause very significant losses in DC cables. The detailed modelling of a number of cable designs has shown that the inclusion of a copper screen has the largest effect on losses and ripple voltage and current levels in a DC grid. Other factors that will have a large effect on distributed cable parameters include:

- Cable Temperature;
- Water blocking sheath thickness.

These considerations must be taken into account when modelling or designing a DC grid.

9.3 Assessment of the DC Grid and Components

The use of a DC network fed from DC-DC converters operating at ±50kV for power collection and transmission in an offshore wind farm has been shown to be practical and to have significant advantages over the alternative AC solution. These advantages are:

- No requirement for offshore substation;
- Reduced losses, reduced costs and greater design flexibility in the power collection network;
- Significantly reduced cable size, weight and material requirements for cables when compared with single core AC cables.

These advantages apply for wind farms close to shore as well as far from shore. In addition to the results from steady state analysis, under fault conditions the discharge

current from the HV filter capacitors is very short lived and its size can be limited using a protective resistor.

It was found that because the HV filter capacitors are linked together by short (and therefore low impedance) sections of cable, they effectively act as a distributed capacitance. This is advantageous in reducing voltage ripple across the network and only a small HV filter capacitor is required in order to manage the voltage ripple in the system. On the other hand, it means that circulating currents can result between converters. The most effective way of limiting these currents is by limiting the ripple content of the unfiltered DC current. The use of a small capacitance has the following advantages:

- Small amount of energy to feed into a cable fault;
- Allows use of film capacitors rather than electrolytic capacitors and therefore reduces rate of failure/replacement of that component;
- Reduces the severity of resonance in the system which makes system behaviour more predictable.

For wind farms up to around 300MW, one pair of bipole cables at ±50kV is adequate to transmit power to shore. Compared to alternative DC solutions (i.e. those that employ a transformer), the topology of the high voltage rectifier is very simple. On the HV side there are no active switching devices, no line reactance is used and only a small film capacitor is necessary for filtering. There is also no requirement for an offshore substation, which would be necessary if a significantly higher DC voltage were proposed.

The limitations for the DC solution at ±50kV are the power transfer limit for one pair of cables and the distance from shore at which cable costs outweigh the costs of a second DC-DC conversion stage and higher DC voltage. Close to shore, it may still

be economic to use additional cables rather than paying the one off cost of the additional conversion stage and accompanying offshore substation.

For the assessed converter topologies, there are a significant number of advantages for DC grid operation in using a three-phase DC-DC converter rather than single-phase. This is particularly the case when:

- The converter is fed by a variable voltage input;
- Converter switching frequencies are significantly lower than 500Hz;
- Wind farm size is significantly larger than 150MW.

In order to develop the concept for application in a wide range of wind farms and to give maximum flexibility in the design process, use of a three-phase DC-DC converter is advantageous.

9.4 Further Work

The conclusion that the DC grid is practical and competitive with the alternatives leads on to a number promising research topics concerning its development. These have been identified in chapters 7 and 8. They include:

- Control of the DC-DC converters and the DC grid as a whole.
- Design of an additional DC-DC step up conversion stage for large wind farms and estimation of the transmission distance and power transfer level above which it is economic compared to the ±50kV solution.
- Thorough economic comparison of all the components in the AC and DC solutions for offshore wind farms.
- Behaviour under fault conditions and protection for all components of the DC grid.

The modelling methods undertaken are also applicable to closely related fields of research and their application to these areas provides more opportunities for further research. This includes:

- Predicting and understanding resonance in AC offshore wind farms.
- Application of FEM to design and performance assessment of AC single core cables with the objective of preventing excessive losses in metallic armour and minimising material cost and weight.

The development of the DC grid concept will benefit greatly from continued cooperation between academic and industrial partners. In choosing the long term project development path and identifying challenges that must be addressed, the research undertaken and the further research proposed here can make a very significant contribution. In order for the research to make a practical contribution to addressing the challenges identified in developing offshore wind power, opportunities to implement it in a wind farm are required.

Appendix A: Analytical Calculation of Cable Behaviour and Comparison to FEM Approach

In order to help understand the results from the FEM work and to show why it is such a useful tool for the work in chapter 3, this section examines the analytical approach to solving coaxial cables and compares it to the FEM approach.

Analytical Approach

The work in this section is based in part on the work in [57], which provides a rigorous and lucid explanation of the application of Maxwell's equations (among others) to this problem.

Figure A.1 shows the results from FEM analysis of an inner copper conductor of radius 5.5mm (cross-sectional area 95mm^2), surrounded by a layer of insulation 8mm thick then a layer of lead 30mm thick. The lead is modelled as having zero voltage gradient (equivalent to it being grounded along its length). There are two reasons for modelling such a thick layer of lead, which are explained when deriving the analytical solution. The return conductor is surrounded by identical layers and its centre is 200mm to the right of the centre of the first conductor. The total current in the core is of magnitude 1A and it is sinusoidal with frequency 1kHz.

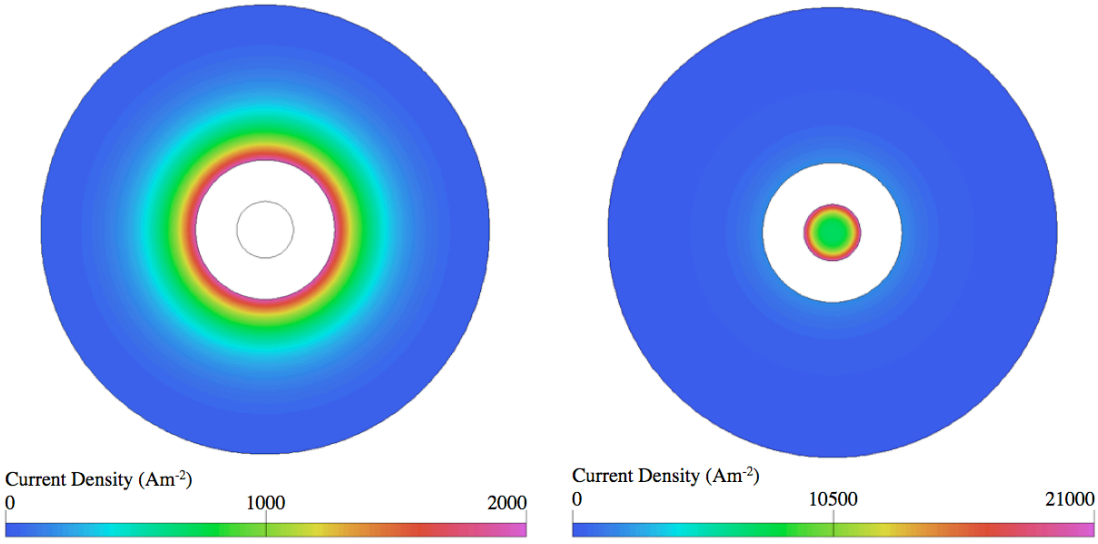

(a) (b)

Figure A.1. Simulated current density distribution in conductor and lead layer. Core separation is 200mm. (a) Lead layer only, (b) copper conductor and lead layer.

The analysis begins with two of Maxwell's equations, (3.2) and (3.3) (Faraday's law of induction and Ampère's circuital law with Maxwell's correction), along with equations (3.5) and (3.6).

$$\nabla \times \underline{E} = -\frac{\partial \underline{B}}{\partial t} \tag{3.2}$$

$$\nabla \times \underline{H} = \underline{J} + \frac{\partial \underline{D}}{\partial t} \tag{3.3}$$

$$\underline{J} = \sigma \underline{E} \tag{3.5}$$

$$\underline{B} = \mu \underline{H} \tag{3.6}$$

Substituting (3.5) and (3.6) into (3.2) to eliminate $\underline{E}$ and $\underline{B}$, approximating the displacement current, $\underline{D}$, to zero and then expanding equations (3.2) and (3.3) into their component parts in circular cylindrical coordinates gives equations (A.1) and (A.2).

$$\begin{pmatrix} \frac{1}{r}\frac{\partial J_z}{\partial \theta} - \frac{\partial J_\theta}{\partial z} \\ \frac{\partial J_r}{\partial z} - \frac{\partial J_z}{\partial r} \\ \frac{1}{r}\left[\frac{\partial}{\partial r}(rJ_\theta) - \frac{\partial J_r}{\partial \theta}\right] \end{pmatrix} = -\mu\sigma\frac{\partial}{\partial t}\begin{pmatrix} H_r \\ H_\theta \\ H_z \end{pmatrix} \tag{A.1}$$

$$\begin{pmatrix} \frac{1}{r}\frac{\partial H_z}{\partial \theta} - \frac{\partial H_\theta}{\partial z} \\ \frac{\partial H_r}{\partial z} - \frac{\partial H_z}{\partial r} \\ \frac{1}{r}\left[\frac{\partial}{\partial r}(rH_\theta) - \frac{\partial H_r}{\partial \theta}\right] \end{pmatrix} = \begin{pmatrix} J_r \\ J_\theta \\ J_z \end{pmatrix} \tag{A.2}$$

Where the subscript denotes the component in the coordinate system (r, θ, z).

Since the driving current is sinusoidal and the permeability is assumed to be constant, it can be assumed that all currents and magnetic fields are sinusoidal and so differentiating with respect to time is equivalent to multiplying by jω.

Referring to Figure A.1, the proximity effect is not noticeable. This is because the layer of lead is thick enough to exclude almost all the influence of the return conductor. This symmetry allows equations (A.1) and (A.2) to be greatly simplified, which is one reason for choosing the particularly thick layer of lead.

Since there is (almost) angular symmetry, derivatives with respect to θ can be approximated to zero. In addition:

- The model is symmetrical in the z-direction, so derivatives with respect to z are zero.
- All currents are in the z-direction, so J_θ and J_r components are zero.
- All magnetic fields are in the θ direction and so H_z and H_r are zero.

This reduces (A.1) and (A.2) to equations (A.3) and (A.4).

$$\frac{\partial J_z}{\partial r} = j\omega\mu\sigma H_\theta \tag{A.3}$$

$$\frac{1}{r}\left[\frac{\partial}{\partial r}(rH_\theta)\right] = \frac{H_\theta}{r} + \frac{\partial H_\theta}{\partial r} = J_z \tag{A.4}$$

Where the product rule is applied in equation (A.4). Equation (A.4) is then differentiated with respect to r, as shown in equation (A.5).

$$\frac{\partial J_z}{\partial r} = \frac{\partial^2 H_\theta}{\partial r^2} + \frac{1}{r}\frac{\partial H_\theta}{\partial r} - \frac{H_\theta}{r^2} \tag{A.5}$$

This is then substituted into equation (A.3) to eliminate J_z and give a second order differential equation in H_θ, equation (A.6).

$$\frac{\partial^2 H_\theta}{\partial r^2} + \frac{1}{r}\frac{\partial H_\theta}{\partial r} - \frac{H_\theta}{r^2} - j\omega\mu\sigma H_\theta = 0 \tag{A.6}$$

Making the following substitutions:

$$\delta = \sqrt{\frac{2}{\sigma\omega\mu}} \tag{3.10}$$

$$\alpha = \frac{1+j}{\delta}$$

equation (A.6) becomes

$$\frac{\partial^2 H_\theta}{\partial r^2} + \frac{1}{r}\frac{\partial H_\theta}{\partial r} - \left(\frac{1}{r^2} + \alpha^2\right)H_\theta = 0 \tag{A.7}$$

Solving (A.7) using Maple gives the expression (A.8) for the H-field.

$$H_\theta(r) = C_1\text{BesselI}(1, \alpha r) + C_2\text{BesselK}(1, \alpha r) \tag{A.8}$$

Where:

BesselI(1, αr) and BesselK(1, αr) are modified Bessel functions of the first and second kind respectively.

C_1 and C_2 are constants defined by the boundary conditions.

In order to derive the boundary conditions, the integral form of Ampère's circuital law is required, as shown in equation (3.11).

$$\oint_C \underline{B} \cdot d\underline{l} = \mu_0 I_{enclosed} \tag{3.11}$$

Where the curve C encloses the current $I_{enclosed}$. For the copper conductor, this equation gives the two boundary conditions:

At r=0, the centre of the conductor, the magnetic field is zero and therefore H_θ =0.

At the outer edge of the conductor, the current enclosed is 1A (magnitude) and this gives the size of the B-field and therefore the H-field.

For the lead layer, the first boundary condition is given at the inner edge of the layer where the current enclosed is 1A. The second boundary condition depends on the fact that the lead layer is thick enough to almost contain the magnetic field (by action of induced currents cancelling out the magnetic field from the current in the copper conductor). Therefore, the second boundary condition is to set H_θ =0 at the outer edge of the lead layer. Enabling this boundary condition to be set is the second reason for modelling a very thick lead layer.

The resulting plots of current density against distance from the conductor centre for the FEM and analytical approaches are shown in Figure A.2 and Figure A.3 respectively.

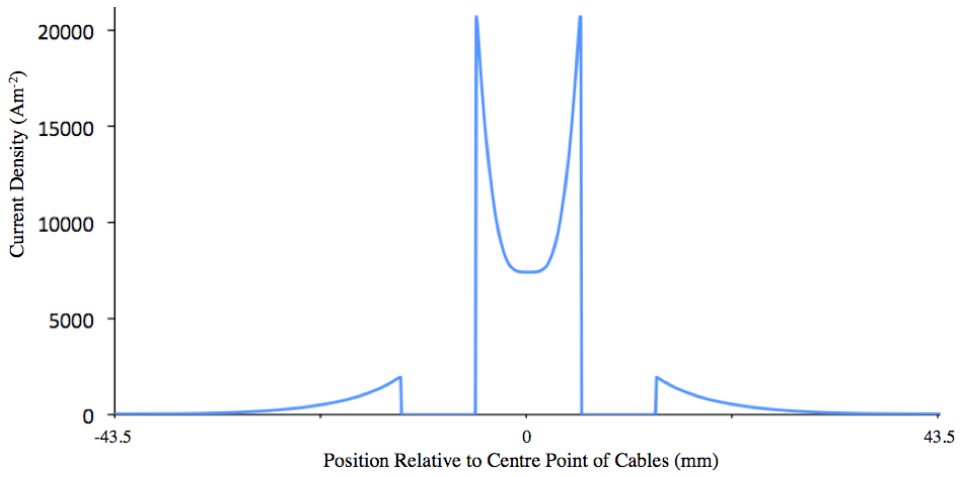

Figure A.2. Current density profile across conducting materials from FEM results.

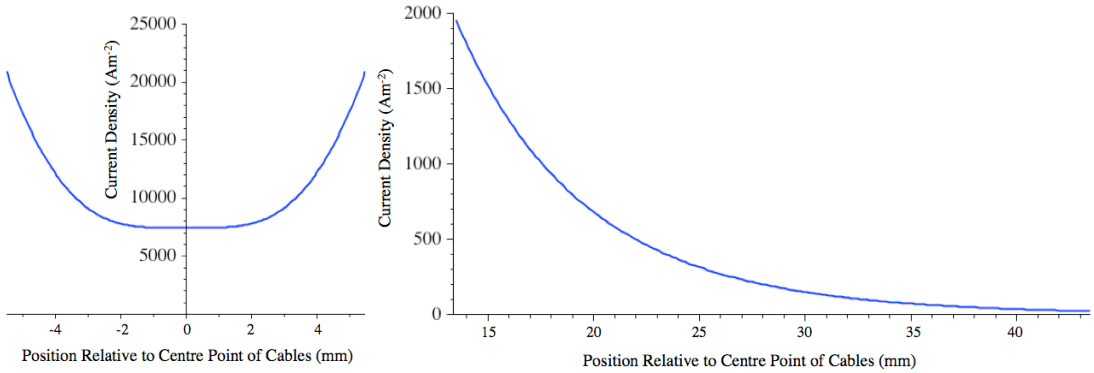

(a) (b)

Figure A.3. Current density profile across conducting materials from analytical calculations for (a) copper conductor and (b) lead layer.

Current density values at a range of points for each approach are shown in Table A.1.

	FEM Model	Analytical Model
Current Density at Centre of Conductor (Am^{-2})	7411	7407
Current Density at Outer Edge of Conductor (Am^{-2})	20693	20873
Current Density at Inner Edge of Lead Layer (Am^{-2})	1953	1955
Current Density at Outer Edge of Lead Layer (Am^{-2})	38	20

Table A.1. Current density results at a range of points in the conducting materials.

The results are very closely matched. Any difference is due either to the small error in the FEM modelling or the fact that some H-field does escape the lead layer and interacts with the return conductor, which is why there is significant error in the current calculated at the outer edge of the lead layer. This observation is important when considering a much thinner layer of lead.

Application to Cable Model

The model shown in Figure A.1 was changed so that the lead layer was only 1.6mm thick. This model now has the same dimensions of core, insulation and lead layer as the base case cable 1 modelled in chapter 3. The separation between the cable cores was initially maintained at the same as the model in Figure A.1 (200mm). The resulting current densities from the FEM model are shown in Figure A.3.

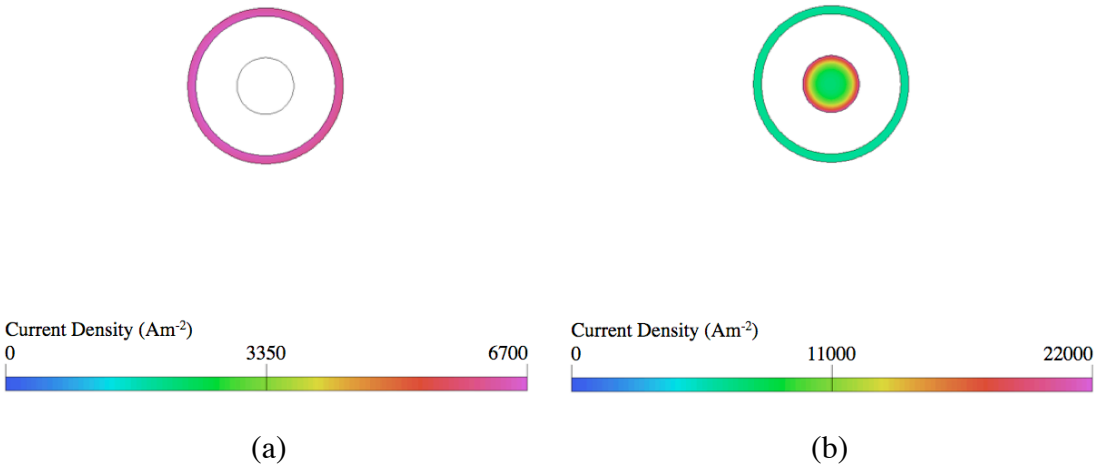

Figure A.4. Simulated current density distribution in conductor and 1.6mm lead layer. Core separation is 200mm. (a) Lead layer only, (b) copper conductor and lead layer.

The current density in the lead layer is much higher than in Figure A.1. The current density in the core has changed very little. Current density values at a range of points for each approach are shown in Table A.2. Where applicable, current density on both sides (i.e. closest to and furthest from the return conductor respectively) are shown to illustrate the proximity effect.

	FEM Model	Analytical Model
Current Density at Centre of Conductor (Am^{-2})	7411	7407
Current Density at Outer Edge of Conductor (Am^{-2})	20811 or 20593	20873
Current Density at Inner Edge of Lead Layer (Am^{-2})	6065 or 6354	-
Current Density at Outer Edge of Lead Layer (Am^{-2})	6360 or 6603	-

Table A.2. Current density results at a range of points in the conducting materials.

Because the main conductors are separated by a significant distance, it is still possible to approximate the model to being symmetrical in θ. For the core, the two boundary conditions still apply as before and therefore the analytical results match the FEM results quite closely. However, it is no longer possible to derive the second boundary condition to solve the equation for the current density in the sheath. It is very clear from the change in current density in the sheath that this boundary condition has changed. This result is not particularly intuitive; however, the experimental validation carried out in chapter 3 confirms it.

The model was changed again, this time bringing the two conductors close together (reducing the separation of the centre points of the conductors to 33mm). The resulting current densities predicted by the FEM are shown in Figure A.5.

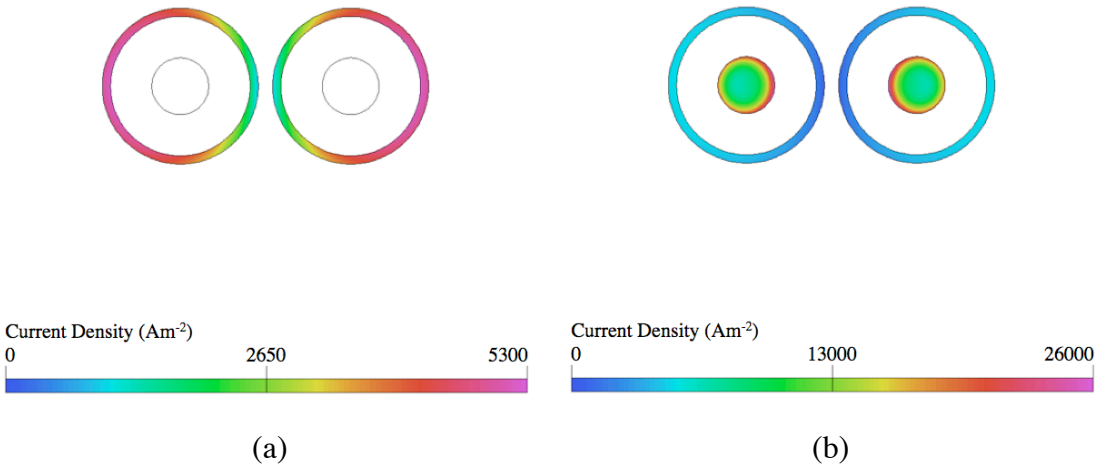

Figure A.5. Simulated current density distribution in conductor and 1.6mm lead layer. Core separation is 33mm. (a) Lead layer only, (b) copper conductor and lead layer.

The symmetry in θ of the model has now been lost and it is no longer possible to apply the analytical method described above. In this case, the FEM provides a practical solution that gives the accuracy of an analytical solution.

Relationship between Inductance and Cable Separation.

One interesting result from chapter 3 was the decrease in inductance for the bipole cables when modelled with a large separation compared to close together. The magnetic B-fields for the models with 1.6mm lead layers are shown in Figure A.6.

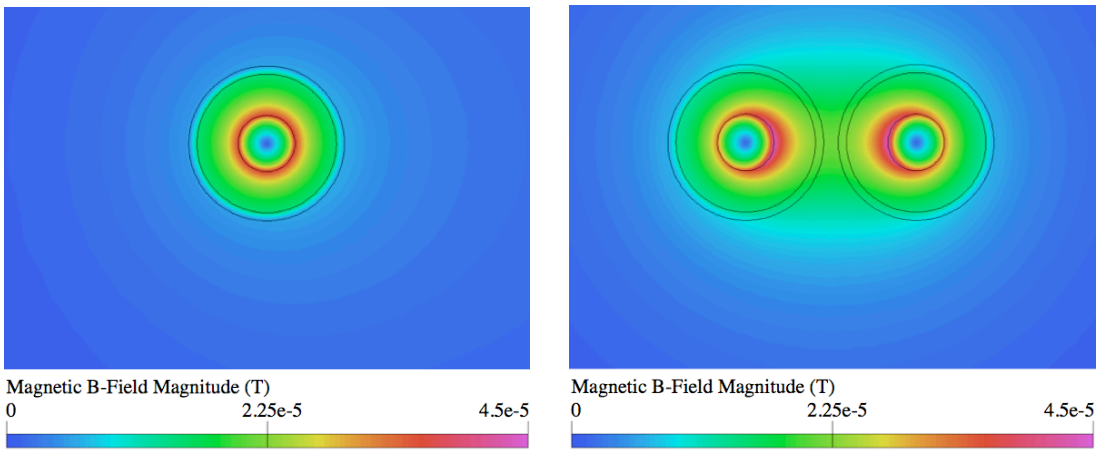

(a) (b)

Figure A.6. Simulated magnetic B-field distribution for conductors surrounded by 1.6mm layer of lead. (a) Separation of conductors is 200mm, (b) Separation of conductors is 33mm.

In the cases here, the inductance for the conductors separated by 200mm is 0.64mH/km and for 33mm separation 0.66mH/km. In order to understand this result, it is necessary to compare Figure A.6(a) and (b). Inductance is proportional to the amount of magnetic energy stored per unit current. The amount of magnetic energy stored is proportional to the magnetic B-field squared (for linear magnetic materials). Therefore, it is possible to understand that more energy is stored with the cables close together, as shown in Figure A.6(b), than far apart, Figure A.6(a). In this case, the FEM provides understanding of the non-intuitive solution.

Appendix B: Components for Single-Phase SLR Experimental Model

The component codes and references to their datasheets or product information from their supplier are given in Table B.1. Further details are in [83].

Component	Code	Reference
DC-DC Controller	UCC25600	[102]
MOSFET Power Driver	IR2110	[103]
LV Side Diodes	1N5817	[104]
HV Side Diodes	1N4148	[105]
Ferrite Inductor Core	TX36/23/15-4C65	[106]
MOSFETs	2SK2613	[107]
Heat Sinks for MOSFETs	TO-220	[108]
Input Smoothing and DC Link Capacitance	ECA1CAM222X	[109]
Output Capacitance	MKS2D022201A00KSSD	[110]
Resonant Capacitance	ECQV1H124JL	[111]
Load Resistor	MP9100	[112]
Transformer Core	ETD29-N97 - B66358GX197	[113]

Table B.1. Component codes and references to supplier information or datasheets.

Appendix C: Frequency Domain Network Calculations

For convenience, Figure 4.7 and equations (4.9), (4.10), and (4.12) are repeated.

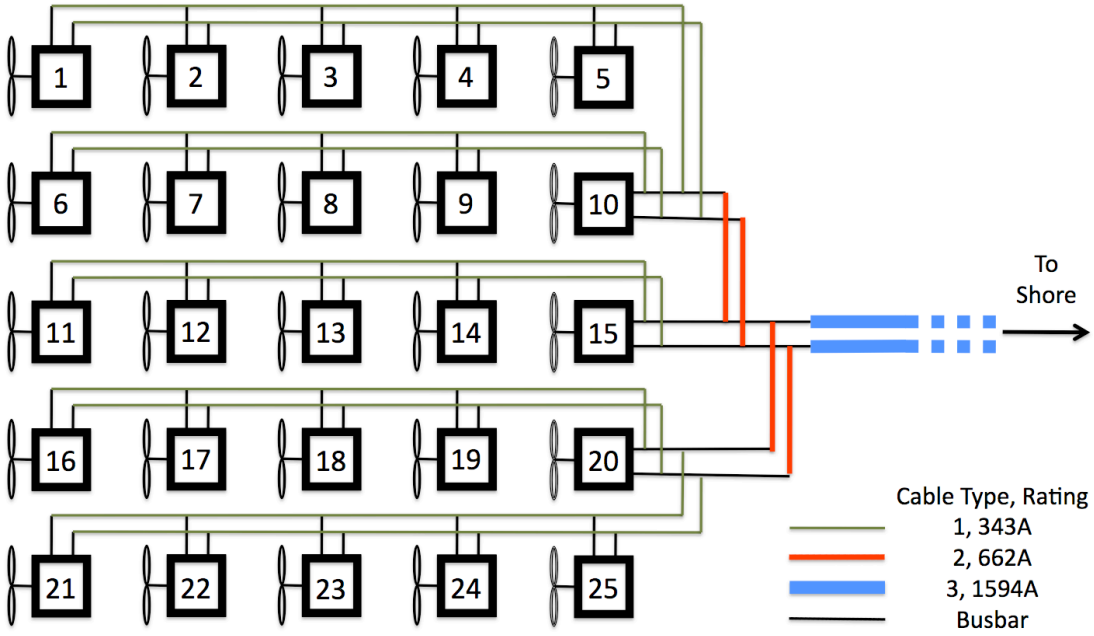

Figure 4.7. Layout of grid with cable types for 25 offshore wind turbines, each with 6MW power output and 600m spacing between turbines.

$$I_S = I_R \cosh(l\gamma) + \frac{V_R}{Z_c} \sinh(l\gamma) \tag{4.9}$$

$$V_S = V_R \cosh(l\gamma) + I_R Z_C \sinh(l\gamma) \tag{4.10}$$

$$Z_{send} = Z_C \frac{Z_R \cosh(l\gamma) + Z_C \sinh(l\gamma)}{Z_C \cosh(l\gamma) + Z_R \sinh(l\gamma)} \tag{4.12}$$

System Admittance

First, an example method for calculating the system admittance from the output of a converter is worked through. The filter capacitors are set at 10μF. The reciprocal of (4.12) is required, which is:

$$Y_{send} = \frac{1}{Z_C} \frac{Y_R Z_C \cosh(l\gamma) + \sinh(l\gamma)}{\cosh(l\gamma) + Y_R Z_C \sinh(l\gamma)} \quad \text{(C.1)}$$

where Y_{send} is the admittance at the sending end of a cable (in the direction along the cable) and Y_R is the admittance at the receiving end.

Choosing converter 2 in Figure 4.7, first note that there are two paths exiting the converter - towards converter 1 or 3. The path towards converter 1 is straightforward. The admittance of the capacitor at converter 1 is $0.000 + j0.063\Omega^{-1}$. Applying equation (C.1) gives an admittance from converter 2 of $0.003 + j0.068\Omega^{-1}$.

The second path is far more complicated and splits up into several paths ending at converters 6, 11, 16, 21 and the onshore converter. To calculate the total admittance, it is necessary to start at the end of each path with its receiving admittance.

For example, the admittance of the capacitor at converter 6 is $0.000 + j0.063\Omega^{-1}$. Again, applying equation (C.1), the admittance from converter 7 along the cable towards 6 is $0.003 + j0.068\Omega^{-1}$. The admittance at converter 7 (for current coming from converter 8) is then the sum of this and the admittance of the capacitor at 7, giving $0.003 + j0.131\Omega^{-1}$. Then the admittance along the cable from 8 to 7 is calculated using equation (C.1) again. In this way, the calculation moves along the path towards converter 2.

At converter 10, the path detailed above joins the other paths. Therefore, the admittance at converter 10 for current from converter 5 is the sum of the admittance to all the paths leaving 10 (except the path to 5, of course) and the admittance of the capacitor at 10.

The total admittance of this second path is 0.129 - j0.073Ω^{-1}. So the path is inductive. The total admittance of the system from converter 2 (not counting its own filter capacitance) is therefore the sum of the two paths, 0.132 - j0.005Ω^{-1}.

Current and Voltage Propagation

Equations (4.9) and (4.10) can be rearranged to give the receiving end voltage and current in terms of those at the sending end [58].

$$I_R = I_S \cosh(l\gamma) - \frac{V_S}{Z_c} \sinh(l\gamma) \tag{C.2}$$

$$V_R = V_S \cosh(l\gamma) - I_S Z_C \sinh(l\gamma) \tag{C.3}$$

Taking converter 2 as an example again, and assuming a 1kHz unfiltered ripple component of 32.12A, the resulting volt rise at the output from converter 2 is calculated. The system admittance is 0.132 - j0.005Ω^{-1} and the admittance of the filter capacitor is 0.000 + j0.063Ω^{-1}. Therefore the total admittance for the ripple is 0.132 + j0.058Ω^{-1}. The resulting volt rise is given by the current divided by the admittance, i.e. 203 - j89.5V.

This voltage causes current to flow towards converter 1 and converter 3. The amount is determined by the admittance in each direction. So 6.70 + j13.6A flows towards converter 1 and 19.8 - j26.4A towards converter 3.

The resulting current and voltage can then be calculated at converters 1 and 3 by applying equations (C.2) and (C.3). For example, at converter 3, the incoming current is 19.7 + j26.5A and the voltage 160 - j96.5V.

The model then uses the value of the voltage and the admittances already calculated in that part of the network to calculate the amount of current that flows into the filter capacitor at converter 3 and the amount that flows along the cable towards converter 4. The sum of these is equal to the current arriving at converter 3 (which is a good check). In this case, 6.06 + j10.0A flows into the capacitor and 13.7 - j36.6A flows along the cable to converter 4. The sum of these equals the incoming current (19.7 + j26.5A), as expected.

Once all currents and voltages, at all frequencies, to and from all converters have been calculated, the total system current and voltage is computed.

Appendix D: System Modelling Approach - Integration of Time and Frequency Domains

The integration of time and frequency domain models is an iterative process in the case of three of the DC-DC converters modelled (the exception being the converter based on the VSC feeding the medium frequency transformer).

The first task is to choose exactly where to draw the line between time and frequency domain modelling. The HV diode bridge must be modelled in the time domain, all cables must be modelled in the frequency domain, but the HV filter capacitor can be modelled in either.

It is both simpler and more computationally efficient to model the capacitor in the frequency domain. This means that the time domain model does not include a capacitor. Instead, the voltage at the output from the diode bridge is modelled as a voltage source for each iterative step in the time domain. The voltage source includes the ripple components of voltage from 1-10kHz for single-phase converters (10 components) and from 3-15kHz for three-phase converters (only 5 components are required due to the significantly lower ripple content).

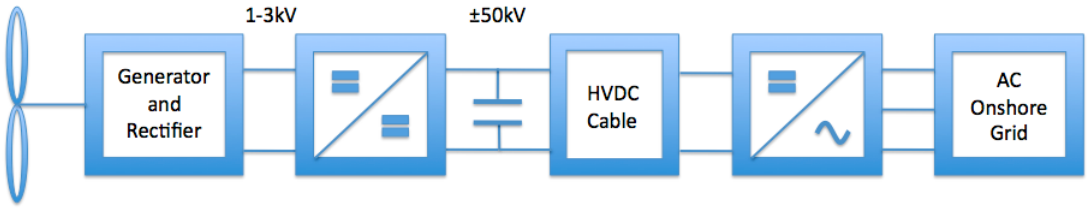

Figure 1.3. Block diagram for single wind turbine in a DC grid with approximate voltage levels.

The line between frequency and time domain is drawn to the left of the filter capacitor, as shown in Figure 1.3. The output from the time domain model for each converter is the unfiltered HVDC current (I_{HV}). This is converted to the frequency domain and, along with the currents from all other converters, used to calculate the voltages at each node. The frequency domain voltage output components are the

converted to a time domain voltage waveform that is used as the voltage source at the converter output in the next time domain iteration.

An example of the outputs from each iterative step follow for the system with the parameters listed:

Single-phase SLR converter;

All converters operating at full power;

Switching phases offset as in case 3;

C_{dc}=2μF;

All models use base case cables at 20ºC;

Transmission distance 100km;

ESR 5mΩ and no protective resistor;

500Hz switching frequency;

Fixed voltage input;

No line or filter inductance.

The output voltage and unfiltered HVDC current components at converter 1 (as shown in Figure 4.7) are shown in Table D.1 and Table D.2.

	Voltage Magnitude (V)						
Frequency (kHz)	Start	Iteration 1	Iteration 2	Iteration 3	Iteration 4	Iteration 5	Final
DC	51961.5	51961.5	51961.5	51961.5	51961.5	51961.5	51961.5
1	0.0	213.9	230.5	230.4	230.4	230.4	230.4
2	0.0	101.7	107.5	107.1	107.1	107.1	107.1
3	0.0	54.7	59.5	60.1	60.1	60.1	60.1
4	0.0	25.4	25.8	25.9	25.9	25.9	25.9
5	0.0	54.2	54.6	54.5	54.5	54.5	54.5
6	0.0	33.7	33.1	33.1	33.1	33.1	33.1
7	0.0	21.6	21.4	21.3	21.3	21.3	21.3
8	0.0	10.2	10.9	11.1	11.1	11.1	11.1
9	0.0	3.6	4.0	4.2	4.2	4.2	4.2
10	0.0	10.7	11.0	10.9	10.9	10.9	10.9

Table D.1. Output voltage components at converter 1 for each iteration.

	Unfiltered HVDC Current Magnitude (A)					
Frequency (kHz)	Iteration 1	Iteration 2	Iteration 3	Iteration 4	Iteration 5	Final
DC	57.7	57.7	57.7	57.7	57.7	57.7
1	30.0	29.6	29.6	29.6	29.6	29.6
2	9.8	9.8	9.8	9.8	9.8	9.8
3	5.9	6.0	6.0	6.0	6.0	6.0
4	4.2	4.3	4.3	4.3	4.3	4.3
5	3.3	3.4	3.4	3.4	3.4	3.4
6	2.7	2.7	2.7	2.7	2.7	2.7
7	2.2	2.3	2.3	2.3	2.3	2.3
8	1.9	2.0	2.0	2.0	2.0	2.0
9	1.7	1.7	1.7	1.7	1.7	1.7
10	1.5	1.5	1.5	1.5	1.5	1.5

Table D.2. Unfiltered HVDC current components at converter 1 for each iteration.

In this case the iteration converges quickly as a result of the relatively low voltage *THD* (maximum of 0.52%). An example where the voltage *THD* is higher is for the same system setup except with converters switching with phases offset as in case 1 and C_{dc}=4.9μF. These results are shown in Table D.3 and Table D.4.

	Voltage Magnitude (V)						
Frequency (kHz)	Start	Iteration 1	Iteration 2	Iteration 3	Iteration 4	Iteration 5	Final
DC	51961.5	51961.5	51961.5	51961.5	51961.5	51961.5	51961.5
1	0.0	1588.8	1633.2	1634.7	1633.2	1633.5	1633.4
2	0.0	406.5	416.6	417.9	418.1	418.0	418.0
3	0.0	113.4	114.2	114.4	114.5	114.4	114.4
4	0.0	51.3	50.6	51.0	51.0	51.0	51.0
5	0.0	20.5	20.3	20.6	20.6	20.6	20.6
6	0.0	5.5	6.1	6.1	6.1	6.1	6.1
7	0.0	3.6	3.7	3.7	3.7	3.7	3.7
8	0.0	5.3	5.4	5.5	5.5	5.5	5.5
9	0.0	5.4	5.6	5.7	5.7	5.7	5.7
10	0.0	4.8	5.0	5.0	5.0	5.0	5.0

Table D.3. Output voltage components at converter 1 for each iteration.

	Unfiltered HVDC Current Magnitude (A)					
Frequency (kHz)	Iteration 1	Iteration 2	Iteration 3	Iteration 4	Iteration 5	Final
DC	57.7	57.7	57.7	57.7	57.7	57.7
1	30.0	26.2	26.1	26.1	26.1	26.1
2	9.8	10.3	10.3	10.3	10.3	10.3
3	5.9	6.0	6.0	6.0	6.0	6.0
4	4.2	4.3	4.3	4.3	4.3	4.3
5	3.3	3.3	3.3	3.3	3.3	3.3
6	2.7	2.7	2.7	2.7	2.7	2.7
7	2.2	2.3	2.3	2.3	2.3	2.3
8	1.9	1.9	1.9	1.9	1.9	1.9
9	1.7	1.7	1.7	1.7	1.7	1.7
10	1.5	1.5	1.5	1.5	1.5	1.5

Table D.4. Unfiltered HVDC current components at converter 1 for each iteration.

Convergence is slightly slower in this case. The maximum voltage *THD* in the system is 3.25%.

The main approximation that is required using this approach is to neglect ripple voltages at frequencies of 11kHz and higher. By doing so, the model effectively treats the capacitive reactance at these frequencies as zero. This is a reasonable approximation because capacitive reactance decreases with increasing frequency and because the current components at these frequencies are small.

Appendix E: System Modelling Results

A selection of results from the modelling described in chapters 6 and 7 is presented.

In each case table (a) shows the fundamental voltage ripple component and THD at the output of each converter. Table (b) shows the fundamental ripple current and the composition of the losses in each section of cable in the wind farm. For the transmission cable, the peak AC losses are shown and the fundamental ripple current at the sending end (i.e. the wind farm end) of the cable.

Some of the modelling parameters for each individual case are given in the caption for each table. The parameters that are not stated can be assumed to be as listed here:

All models use base case cables at 20ºC;

Transmission distance 100km;

ESR 5mΩ and no protective resistor unless stated;

500Hz switching frequency;

Fixed voltage input;

No line or filter inductance.

Converter Number	Magnitude Fundamental Voltage Ripple (V)	Voltage THD
1	230.38	0.52%
2	205.18	0.46%
3	144.17	0.35%
4	72.82	0.24%
5	36.23	0.18%
6	205.36	0.50%
7	175.90	0.43%
8	110.33	0.31%
9	38.58	0.21%
10	26.09	0.14%
11	182.88	0.46%
12	156.29	0.39%
13	96.18	0.29%
14	29.46	0.21%
15	15.96	0.12%
16	195.52	0.50%
17	172.18	0.43%
18	116.57	0.33%
19	53.05	0.24%
20	13.86	0.13%
21	211.06	0.50%
22	186.20	0.42%
23	127.46	0.32%
24	59.39	0.28%
25	20.93	0.22%

(a)

Converter Numbers at Ends of Cable Section		DC Losses (W/m)	Maximum AC Losses (W/m)	Maximum Total Losses (W/m)	Fundamental Ripple Current Component Magnitude (A)	Cable Rated Losses (W/m)
1	2	0.627	0.717	1.344	32.26	28.2
2	3	2.510	1.581	4.091	52.49	28.2
3	4	5.648	1.710	7.357	53.75	28.2
4	5	10.043	0.852	10.895	33.26	28.2
5	10	15.698	0.242	15.941	7.74	28.2
6	7	0.628	0.696	1.324	31.94	28.2
7	8	2.513	1.678	4.191	53.38	28.2
8	9	5.655	1.680	7.335	54.14	28.2
9	10	10.056	0.918	10.973	32.82	28.2
10	15	19.877	0.263	20.140	12.43	33.2
11	12	0.629	0.707	1.336	32.12	28.2
12	13	2.515	1.697	4.212	53.92	28.2
13	14	5.659	1.662	7.321	54.00	28.2
14	15	10.064	0.933	10.997	32.78	28.2
15	Shore	26.628	0.006	26.634	0.89	41.3
16	17	0.628	0.751	1.379	32.65	28.2
17	18	2.513	1.732	4.245	53.97	28.2
18	19	5.655	1.650	7.305	53.29	28.2
19	20	10.056	0.961	11.017	32.23	28.2
20	15	19.877	0.255	20.132	11.14	33.2
21	22	0.627	0.798	1.426	32.74	28.2
22	23	2.510	1.707	4.216	52.61	28.2
23	24	5.648	1.592	7.240	52.14	28.2
24	25	10.043	0.684	10.728	31.62	28.2
25	20	15.698	0.367	16.066	6.51	28.2

(b)

Table E.1. Single-phase SLR converter, switching phases offset case 3, full power, C_{dc}=2μF.

Converter Number	Magnitude Fundamental Voltage Ripple (V)	Voltage THD
1	1019.25	1.99%
2	1017.30	1.98%
3	1013.23	1.98%
4	1007.34	1.96%
5	1000.08	1.95%
6	1002.83	1.96%
7	1001.76	1.95%
8	999.42	1.95%
9	996.06	1.94%
10	992.00	1.94%
11	983.47	1.92%
12	983.45	1.92%
13	983.17	1.92%
14	982.80	1.92%
15	982.55	1.92%
16	1002.83	1.96%
17	1001.76	1.95%
18	999.42	1.95%
19	996.06	1.94%
20	992.00	1.94%
21	1019.25	1.99%
22	1017.30	1.98%
23	1013.23	1.98%
24	1007.34	1.96%
25	1000.08	1.95%

(a)

Converter Numbers at Ends of Cable Section		DC Losses (W/m)	Maximum AC Losses (W/m)	Maximum Total Losses (W/m)	Fundamental Ripple Current Component Magnitude (A)	Cable Rated Losses (W/m)
1	2	0.627	0.004	0.632	2.82	28.2
2	3	2.510	0.017	2.527	5.56	28.2
3	4	5.648	0.036	5.683	8.16	28.2
4	5	10.043	0.058	10.102	10.51	28.2
5	10	15.698	0.083	15.781	12.57	28.2
6	7	0.628	0.004	0.632	2.50	28.2
7	8	2.513	0.014	2.526	4.82	28.2
8	9	5.655	0.028	5.683	7.02	28.2
9	10	10.056	0.045	10.101	9.02	28.2
10	15	19.877	0.209	20.086	23.20	33.2
11	12	0.629	0.004	0.633	2.28	28.2
12	13	2.515	0.014	2.529	4.23	28.2
13	14	5.659	0.027	5.686	6.09	28.2
14	15	10.064	0.040	10.104	7.78	28.2
15	Shore	26.628	0.623	27.251	54.75	41.3
16	17	0.628	0.004	0.632	2.50	28.2
17	18	2.513	0.014	2.526	4.82	28.2
18	19	5.655	0.028	5.683	7.02	28.2
19	20	10.056	0.045	10.101	9.02	28.2
20	15	19.877	0.209	20.086	23.20	33.2
21	22	0.627	0.004	0.632	2.82	28.2
22	23	2.510	0.017	2.527	5.56	28.2
23	24	5.648	0.036	5.683	8.16	28.2
24	25	10.043	0.058	10.102	10.51	28.2
25	20	15.698	0.083	15.781	12.57	28.2

(b)

Table E.2. Single-phase SLR converter, converters switching in phase, full power, C_{dc}=4.9μF.

Converter Number	Magnitude Fundamental Voltage Ripple (V)	Voltage THD
1	1633.42	3.25%
2	1541.41	3.06%
3	1360.29	2.69%
4	1097.26	2.16%
5	765.26	1.49%
6	998.31	2.15%
7	933.74	1.99%
8	807.06	1.68%
9	624.50	1.26%
10	399.95	0.77%
11	711.07	1.66%
12	646.39	1.49%
13	519.60	1.18%
14	336.60	0.74%
15	114.38	0.23%
16	1029.11	2.25%
17	951.59	2.06%
18	799.43	1.70%
19	578.97	1.20%
20	299.41	0.59%
21	1007.09	2.07%
22	950.05	1.95%
23	838.46	1.70%
24	678.65	1.36%
25	484.37	0.95%

(a)

Converter Numbers at Ends of Cable Section		DC Losses (W/m)	Maximum AC Losses (W/m)	Maximum Total Losses (W/m)	Fundamental Ripple Current Component Magnitude (A)	Cable Rated Losses (W/m)
1	2	0.627	2.847	3.474	70.34	28.2
2	3	2.510	10.957	13.466	139.26	28.2
3	4	5.648	23.057	28.705	203.71	28.2
4	5	10.043	37.440	47.483	261.74	28.2
5	10	15.698	52.151	67.850	311.47	28.2
6	7	0.628	1.805	2.433	49.03	28.2
7	8	2.513	6.765	9.278	96.82	28.2
8	9	5.655	13.745	19.400	141.38	28.2
9	10	10.056	21.374	31.430	181.29	28.2
10	15	19.877	73.624	93.501	439.68	33.2
11	12	0.629	1.735	2.363	48.58	28.2
12	13	2.515	6.462	8.977	95.53	28.2
13	14	5.659	13.008	18.667	138.71	28.2
14	15	10.064	19.943	30.007	176.35	28.2
15	Shore	26.628	0.010	26.638	6.37	41.3
16	17	0.628	2.387	3.015	58.19	28.2
17	18	2.513	8.945	11.458	114.46	28.2
18	19	5.655	18.071	23.726	165.92	28.2
19	20	10.056	27.746	37.802	210.42	28.2
20	15	19.877	56.219	76.095	380.40	33.2
21	22	0.627	1.207	1.834	43.56	28.2
22	23	2.510	4.564	7.073	86.01	28.2
23	24	5.648	9.398	15.046	125.43	28.2
24	25	10.043	14.848	24.891	160.37	28.2
25	20	15.698	20.122	35.820	189.67	28.2

(b)

Table E.3. Single-phase SLR converter, switching phases offset case 1, full power, C_{dc}=4.9µF.

Converter Number	Magnitude Fundamental Voltage Ripple (V)	Voltage THD
1	110.16	0.29%
2	76.52	0.20%
3	21.48	0.09%
4	57.03	0.16%
5	88.02	0.28%
6	110.80	0.29%
7	77.82	0.20%
8	23.86	0.09%
9	56.31	0.16%
10	87.16	0.27%
11	111.16	0.29%
12	78.91	0.20%
13	26.31	0.10%
14	55.81	0.15%
15	86.28	0.27%
16	110.80	0.29%
17	77.82	0.20%
18	23.86	0.09%
19	56.31	0.16%
20	87.16	0.27%
21	110.16	0.29%
22	76.52	0.20%
23	21.48	0.09%
24	57.03	0.16%
25	88.02	0.28%

(a)

Converter Numbers at Ends of Cable Section		DC Losses (W/m)	Maximum AC Losses (W/m)	Maximum Total Losses (W/m)	Fundamental Ripple Current Component Magnitude (A)	Cable Rated Losses (W/m)
1	2	0.627	0.805	1.432	33.07	28.2
2	3	2.510	1.728	4.238	53.12	28.2
3	4	5.648	1.751	7.399	51.78	28.2
4	5	10.043	0.848	10.891	30.18	28.2
5	10	15.698	0.003	15.701	1.19	28.2
6	7	0.628	0.805	1.434	33.10	28.2
7	8	2.513	1.726	4.239	53.24	28.2
8	9	5.655	1.757	7.412	52.09	28.2
9	10	10.056	0.860	10.916	30.55	28.2
10	15	19.877	0.007	19.883	2.09	33.2
11	12	0.629	0.808	1.437	33.12	28.2
12	13	2.515	1.725	4.239	53.34	28.2
13	14	5.659	1.765	7.424	52.31	28.2
14	15	10.064	0.883	10.947	30.87	28.2
15	Shore	26.628	0.019	26.647	4.81	41.3
16	17	0.628	0.805	1.434	33.10	28.2
17	18	2.513	1.726	4.239	53.24	28.2
18	19	5.655	1.757	7.412	52.09	28.2
19	20	10.056	0.860	10.916	30.55	28.2
20	15	19.877	0.007	19.883	2.09	33.2
21	22	0.627	0.805	1.432	33.07	28.2
22	23	2.510	1.728	4.238	53.12	28.2
23	24	5.648	1.751	7.399	51.78	28.2
24	25	10.043	0.848	10.891	30.18	28.2
25	20	15.698	0.003	15.701	1.19	28.2

(b)

Table E.4. Single-phase SLR converter, switching phases offset case 2, full power, C_{dc}=4.9µF.

Converter Number	Magnitude Fundamental Voltage Ripple (V)	Voltage THD
1	342.51	0.68%
2	301.25	0.60%
3	217.65	0.44%
4	130.08	0.28%
5	79.07	0.20%
6	262.94	0.56%
7	221.31	0.46%
8	139.55	0.32%
9	61.33	0.19%
10	40.34	0.12%
11	253.23	0.54%
12	215.13	0.45%
13	136.38	0.31%
14	52.29	0.17%
15	8.50	0.08%
16	272.98	0.57%
17	232.20	0.48%
18	151.55	0.34%
19	70.43	0.19%
20	30.66	0.10%
21	236.91	0.49%
22	194.34	0.39%
23	116.76	0.27%
24	53.84	0.20%
25	50.83	0.20%

(a)

Converter Numbers at Ends of Cable Section		DC Losses (W/m)	Maximum AC Losses (W/m)	Maximum Total Losses (W/m)	Fundamental Ripple Current Component Magnitude (A)	Cable Rated Losses (W/m)
1	2	0.627	0.979	1.607	39.68	28.2
2	3	2.510	2.340	4.849	65.26	28.2
3	4	5.648	2.480	8.128	66.31	28.2
4	5	10.043	0.993	11.036	41.70	28.2
5	10	15.698	0.757	16.456	32.06	28.2
6	7	0.628	0.971	1.599	37.47	28.2
7	8	2.513	2.227	4.739	62.61	28.2
8	9	5.655	2.332	7.987	61.75	28.2
9	10	10.056	0.852	10.908	35.75	28.2
10	15	19.877	0.953	20.830	45.47	33.2
11	12	0.629	0.985	1.613	37.75	28.2
12	13	2.515	2.274	4.789	63.94	28.2
13	14	5.659	2.383	8.042	63.38	28.2
14	15	10.064	0.954	11.018	38.47	28.2
15	Shore	26.628	0.002	26.631	0.47	41.3
16	17	0.628	0.991	1.619	38.98	28.2
17	18	2.513	2.252	4.764	63.79	28.2
18	19	5.655	2.245	7.899	61.15	28.2
19	20	10.056	0.818	10.874	35.66	28.2
20	15	19.877	0.824	20.700	38.17	33.2
21	22	0.627	1.028	1.655	37.40	28.2
22	23	2.510	2.058	4.567	58.65	28.2
23	24	5.648	1.871	7.519	55.18	28.2
24	25	10.043	0.519	10.562	28.79	28.2
25	20	15.698	0.530	16.229	18.76	28.2

(b)

Table E.5. Single-phase SLR converter, switching phases offset case 3, full power, C_{dc}=4.9µF.

Converter Number	Magnitude Fundamental Voltage Ripple (V)	Voltage THD
1	500.86	1.00%
2	513.71	1.02%
3	496.42	0.98%
4	441.86	0.88%
5	379.21	0.76%
6	612.77	1.25%
7	585.54	1.18%
8	510.80	1.03%
9	416.02	0.84%
10	349.05	0.70%
11	519.34	1.04%
12	471.77	0.94%
13	390.30	0.78%
14	330.96	0.67%
15	308.37	0.62%
16	312.34	0.68%
17	268.70	0.59%
18	230.04	0.50%
19	241.25	0.51%
20	260.10	0.53%
21	93.91	0.40%
22	68.61	0.32%
23	101.35	0.34%
24	152.67	0.40%
25	207.07	0.46%

(a)

Converter Numbers at Ends of Cable Section		DC Losses (W/m)	Maximum AC Losses (W/m)	Maximum Total Losses (W/m)	Fundamental Ripple Current Component Magnitude (A)	Cable Rated Losses (W/m)
1	2	0.638	0.719	1.357	31.51	28.2
2	3	2.552	1.754	4.306	54.83	28.2
3	4	5.742	2.332	8.074	64.18	28.2
4	5	10.212	1.839	12.051	54.54	28.2
5	10	15.962	0.639	16.601	29.82	28.2
6	7	0.639	0.861	1.499	35.49	28.2
7	8	2.555	2.385	4.939	63.90	28.2
8	9	5.750	2.928	8.678	71.70	28.2
9	10	10.225	1.768	11.993	50.41	28.2
10	15	20.210	1.721	21.931	62.58	33.2
11	12	0.639	0.885	1.524	37.26	28.2
12	13	2.557	2.154	4.711	61.89	28.2
13	14	5.754	1.732	7.487	55.64	28.2
14	15	10.233	0.697	10.929	27.97	28.2
15	Shore	15.640	0.067	15.707	17.18	41.3
16	17	0.639	0.793	1.432	33.69	28.2
17	18	2.557	1.495	4.051	49.08	28.2
18	19	5.753	1.114	6.868	42.20	28.2
19	20	5.753	1.050	6.803	40.01	28.2
20	15	5.055	2.087	7.142	70.91	33.2
21	22	0.639	0.714	1.353	30.54	28.2
22	23	2.557	1.389	3.946	47.59	28.2
23	24	2.557	1.285	3.841	46.32	28.2
24	25	2.557	1.194	3.751	44.33	28.2
25	20	2.557	1.185	3.741	41.67	28.2

(b)

Table E.6. Single-phase SLR converter, switching phases offset case 3, turbines 15, 19, 20, 23, 24, 25 off and all others full power, C_{dc}=2µF.

Converter Number	Magnitude Fundamental Voltage Ripple (V)	Voltage THD
1	268.31	0.60%
2	241.69	0.53%
3	177.57	0.42%
4	104.26	0.29%
5	67.68	0.21%
6	208.84	0.52%
7	169.17	0.43%
8	108.22	0.31%
9	63.53	0.22%
10	54.83	0.16%
11	150.94	0.45%
12	113.10	0.36%
13	53.96	0.26%
14	10.92	0.19%
15	32.45	0.12%
16	169.22	0.50%
17	138.34	0.42%
18	86.85	0.31%
19	37.94	0.22%
20	17.32	0.12%
21	208.24	0.51%
22	173.86	0.42%
23	117.53	0.33%
24	64.52	0.27%
25	36.00	0.20%

(a)

Converter Numbers at Ends of Cable Section		DC Losses (W/m)	Maximum AC Losses (W/m)	Maximum Total Losses (W/m)	Fundamental Ripple Current Component Magnitude (A)	Cable Rated Losses (W/m)
1	2	0.637	0.755	1.391	32.90	28.2
2	3	2.547	1.658	4.205	53.62	28.2
3	4	5.731	1.812	7.543	55.12	28.2
4	5	10.191	0.888	11.079	34.03	28.2
5	10	15.930	0.264	16.195	10.02	28.2
6	7	0.638	0.707	1.344	32.36	28.2
7	8	1.843	1.280	3.123	45.81	28.2
8	9	3.674	1.091	4.765	41.20	28.2
9	10	6.131	0.592	6.723	21.46	28.2
10	15	15.620	0.440	16.060	25.60	33.2
11	12	0.638	0.715	1.353	32.22	28.2
12	13	1.844	1.247	3.092	45.06	28.2
13	14	3.575	1.056	4.631	39.84	28.2
14	15	5.874	0.642	6.517	21.09	28.2
15	Shore	16.839	0.005	16.844	1.81	41.3
16	17	0.638	0.761	1.399	32.77	28.2
17	18	1.843	1.304	3.147	45.50	28.2
18	19	3.573	1.129	4.702	40.46	28.2
19	20	5.743	0.748	6.491	23.09	28.2
20	15	10.559	0.506	11.065	28.54	33.2
21	22	0.637	0.773	1.410	33.03	28.2
22	23	1.842	1.249	3.090	44.76	28.2
23	24	3.570	1.019	4.589	39.91	28.2
24	25	5.737	0.467	6.205	22.69	28.2
25	20	8.264	0.508	8.772	18.21	28.2

(b)

Table E.7. Single-phase SLR converter, switching phases offset case 3, wake effect with wind direction along diagonal from turbine 1 to turbine 25, C_{dc}=2μF.

Converter Number	Magnitude Fundamental Voltage Ripple (V)	Voltage THD
1	50.77	0.10%
2	42.68	0.09%
3	34.21	0.07%
4	25.40	0.05%
5	16.58	0.03%
6	10.12	0.02%
7	9.84	0.02%
8	9.36	0.02%
9	8.94	0.02%
10	8.95	0.02%
11	7.05	0.01%
12	6.85	0.01%
13	6.52	0.01%
14	6.22	0.01%
15	6.23	0.01%
16	5.91	0.01%
17	5.75	0.01%
18	5.47	0.01%
19	5.22	0.01%
20	5.23	0.01%
21	5.43	0.01%
22	5.28	0.01%
23	5.02	0.01%
24	4.79	0.01%
25	4.80	0.01%

(a)

Converter Numbers at Ends of Cable Section		DC Losses (W/m)	Maximum AC Losses (W/m)	Maximum Total Losses (W/m)	Fundamental Ripple Current Component Magnitude (A)	Cable Rated Losses (W/m)
1	2	0.674	0.013	0.687	3.86	28.2
2	3	0.674	0.011	0.686	3.59	28.2
3	4	0.674	0.010	0.685	3.50	28.2
4	5	0.674	0.010	0.685	3.49	28.2
5	10	0.674	0.010	0.685	3.46	28.2
6	7	0.000	0.000	0.000	0.26	28.2
7	8	0.000	0.000	0.000	0.53	28.2
8	9	0.000	0.001	0.001	0.78	28.2
9	10	0.000	0.001	0.001	1.01	28.2
10	15	0.213	0.003	0.217	2.51	33.2
11	12	0.000	0.000	0.000	0.18	28.2
12	13	0.000	0.000	0.000	0.37	28.2
13	14	0.000	0.000	0.000	0.54	28.2
14	15	0.000	0.000	0.000	0.70	28.2
15	Shore	0.046	0.000	0.046	0.41	41.3
16	17	0.000	0.000	0.000	0.15	28.2
17	18	0.000	0.000	0.000	0.31	28.2
18	19	0.000	0.000	0.000	0.46	28.2
19	20	0.000	0.000	0.000	0.59	28.2
20	15	0.000	0.001	0.001	1.34	33.2
21	22	0.000	0.000	0.000	0.14	28.2
22	23	0.000	0.000	0.000	0.28	28.2
23	24	0.000	0.000	0.000	0.42	28.2
24	25	0.000	0.000	0.000	0.54	28.2
25	20	0.000	0.000	0.000	0.65	28.2

(b)

Table E.8. Single-phase SLR converter, only turbine 1 operating, turbine 1 at full power, C_{dc}=2μF.

Converter Number	Magnitude Fundamental Voltage Ripple (V)	Voltage THD
1	458.78	0.88%
2	420.52	0.81%
3	347.23	0.67%
4	247.31	0.48%
5	134.66	0.26%
6	328.27	0.63%
7	297.25	0.57%
8	237.70	0.46%
9	155.78	0.30%
10	60.77	0.12%
11	363.41	0.70%
12	328.69	0.63%
13	262.01	0.51%
14	170.16	0.33%
15	62.49	0.12%
16	296.16	0.57%
17	270.29	0.52%
18	220.61	0.43%
19	152.38	0.29%
20	73.65	0.14%
21	180.51	0.35%
22	164.91	0.32%
23	135.71	0.26%
24	98.70	0.19%
25	68.34	0.13%

(a)

Converter Numbers at Ends of Cable Section		DC Losses (W/m)	Maximum AC Losses (W/m)	Maximum Total Losses (W/m)	Fundamental Ripple Current Component Magnitude (A)	Cable Rated Losses (W/m)
1	2	0.627	0.162	0.789	13.58	28.2
2	3	2.510	0.597	3.107	26.47	28.2
3	4	5.648	1.130	6.777	36.64	28.2
4	5	10.043	1.551	11.594	43.08	28.2
5	10	15.698	1.704	17.402	45.25	28.2
6	7	0.628	0.101	0.729	10.74	28.2
7	8	2.513	0.370	2.883	20.87	28.2
8	9	5.655	0.699	6.353	28.85	28.2
9	10	10.056	0.958	11.014	33.90	28.2
10	15	19.877	1.038	20.915	44.12	33.2
11	12	0.629	0.127	0.755	12.05	28.2
12	13	2.515	0.465	2.979	23.40	28.2
13	14	5.659	0.879	6.538	32.35	28.2
14	15	10.064	1.206	11.269	38.02	28.2
15	Shore	26.628	0.004	26.633	4.08	41.3
16	17	0.628	0.070	0.698	8.94	28.2
17	18	2.513	0.258	2.771	17.40	28.2
18	19	5.655	0.487	6.142	24.06	28.2
19	20	10.056	0.668	10.724	28.28	28.2
20	15	19.877	0.588	20.465	33.23	33.2
21	22	0.627	0.028	0.656	5.70	28.2
22	23	2.510	0.104	2.613	11.04	28.2
23	24	5.648	0.195	5.843	15.24	28.2
24	25	10.043	0.267	10.310	17.91	28.2
25	20	15.698	0.293	15.991	18.81	28.2

(b)

Table E.9. Three-phase SLR converter, switching phases offset case 1, full power, C_{dc}=2μF.

Converter Number	Magnitude Fundamental Voltage Ripple (V)	Voltage THD
1	116.69	0.23%
2	115.93	0.22%
3	114.26	0.22%
4	111.85	0.22%
5	109.00	0.21%
6	110.12	0.21%
7	109.65	0.21%
8	108.61	0.21%
9	107.30	0.21%
10	106.05	0.21%
11	96.02	0.19%
12	96.65	0.19%
13	97.90	0.19%
14	100.08	0.19%
15	103.41	0.20%
16	110.12	0.21%
17	109.65	0.21%
18	108.61	0.21%
19	107.30	0.21%
20	106.05	0.21%
21	116.69	0.23%
22	115.93	0.22%
23	114.26	0.22%
24	111.85	0.22%
25	109.00	0.21%

(a)

Converter Numbers at Ends of Cable Section		DC Losses (W/m)	Maximum AC Losses (W/m)	Maximum Total Losses (W/m)	Fundamental Ripple Current Component Magnitude (A)	Cable Rated Losses (W/m)
1	2	0.627	0.000	0.627	0.22	28.2
2	3	2.510	0.000	2.510	0.54	28.2
3	4	5.648	0.001	5.648	0.82	28.2
4	5	10.043	0.001	10.044	1.00	28.2
5	10	15.698	0.001	15.700	1.09	28.2
6	7	0.628	0.000	0.628	0.52	28.2
7	8	2.513	0.001	2.514	0.97	28.2
8	9	5.655	0.002	5.656	1.34	28.2
9	10	10.056	0.002	10.058	1.58	28.2
10	15	19.877	0.003	19.880	2.51	33.2
11	12	0.629	0.001	0.629	0.97	28.2
12	13	2.515	0.003	2.517	1.77	28.2
13	14	5.659	0.005	5.664	2.39	28.2
14	15	10.064	0.006	10.070	2.78	28.2
15	Shore	26.628	0.012	26.640	6.75	41.3
16	17	0.628	0.000	0.628	0.52	28.2
17	18	2.513	0.001	2.514	0.97	28.2
18	19	5.655	0.002	5.656	1.34	28.2
19	20	10.056	0.002	10.058	1.58	28.2
20	15	19.877	0.003	19.880	2.51	33.2
21	22	0.627	0.000	0.627	0.22	28.2
22	23	2.510	0.000	2.510	0.54	28.2
23	24	5.648	0.001	5.648	0.82	28.2
24	25	10.043	0.001	10.044	1.00	28.2
25	20	15.698	0.001	15.700	1.09	28.2

(b)

Table E.10. Three-phase SLR converter, converters switching in phase, full power, C_{dc}=2μF.

Converter Number	Magnitude Fundamental Voltage Ripple (V)	Voltage THD
1	69.77	0.14%
2	67.17	0.13%
3	58.65	0.12%
4	44.84	0.09%
5	27.39	0.06%
6	38.46	0.08%
7	34.58	0.07%
8	27.30	0.05%
9	18.07	0.04%
10	11.31	0.02%
11	20.00	0.04%
12	17.98	0.04%
13	14.20	0.03%
14	9.39	0.02%
15	5.88	0.01%
16	11.85	0.02%
17	10.65	0.02%
18	8.41	0.02%
19	5.56	0.01%
20	3.48	0.01%
21	8.43	0.02%
22	7.58	0.02%
23	5.98	0.01%
24	3.96	0.01%
25	2.48	0.01%

(a)

Converter Numbers at Ends of Cable Section		DC Losses (W/m)	Maximum AC Losses (W/m)	Maximum Total Losses (W/m)	Fundamental Ripple Current Component Magnitude (A)	Cable Rated Losses (W/m)
1	2	0.674	0.011	0.685	3.43	28.2
2	3	0.674	0.014	0.688	3.96	28.2
3	4	0.674	0.024	0.699	5.35	28.2
4	5	0.674	0.037	0.712	6.65	28.2
5	10	0.674	0.046	0.720	7.40	28.2
6	7	0.000	0.002	0.002	1.45	28.2
7	8	0.000	0.007	0.007	2.81	28.2
8	9	0.000	0.013	0.013	3.88	28.2
9	10	0.000	0.017	0.017	4.56	28.2
10	15	0.213	0.010	0.224	4.35	33.2
11	12	0.000	0.001	0.001	0.75	28.2
12	13	0.000	0.002	0.002	1.46	28.2
13	14	0.000	0.003	0.003	2.02	28.2
14	15	0.000	0.005	0.005	2.37	28.2
15	Shore	0.046	0.000	0.046	0.38	41.3
16	17	0.000	0.000	0.000	0.45	28.2
17	18	0.000	0.001	0.001	0.87	28.2
18	19	0.000	0.001	0.001	1.20	28.2
19	20	0.000	0.002	0.002	1.41	28.2
20	15	0.000	0.003	0.003	2.23	33.2
21	22	0.000	0.000	0.000	0.32	28.2
22	23	0.000	0.000	0.000	0.62	28.2
23	24	0.000	0.001	0.001	0.85	28.2
24	25	0.000	0.001	0.001	1.00	28.2
25	20	0.000	0.001	0.001	1.05	28.2

(b)

Table E.11. Three-phase SLR converter, only turbine 1 operating, turbine 1 at full power, C_{dc}=2μF.

Appendix F: Publications

Two papers based on this research have so far been published or accepted for publication.

Ripple Current Propagation in Bipole HVDC Cables and Applications to DC Grids

T Wood, D E Macpherson, C Smith, S Finney.

This paper has been accepted for publication in the IEEE Transactions on Power Delivery.

HVDC Networks for Offshore Wind Power: Current Ripple and Cables

T B Wood, D E Macpherson, D Banham-Hall, S J Finney.

This paper was published at the 2012 IET ACDC conference.

References

[1] A. Dingley, edited by M. M. Karim, "Barrow Offshore wind turbines NR," Wikimedia Commons, 19 Apr 2009, available online: http://upload.wikimedia.org/wikipedia/commons/a/a7/Barrow_Offshore_wind_turbines_NR.jpg

[2] The Crown Estate, "Round 3 offshore wind site selection at national and project levels," May 2012, p26, available online: http://www.thecrownestate.co.uk/media/310531/round_3_offshore_wind_site_selection_at_national_and_project_levels.pdf

[3] C. Zhan , C. Smith, A. Crane, A. Bullock and D. Grieve, "DC Transmission and Distribution System for a Large Offshore Wind Farm," 9th IET International Conference on AC and DC Power Transmission, 19-21 October 2010, pp. 1-5

[4] F. Schettler, M-S. Balavoine, M. Callavik, J. Corbett, N. Kuljaca, V. S. Larsen, N. MacLeod, B. Sonerud, B. Jacobson, H. Laurie, C. Lemaitre and S. El Oukaili, "Roadmap to the Supergrid Technologies, Final Report," Friends of the Supergrid, March 2012, vailable online: http://mainstream-downloads.opendebate.co.uk/downloads/FOSG_WG2_Final-report.pdf

[5] The Crown Estate, "UK Offshore Wind Report 2012," 2012, available online: www.thecrownestate.co.uk

[6] Renewable UK: Renewable Energy, Wind Energy, Offshore Wind. Accessed 2 Aug 2013, available online: http://www.renewableuk.com/en/renewable-energy/wind-energy/offshore-wind/

[7] Scottish Enterprise, "Innovation in Offshore Wind: Support Structures," c.2011, available online: www.scottish-enterprise.com/~/media/SE/Resources/Documents/GHI/Innovation%20in%20Offshore%20Wind%20Foresighting%20Report.pdf

[8] Offshore Wind Cost Reduction Task Force, "Offshore Wind Cost Reduction Task Force Report," Jun 2012, available online:

https://www.gov.uk/government/uploads/system/uploads/attachment_data/file/66776/5584-offshore-wind-cost-reduction-task-force-report.pdf

[9] J. Phillips, O. Fitch-Roy, P. Reynolds and P. Gardner, "A guide to UK Offshore Wind Operations and Maintenance," GL Garrad Hassan, Jun 2013, available online: www.scottish-enterprise.com/~/media/SE/Resources/Documents/MNO/Offshore-wind-guide-June-2013.pdf

[10] M. Dicorato, G. Forte, M. Pisani and M. Trovato, "Guidelines for assessment of investment cost for offshore wind generation," Renewable Energy, Volume 36, Issue 8, August 2011, pp. 2043–2051

[11] The Crown Estate, "A Guide to an Offshore Wind Farm," accessed Nov 2013, available online: http://www.thecrownestate.co.uk/tcform/TandCsDialog?f=%2fmedia%2f211144%2fguide_to_offshore_windfarm.pdf&fn=A+guide+to+an+offshore+windfarm&m=1

[12] M. Dicorato, G. Forte, M. Pisani and M. Trovato, "Guidelines for assessment of investment cost for offshore wind generation," Renewable Energy, Volume 36, Issue 8, Aug. 2011, pp. 2043-2051

[13] M. Scheu, D. Matha, M. Hofmann and M. Muskulus, "Maintenance strategies for large offshore wind farms," Deep Sea Offshore Wind R&D Conference, 19-20 January 2012, pp. 281-288

[14] Elsevier Inc., "Offshore Wind Chapter 17: Repairing Offshore Wind Farms," 2012

[15] B. Pérez, R. Mínguez and R. Guanche, "Offshore wind farm layout optimization using mathematical programming techniques," Renewable Energy 53, 2013, pp. 389-399

[16] M. Méchali, R. Barthelmie, S. Frandsen, L. Jensen and P-E. Réthoré, "Wake effects at Horns Rev and their influence on energy production," Elsam Engineering and Risø National Laboratory, c.2006, available online: http://www.google.co.uk/url?sa=t&rct=j&q=wake%20effects%20at%20horns%20re

v%20and%20their%20influence%20on%20energy%20pro-%20%20duction%20&source=web&cd=1&cad=rja&ved=0CDUQFjAA&url=http%3A%2F%2Fwww.dongenergy.com%2Fsitecollectiondocuments%2Fnew%2520corporate%2Fpdf%2Fengineering%2F40.pdf&ei=dCwBUq7kJIj6PPrDgZAO&usg=AFQjCNF9SiAVzNK8GR15U3h1WSZkp4SHjQ&bvm=bv.50310824,d.d2k

[17] C. Meyer, M. Hoing, A. Peterson and R. W. De Doncker, "Control And Design of DC Grids for Offshore Wind Farms," IEEE Transactions on Industry Applications, Vol. 43, No. 7, Nov/Dec 2007, pp. 1475-1482

[18] J. Arrillaga, Y. H. Liu and N. R. Watson, "Flexible Power Transmission: The HVDC Options," Wiley-Blackwell, 24 Aug 2007

[19] M. O. Faruque, Y. Zhang and V. Dinavahi, "Detailed Modeling of CIGRÉ HVDC Benchmark System Using PSCAD/EMTDC and PSB/SIMULINK," IEEE Transactions on Power Delivery, vol. 21, no. 1, Jan 2006, pp. 378-387

[20] C-K. Kim, V. K. Sood, G-S. Jang, S-J. Lim and S-J. Lee. "HVDC transmission: power conversion applications in power systems," Wiley, 2009, pp. 235-242

[21] C. Gao, X. Jiang, Y. Li, Z. Chen and J. Liu, "A DC-Link Voltage Self-Balance Method for a Diode-Clamped Modular Multilevel Converter With Minimum Number of Voltage Sensors," IEEE Transactions on Power Electronics, Vol. 28, NO. 5, May 2013, pp. 2125-2139

[22] S. Rohner, S. Bernet, M. Hiller and R. Sommer, "Modelling, Simulation and Analysis of a Modular Multilevel Converter for Medium Voltage Applications," IEEE International Conference on Industrial Technology (ICIT), 14-17 Mar 2010, pp. 775-782

[23] S. Debnath and M. Saeedifard, "A New Hybrid Modular Multilevel Converter for Grid Connection of Large Wind Turbines," IEEE Transactions on Sustainable Energy, in Press, 2013

[24] R. Marquardt and A. Lesnicar, "New Concept for High Voltage – Modular Multilevel Converter," PESC Conference, 2004

[25] M. Davies, M. Dommaschk, J. Dorn, J. Lang, D. Retzmann and D. Soerangr, "HVDC PLUS – Basics and Principle of Operation," Siemens AG, 2009, available online: http://www.energy.siemens.com/br/pool/hq/power-transmission/HVDC/HVDC_Plus_Basics_and_Principle.pdf

[26] J. Qin and M. Saeedifard, "Predictive Control of a Modular Multilevel Converter for a Back-to-Back HVDC System," IEEE Transactions on Power Delivery, Vol. 27, No. 3, Jul 2012, pp. 1528-1547

[27] X. Li, Q. Song, W Liu, H Rao, S Xu and L Li, "Protection of Nonpermanent Faults on DC Overhead Line in MMC-Based HVDC Systems," IEEE Transactions on Power Delivery, Vol. 28, No. 1, Jan 2013, pp. 483-490

[28] O. Gomis-Bellmunt, A. Egea-Alvarez, A. Junyent-Ferre, J. Liang, J. Ekanayake and N. Jenkins, "Multiterminal HVDC-VSC for offshore wind power integration," IEEE Power and Energy Society General Meeting, pp. 1-6, 24-29 July 2011

[29] N. R. Chaudhuri, R. Majumder, B. Chaudhuri, J. Pan and R. Nuqui, "Modeling and Stability Analysis of MTDC Grids for Offshore Wind Farms: A Case Study on the North Sea Benchmark System," IEEE Power and Energy Society General Meeting, 24-29 July 2011, pp. 1-7

[30] A. A. van der Meer, R. L. Hendriks and W. L. Kling, "Combined Stability and Electro-Magnetic Transients Simulation of Offshore Wind Power Connected through Multi-Terminal VSC-HVDC," IEEE Power and Energy Society General Meeting, 25-29 July 2010, pp. 1-7

[31] D. Schmitt, Y. Wang, Th. Weyh and R. Marquardt, "DC-Side Fault Current Management in extended Multiterminal-HVDC-Grids," 9th International Multi-Conference on Systems, Signals and Devices (SSD), March 2012, pp. 1-5, 20-23

[32] F. Mura, C. Meyer and R. W. De Doncker, "Stability Analysis of High-Power DC Grids," IEEE Transactions on Industry Applications, vol. 46, no. 2, March/April 2010, pp. 584-591

[33] Y. Zhou, D. E. Macpherson, W. Blewitt, and D Jovcic, "Comparison of DC-DC converter topologies for offshore wind-farm application," Power Electronics, Machines and Drives Conference, 27-29 Mar 2012, pp. 1-6.

[34] F. Deng and Z. Chen, "Design of Protective Inductors for HVDC Transmission Line Within DC Grid Offshore Wind Farms," IEEE Transactions on Power Delivery, Vol. 28, No. 1, January 2013, pp. 75-83

[35] C. Meyer and R. W. De Doncker, "Design of a Three-Phase Series Resonant Converter for Offshore DC Grids," IEEE Industry Applications Conference, 42nd IAS Annual Meeting, 23-27 Sep 2007, pp. 216-223

[36] Based on discussions with GE Power Conversion

[37] EPCOS, "Aluminum Electrolytic Capacitors: General Technical Information," Nov. 2012, available online: http://www.epcos.com/web/generator/Web/Sections/ProductCatalog/Capacitors/AluminumElectrolytic/PDF/PDF__GeneralTechnicalInformation,property=Data__en.pdf

[38] Electronicon, "AC/DC Film Capacitors E51_E53_E55," 2013, available online: http://www.electronicon.com/fileadmin/inhalte/pdfs/downloadbereich/Katalog/neue_Kataloge_2011/E51_E53_E55.pdf

[39] Gab-Su Seo, Bo-Hyung Cho and Kyu-Chan Lee, "Electrolytic capacitor-less PV converter for full lifetime guarantee interfaced with DC distribution," 7th International Power Electronics and Motion Control Conference (IPEMC), 2-5 Jun 2012, Volume 2, pp. 1235-1240

[40] T. Worzyk, "Submarine Power Cables," Springer, 2009

[41] W. Thue, "Electrical Power Cable Engineering," Third Edition, CRC Press, 2012

[42] F. Deng and Z. Chen, "Design of Protective Inductors for HVDC Transmission Line Within DC Grid Offshore Wind Farms," IEEE Transactions on Power Delivery, Vol. 28, No. 1, January 2013, pp. 75-83

[43] R. Svoma, D.L. Williams, "Enhancing Power Cable Standards to Improve Reliability of Offshore Windfarms," PowerSure Technology Ltd, CIRED, 18th International Conference on Electricity Distribution, 6-9 Jun 2005

[44] Europacable, "An Introduction to High Voltage Direct Current (HVDC) Subsea Cables Systems," 16 July 2012, available online: http://www.europacable.com/images/Document_Uploads/Introduction%20to%20HVDC%20Subsea%20Cables%2016%20July%202012.pdf

[45] Based on Discussions with Paul Cunningham, Scottish Power

[46] ABB, "HVDC Light power cables: Submarine and land power cables," 2006, available online: http://www.google.co.uk/url?sa=t&rct=j&q=hvdc%20light%20cables%20submarine%20and%20land%20power%20cables&source=web&cd=3&cad=rja&ved=0CDcQFjAC&url=http%3A%2F%2Fwww05.abb.com%2Fglobal%2Fscot%2Fscot221.nsf%2Fveritydisplay%2F564b3711c060164dc1257b0c00552e50%2F%24file%2FHVDC%2520Light%2520power%2520cables.pdf&ei=UwEAUuXKNcnLPYXmgNAL&usg=AFQjCNHEVW9rol9oZFqbuO5TQ1Se2w8Ojg&bvm=bv.50165853,d.d2k

[47] NKT Cables, "High Voltage Cable Systems. Cables and Accessories up to 550 kV," 2009, available online: http://www.nktcables.com/support/download/catalogues-and-brochures/high-voltage-and-offshore/

[48] ABB, "XLPE Submarine Cable Systems: Attachment to XLPE Land Cable Systems - User's Guide," Apr 2010, available online: http://www.google.co.uk/url?sa=t&rct=j&q=xlpe%20submarine%20cable%20systems%3A%20attachment%20to%20xlpe%20land%20cable%20systems%20-%20user%C2%B4s%20guide&source=web&cd=1&cad=rja&ved=0CDYQFjAA&url=http%3A%2F%2Fwww05.abb.com%2Fglobal%2Fscot%2Fscot245.nsf%2Fveritydisplay%2F2fb0094306e48975c125777c00334767%2F%24file%2Fxlpe%2520submarine%2520cable%2520systems%25202gm5007%2520rev%25205.pdf&ei=PwcAUs

q5DIXfPZGdgfAH&usg=AFQjCNENkfbRsS9pSCdRwuQ4kBl-OLqq6Q&bvm=bv.50165853,d.d2k

[49] B. Gustavsen, J. A. Martinez, and D. Durbak, "Parameter Determination for Modeling System Transients—Part II: Insulated Cables," IEEE Transactions on Power Delivery, Vol. 20, No. 3, Jul 2005, pp. 2045-2050

[50] B. Gregory, "EHV Cable Systems- A Balanced View," IEEE Power Engineering Society Winter Meeting, Vol.1, 23-27 Jan, pp. 663 - 669

[51] W. H. Avery and C. Wu, "Renewable Energy From the Ocean," Oxford University Press, 1994, p. 181

[52] R. Stølan, "Losses and Inductive Parameters in Subsea Power Cables," MSc Thesis, Norwegian University of Science and Technology, Department of Electric Power Engineering, July 2009

[53] T. Kojima and A. MacPhail, "DC1 and DC2 submarine cable condition and life assessment," B. C. Hydro, Transmission Engineering Department, Cables Section, Mar 1999, pp. 9, 19

[54] S. Lundberg, "Performance comparison of wind park configurations," Department of Electric Power Engineering, Chalmers University of Technology, 2003, available online: http://www.google.co.uk/url?sa=t&rct=j&q=&esrc=s&source=web&cd=1&cad=rja&ved=0CC0QFjAA&url=http%3A%2F%2Fwebfiles.portal.chalmers.se%2Fet%2FReports%2FPCWPC_Reports.pdf&ei=WlIBUsmML6Ox0QW7poGgCA&usg=AFQjCNE2quNDwD-CX6U0GYP3UNjGffmAeA&bvm=bv.50310824,d.d2k

[55] C. H. Chien and R. W. G. Bucknall, "Analysis of Harmonics in Subsea Power Transmission Cables Used in VSC–HVDC Transmission Systems Operating Under Steady-State Conditions" IEEE Transactions Power Delivery, vol. 27, no. 4, Oct. 2007, pp. 2489–2497

[56] IEEE Guide on Shielding Practice for Low Voltage Cables, IEEE Standard 1143, Sep. 1994

[57] R. L. Stoll, "The Analysis of Eddy Currents," Clarendon Press, 1974

[58] W. D. Stevenson, Jr, "Elements of Power System Analysis," Second Edition, McGraw Hill Kogakusha, 1962, pp. 94-113

[59] Koppelius, "Rødsand_I_and_II," 10 Jun 2011, available online: http://commons.wikimedia.org/wiki/File:Rødsand_I_and_II.jpg

[60] M. Nandigam and S. K. Dhali, "Optimal Design of an Offshore Wind Farm Layout," International Symposium on Power Electronics, Electrical Drives, Automation and Motion, 11-13 Jun 2008, pp. 1470-1474

[61] S. Lumbreras and A. Ramos, "Optimal Design of the Electrical Layout of an Offshore Wind Farm Applying Decomposition Strategies," IEEE Transactions on Power Systems, Vol. 28, No. 2, May 2013, pp. 1434-1441

[62] The Hongkong Electric Co., Ltd., "Project Profile: Development of a 100MW Offshore Wind Farm in Hong Kong," Jul 2006, available online: http://www.google.co.uk/url?sa=t&rct=j&q=development%20of%20a%20100mw%20%20offshore%20wind%20farm%20in%20hong%20kong%20&source=web&cd=1&ved=0CDYQFjAA&url=http%3A%2F%2Fwww.epd.gov.hk%2Feia%2Fregister%2Fprofile%2Flatest%2Fesb151.pdf&ei=hy0BUoHQOInbOZqFgegB&usg=AFQjCNG5kQq3Tz3-37ba4-cmafTOv7KDxQ&cad=rja

[63] Cobham Technical Services, "Opera-2d Reference Manual, Version 15R1," Vector Fields Software, Mar 2012, pp. 372-374, 445

[64] Prysmian Cables & Systems, "High Voltage Cables," accessed Aug 2012, available online: http://www.google.co.uk/url?sa=t&rct=j&q=&esrc=s&source=web&cd=1&cad=rja&ved=0CC0QFjAA&url=http%3A%2F%2Fwww.prysmian.nl%2Fexport%2Fsites%2Fprysmian-nlNL%2Fattach%2Fpdf%2FPrysmian_HVC_LR.pdf&ei=RssQUryCMKGJ7Aa8wIGABg&usg=AFQjCNFNtVQJ2L1mkQLvhhLCGX_0t4pv_w&bvm=bv.50768961,d.d2k

[65] J. S. Barrett and G. J. Anders. "Circulating current and hysteresis losses in screens, sheaths and armour of electric power cables - mathematical models and comparison with IEC Standard 287," IEE Proceedings on Science, Measurement and Technology, vol. 144, no 3, May 1997, pp. 101-110

[66] J. D. Kraus, "Electromagnetics, Fourth Edition," Mcgraw-Hill Series in Electrical Engineering, 1991, p 502

[67] K. D. Patil and W. Z. Gandhare, "Effects of Harmonics in Distribution Systems on Temperature Rise and Life of XLPE Power Cables," International Conference on Power and Energy Systems (ICPS), 22-24 Dec 2011, pp. 1-6

[68] Premier Farnell UK Ltd, "Nexans 5603-AZZD Product Information," accessed Sep 2012, previously available online: http://uk.farnell.com/nexans/5603-azzd/cable-coax-urm67-per-m/dp/1218581?Ntt

[69] Andrew, Heliax, "Coaxial Cable Product Specification," Mar 2002, available online: http://www.rfparts.com/pdf_docs/AndrewHeliax/ LDF4-50a.pdf

[70] W. R. Smythe, "Static and Dynamic Electricity, Second Edition," McGraw-Hill Book Company, Inc., 1950, p393

[71] C. Fanggao, G. A. Saunders, R. N. Hampton, S. M. Moody and A. M. Clark, "The Effect of Hydrostatic Pressure and Temperature on the Permittivity of Crosslinked Polyethylene," Seventh International Conference on Dielectric Materials, Measurements and Applications, 23-26 Sep 1996, pp. 267-270

[72] O. E. Gouda, and Z. Matter, "Effect of the Temperature Rise on the XLPE Dielectric Properties," Proceedings of the 35th Midwest Symposium on Circuits and Systems, 9-12 Aug 1992, vol. 1, pp .95-98

[73] J. -N. Seguin, J. M. Fourmigue and J. L. Parpal, "Multiple dielectric relaxation mechanisms in XLPE cable insulation," Conference on Electrical Insulation and Dielectric Phenomena, 18 Oct 1992-21 Oct 1992, pp. 618-625

[74] P. D. Simon, J. T. Schmidt and B. K. Mumme, "Dynamic Nature of HVAC Induced Current Density on Collocated Pipelines," Corrosion 2007, Mar 11-15 2007

[75] M. Ormellese, L. Lazzari and A. Brenna, “AC-Induced Corrosion on Passive Metals,” Corrosion 2010, Mar 14-18 2010

[76] S. A. Papathanassiou and M. P. Papadopoulos, "Harmonic Analysis in a Power System with Wind Generation," IEEE Transactions on Power Delivery, vol. 21, no. 4, pp. 2006-2016, October 2006

[77] Siemens, "Siemens starts operating its first 6 megawatt wind turbine,” 9 Jun 2011, available online:

http://www.siemens.co.uk/en/news_press/index/news_archive/siemens-6-megawatt-wind-turbine.htm, 2011

[78] Q. Tu, Z. Xu, Y. Chang and L. Guan, "Suppressing DC Voltage Ripples of MMC-HVDC Under Unbalanced Grid Conditions," IEEE Transactions on Power Delivery, vol. 27, no. 3, Jul 2012, pp. 1332-1338

[79] M. Zubiaga, G. Abad, J. A. Barrena, S. Aurtenetxea and A. Carcar, "Spectral Analysis of a Transmission System based on AC Submarine Cables for an Offshore Wind Farm," 35th Annual Conference of Industrial Electronics, 3-5 Nov 2009, pp. 871-876

[80] Liangzhong Yao, "Experience on Technical Solutions for Grid Integration of Offshore Windfarms," AREVA T&D Technology Centre, 18 Jun 2007, available online:
http://www.google.co.uk/url?sa=t&rct=j&q=&esrc=s&source=web&cd=1&cad=rja&ved=0CDEQFjAA&url=http%3A%2F%2Fwww.we-at-sea.org%2Fwp-content%2Fuploads%2F2013%2F01%2FSessie-2_Liangzhong_Areva_Experience-on-technical-solutions-for-grid-intgration.pdf&ei=wCodUrDdA4mm0wWz2oCYBg&usg=AFQjCNHTbs0EHWb722sR7GzT1eDEWtMcsQ&bvm=bv.51156542,d.d2k

[81] C. H. Ng, M. A. Parker, L. Ran, P. J. Tavner, J. R. Bumby and E. Spooner, “A Multilevel Modular Converter for a Large, Light Weight Wind Turbine Generator,” IEEE Transactions on Power Electronics, Vol. 23, No. 3, pp.1062-1074, May 2008

[82] X. Yuan, “Multilevel Modular High Power Converters for 10MW Wind Turbines,” IEEE International Symposium on Industrial Electronics (ISIE), 28-31 May 2013, pp. 1-7

[83] X. Rong, “Design and Testing of a Series Load Resonant DC-DC Converter,” BEng Dissertation Thesis Bachelor of Engineering with Honours Electronics and Electrical Engineering, the University of Edinburgh, Mar 2013

[84] RS Components, “RS Components Part # 6655851 - URM 70 PVC Black,” 5 Jun 2008, available online: http://uk.rs-online.com/web/p/coaxial-cable/6655851/?origin=PSF_412604|alt

[85] Nexans Deutschland GmbH, "Submarine Power Cables,” Jun 2013, available online: www.nexans.co.uk/eservice/UK-en_GB/documentDownload_297/Power%20Submarine%20cables%20catalogue

[86] J. Yang, J. E. Fletcher and J. O'Reilly, "Multiterminal DC Wind Farm Collection Grid Internal Fault Analysis and Protection Design,” IEEE Transactions on Power Delivery, vol. 25, no. 4, Oct. 2010, pp. 2308–2318

[87] ABB, "ABB solves 100-year-old electrical puzzle – new technology to enable future DC grid,” Nov. 7 2012, available online:

http://www.abb.co.uk/cawp/seitp202/68594a4626d9ead0c1257aaf005885a3.aspx?utm_source

[88] Dynex Semiconductor Ltd, "Rectifier Diodes,” 2013, available online:

http://www.dynexpowersemiconductors.com/product-area/rectifier-diodes

[89] N. Barberis Negra, J. Todorovic and T. Ackermann, “Loss evaluation of HVAC and HVDC transmission solutions for large offshore wind farms,” Electric Power Systems Research, Volume 76, Issue 11, 2 May 2006, pp. 916-927

[90] G. Guidi and O. B. Fosso, “Investment Cost of HVAC Cable Reactive Power Compensation Off-shore,” Energy Conference and Exhibition (ENERGYCON), 9-12 Sep. 2012, pp. 299-304

[91] M. Zubiaga, G. Abad, J. A. Barrena, S. Aurtenetxea and A. Carcar, "Evaluation and selection of AC transmission lay-outs for large offshore wind farms," 13th European Conference on Power Electronics and Applications, 8-10 Sep 2009, pp. 1-10

[92] J. P. Coelingh, A. J. M. van Wijk and A.A.M. Holtslag, "Analysis of wind speed observations over the North Sea," Journal of Wind Energy and Industrial Aerodynamics, Volume 61, Issue 1, Jun. 1996, pp. 51-69

[93] E. Lozano-Minguez, A. J. Kolios and F. P. Brennan, "Multi-criteria assessment of offshore wind turbine support structures," Renewable Energy, Volume 36, Issue 11, Nov. 2011, pp. 2831-2837

[94] Siemens, "Siemens 6.0 MW Offshore Wind Turbine," 2011, available online: http://www.energy.siemens.com/hq/pool/hq/power-generation/renewables/wind-power/6_MW_Brochure_Jan.2012.pdf

[95] HM Government, "Levy Control Framework and Draft CfD Strike Prices," 2013, pp. 1-2, available online:

https://www.gov.uk/government/uploads/system/uploads/attachment_data/file/209361/Levy_Control_Framework_and_Draft_CfD_Strike_Prices.pdf

2Fprofile%2Flatest%2Fesb151.pdf&ei=hy0BUoHQOInbOZqFgegB&usg=AFQjCNG5kQq3Tz3-37ba4-cmafTOv7KDxQ&cad=rja

[96] London Metal Exchange, "Historical price graph for copper," accessed 28 Oct 2013, available online: http://www.lme.com/metals/non-ferrous/copper/#tab2

[97] Anixter, "Technical Information Handbook Wire and Cable," Fifth Edition, ISBN: 978-0-615-24926-1, 2013, p10

[98] Hubbell Power Systems, Inc., "Technical Data: A Reference for the Electrical Power Industry," 2008, p42, available online: www.hubbellpowersystems.com/literature/connectors/AEC-41.pdf

[99] Joseph. R. Davis, "Copper and Copper Alloys," ASM International, 15 Aug 2001

[100] Lexco Cable, "Galvanized Steel Strand - ASTM A475, A363 1x7, 1x19," 2006, available online: http://www.lexcocable.com/Galvanized-Steel-Strand.html

20%20offshore%20wind%20farm%20in%20hong%20kong%20&source=web&cd=1&ved=0CDYQFjAA&url=http%3A%2F%2Fwww.epd.gov.hk%2Feia%2Fregister%2Fprofile%2Flatest%2Fesb151.pdf&ei=hy0BUoHQOInbOZqFgegB&usg=AFQjCNG5kQq3Tz3-37ba4-cmafTOv7KDxQ&cad=rja

[101] J. F. Manwell, J. G. McGowan and A. L. Roger, "Wind Energy Explained," Wiley, 2002, pp. 315-316.

[102] Texas Instruments, " 8-PinHigh-PerformanceResonant ModeController," Mar 2009, available online: http://docs-europe.electrocomponents.com/webdocs/0e7a/0900766b80e7a9e2.pdf

[103] International Rectifier, "High And Low Side Driver," accessed Nov 2013, available online: http://docs-europe.electrocomponents.com/webdocs/0791/0900766b807910a1.pdf

[104] Vishay Semiconductors, "Schottky Barrier Rectifiers," 10 Aug 2007, available online: http://www.farnell.com/datasheets/13162.pdf

[105] Vishay Semiconductors, "Small Signal Fast Switching Diodes," 2 Oct 2012, available online: http://www.vishay.com/docs/81857/1n4148.pdf

[106] Ferroxcube, "TX36/23/15: Soft Ferrites," 1 Sep 2008, available online: http://www.farnell.com/datasheets/1595846.pdf

[107] Toshiba "Toshiba Field Effect Transistor: 2SK2613," 29 Jan 2010, available online: http://www.google.co.uk/url?sa=t&rct=j&q=&esrc=s&source=web&cd=2&cad=rja&ved=0CDsQFjAB&url=http%3A%2F%2Fwww.semicon.toshiba.co.jp%2Finfo%2Fdocget.jsp%3Fpid%3D2SK2613%26lang%3Den%26type%3Ddatasheet&ei=EJ1_

UuTgHqSV0QWDzYDgAw&usg=AFQjCNELemTdAh_E-Do6JLb7nX3NzgpviA&bvm=bv.56146854,d.d2k

[108] Aavid Thermalloy, "Economy narrow base low profile channel style heat sink," accessed Nov 2013, available online: http://www.aavid.com/products/standard/507302b00000g

[109] Panasonic, "Product Specification: CE-AAMX-CEM-0-5," 11 Mar 2013, available online: http://www.farnell.com/datasheets/1700589.pdf

[110] WIMA, "Metallized Polyester (PET) Capacitors in PCM 5mm," accessed Nov 2013, available online: http://www.farnell.com/datasheets/815363.pdf

[111] Panasonic, "Stacked Metallized Plastic Film Capacitor," accessed Nov 2013, available online: http://www.farnell.com/datasheets/817128.pdf

[112] Caddock Electronics Inc., "MP900 and MP9000 Series Kool-Pak ®," 2004, available online: http://www.caddock.com/Online_catalog/Mrktg_Lit/MP9000_Series.pdf

[113] Epcos, "ETD Cores And Accessories," accessed Nov 2013, available online: http://cpc.farnell.com/jsp/level5/module.jsp?moduleId=cpc/645384.xml